NASA CONTRACTOR REPORT

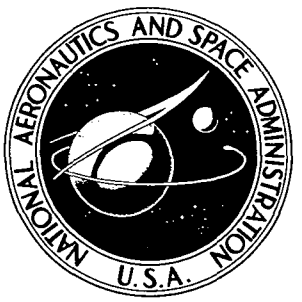

NASA CR-2484

NASA CR-2484

INVESTIGATION OF NORTHROP F-5A WING BUFFET INTENSITY IN TRANSONIC FLIGHT

by Chintsun Hwang and W. S. Pi

Prepared by
NORTHROP CORPORATION
Hawthorne, Calif.
for Ames Research Center

NATIONAL AERONAUTICS AND SPACE ADMINISTRATION • WASHINGTON, D. C. • NOVEMBER 1974

1. Report No.	2. Government Accession No.	3. Recipient's Catalog No.
NASA CR - 2484		

4. Title and Subtitle	5. Report Date
INVESTIGATION OF NORTHROP F-5A WING BUFFET INTENSITY IN TRANSONIC FLIGHT	November 1974
	6. Performing Organization Code
7. Author(s)	8. Performing Organization Report No.
Chintsun Hwang and W. S. Pi	
	10. Work Unit No.
9. Performing Organization Name and Address	
Northrop Corporation Aircraft Division Hawthorne, CA	11. Contract or Grant No. NAS 2-6475
	13. Type of Report and Period Covered Contractor Report
12. Sponsoring Agency Name and Address	
National Aeronautics and Space Administration Washington, D. C. 20546	14. Sponsoring Agency Code

15. Supplementary Notes

16. Abstract

The report describes a flight test and data processing program utilizing a Northrop F-5A aircraft instrumented to acquire buffet pressures and response data during transonic maneuvers. The data are presented in real-time format followed by spectral and statistical analyses. Also covered is a comparison of the aircraft response data with computed responses based on the measured buffet pressures.

17. Key Words (Suggested by Author(s))	18. Distribution Statement
Flight Test Buffet Transonic	UNCLASSIFIED-UNLIMITED CAT. 01

19. Security Classif. (of this report)	20. Security Classif. (of this page)	21. No. of Pages	22. Price*
UNCLASSIFIED	UNCLASSIFIED	179	5.50

*For sale by the National Technical Information Service, Springfield, Virginia 22151

TABLE OF CONTENTS

LIST OF ILLUSTRATIONS

LIST OF ILLUSTRATIONS (Continued)

LIST OF ILLUSTRATIONS (Continued)

LIST OF ILLUSTRATIONS (Continued)

LIST OF ILLUSTRATIONS (Continued)

INVESTIGATION OF NORTHROP F-5A WING BUFFET INTENSITY IN TRANSONIC FLIGHT

By Chintsun Hwang and W.S. Pi
Northrop Corporation, Aircraft Division
Hawthorne, California

SUMMARY

The report describes the findings and conclusions of a buffet flight test and data processing program entitled "Investigation of Buffet Intensity in Transonic Flight." The program used a fully instrumented Northrop F-5A aircraft to acquire buffet pressure and response data during transonic maneuvers. In the report, the detailed instrumentation, the data flow sequences, and the flight conditions used in the maneuvers are described. The dynamic buffet pressure and response data, as recorded by Pulse-Code Modulation (PCM) and FM systems, are presented in real-time format for general evaluation. These are followed by spectral and statistical processing procedures where the pressure and response spectral density functions and other statistical data are presented. Furthermore, the spatial correlation of the individual pressure data and the correlation between buffet pressure and aircraft response are described. Also covered is an analytical procedure to correlate the aircraft response data with computed responses based on measured buffet pressures.

Section 1

INTRODUCTION

Buffet is a dynamic behavior of aircraft flying at a high angle of attack. It occurs in the transonic region where the aircraft has substantial forward speed, and the angle of attack becomes large due to certain maneuvers initiated by the pilot. The initial phase of buffet is called buffet onset when noticeable vibrations or oscillations are observed. When the angle of attack is further increased, the aircraft responds to the dynamic buffet pressure with severe structural vibration which may be coupled with rigid body motion oscillations or control system-induced oscillations. This latter phenomenon of sustained, large-amplitude aircraft buffeting is called wing rock.

1.1 Background

As is well known, the major cause of aircraft buffet in the transonic region is flow separation on top of the wing surface when the angle of attack reaches a certain amplitude. The separated flow may be induced by a shock or by other disturbances. The dynamic loads exerted on the aircraft may be due to the instability of the shock (in intensity and location), or due to the dynamic pressure components of the turbulent flow especially in the separated region, or both. Furthermore, the separated flow wake may engulf the tail sections, which causes additional instability in the aircraft responses and deterioration of the flight control qualities.

Earlier work on aircraft buffeting may be traced to the associated subject of stalling flutter (References 1, 2, 3). Both stalling flutter and aircraft buffeting are caused by flow separation at high angle of attack. In stalling flutter, the airfoil motion (for instance, torsional motion) contributes to the cyclic flow pattern which causes a sustained oscillation. In aircraft buffeting, the structural elasticity usually is not a major contributing factor (at least in the initial phase of the transonic maneuver). The buffeting loads are aerodynamic in origin; they exist even if the aircraft, or aircraft model, is perfectly rigid.

The subject of aircraft buffeting started to attract the attention of designers and research workers in the 1950's when aircraft development reached such a stage that transonic flights and maneuvers became a routine matter. Typical works by Huston and associates appearing at that time are given as References 4 through 7. Wind tunnel investigations on airfoil or aircraft buffet in this period include those by Humphreys, Coe, Sutter, and associates (References 8, 9, 10, 11). A corresponding work carried out in England by Pearcey is given as Reference 12. Pearcey at a later date also wrote a very informative article on shock-induced separation and buffet loads (Reference 13).

Starting in 1960, research and development on aircraft buffeting were conducted at an accelerated pace. A large number of papers and reports were published dealing with the various aspects of aircraft buffet including theoretical treatment (e.g., References 14, 15), flight test evaluation (References 16, 17, 18), and wind tunnel testing (References 19 through 22). Still more recent works dealing with buffet of present-day and future aircraft are listed as References 23 through 30. Reference 26 describes the results of F-5A buffet flight tests, with emphasis on stability and control. Comprehensive buffet onset and wing tuft data and limited amounts of total and static pressure data were acquired in this test program. Reference 27 gives the buffet onset data of the F-8D based on both flight tests and wind tunnel tests. References 28 through 30 describe the buffet characteristics and the dynamic buffet loads of the YF-4E aircraft where the dynamic pressure components on the top surfaces of the wing were greatly affected by vortices generated at the leading edges and wingtips.

1.2 Basic Program Approach

The work described in this report deals with the flight test and data evaluations of the Northrop F-5A aircraft in transonic maneuver. A unique feature of the subject program involves the extensive dynamic pressure instrumentation using miniaturized semi-conductor type transducers. Both fluctuating buffet pressure and significant aircraft response data were recorded on a wideband FM recording system used for real-time and spectral analyses. For instance, using digital tapes generated from the precisely clocked FM data, spatial correlations (as a function of the time parameter) and normalized cross-covariance functions were generated between two pressure stations, between the pressure and the response function, and between two selected response functions.

Another feature of the subject program involved the spectral processing of the flight data using various time segments obtained during the transonic maneuver. The basic transonic maneuver was the wind-up turn executed at specific Mach number and starting altitude. The complete maneuver lasted from 12 to 18 seconds which included level flight entry, buffet onset, wing rock, recovery, and the intermediate stages. The data acquired in a small time segment of the maneuver (approximately two seconds, depending on frequency range) were assumed to be stationary so that auto- and cross-power spectra could be generated. The display of a set of power spectra generated for various time segments of the maneuver yielded results that illustrated the various phases of the buffet phenomenon.

To complement the flight test program, work was carried out to correlate the response data using the measured buffet pressure and analytical computation technique taking into account the aircraft structural and aerodynamic characteristics. The correlation procedure and other statistical processing techniques are described in a later section of the report.

In summary, the data evaluation and correlation work of the subject program consisted of the following specific tasks:

1. Make cross-spectral analysis of the wing pressures and compute the wing responses.
2. Make spectral analysis of the response parameters for comparison with the computations and with each other.
3. Determine the probability distribution of one of the wing response parameters.
4. Make other analysis as may appear useful in estimating buffet loads for general use.

The program was conducted under the sponsorship of Ames Research Center, National Aeronautics and Space Administration. The NASA program monitor was Mr. Donald Buell. At Northrop, Messrs. Carl Balmer and Merv Burne assumed major responsibilities in aircraft instrumentation and data recording. Mr. Frank Jacobs contributed to the digital data processing. Dr. Wilford Wong carried out the evaluation of the real-time data and contributed to the preparation of the report. The authors wish to acknowledge the assistance and support rendered by Northrop F-5 project personnel in both Dynamics Department and Aerodynamics Department. The F-5A aircraft bailment was arranged through Major Horace Russell of the Air Force Flight Dynamics Laboratory. The authors also wish to acknowledge the enthusiastic support of Mr. Charles Coe of NASA and Mr. Hugo Pink of Northrop.

1.3 Symbols and Units

$A_{(\ )}$	Fourier transform of the deterministic time function $e_{(\ )}$, seconds
b	Span (clean tips), meters
$b_r = \frac{1}{2} c$	Reference semi-chord, meters
B_e	Equivalent resolution bandwidth, Hz
c	Mean aerodynamic chord, meters
$C_{z\dot{\alpha}}$, $C_{z\alpha}$, $C_{m\dot{\alpha}}$, $C_{m\alpha}$, C_{mq}	Aerodynamic derivatives as defined in Chapter 6, Reference 59
$e_{(\ )}$	Deterministic time functions for various time segments
f	Frequency, Hz
f_c	Cutoff frequency, Hz
$F_{(\ )}$	Fourier transforms, newton/meter^2, etc.
$g_{(\ )}$	Modal structural damping coefficients
$g_{A_{(\ )}} = 1 + \epsilon_{(\ )} + \beta_{(\ )}$	$(1-\beta)$ · (Modal aero damping coefficients) + 1
G	Gravitational acceleration, meters/second^2
h	Flight altitude, meters
$I^a_{(\ )}$	Modal influence functions for various time segments, G/newton, etc.
$k_r = \omega b_r / V$	Reduced frequency
L	Maximum correlation lag, seconds
m	Total mass of the aircraft, kilograms
$m_{(\ )}$	Modal masses, kilograms
M_o	Mach number
n	Total number of time segments in Appendix III
N	Sample size
N_A, N_Y, N_Z	Longitudinal, lateral, and normal accelerations, multiples of G

p	Probability density function, meter^2/newton, etc.; also pressure load, newtons/meter^2
P	Cumulative probability distribution function
ΣP	Total force, newton
ΣPX	Total torsional moment, newton-meter
ΣPY	Total bending moment, newton-meter
$Q_{(\ )}$	Segmentwise stationary modal forces, newtons
r	Distance between two points, meters
$R_{(\ )}$	Correlation functions, (newton/meter^2), ^{2}, etc.
S	Reference length in Appendix I, meters; also reference area in Appendix III, meter^2
t, τ	Time, seconds
$t_{(\ )a}$	Initial time of various time segments, seconds
$t_{(\ )b}$	Terminal time of various time segments, seconds
T	Time span, seconds
$\Delta T = t_{(\ )b} - t_{(\ )a}$	Time span for each individual time segment, seconds
V	Aircraft speed, meters/second
V_c	Convection speed, meters/second
w	Structure deflection at a specified location, meters
x, y, z	Cartesian coordinates, meters
x_T	Truncated function of x(t) with time span T
α	Angle of attack, degrees
β	A factor defining the portion of induced pressures to be assigned to the upper wing surface
$\beta_{(\ )}$	$(1-\beta) \cdot$ (Imaginary part of modal aero-damping coefficients)
$\gamma^2_{(\ )}$	Coherence functions
δ	Spatial decay constant

δ_n	Leading edge flap angle, degrees
δ_f	Trailing edge flap angle, degrees
ϵ	Normalized standard error
$\epsilon_{(\ )}$	$(1-\beta)$. (Real part of modal aero-damping coefficients)
ζ	Relative magnitude of the induced pressure at the top wing surface to the measured pressure
$\mu_{(\ )}$	Mean values
θ	Phase angle, radians
ρ	Air density, kilograms/meter^3
ρ_o	Normalized auto-correlation function
$\rho_{(\ )}$	Correlation function coefficient or normalized cross-covariance functions
$\Phi(\ ), \Phi(\ )$	One-sided spectral density functions, (newton/meter^2)^2/Hz
$\widetilde{\Phi}_{(\ )}$	Raw estimate of the true power spectral density function $\Phi_{(\ )}$, (newton/meter^2)^2/Hz, etc.
$\sigma_{(\ )}$	rms values
$\omega = 2\pi f$	Circular frequency, radians/second
$\omega_{(\ )}$	Non-zero natural circular frequency, radians/second

Matrix Conventions

$[\ \ ]$	Square or rectangular matrix
$\{\ \ \}$	Column matrix
$[\ \ ]$	Diagonal matrix
$\lfloor\ \ \rfloor$	Row matrix
$[\ \ ]^T$	Transposed matrix
$[\ \ ]^{-1}$	Inverse matrix

Matrices

$[A]$	Wing subarea matrix associated with pressure transducers, meter^2
$[\bar{A}]$	Generalized AIC matrix, kilograms
$[A_F]$	Flutter characteristic matrix, newtons/meter
$[B_{(\ )}]$	Generalized work coefficient matrices due to external forces
$[C]$	Damping coefficient matrix corresponding to control point velocity, newton-second/meter
$[C_h]$	Oscillatory AIC matrix for control point motion
$[C_F]$	Generalized damping matrix, newton-second/meter
$\{f_{(\ )}\}$	Fourier transforms of modal force matrix, newtons; also Fourier transforms of collocation force matrix in Appendix I
$[g_F]$	Structural damping coefficient matrix
$\{h_{(\ )}\}$	Fourier transforms of deflection matrices corresponding to control points or reference point, meters or radians
$[H]$	Modal transfer function matrix, meters/newton; or radians/(newton-meter)
$[I_{(\ )}]$	Modal deflection influence function matrix for various time segments, meters/newton or radians/newton-meter
$[I^a_{(\ )}]$	Modal acceleration influence function matrix for various time segments, newton^{-1}, etc.
$[k_F]$	Generalized stiffness matrix, newtons/meter
$[k_{(\ )}]$	Structural stiffness matrices, newtons/meter
$[M_F]$	Generalized (modal) mass matrix, kilograms
$[M_{(\ )}]$	Mass matrix, kilograms, etc.
$[\overline{M}_{(\ )}]$	Generalized mass plus aero matrices, kilograms, etc.
$\{p_{(\ )}\}$	Measured pressure matrix for various time segments, newtons/meter^2

$[Q_{(\ )}]$	Modal shape matrices corresponding to pressure transducer locations
$[S_{(\ )}]$	Two-sided spectral density matrices, (newton/meter$^{2)2}$/(radian/second), etc.
$[T]$	Rigid modal shape matrix corresponding to control points, meters
$[W]$	Aeordynamic weighting matrix
$[X] = \left[[Q_F]\ [Q_R]\right]$	Modal shape matrix corresponding to pressure transducer locations, non-dimensional or meters
$[X_{(\ )}]$	Flexible modal matrix correspondings to control points or reference point, non-dimensional or meters
$[Y]$	Modal shape matrix corresponding to a specified accelerometer location, non-dimensional or meters
$[Z] = [H]^{-1}$	Modal impedance matrix, newtons/meter or newton-meters/radian
$[Z_R]$	Impedance matrix corresponding to the downward displacement and the pitch angle, newtons/meter, newton-meters/radian, etc.
$\left\{\alpha_{(\ )}\right\}$	Fourier transforms of modal amplitudes (generalized coordinates), meters or radians
$\left\{\epsilon_{(\ )}\right\}$	Error in series solution
$\left\{X_{(\ )}\right\}$	Eigenvector matrix corresponding to control points and reference point, meters or radians

Subscripts and Signs

$(\ )_1$	Refers to control points (Appendices I and III)
$(\ )_2$	Refers to reference point (Appendices I and III)
$(\ )_b$	Refers to buffet pressures
$(\ )_f$	Refers to modal forces; also refers to flexible modes in Appendix III
$(\ )_F$	Refers to flexible modes

$( )_i$	Refers to induced aerodynamic pressures
$( )_k$, $( )_l$	Refers to modes in Appendix III
$( )_m$	Refers to measured pressures
$( )_p$	Refers to pressures
$( )_r$, $( )_s$	Refers to time segments in Appendix III
$( )_R$	Refers to rigid body modes
$( )_\alpha$	Refers to modal amplitudes
$\lvert \quad \rvert$	Denotes absolute value
$\dot{( )}$	Denotes time derivative
$( )^*$	Denotes complex conjugate
$\overline{( )}$	Denotes complex mass which includes oscillatory aerodynamic effects
$\overline{( )}^2$	Denotes mean square value
$\Delta( )$	Denotes increment

Special Symbols

(N/M**2)**2/HZ	(newton/meter^2)^2/Hz
RW32B18	Strain gage at RH W.S. 32 designated B18, used with other gages to determine sectional bending moment
RW32B24	Strain gage at RH W.S. 32 designated B24, used with other gages to determine sectional bending moment
RW32S21S	Strain gage at RH W.S. 32 designated S21S, used with another gage to determine sectional shear force
RW32S44S	Strain gage at RH W.S. 32 designated S44S, used with another gage to determine sectional shear force
RW68B18	Strain gage at RH W.S. 68 designated B18, used with other gages to determine sectional bending moment
RW68T30	Strain gage at RH W.S. 68 designated T30, used with other gages to determine sectional torsional moment

Section 2

FLIGHT TEST PROGRAM

The buffet flight test program of the F-5A was carried out on a fully instrumented aircraft (No. 63-8372, N6009). This is the same aircraft used in a previous buffet test program which collected excellent data on buffet onset, wing surface tufts behavior, and other items of general interest (see Reference 26). As mentioned in Section 1, the objectives of the present program include the acquisition and processing of the dynamic pressure and response data covering all stages of the transonic maneuver. For this purpose, new and additional instrumentation was installed on the aircraft prior to the flight tests. Because the buffet pressures in the shock and separated flow region are at times quite transient in nature, and because the pressure spectrum covers a wide frequency range corresponding to all stages of the transonic maneuver, an FM recording system was installed on the aircraft to record the physical phenomenon.

2.1 Aircraft Configuration

The F-5A used in the test program was a single-seat fighter capable of carrying stores at wing fuselage pylon stations. Due to the requirements of another research program being carried out simultaneously on the same airplane, the test was conducted with two wingtip stores (AIM-9B Missiles) with guide rails; otherwise the wing was clean. A three-view drawing of the F-5A is shown as Figure 1.

The basic wing airfoil of the F-5A is a NACA 65A004.8 section modified as follows. From the 40% chord to the 66.6% chord, the thickness distribution corresponds to a NACA 004.8-64 airfoil. Aft of the 82% chord, the airfoil is composed of straight lines forming a 7° trailing edge angle. Between the 66.6% chord and the 82% chord, the section has been curve-fitted so that the ordinates, slopes, and curvature at the end points are continuous. The airfoil is cambered to a NACA (.65) 50 five-digit series mean line. The mean line ordinates are obtained by multiplying the standard NACA 250 series mean line by the ratio .65/2. The mean line is rotated so that

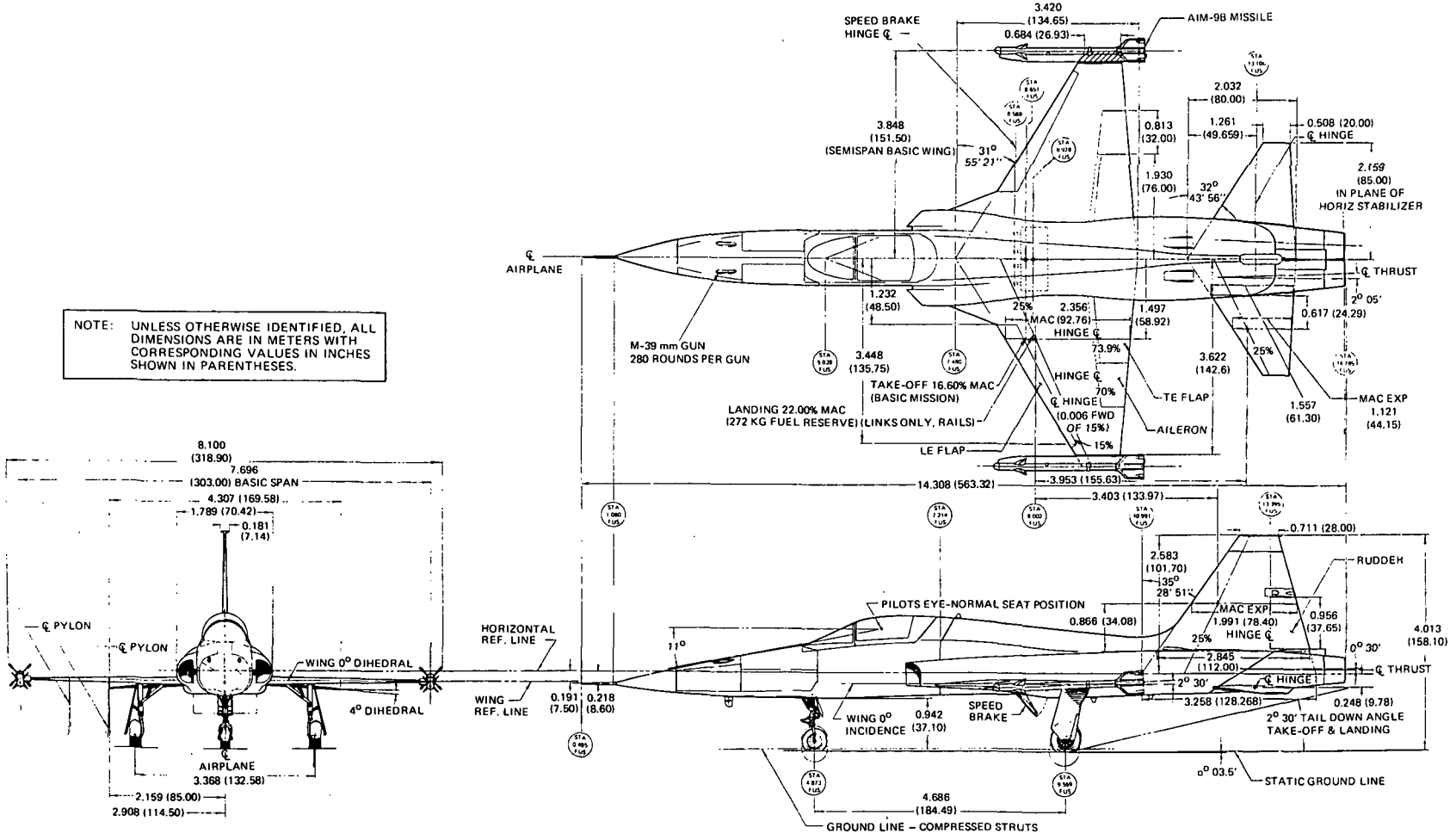

Figure 1. Three-View Drawing of F-5A Test Aircraft

the straight aft portion lies in the wing chord plane and the camber appears as a 1% leading edge droop. The airfoil is constant over the entire span.

For the flight test program, the leading edge flaps were fixed at 0° for some flights and at 4° for others. Likewise, the trailing edge flap systems were modified to provide flap travel limits of 0° to 8° for certain flights and 0° to 12° for others. (The flap could not be stopped at intermediate positions.) The basic wing airfoil section with variable flap configurations is shown in Figure 2.

Data Description of Wing

Area (Reference)	15.79 m^2	(170.00 ft^2)
Span (clean tips)	7.696 m	(25.25 ft)
Aspect Ratio	3.75	
Taper Ratio	.20	
Sweepback (25% Chord)	24°	
Mean Aerodynamic Chord (Reference)	2.356 m	(7.73 ft)
Thickness Ratio	4.8%	
Dihedral Angle	0	
Incidence Angle	0	
Root Chord	3.420 m	(11.22 ft)
Tip Chord	.683 m	(2.24 ft)
15% Chord Leading Edge Flap (with built-in twist) Deflection When Wholly Extended (Nominal flap deflection angle is measured at the root)	23° at the root 18° at the tip	
T.E. Flap Deflection When Wholly Extended	20°	
AIM-9B Missile Diameter	0.127 m	(5.00 in.)
AIM-9B Missile Length	2.832 m	(9.29 ft)

The horizontal tail of the F-5A is all-movable and has an unmodified NACA 65A004 section with the following physical dimensions and configurations:

Data Description of Horizontal Tail

Area, Total	5.48 m^2	(59 ft^2)
Area, Exposed	3.07 m^2	(33.03 ft^2)
Aspect Ratio, Exposed	2.88	
Sweepback (25% Chord)	25°	

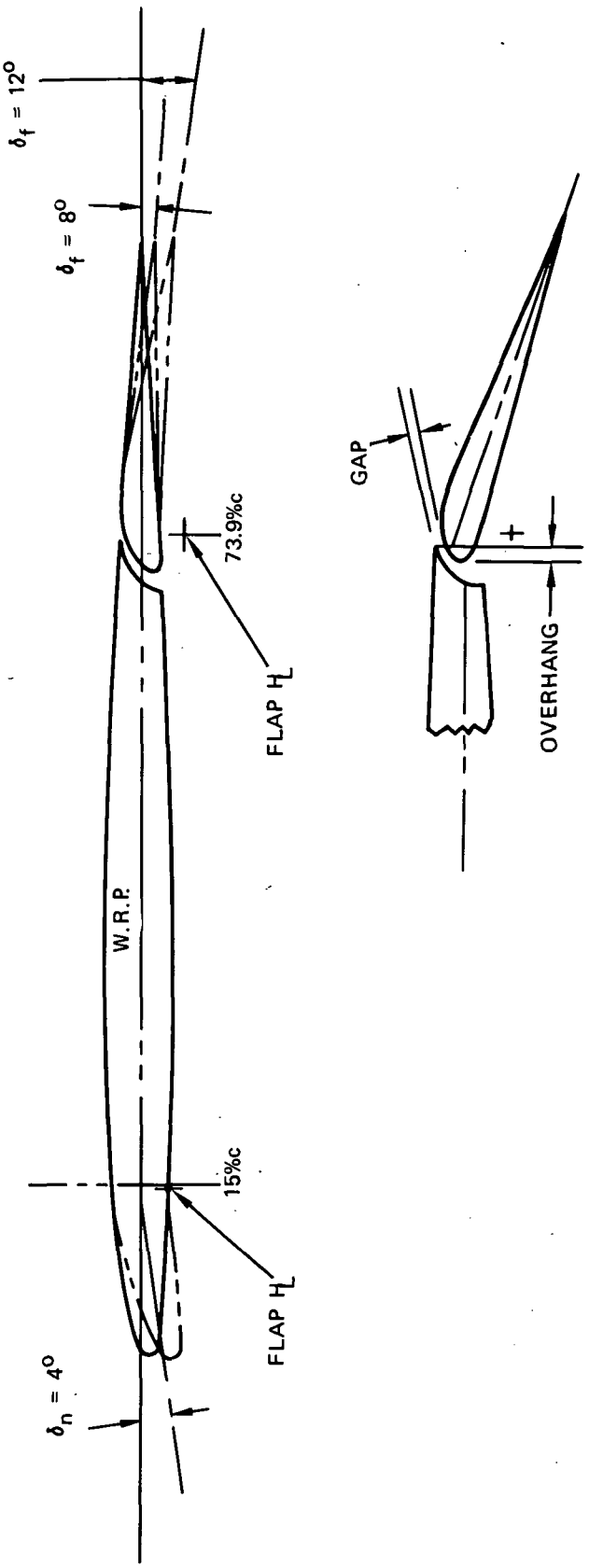

Figure 2. Wing Airfoil Section and Flap Configurations

Taper Ratio, Exposed	.33	
Cathedral Angle	4°	
Mean Aerodynamic Chord, Exposed	1.122 m	(3.68 ft)

The vertical tail airfoil is a modified NACA 65A004 section. The airfoil is composed of straight lines aft of the 72% chord. Between the 60% chord and 72% chord, the airfoil consists of a transition curve which matches the ordinate, slope, and radius of curvature of the true airfoil at 60% and the ordinate, slope, and infinite radius of curvature at the 72% chord.

Data Description of Vertical Tail

Area, Exposed	3.83 m^2	(41.2 ft^2)
Aspect Ratio, Exposed	1.22	
Taper Ratio, Exposed	.25	
Sweepback (25% Chord)	25°	
Mean Aerodynamic Chord, Exposed	1.990 m	(6.53 ft)

Useable Fuel, Weight, and Power Plant Data

Internal Fuel	1,719 KG, 2207 liters	(3,790 lbs, 583 gal.)
Aircraft Weight with Full Fuselage Tank and AIM-9B's	6,211 KG	(13,694 lbs)
AIM-9B Missile Weight (Including Launch Rail), Each	92.5 KG	(204 lbs)
Power Plant	2 (J85-GE-5) Turbo-jets with Afterburners	

2.2 Test Aircraft Instrumentation

In the flight test program, acquisition of data, other than flight condition parameters, was accomplished by a magnetic tape system utilizing digital pulse code modulation (PCM) and analog frequency modulation (FM) recording. The PCM data were recorded in serial format on two tracks of a 14-track, 2.54-cm-wide (1-inch) magnetic tape. Eleven tracks were utilized for FM recording and one track was used to record pilot's voice annotations and event mark signals. The wideband magnetic tape recorder, operating at 38.1 cm per second (15 inches per second), provided suitable frequency response characteristics and allowed 60 minutes of recording time on one tape reel. The FM data were subsequently digitized at a sample rate of 5,000 points per second to be used for real-time and spectral processing.

The PCM instrumentation installed in the test aircraft consisted of two encoding units, analog signal conditioning and presample data filtering equipment, synchro-to-digital and frequency-to-digital converters, a digital control unit, and a subsystem interface unit. The PCM encoders was used to perform analog signal multiplexing, analog-to-digital conversion, and digital output formatting. The system operated at a rate of 100,000 bits per second to output successive frames of 72 10-bit digital words (± 512 counts full-scale) in serial format at a rate of 138.9 frames per second. Direct entry of digital words from the synchro and frequency converters was accomplished by the digital control unit. The nominal frequency response of the PCM system operating at 138.9 samples per second was 30 Hz as established by the pre-sample data filters which rolled off at 18db per octave above 30 Hz to prevent aliasing of encoded data. Five parameters were recorded at a rate of 555.6 samples per second by cross-strapping together four prime channels each. These channels were provided with 120-Hz filters. All parameters recorded by the PCM system specifically for the buffet flight test program are listed in Table 1.

Since the buffet test program was carried out simultaneously with another flight test program, additional PCM data were recorded which were available to the present program. This point will be explained later relating to flight test data flow.

TABLE 1

PULSE CODE MODULATION RECORDING

Item	Parameter	Samples Per Second
1	Pressure Pickup No. 4, Upper RH W.S. 128.31,* 90%C (85% b/2)	556
2	19, Lower RH W.S. 128.31, 20%C (85% b/2)	
3	20, 60%C	
4	21, 90%C	
5	24, W.S. 93.00, 60%C (61% b/2)	
6	Normal Load Factor at C.G.	139
7	Longitudinal Load Factor at C.G.	
8	Normal Load Factor, RH Wingtip, Aft 80%C	
9	RH Wingtip, Fwd 30%C	
10	Pilot's Seat	
11	Lateral Load Factor, Pilot's Seat	
12	Angle of Attack, CADC (Central Air Data Computer) Output	
13	Pitch Rate	
14	Pitch Attitude	
15	Right-Hand Aileron Position	
16	Strain Gage, RH W.S. 127, Designated B40	
17	Right-Hand Trailing Edge Flap Hinge Moment	
18	Camera Frame	
19	Event Mark	

* Multiply Wing Station data by .0254 to obtain Station distance in meters.

An FM instrumentation system permitted recording of dynamic data at frequencies up to 1,600 Hz based on a modulation index of 5. Frequency multiplexing was used to carry three data parameters on each of the eleven FM recording tracks. The center frequencies of the discriminators were 64, 96, 128 KHz respectively. The bandwidth of the modulated frequency was ± 8 KHz. The parameters recorded in this manner are listed in Table 2. The details of the pressure transducers (PCM items 1 through 5, FM items 1 through 20) are described in a latter part of this subsection.

TABLE 2

FREQUENCY MODULATION RECORDING

Item	Parameter					
1	Pressure Pickup No.	1,	Upper RH	W.S. 128.31, *	20%C	(85% b/2)
2		2,			40%C	
3		3,			60%C	
4		4,			90%C	
5		5,		W.S. 110.30,	20%C	(72.8% b/2)
6		6,			40%C	
7		7,			60%C	
8		8,			75%C	
9		9,			90%C	
10		10,		W.S. 93.00,	20%C	(61% b/2)
11		11,			40%C	
12		12,			60%C	
13		13,		W.S. 71.40,	60%C	(47% b/2)
14		14,		W.S. 71.40,	80%C	(47% b/2)
15		15,		W.S. 50.00,	20%C	(33% b/2)
16		16,			40%C	
17		17,			60%C	
18		18,			80%C	
19		22,		W.S. 126.31,	75%C	(83.4% b/2)
20		23,		W.S. 71.40,	40%C	(47% b/2)
21	Strain Gage,	RH W.S. 32,	Designated B24			
22			Designated S21S			
23			Designated S44S			
24			Designated B18			
25		RH W.S. 68,	Designated B18			
26		RH W.S. 68,	Designated T40			
27	Normal Load Factor,		RH Wingtip, Fwd W.S. 144.85		30%C	
28			RH Wingtip, Aft W.S. 144.85		86%C	
29			C.G.			
30			LH Wingtip, Aft			
31	Right-Hand Aileron Hinge Moment					
32	Event Mark					

* Multiply Wing Station data by .0254 to obtain Station distance in meters.

Flight and engine condition instruments and aircraft system status lights were located on a panel and photographed by a 35mm frame-pulsed camera at one-second intervals. The parameters recorded are listed in Table 3.

TABLE 3

PHOTO-PANEL RECORDING

Item	Parameter
1	Indicated Airspeed, Production Boom
2	Pressure Altitude, Production Boom
3	Outside Air Temperature, Rosemount Probe
4	Left-Hand Fuel Quantity
5	Right-Hand Fuel Quantity
6	Event Light
7	Correlation Counter

2.3 Dynamic Pressure Transducers

To record the dynamic pressures, 24 miniaturized differential pressure transducers (SENSOTEC Model SD-M-7F) were installed on the right wing of the test aircraft. These pressure transducers had a diaphram sensor unit. Four-arm semiconductor gages connected in a bridge circuit were mounted on the internal face of the diaphram. Temperature compensation was achieved through thermistors and active temperature components (resistors) located within the transducers.

In addition to the four-wire bridge connection, each transducer had a reference pressure outlet which was connected to the reference source. The transducers selected for the test program had a diaphram diameter of 0.635 cm (0.250 inch) with 0.076 cm (0.030 inch) thickness and 1.270 cm (0.500 inch) overall length. The nominal pressure range was 1.724 N/cm^2 (2.5 psi) with an overpressure tolerance of 3.448 N/cm^2. In addition to the calibration data furnished by the manufacturer, the transducers were calibrated dynamically prior to installation using Photocon Acoustic Calibrator and B & K Microphone.

To minimize the interference to natural flow conditions, the transducers were flush-mounted on the right wing surfaces together with a 0.1016 cm (0.040 inch) plexiglass jacket assembled in 30.48 cm (12 inch) strips. The plexiglass jacket covered

almost 80% of the exposed area of the top surface and was laid in two 30.48 cm (12 inch) strips on the bottom surface. (The covered areas are indicated by the heavy outlines on Figure 3.) Prior to the jacket installation, all the transducer harness wires and reference pressure tubings were assembled and laid on the wing surface, and the terminals were led into the internal space of the wing structure through rivet holes. Properly located channels were cut on the underside of the plexiglass jacket, together with circular holes, prior to its bonding to the metal skin of the wing. These channels served to accommodate the transducer harnesses, while the circular holes were located where the pressure transducers were to be mounted. A 15-to-1 taper was cut on the outer circumference of the jacket to minimize flow interference. After the plexiglass sheets were trimmed and bonded by adhesives to the wing, the transducers were cemented in place and connected to the electric wirings and the reference pressure tubing (Figure 4). Pre-cut metal plugs were cemented over the remaining space of the circular hole to form a smooth airfoil surface on the wing. A photograph showing the top surface of the right wing after the installation of the pressure transducers is shown in Figure 5.

Internally, the reference pressure tubings from all transducers were plumbed into a common manifold chamber located inside the lower right hand section of the fuselage at F.S. 349.5*, where a precision altimeter also was installed. The pressure transducers, numbered 1-18, 22, and 23 on the top wing surface (see Figures 3 and 5), were listed as FM recording data entries in Table 2. The four pressure transducers at the bottom surface, designated Numbers 19, 20, 21, 24, were shown in Table 1 as PCM data entries. Pressure transducer Number 4 was connected to both FM and PCM systems to evaluate the recording system accuracies.

The signals from the pressure transducers were amplified through a two-stage amplifier unit with adjustable gains (BURR-BROWN Models 3620K-3621K). The signal conditioning circuit included a high-pass filter with 1/2-Hz cut-off frequency between the two amplifier stages. The signal from the first stage was input to the PCM system through a presampling (low-pass) filter. The signal from the second stage was input to the FM system so that the low-frequency and steady-state pressure data were not reflected in the FM data. A schematic showing the FM recording system for the upper Wing surface pressure transducers is given in Figure 6.

*Multiply Fuselage Station Number by .0254 to obtain Station distance in meters.

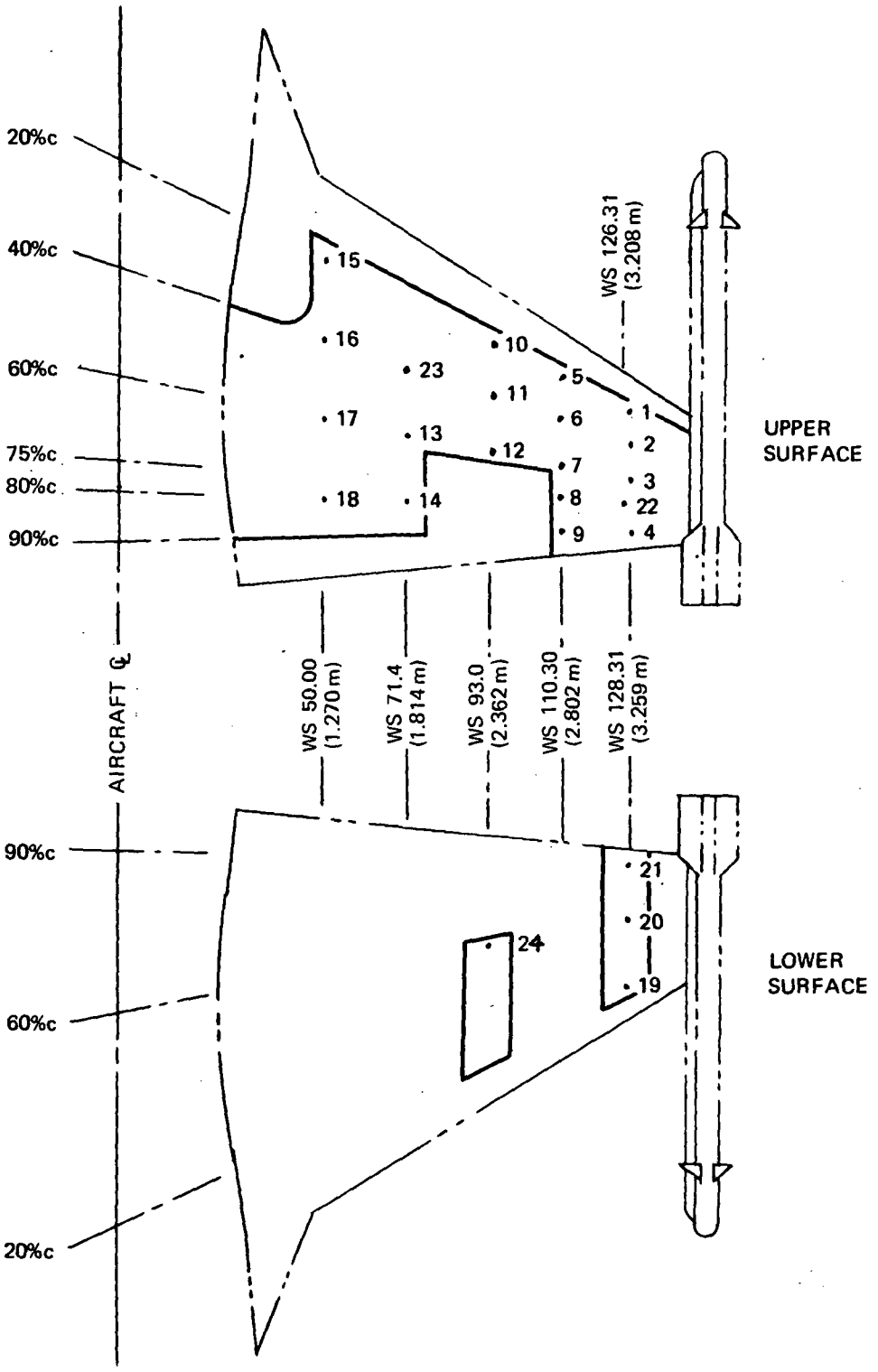

Figure 3. Dynamic Pressure Transducer Locations On F-5A Right Wing

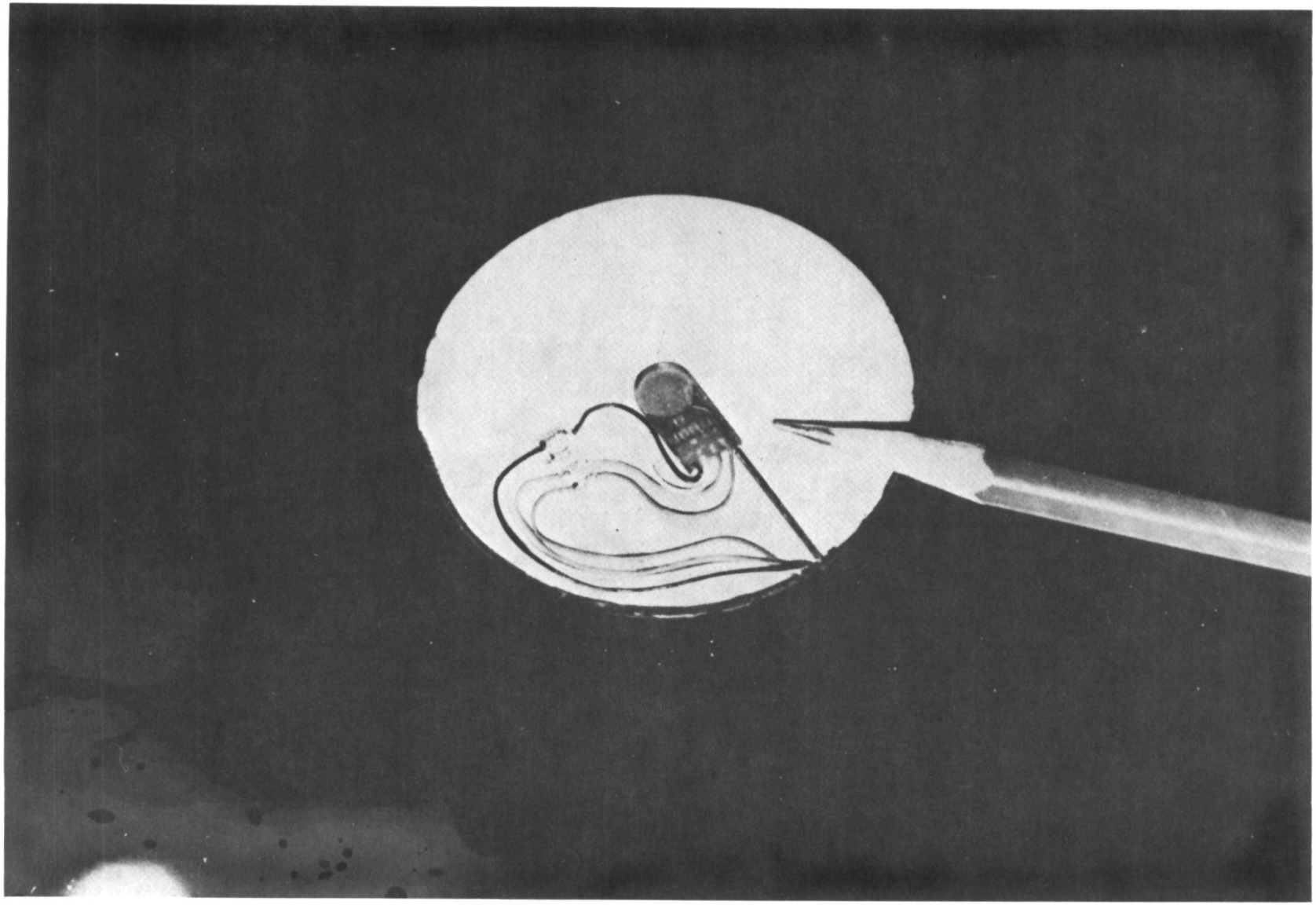

Figure 4. Sensotec Pressure Transducer Mounted on the F-5A Wing

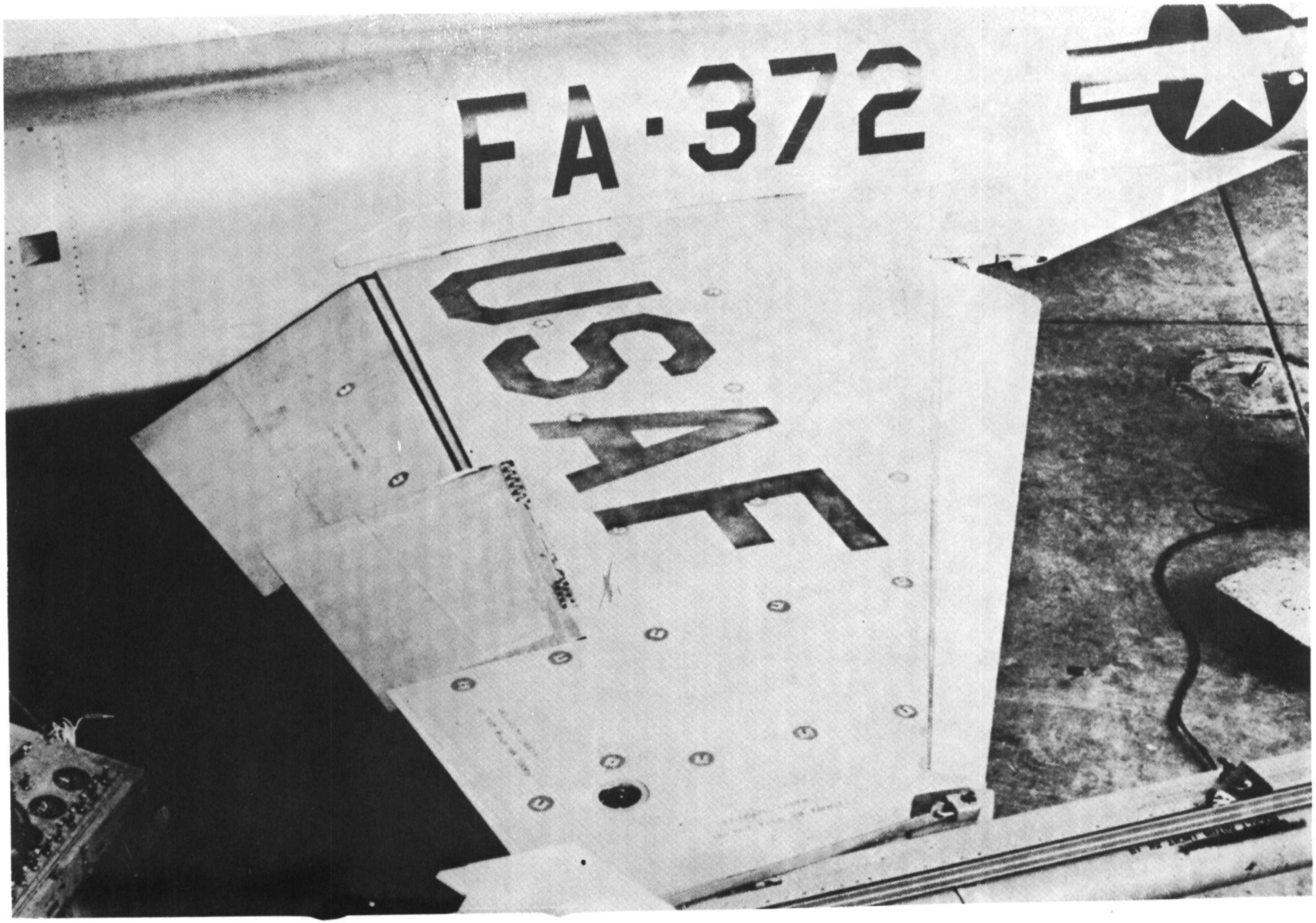

Figure 5. Right Wing of F-5A Aircraft After Installation of Dynamic Pressure Transducers

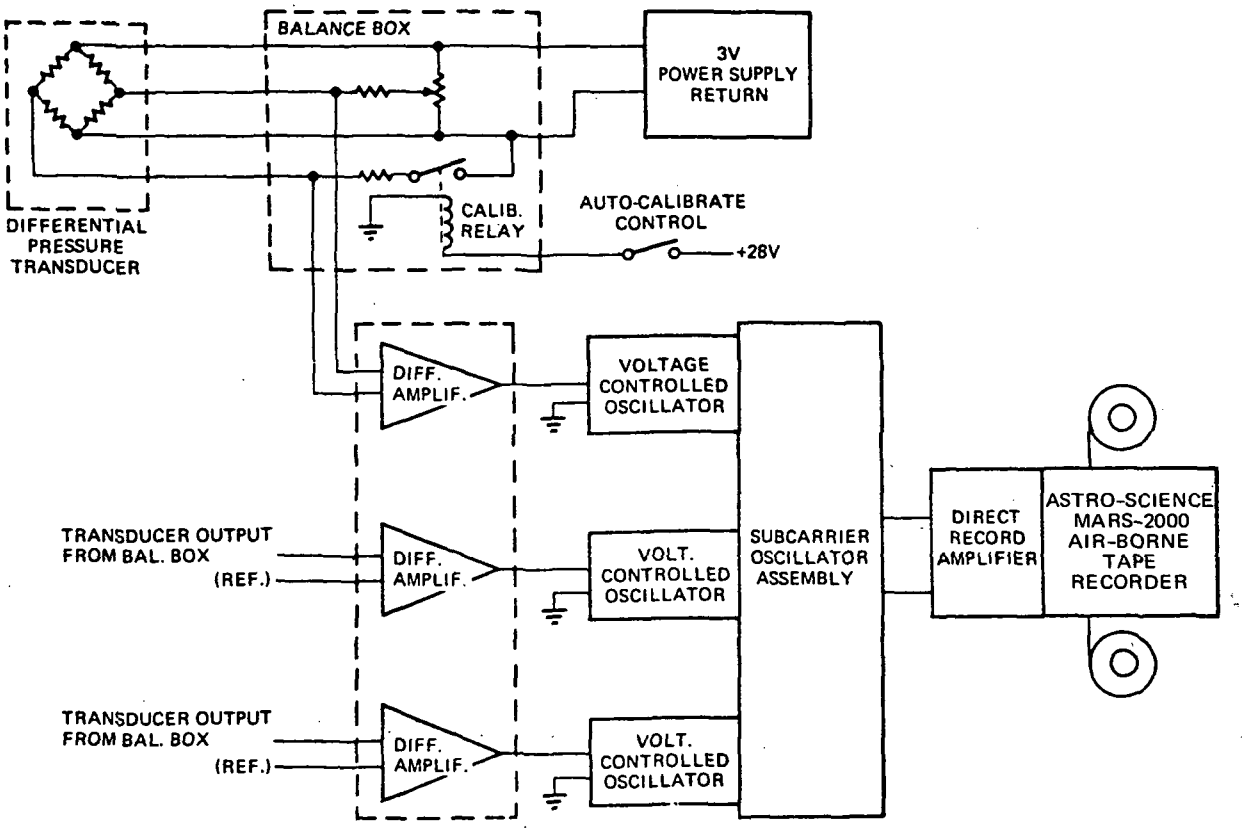

Figure 6. Recording Circuit-Upper Wing Differential Pressure Transducers

2.4 Data Flow and Processing Sequence

As mentioned previously, both FM and PCM recording systems were used in the flight test program. Figure 7 shows the PCM and telemetery data flow from test aircraft through the Edwards Air Force Base Test Facility to the Northrop Hawthorne Data Processing Facility. Except for differences in signal conditioning amplification and multiplexing techniques, as well as the final decoding and digital tape conversion, the FM data were handled in a similar flow pattern as the PCM data. Certain flight data parameters were recorded in addition to those listed in Table 1 (see Figure 7). These additional data were shared with a simultaneous flight test program and were used in the final buffet data evaluation. As part of the data flow concept, the Edwards Data Processing System provided quicklook data editing and instrumentation diagnostics from the flight data tape.

Upon completion of a test flight, the PCM data were played back from the airborne data tape. The recorded high-frequency analog channels were read out into FM discriminators which separated out each VCO frequency and demodulated the analog data. These high-frequency analog data were then recorded on oscillographs for preliminary editing operations. Further analysis of the analog data was performed on selected data segments at the Hawthorne Data Processing Facility. The Hawthorne Facility was equipped with tape playback machines, discriminators, digital-to-analog converters, and digitizing and transcribing equipment to process the buffet test data. Quick evaluation of PCM and FM recording was performed by transcribing the data on an oscillograph tape to determine periods of interest for further processing. The data flow to the computer and to the SC-4020 system is shown in Figures 8 and 9, respectively. Photo recorder data which were eventually integrated into the other recorded data flow also were reduced.

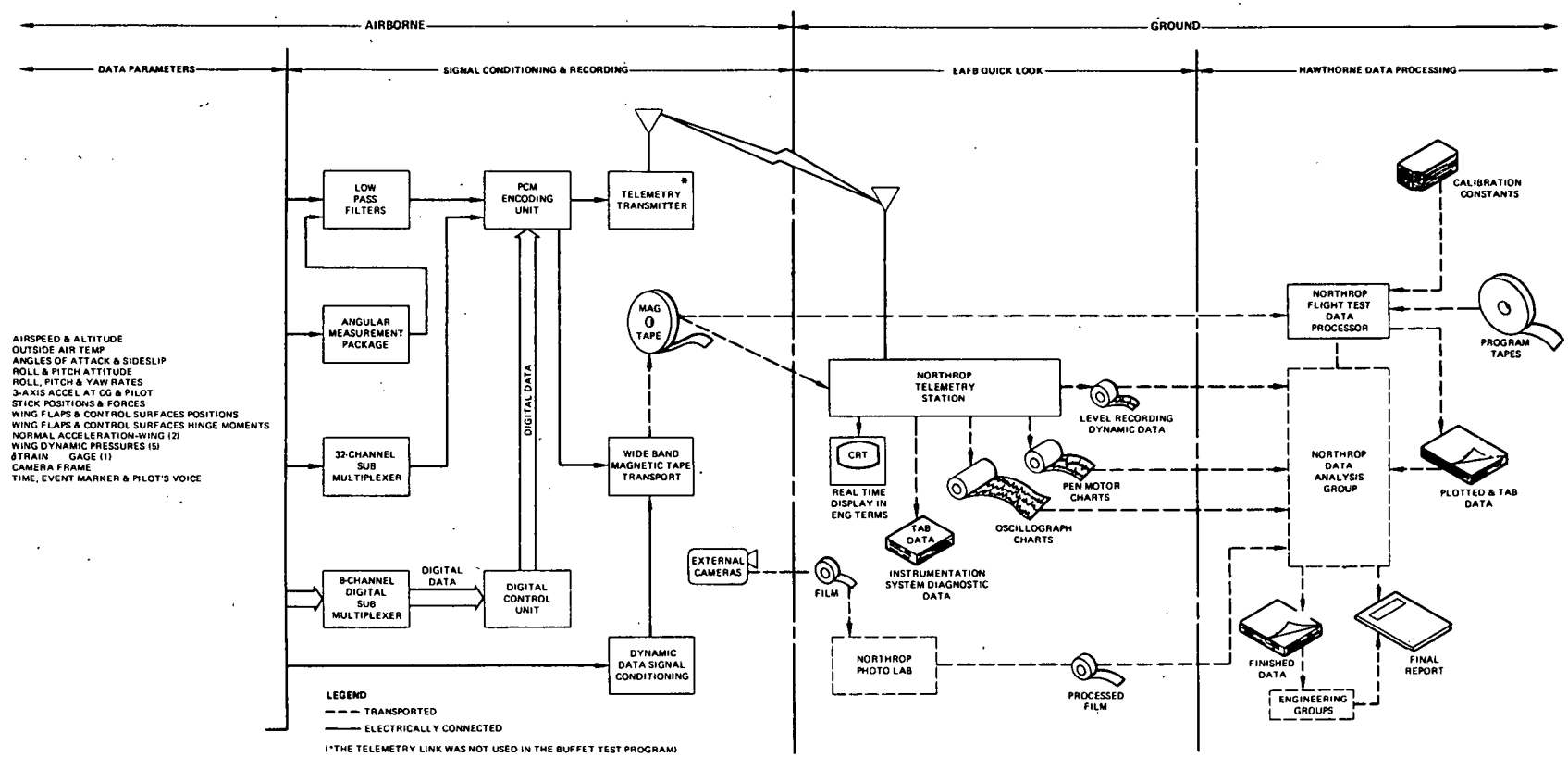

Figure 7. Flight Test Data Flow Diagram

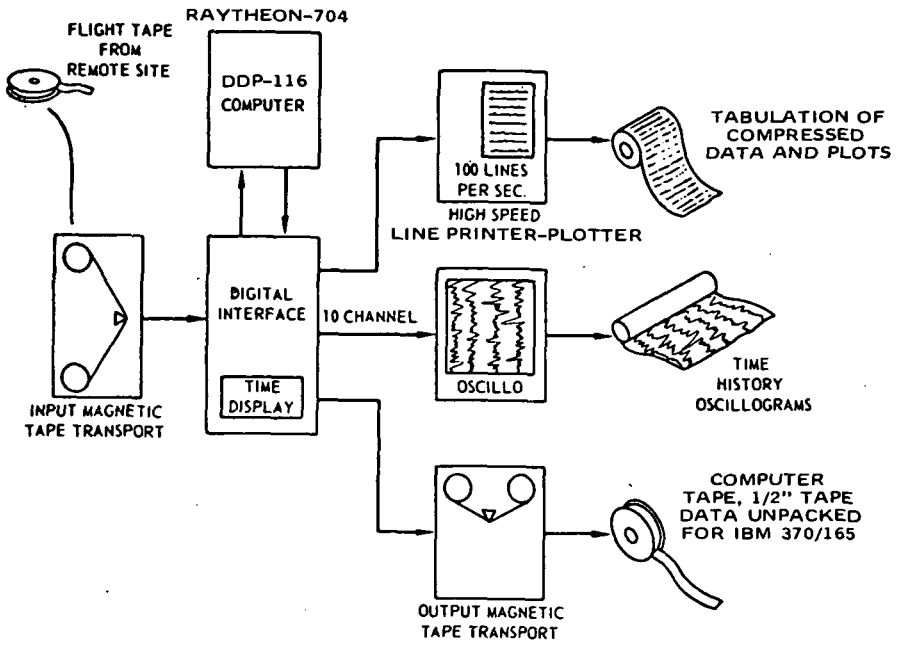

FIGURE 8. DATA FLOW TO COMPUTER FOR BUFFET TEST PROGRAM

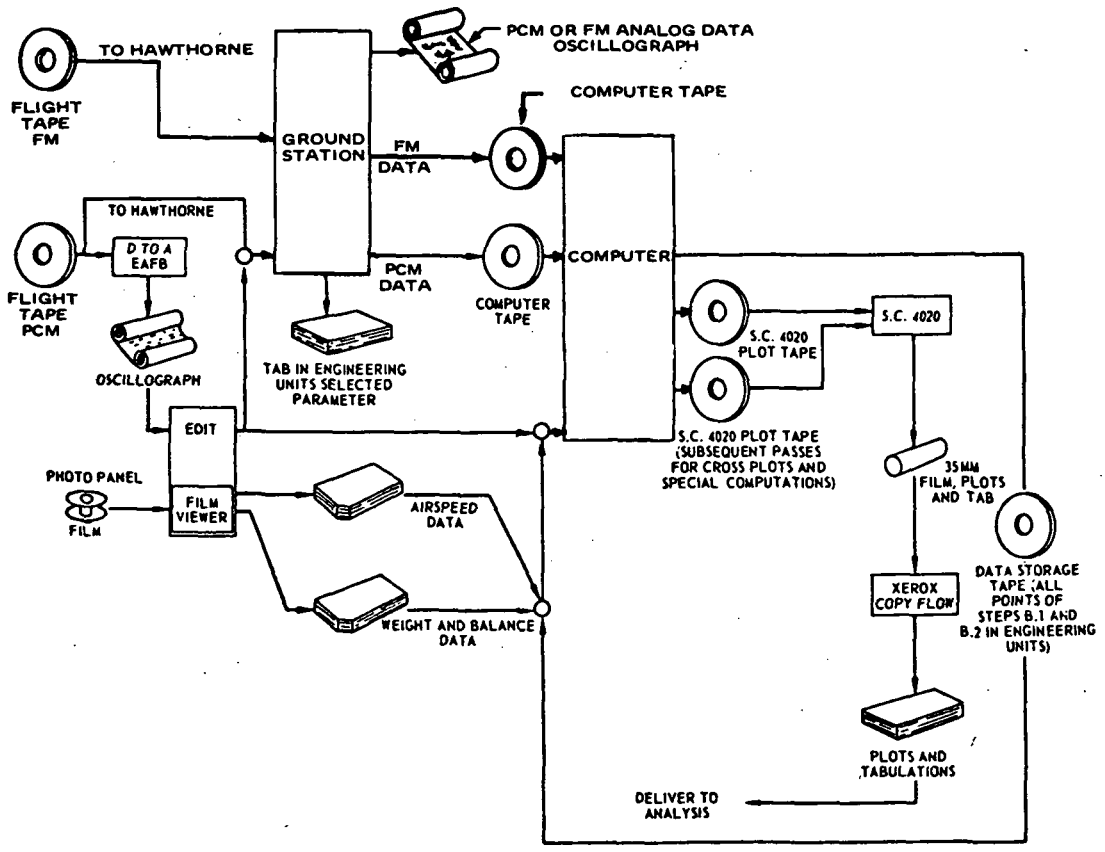

Figure 9. Data Flow to SC 4020 for Buffet Test Program

2.5 Flight Conditions

The basic maneuver used in the test program was the wind-up turn at constant Mach number. Specifically, wind-up turn maneuvers to maximum lift were performed corresponding to the configurations and flight conditions of Table 4. Prior to each maneuver, the aircraft was held in level flight at the desired test condition for 60 seconds or more to stabilize the transducer reference pressure, etc. Data were recorded from 1-G level flight through recovery from the maneuver. The speed brakes remained closed and the wing flap settings were maintained throughout each maneuver. The tests were conducted in a manner such that full aft stick was attained for 7 to 12 seconds after maneuver initiation. Satisfactory data were obtained from at least two maneuvers for each condition. Furthermore, roller-coaster maneuver from -0.5G to 1.8G load factor was performed during each flight at 7,620 m (25,000 ft), and 0.70 Mach number to provide the zero-G strain gage response references necessary for computation of absolute values of W.S. 32 bending moment, shear, and torsion loads.

The altitude-Mach number combination (Table 4) chosen for the wind-up turns was selected based on a constant q of approximately 14.36×10^3 N/M^2 (300 psf). The three conditions are plotted on the speed profile of the F-5A corresponding to various gross weight figures (see Figure 10).

TABLE 4

TEST CONFIGURATIONS AND FLIGHT CONDITIONS

Configuration Number	Flap Position (Degrees) LE	Flap Position (Degrees) TE	Wingtip Configuration	Test Conditions: Altitude m (ft)	Test Conditions: Mach. No.
1	0	0	AIM-9B Missiles	7,772 (25,500)	.75
				9,449 (31,000)	.85
				10,668 (35,000)	.925
2	0	8	↓	↓	↓
3	0	12			
4	4	0			
5	4	8			
6	4	12			

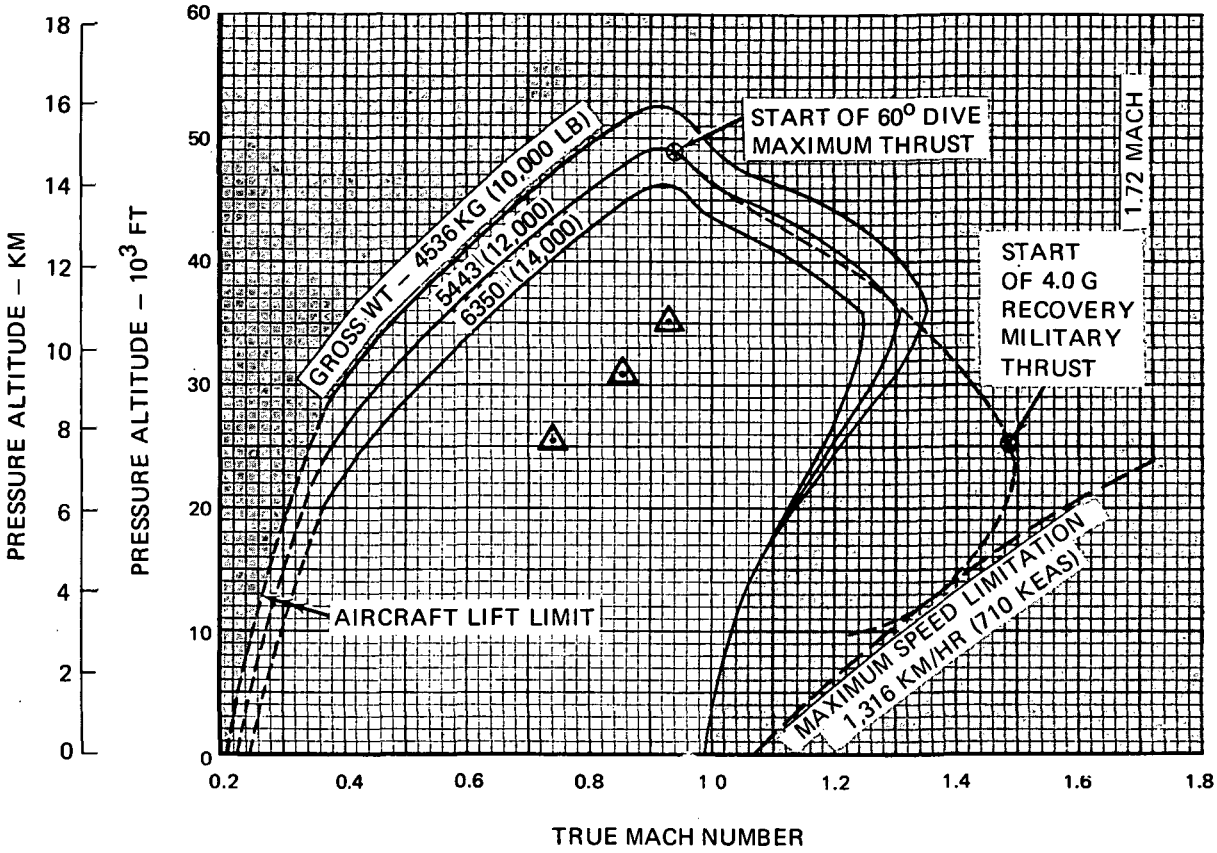

Figure 10. Speed Profile of F-5A with Maximum Thrust and (2) AIM-9B Missiles (Buffet Test Conditions Are Marked by Triangles)

SECTION 3

BUFFET DATA ACQUISITION AND INITIAL PROCESSING

Following extensive ground checkout of test aircraft new instrumentation, including the dynamic pressure transducers, the associated signal conditioning and amplifier circuits, the FM recording system, etc., shakedown flights were made in late 1971. The actual buffet flight tests were conducted starting in February 1972. All the flight conditions specified in Table 4 were performed and the data recorded. After a fast scan of flight test results, the recorded data were converted into digital tapes which were subjected to both real-time and spectral processing. In this section, the processing and evaluation of the real-time buffet data are described, followed in a subsequent section by the spectral analysis of the same data.

The manner by which the transonic maneuver tests were carried out is described below. Prior to entering the basic maneuver (the wind-up turn), the pilot maintained the aircraft at the specified altitude and Mach number. The maneuver was executed by a combined turn and roll motion at maximum thrust. The aircraft was allowed to lose altitude so that the Mach number was maintained. In a typical wind-up turn at the test altitude range, 7,772 to 10,668 m (25,500 to 35,000 ft), the lost altitude was in the range of 152-305 m (500-1000 feet). During this time, the angle of attack was increased gradually to a maximum value. As the angle of attack increased, the buffet onset was first encountered. The buffet onset could be detected either based on instrumentation (e.g., accelerometer under the pilot seat) or based on pilot perception. As the angle of attack reached its maximum, sustained structural vibration of the aircraft (i.e., wing rock) took place. Wing rock usually was accompanied by severe rigid body oscillations such as the yaw and pitch motions. The structural vibrations and the rigid body oscillations both affected and degraded the aircraft's tracking ability. To terminate the maneuver, the pilot pushed the stick forward and returned the aircraft to a level position.

Typical oscillographs giving time histories of the angle of attack, the sideslip angle, the roll angle, and the lift coefficient (computed) of a wind-up

turn are shown in Figures 11 and 12. The data were collected in a previous program (Reference 26) with M_o = 0.89 and altitude h = 10,668 m (35,000 ft). The oscillographs clearly showed the oscillatory motions of the aircraft during the maneuver as the angle of attack increased. They are typical and similar to data collected in the present program and are described in the following subsections.

3.1 PCM Data

During the buffet flight test program, both the PCM and FM recording systems were activated. The PCM system recorded most flight condition parameters as well as the dynamic pressure data on the bottom surface of the right wing (4 transducers) plus Pressure Transducer No. 4 on the top surface (see Figure 3). The data passed through the presampling (low-pass) filters which retained the steady-state* and low-frequency components up to 30 Hz (120 Hz for super-commutated PCM data). The data were valuable in assessing the general behavior and response of the aircraft during the maneuver. This was in contrast to the FM data which were screened by the high-pass filters so that the dynamic components related to shock and shock oscillation could be amplified and studied in detail by eliminating the steady-state data. Typical PCM data recorded in Flight 825 are presented in this subsection. In Run Number 5 of the flight, the Mach number was 0.925 and the initial altitude was 10,668 m (35,000 ft). The leading edge and trailing edge flaps were in retracted position during this run.

Figure 13 shows the pitch, roll, and yaw rate time histories during the wind-up turn. The elapsed time in seconds as recorded on the flight recorder magnetic tape is entered on top of the oscillographs. Also attached is the instantaneous angle of attack data retrieved from another PCM channel. The data showed that the aircraft entered the maneuver with a combined roll and yaw motion at least 1 second before the angle of attack increased significantly. At the time interval when the angle of attack was highest, significant low frequency roll oscillation was observed which was consistent with the general definition of "wing rock."

Figure 14 gave the pilot seat lateral and normal accelerations N_Y, N_Z during the maneuver. Referring to the figure, the peak load factor appeared at the time span

*The steady-state data as defined here indicate the instantaneous mean values after the dynamic components above approximately 1/2 Hz have been extracted. Since the transonic maneuver was dynamic in nature, all the physical data varied with time, including the so-called steady-state data.

when wing rock took place. A negative load factor was recorded during the recovery stage of the wind-up turn.

Typical PCM recordings of the dynamic pressure transducer "steady state" output are given in Figure 15 made for the same run (Run 5, Flight 825). The oscillographs were transcribed from a single PCM data set as compared to the digital tape data which were compiled from the super-commutated PCM data sets. (Reference Section 2.2.) Pressure Transducer Number 4 was located at 85% semi-span and 90% chordwise position at the top surface of the right wing. The data showed a substantial decrease in pressure (increase in lift) as the angle of attack increased. This is consistent with the flow behavior prior to and during the development of a shock induced separation wake on the airfoil surface.

The remaining traces of Figure 15 give the steady-state and low-frequency pressure data on W.S. 128.31 (85% semi-span) at the bottom surface of the right wing. The three traces were for 20%, 60%, and 90% chordwise positions (Transducer Numbers 19, 20, and 21) respectively. As the angle of attack increased, the pressure increased correspondingly at 20% and 60% positions, with the increase at the 20% position substantially higher than that at 60%. A decrease in steady-state pressure was registered at 90% chordwise position due to the wake flow developed at the trailing edge area and the upstream shock on the top surface. The pressure data of Figure 15 were pressures relative to a static source registered in the manifold chamber at F.S. 349.5. At this altitude, 10,668 m (35,000 ft), the aircraft lost approximately 259 m (850 ft) during the maneuver. The reference pressure increased approximately 1372 N/M^2 (0.199 psi) corresponding to the drop in altitude. This substantial variation in reference pressure during the transonic maneuver should be considered in evaluating the steady-state pressure data.

Figure 16, taken from Reference 13, gives a qualitative description of the shock and separated flow development on a two-dimensional airfoil as the angle of attack is increased, while the Mach number is kept constant. Recognizing the significant difference of a two dimensional flow and the effect of the airfoil thickness, etc., Figure 16 is nevertheless included here to assist in visualizing the shock formation and movement and the corresponding steady state pressure changes.

The set of PCM data as presented, based on Run 5, is concluded with Figure 17, which gives the normal and longitudinal accelerations (N_Z, N_A) at the C.G. of the aircraft as well as the normal accelerations recorded at two stations of the right-hand wingtip.

The normal acceleration at the C.G. was similar in general pattern to those under the pilot seat (Figure 14, top trace), while the amplitude was somewhat lower at the cg, as was to be expected. The wingtip normal accelerations indicated that structural vibrations were superimposed over the rigid body motions of the aircraft. The dynamic components of the wing accelerations will be discussed later in the report.

At lower altitude, 7,772 m (25,500 ft), and lower Mach number, $M_o = 0.75$, a test run (Run 7) was made in Flight 825. In general, the steady-state pressure pattern was similar to the previous case ($M_o = 0.925$, h = 10,668 m), while the amplitudes were somewhat lower for the lower Mach number case. Correspondingly, the load factor oscillographs showed the same general pattern with relatively lower peak amplitudes. The normal and longitudinal accelerations at cg and the wingtip normal acceleration data for Run 7 are given in Figure 18. The data may be compared with those of $M_o = 0.925$ (Figure 17) to observe the Mach number effect.

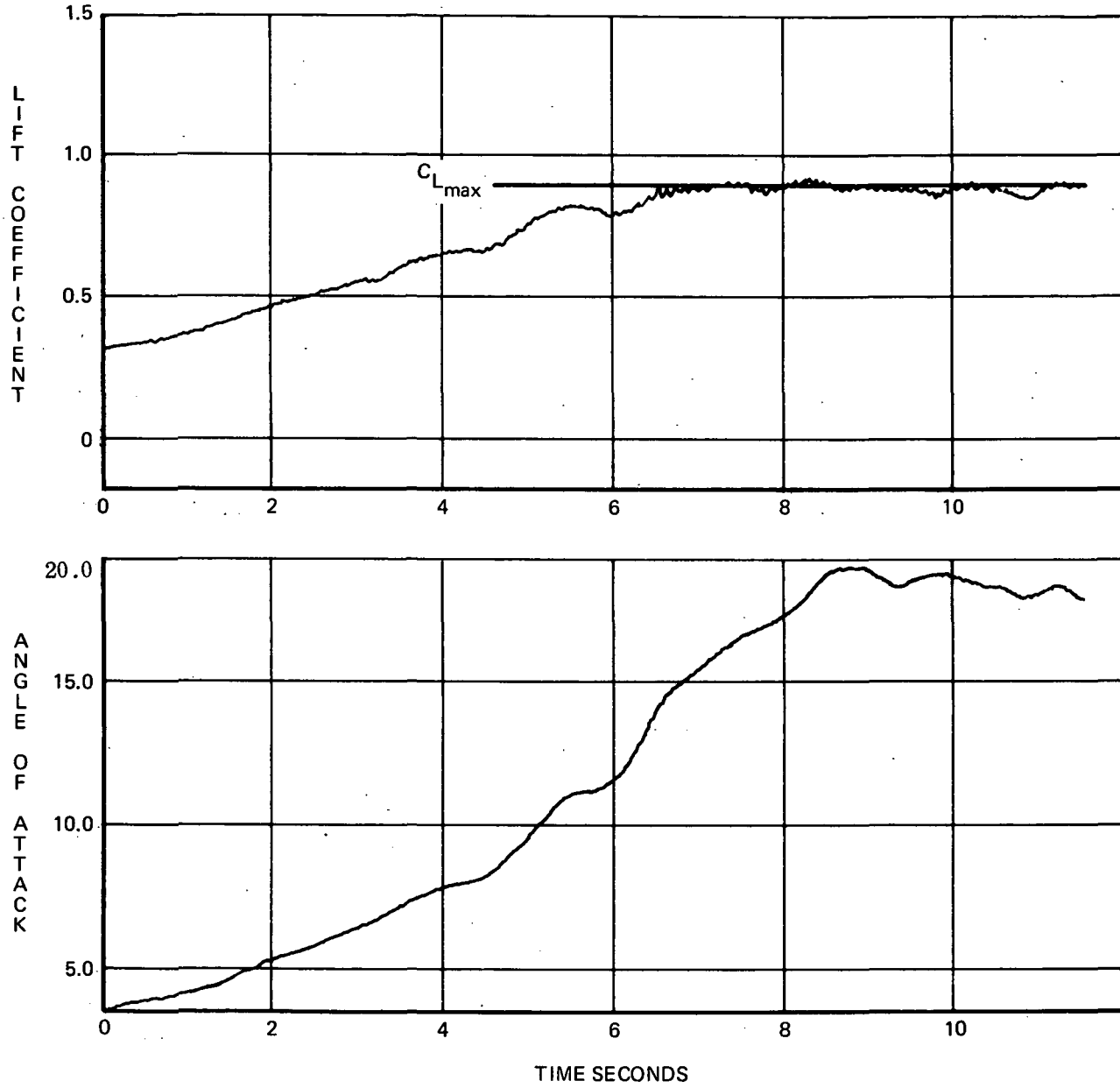

Figure 11. Lift Coefficient and Angle of Attack Histories of a Wind-Up Turn, $M_o = 0.89$, h = 10,668 m (35,000 feet) $\delta_n = 0°$, $\delta_f = 0°$

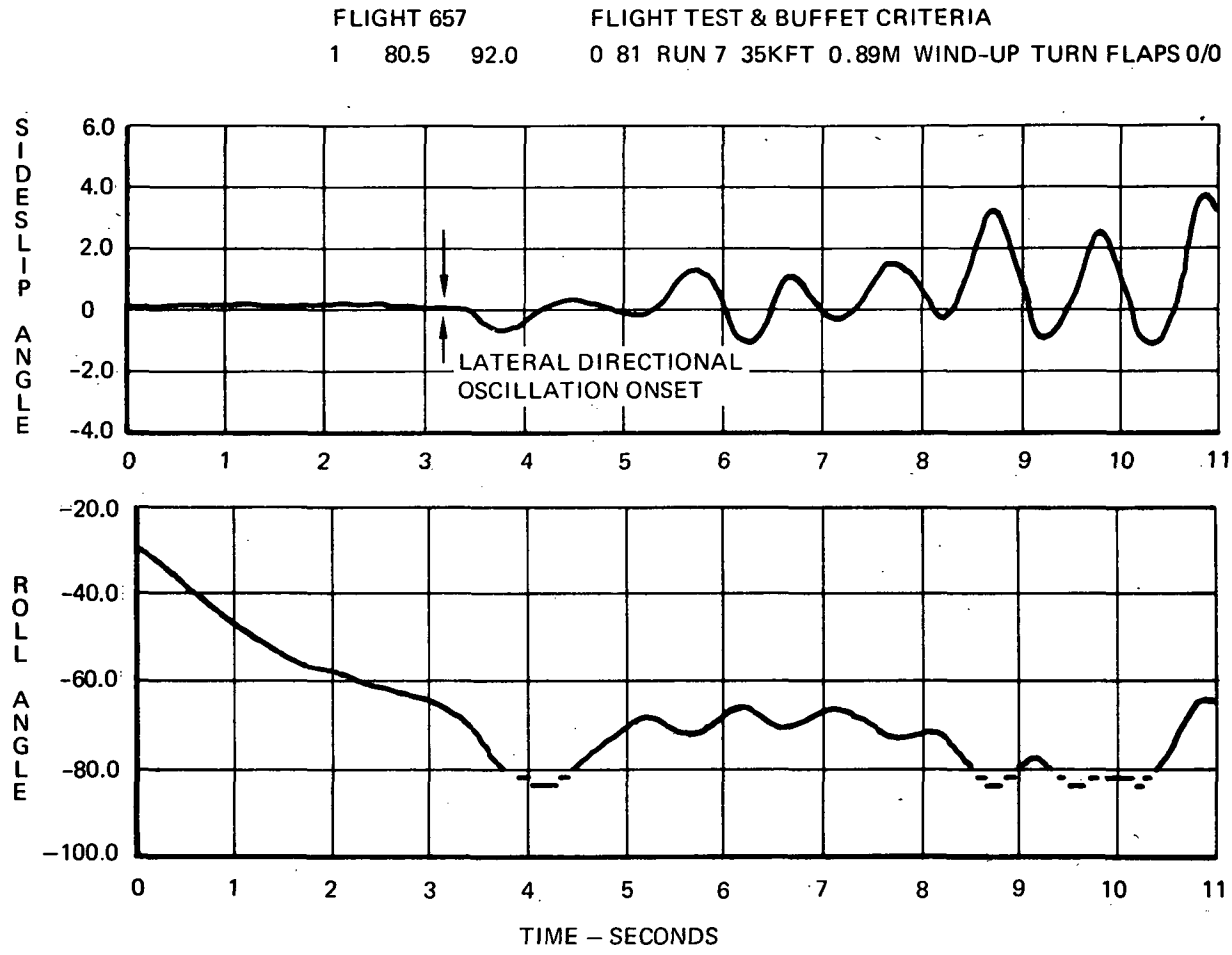

Figure 12. Lateral-Directional Oscillation Histories of a Transonic Wind-Up Turn, $M_o = 0.89$, h = 10,668 m (35,000 feet) $\delta_n = 0°$, $\delta_f = 0°$

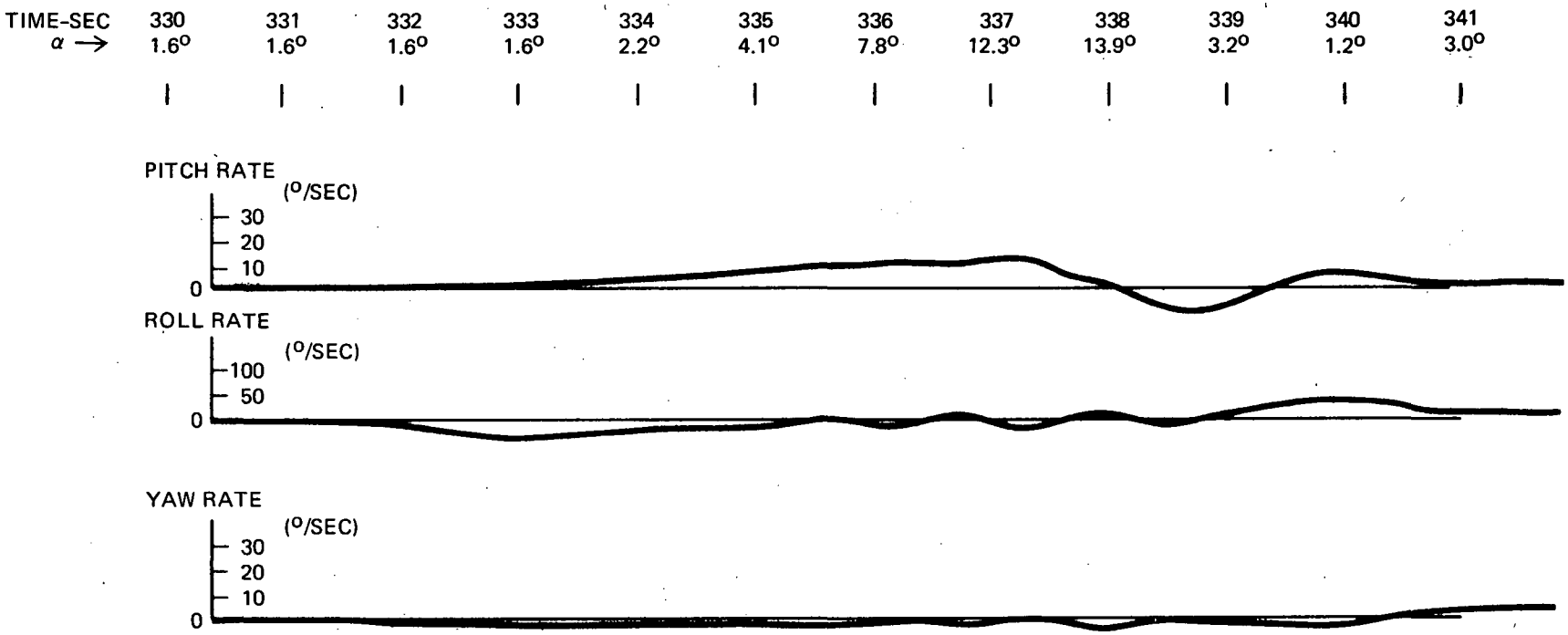

Figure 13. Pitch, Roll, and Yaw Rate Time Histories of Flight 825, Run 5, $M_o = 0.925$, h = 10,668 m, $\delta_n = 0°$, $\delta_f = 0°$

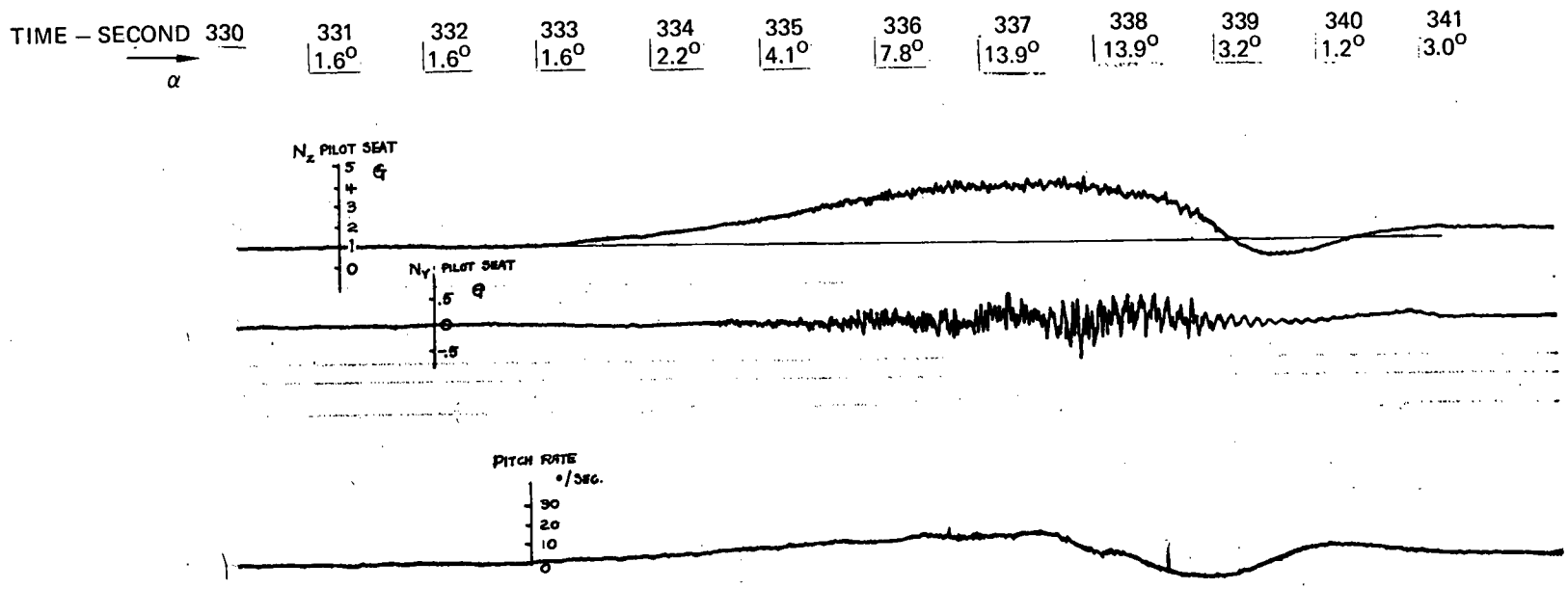

Figure 14. Pilot Seat Normal and Lateral Acceleration and Aircraft Pitch Rate Time Histories of Flight 825, Run 5, $M_o = 0.925$, $h = 10,668$ m, $\delta_n = 0°$, $\delta_f = 0°$

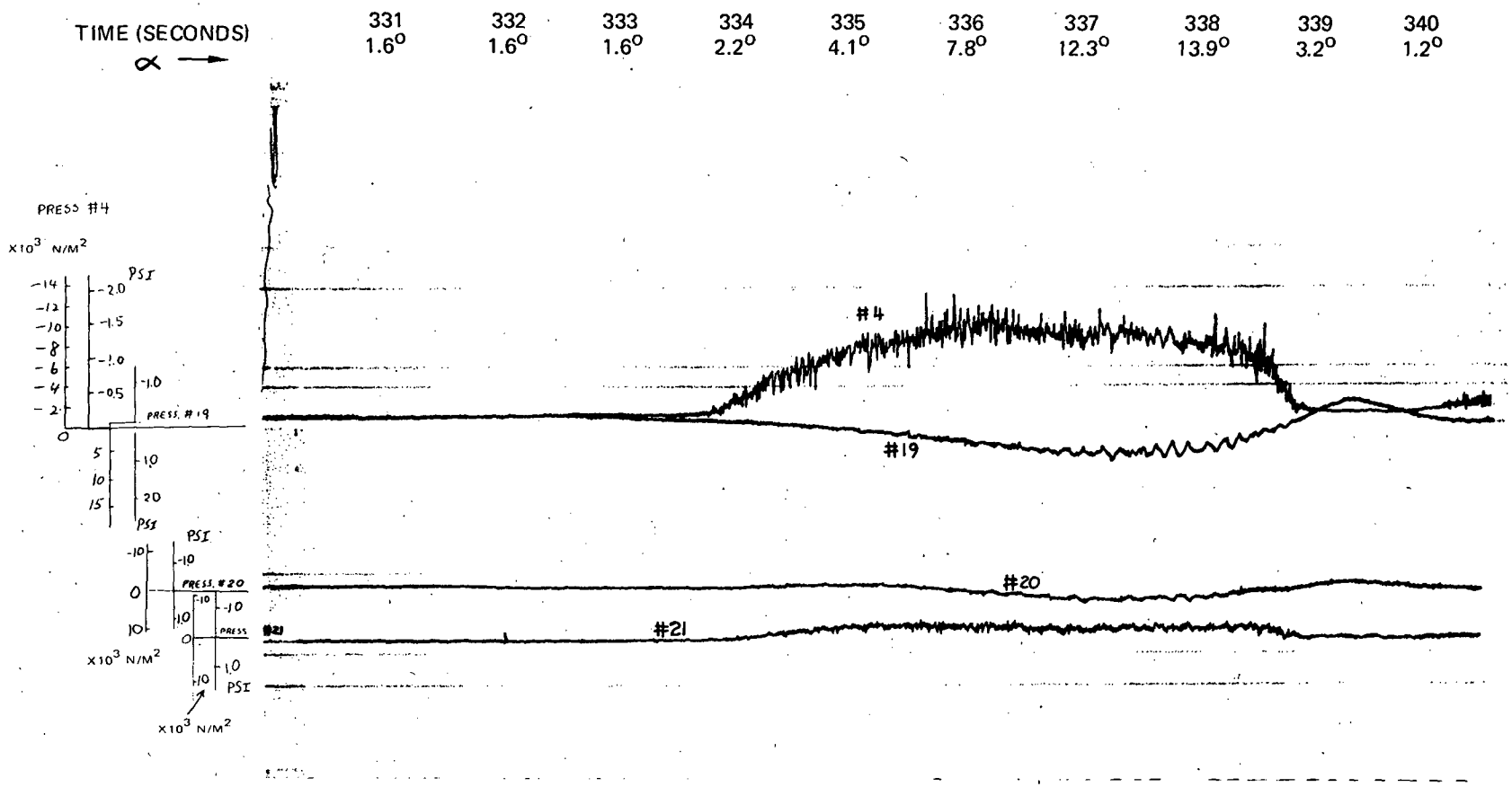

Figure 15. Typical Wing Top and Bottom Surface Pressure Histories of Flight 825, Run 5, $M_o = 0.925$, h = 10,668 m, $\delta_n = 0°$, $\delta_f = 0°$

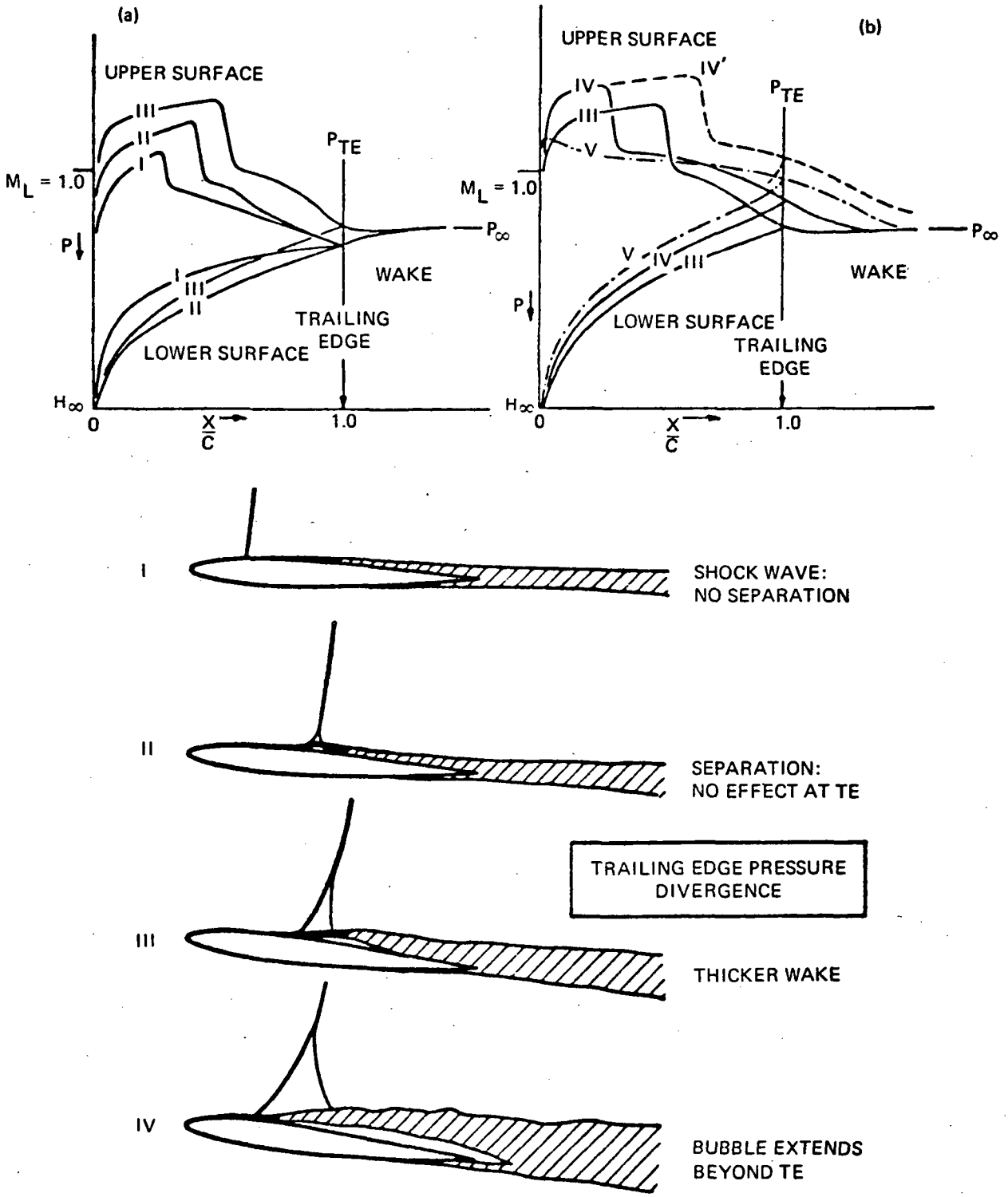

Figure 16. Successive Stages in an Incidence Increase at Fixed M_0 (Pressure Distribution is Shown in Top Charts; Corresponding Flow Patterns Are Shown in Lower Sketches . . . From Reference 13)

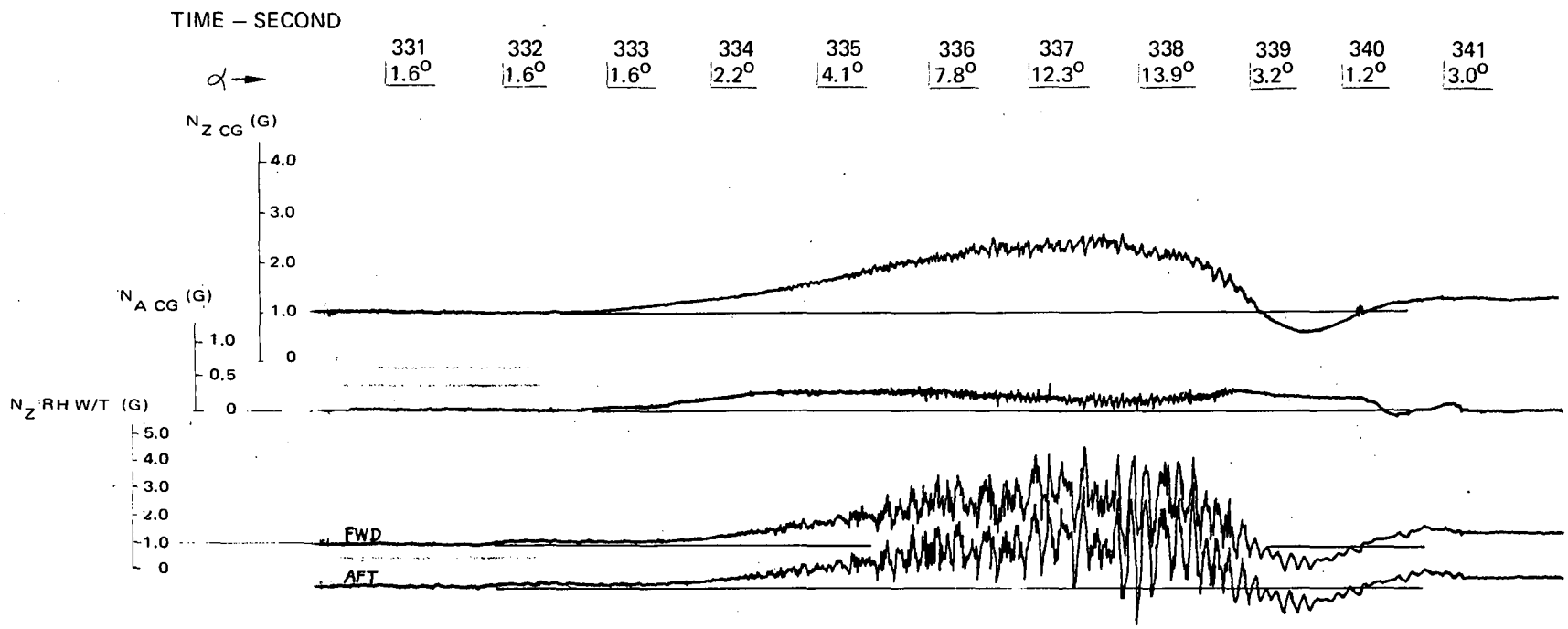

Figure 17. CG and Right Wing Tip (Forward and Aft) Acceleration Time Histories of Flight 825, Run 5, $M_o = 0.925$, $h = 10,668$ m, $\delta_n = 0°$, $\delta_f = 0°$

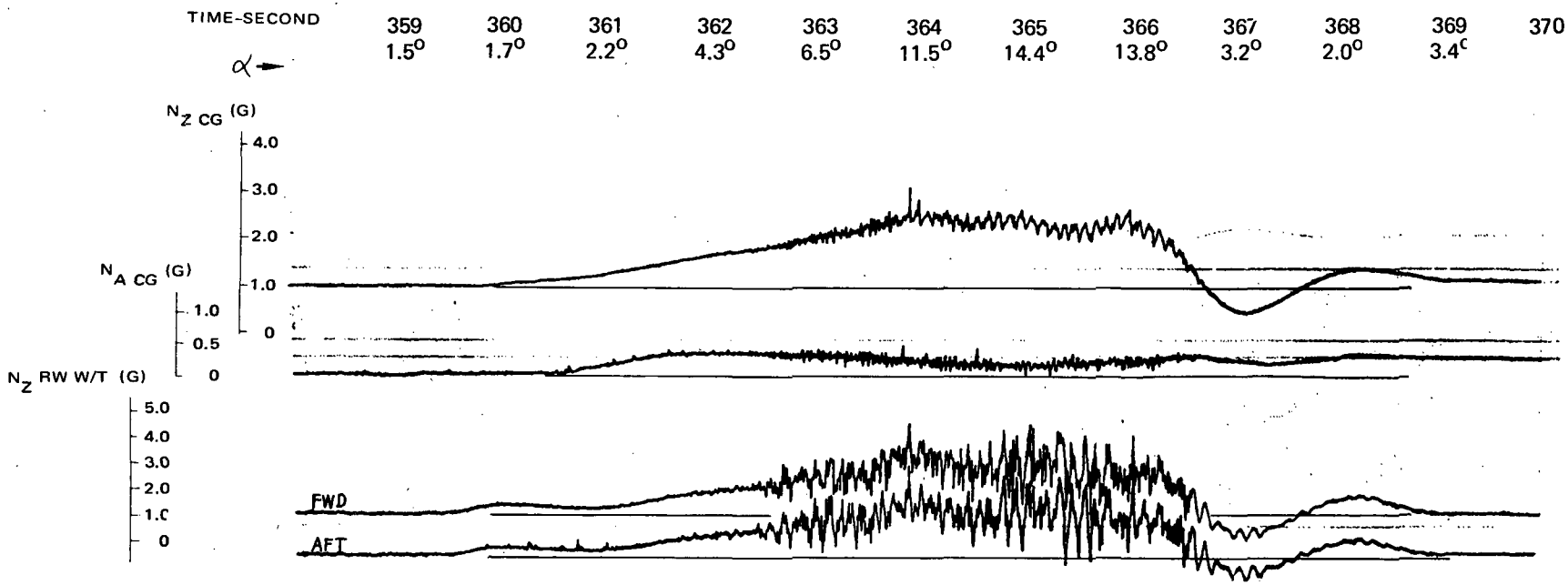

Figure 18. CG and Right Wing Tip (Forward and Aft) Acceleration Time Histories of Flight 825, Run 7, $M_o = 0.75$, h = 7,772 m, $\delta_n = 0°$, $\delta_f = 0°$

3.2 FM Data

In the buffet flight tests, 31 channels of data were recorded in the FM system in addition to the event marker. In order to obtain high-quality transient dynamic data, high-pass filters with a cutoff frequency of 1/2 Hz were used to eliminate the so-called steady-state components. The data list was given in Table 2 of the report. Specifically, of the 31 channels, 20 channels were used to record the dynamic pressure data acquired by the pressure transducers on the right wing top surface (Figure 3). Six channels were assigned to strain gage inputs. The strain gage data were used to compute the wing structural loads. One channel was used to record the right hand aileron hinge moment, and the remaining four were for dynamic loads data recorded by accelerometers.

A set of typical FM data acquired in Flight 871, Run 2 (M_o = 0.925, h = 10,668m or 35,000 ft) is presented in this subsection. During Run 2, the leading edge and trailing edge flaps were extended to δ_n/δ_f = (4°/12°). In general, the dynamic pressure data at the outboard wing stations were less significantly affected by the extension of the flaps as compared to the lower Mach number case. The corresponding pressure data at the inboard stations, especially those wing stations covered by the trailing edge flaps (see Figures 1 and 3), were to a larger degree influenced by the flap settings.

The dynamic pressure data acquired by the FM system are presented in Figures 19 through 25. Each figure has three oscillographs that are properly identified (see Figure 3 for station number identifications). On top of these figures, the time counts in seconds are noted, as well as the instantaneous angle of attack data. The traces covered 14 seconds during which a wind-up turn was performed. As the angle of attack was increased, the first major noticeable pressure oscillation appeared at t = 073.0 at station Number 2 (Figure 19). The pattern indicated oscillation of the shock front as a result of downstream separation during the maneuver. Downstream separation can be seen in the pressure fluctuation at stations 3 and 4 at t = 073.0 This can be defined as the buffet onset point. It seemed that the pressure drop across the

shock front may be determined, at least approximately, by the amplitude of the pressure oscillation (about 6000 N/M^2 or 0.87 psi). The pressure oscillations defining the location of the shock induced separation did not show significant influence on the fluctuating pressure at upstream locations. They did affect the downstream stations where the separated flow took place (see Pressure Traces Numbers 3, 4, 22). As the angle of attack was further increased (to approximately 6.2° at t = 076.0, the separation boundary (as defined by the shock front oscillation) moved to Station No. 1 (20% chordwise position) at 85% semi-span section. A comparison of Pressure Traces Numbers 1 and 2 indicated that as the angle of attack was increased, the shock-induced separation boundary stayed in the neighborhood of Station Number 2 for approximately two seconds, during which α increased 2.2°. It moved more speedily through Station Number 1 toward the leading edge of the wing. The pressure traces behaved in a somewhat random fashion when the angle of attack continued to increase and the local station was under the separated flow.

Similar shock and pressure fluctuation behavior was observed at W.S. 110.30 (72.8% semi-span, Pressure Station Numbers 5, 6, 7, 8, 9) and W.S. 93.0 (61% semi-span, Pressure Station Numbers 10, 11, 12). A special point of interest was noted in Pressure Trace Numbers 6 and 11 where the distinct pressure oscillation appeared and disappeared in less than 0.20 second. The pressure across the shock, as indicated by Pressure Trace Numbers 5 and 10, was almost identical to those based on Pressure Trace Number 1 (6000 N/M^2). The approximate time when the complete top wing surface was under separated flow was identified through Pressure Trace Number 15 when large amplitude random oscillation appeared abruptly at t = 078.9, with α = 9.4°. Pressure Stations 14 and 18 were on the trailing edge flap surface. Except for a somewhat higher peak-to-peak oscillation amplitude, no major variations of these pressure traces were observed as compared to those of nearby stations.

Typical wing structure strain gage data were recorded as the third trace of Figure 25, three traces of Figure 26, and the first and second traces of Figure 27. These strain gage data were used to determine the dynamic loads at a given section based on empirical formulas established in ground tests. Figure 28 gives the right-hand aileron hinge moment and normal accelerations at cg and the right-hand wingtip (forward position). The aileron hinge moment showed fairly high-frequency oscillations which may be damped out by the control linkage. Also, good correlation was observed between the aileron hinge moment data and the pressure data picked up at a location

close to the hinge (Pressure Number 12). The accelerometer data for N_z at the C.G. and the wingtip during buffet onset and wing rock will be discussed later in the section dealing with analytical correlation.

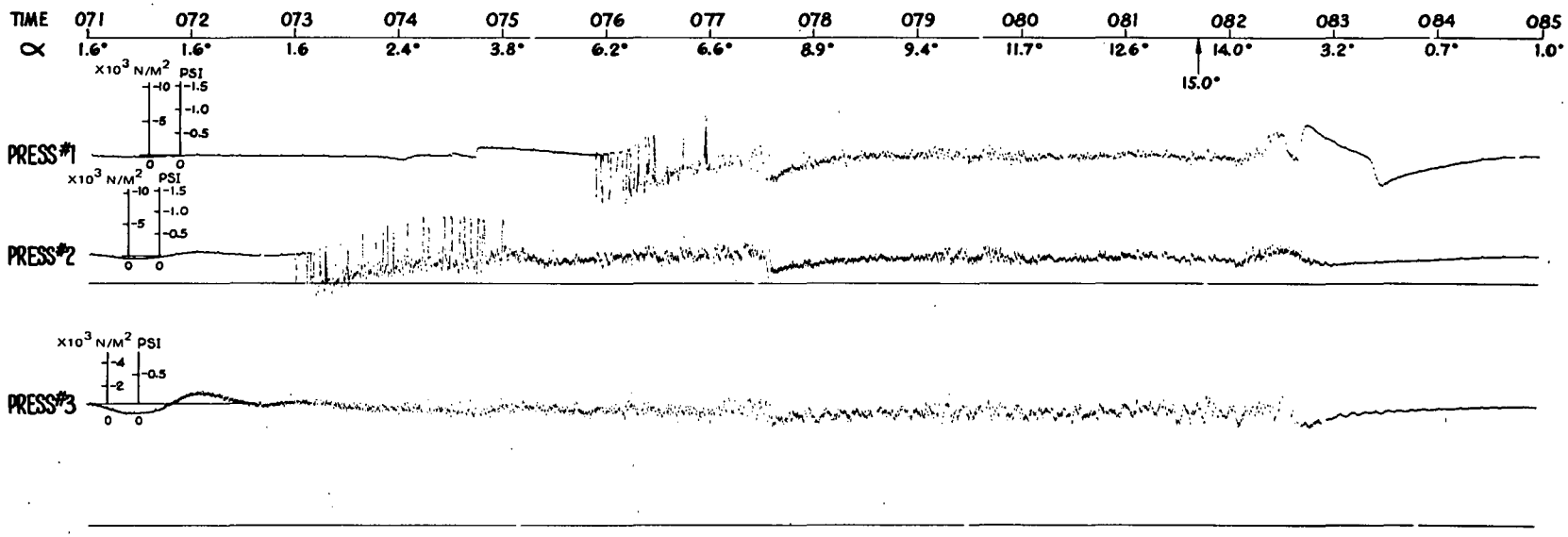

Figure 19. Oscillographs of Pressure Station Numbers 1, 2, 3, Recorded in Run 2, Flight 871. $M_o = 0.925$, h = 10,668 m, $\delta_n = 4°$, $\delta_f = 12°$.

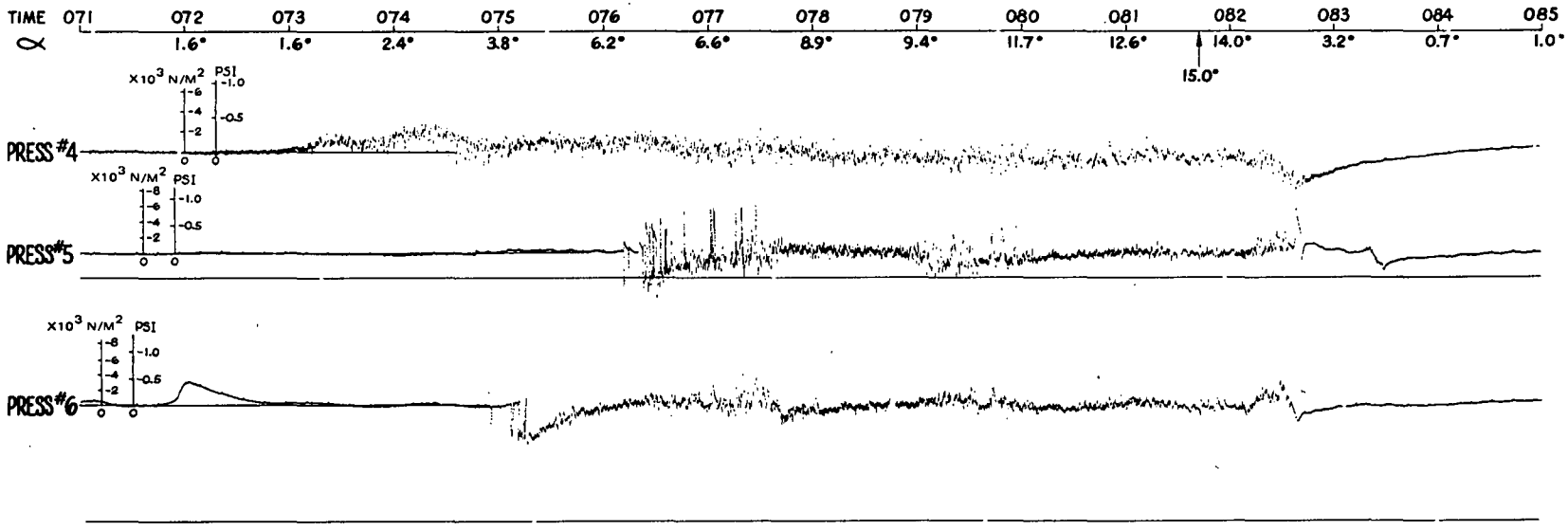

Figure 20. Oscillographs of Pressure Stations Numbers 4, 5, 6, Recorded in Run 2, Flight 871. $M_o = 0.925$, h = 10,668 m, $\delta_n = 4°$, $\delta_f = 12°$.

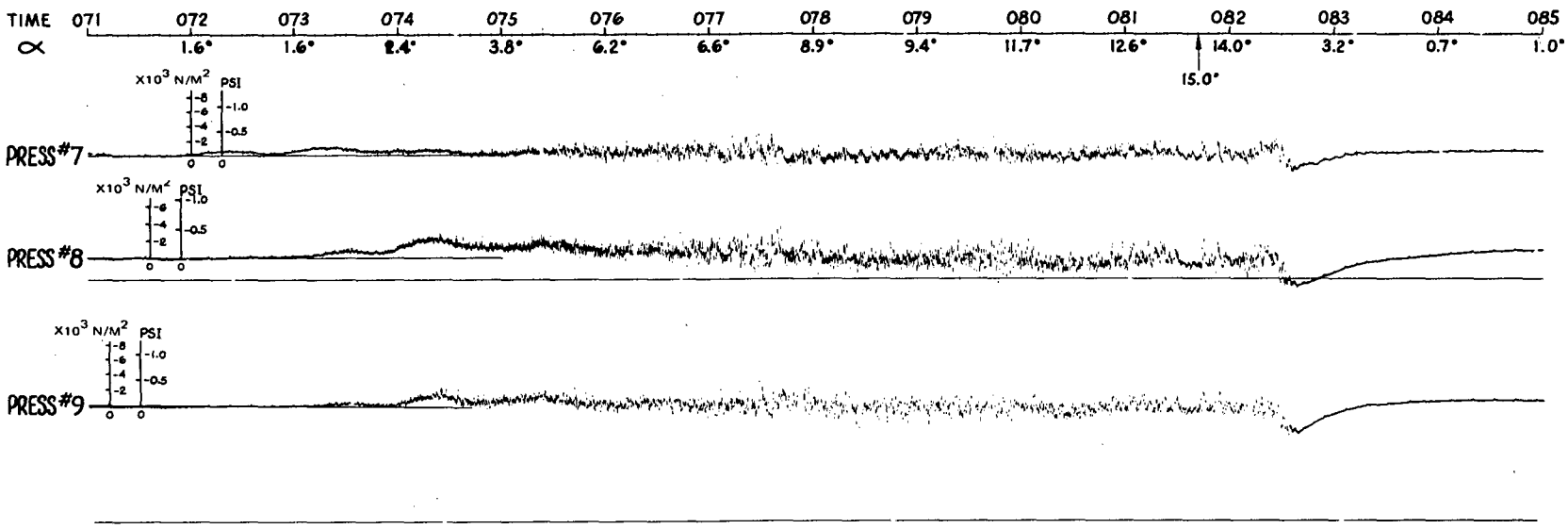

Figure 21. Oscillographs of Pressure Station Numbers 7, 8, 9, Recorded in Run 2, Flight 871. $M_o = 0.925$, $h = 10{,}668$ m, $\delta_n = 4°$, $\delta_f = 12°$.

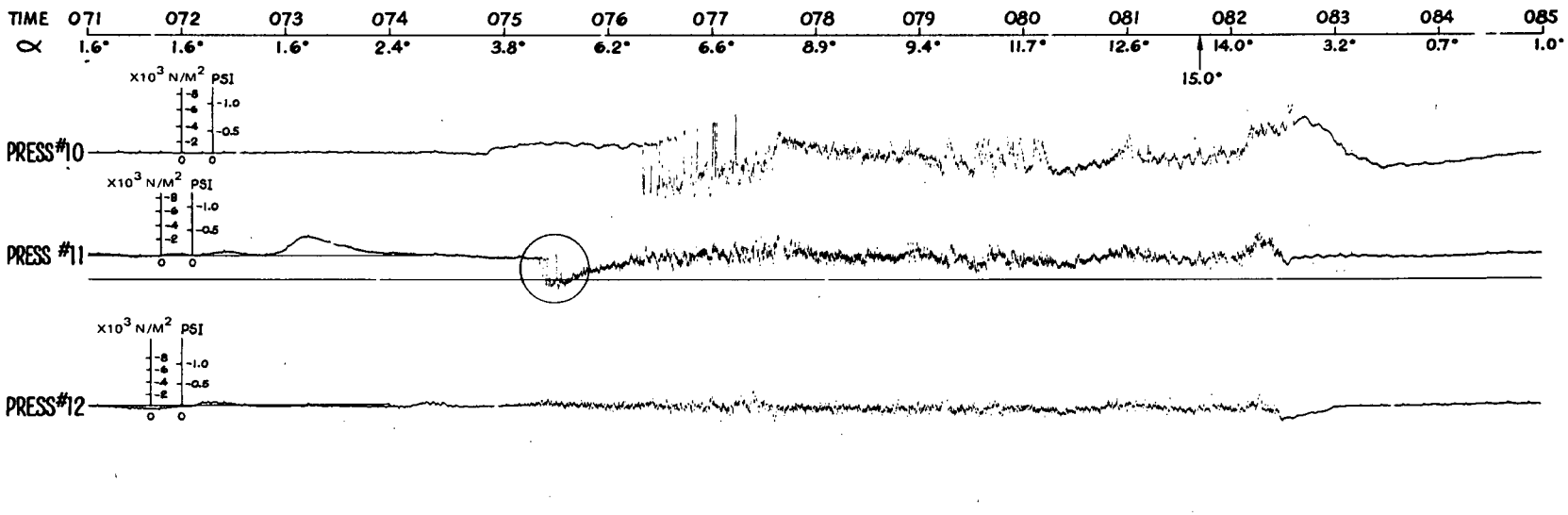

Figure 22. Oscillographs of Pressure Station Numbers 10, 11, 12, Recorded in Run 2, Flight 871. $M_o = 0.925$, h = 10,668 m, $\delta_n = 4°$, $\delta_f = 12°$.

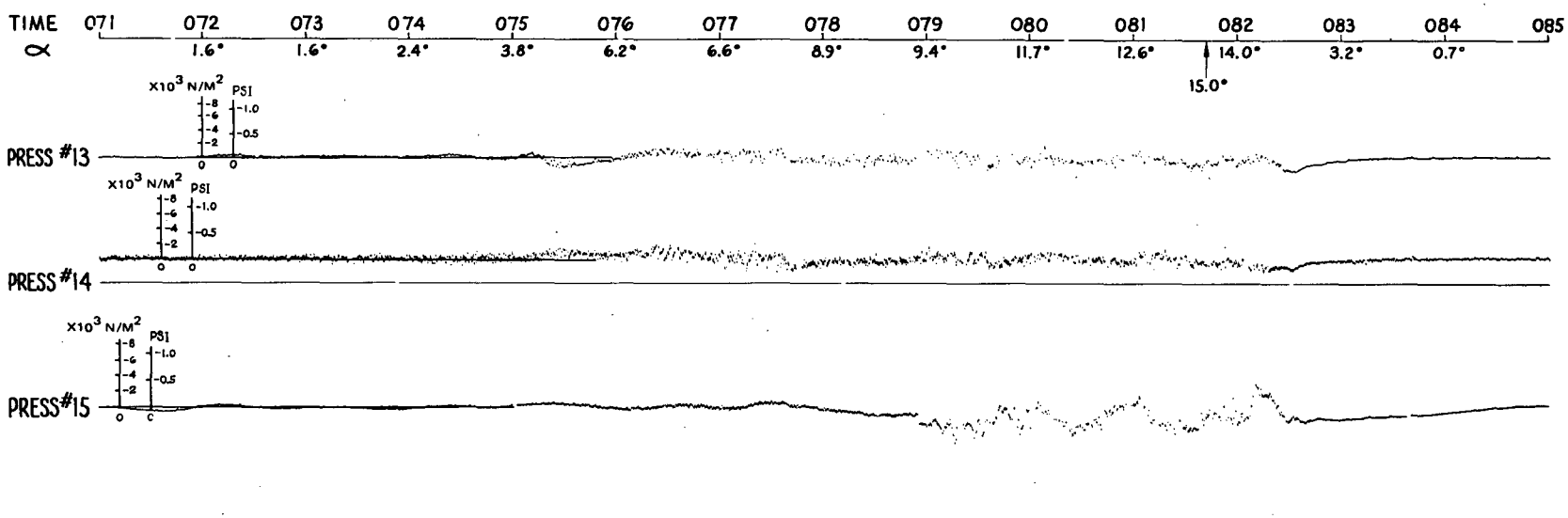

Figure 23. Oscillographs of Pressure Station Numbers 13, 14, 15, Recorded in Run 2, Flight 871. $M_o = 0.925$, h = 10,668 m, $\delta_n = 4°$, $\delta_f = 12°$.

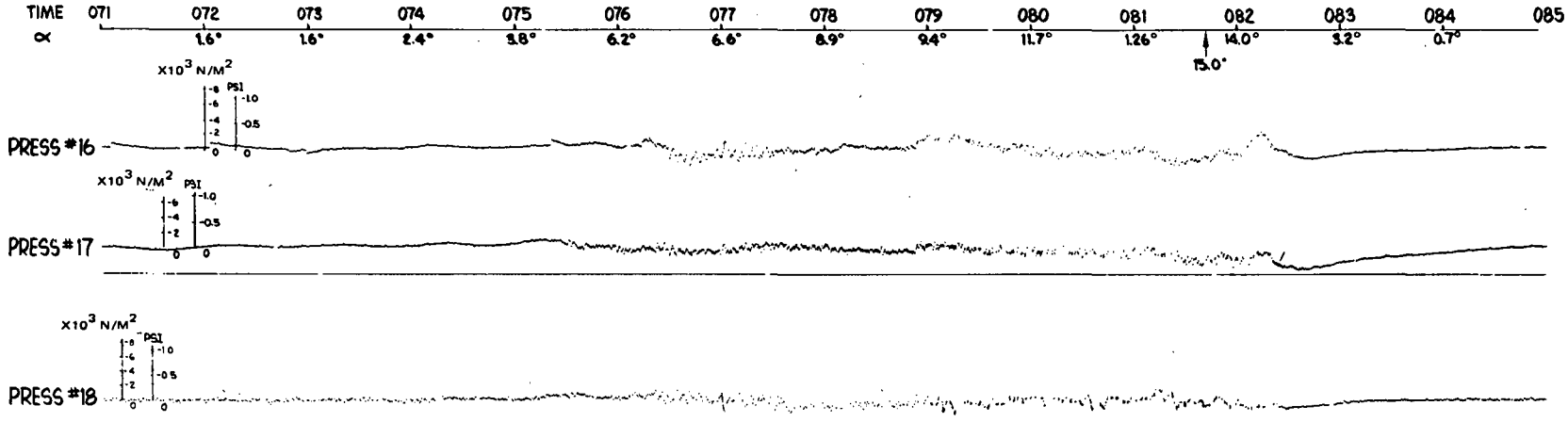

Figure 24. Oscillographs of Pressure Station Numbers 16, 17, 18, Recorded in Run 2, Flight 871. $M_o = 0.925$, $h = 10{,}668$ m, $\delta_n = 4°$, $\delta_f = 12°$.

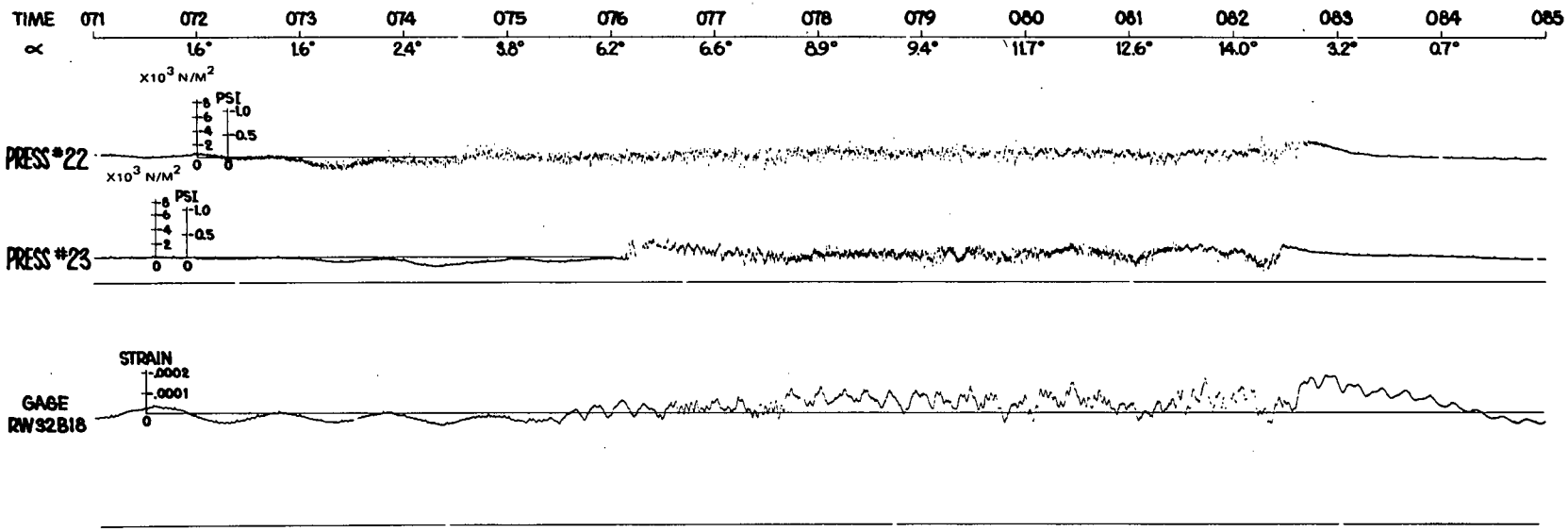

Figure 25. Oscillographs of Pressure Station Numbers 22, 23, and Gage RW32B18 Recorded in Run 2, Flight 871. $M_o = 0.925$, h = 10,668 m, $\delta_n = 4°$, $\delta_f = 12°$.

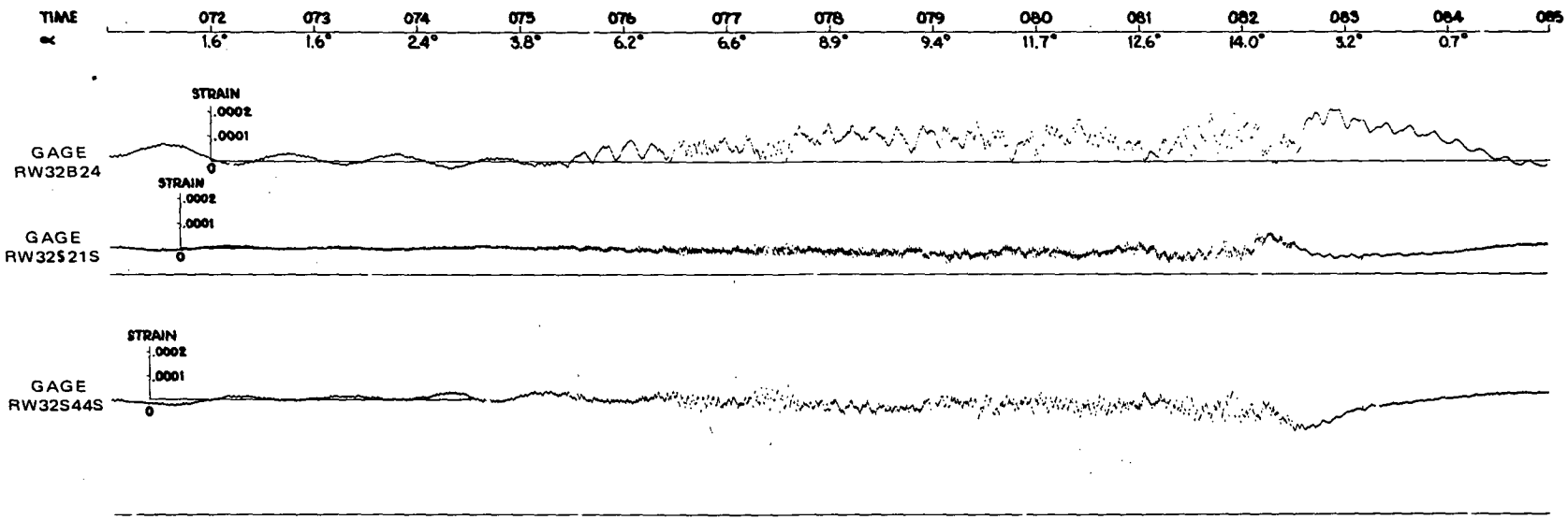

Figure 26. Oscillographs of Gages RW32B24, RW32S21S, RW32S44S, Recorded in Run 2, Flight 871. $M_o = 0.925$, h = 10,668 m, $\delta_n = 4°$, $\delta_f = 12°$.

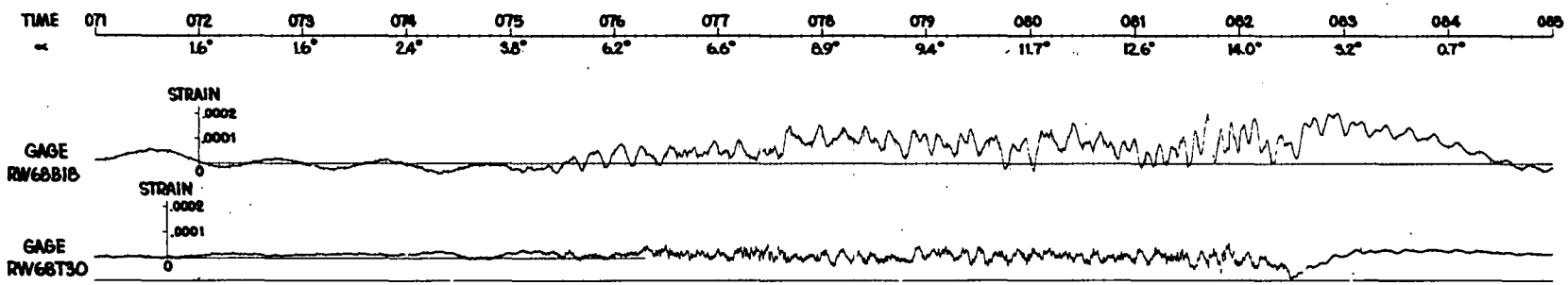

Figure 27. Oscillographs of Gages RW68B18, RW68T30, Recorded in Run 2, Flight 871. $M_o = 0.925$, h = 10,668 m, $\delta_n = 4°$, $\delta_f = 12°$.

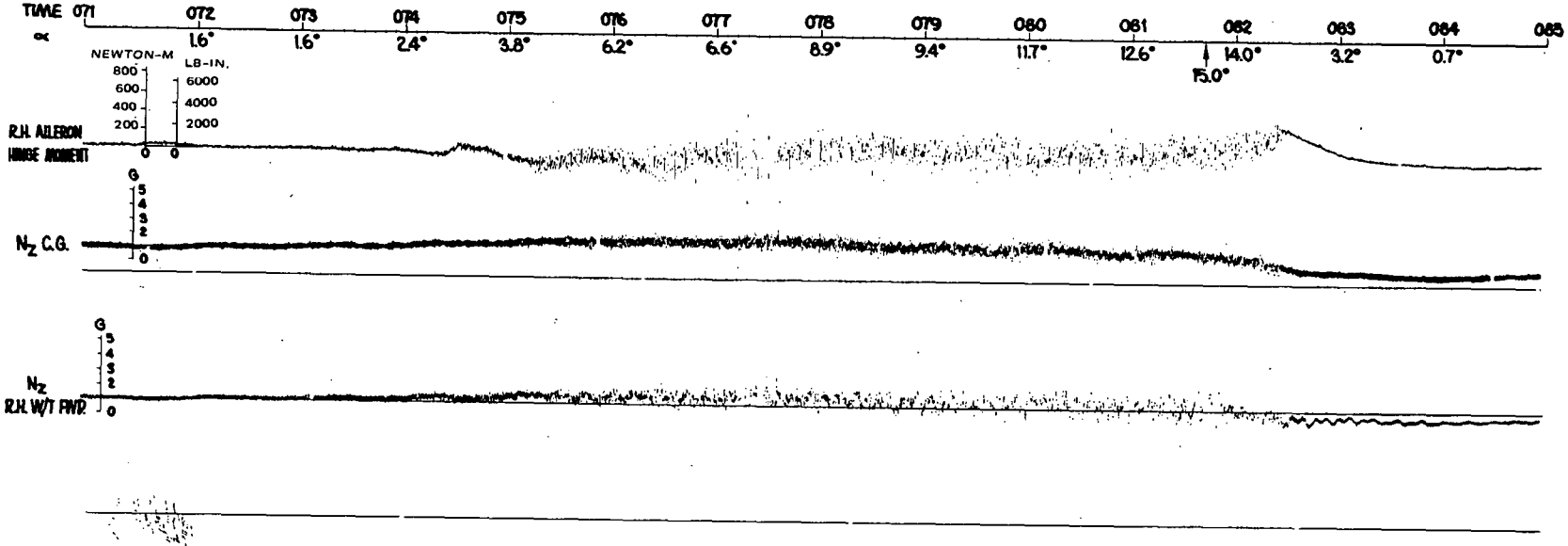

Figure 28. Oscillographs of Right Hand Aileron Hinge Moment, Normal Accelerations at C.G. and Right Hand Wing Tip Recorded in Run 2, Flight 871.
$M_o = 0.925$, $h = 10{,}668$ m, $\delta_n = 4°$, $\delta_f = 12°$.

3.3 Flap Setting and Mach Number Effects

Through visual examination of the real-time pressure data corresponding to identical Mach number and altitude, but with varying leading edge and trailing edge flap settings, the effect of the latter to the shock pressure oscillation patterns may be evaluated. Other flap setting effects such as the development of the separated flow region with increasing angle of attack, the influence on dynamic loads, etc., will be discussed later in the report.

Figures 29, 30 give the pressure transducer oscillographs obtained at Station Numbers 1, 2, 3, and Numbers 10, 11, 12 respectively. The oscillographs were obtained based on Flight 825, Run 5, where M_o =0.925, h = 10,668m (35,000 ft) and both leading edge and trailing edge flaps were retracted. The data may be compared with Figures 19, 22 respectively, where the Mach number and altitude were identical while the flaps were set at (4°/12°). It may be noted that the flap retracted maneuver was conducted at a faster pace. The elapsed time of the maneuver lasted approximately seven seconds so that the peak angle of attack (14.4°) was reached at a comparatively short time after the first shock appeared on the wing surface.

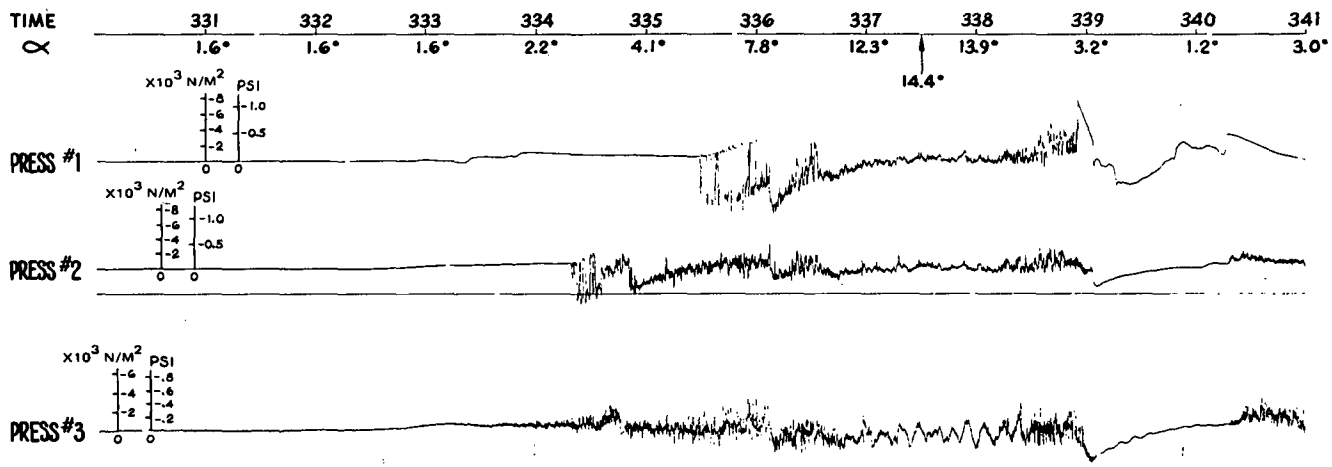

Figure 29. Oscillographs of Pressure Station Numbers 1, 2, 3, Recorded in Run 5, Flight 825. $M_o = 0.925$, h = 10,668 m, $\delta_n = 0°$, $\delta_f = 0°$.

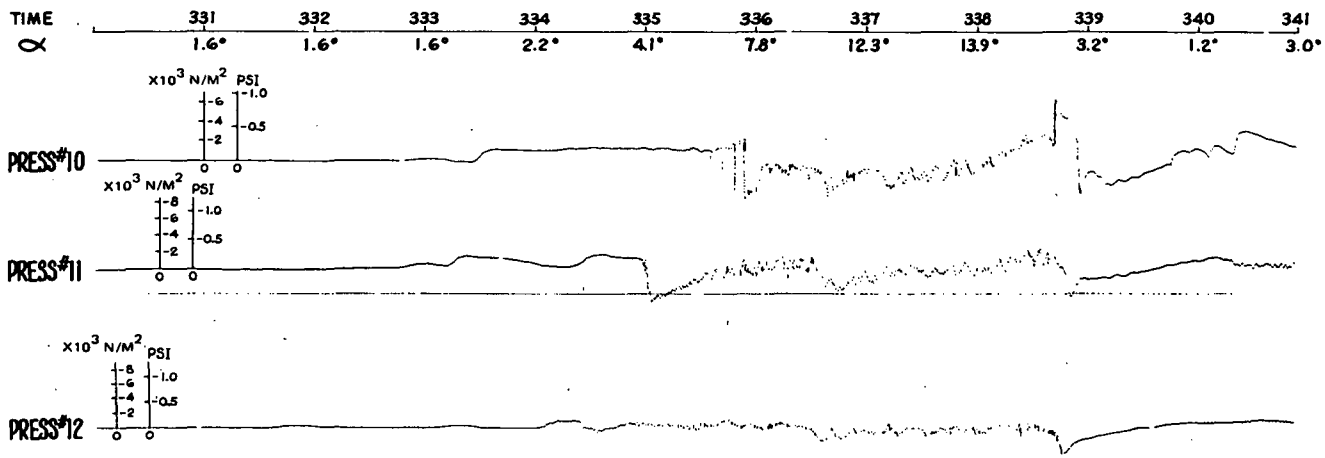

Figure 30. Oscillographs of Pressure Station Numbers 10, 11, 12, Recorded in Run 5, Flight 825. $M_o = 0.925$, $h = 10{,}668$ m, $\delta_n = 0°$, $\delta_f = 0°$.

The Mach number effect may be observed in a similar manner by examining the real-time data obtained in two runs where other conditions were equal except for Mach numbers and flight altitudes with the q value unchanged.

Figures 31, 32 are the fluctuating pressure tracks at Stations Numbers 1, 2, 3, and Numbers 10, 11, 12 respectively for Run 12 of Flight number 871. The run was executed at $M_o = 0.75$ and h = 7,772 m (25,500 ft). The leading edge and trailing edge flap settings were (4°/0°). At time count 538, a brief reduction of the angle of attack was noted. In reviewing the other channels of the flight test data, it was determined that the temporary reduction in the angle of attack was caused by the pilot. A comparison of these figures with Figures 19, 22, ($M_o = 0.925$, h = 10,668 m) revealed the difference in buffet pressure behavior at a lower Mach number. The difference in trailing edge deflection is not considered to have significantly affected the comparison.

Figure 33 gives the pressure traces at Stations 1, 2, 3, for $M_o = 0.75$, h = 7,772 m while the leading edge and trailing edge flaps were retracted. These data may be compared to those of Figure 31 where the leading edge flap was extended ($\delta_n/\delta_f = 4°/0°$). Figure 31 showed that the pressure oscillations at Station Numbers 1, 2 were somewhat delayed as the angle of attack was increasing when compared to Figure 33. This delay in buffet onset was attributed to the deflected leading edge flap (4°).

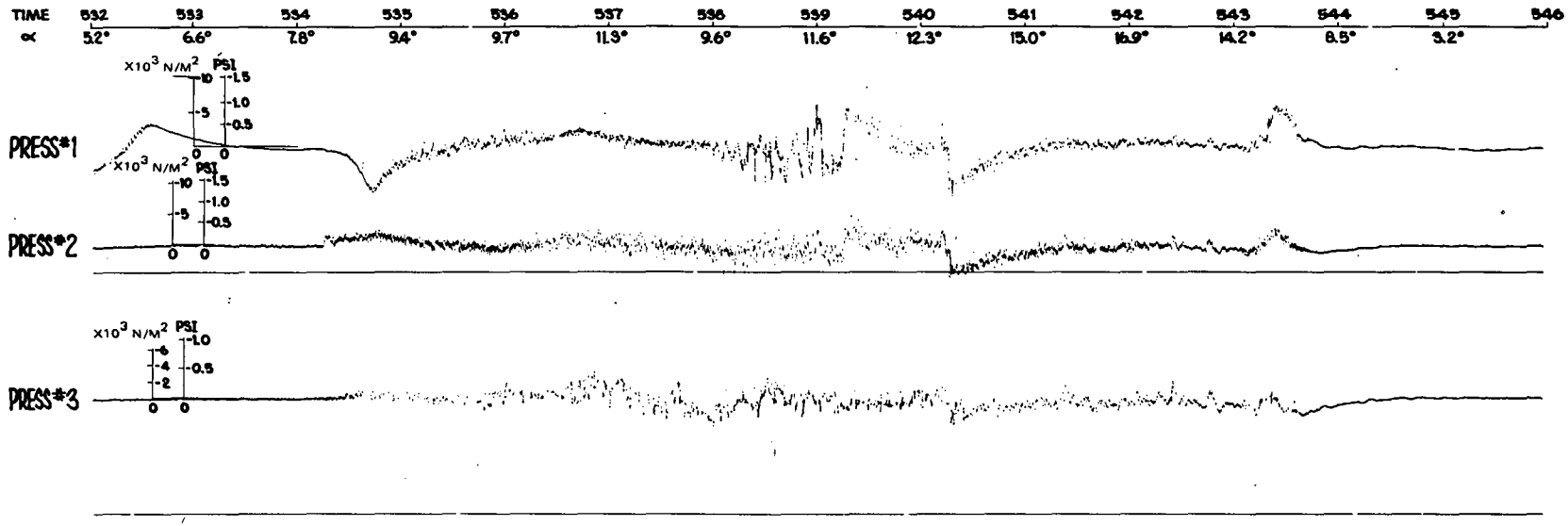

Figure 31. Oscillographs of Pressure Station Numbers 1, 2, 3, Recorded in Run 12, Flight 871. $M_o = .75$, $h = 7{,}772$ m, $\delta_n = 4°$, $\delta_f = 0°$.

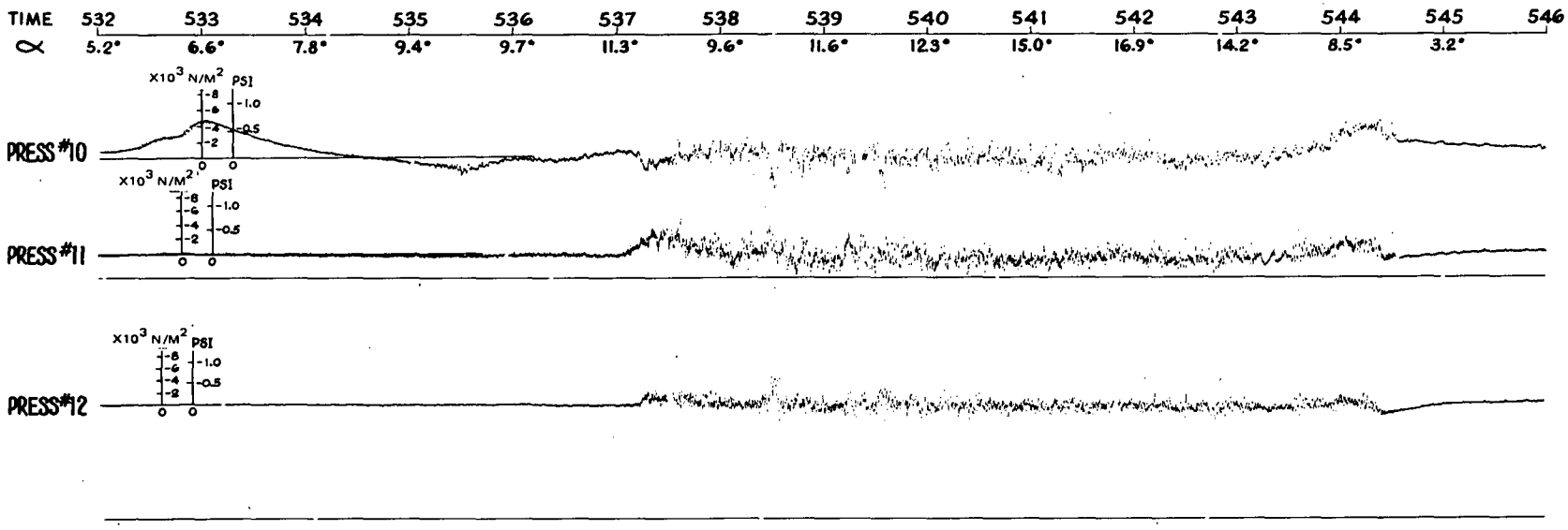

Figure 32. Oscillographs of Pressure Station Numbers 10, 11, 12, Recorded in Run 12, Flight 871. $M_o = .75$, $h = 7,772$ m, $\delta_n = 4°$, $\delta_f = 0°$.

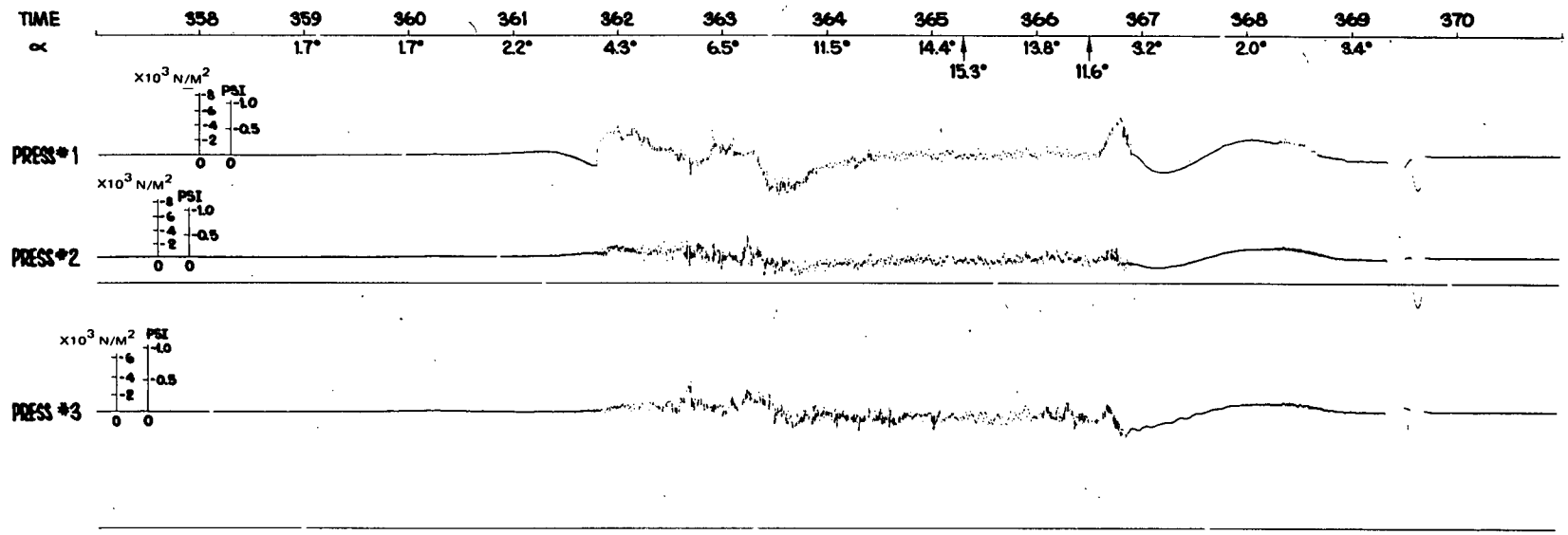

Figure 33. Oscillographs of Pressure Station Numbers 1, 2, and 3, Recorded in Run 7, Flight 825, $M_o = .75$, h = 7,772 m, $\delta_n = 0°$, $\delta_f = 0°$.

3.4 Additional Observations

In this subsection, the real-time data acquired from three runs in Flight 825 are further reviewed. Flight 825 was conducted with leading edge and trailing edge flaps retracted ($\delta_n/\delta_f = 0°/0°$). The runs (Numbers 7, 6, 5 according to the sequence of presentation in this subsection) were conducted at $M_o = 0.75$, 0.85, 0.925 respectively.

Figure 34 illustrates schematically the variation of the separation boundary with time obtained from the real-time pressure data such as presented in Figures 29, 30, 33. In determining the boundary details where the local fluctuating pressure data were unavailable, use was made of the tuft data obtained in a previous flight test program (Reference 26). Figure 35, 36 presents the variation of peak-to-peak pressure turbulence with time and α for transducers located along three spanwise station (W.S. 128.31, 93.0, 50.00). The values, measured from time histories, were for M_o = 0.75 and 0.925 (Run Numbers 7, 5) respectively.

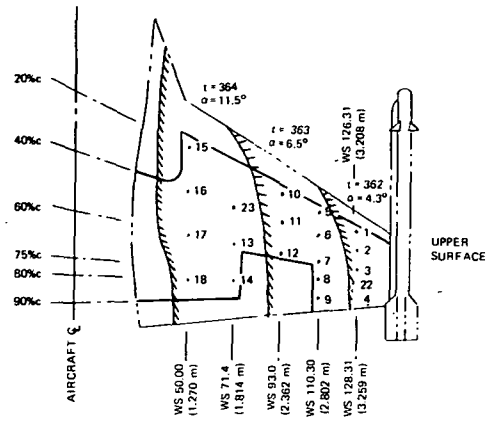

(a) RUN 7, M_o = 0.75, h = 7,772 m

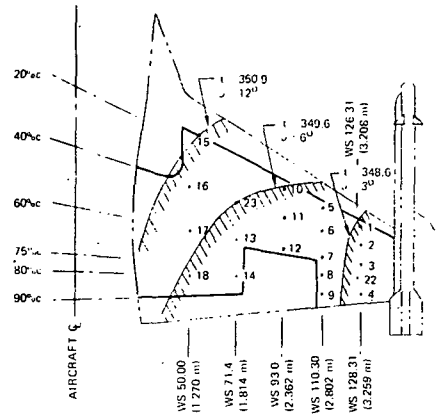

(b) RUN 6, M_o = 0.85, h = 9,449 m

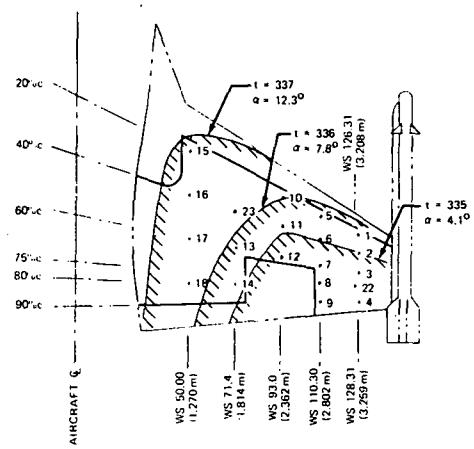

(c) RUN 5, M_o = 0.925, h = 10,668 m

Figure 34. Upper Wing Surface Separation Boundary Mapping for Three Runs of Flight 825, ($\delta_n/\delta_f = 0°/0°$)

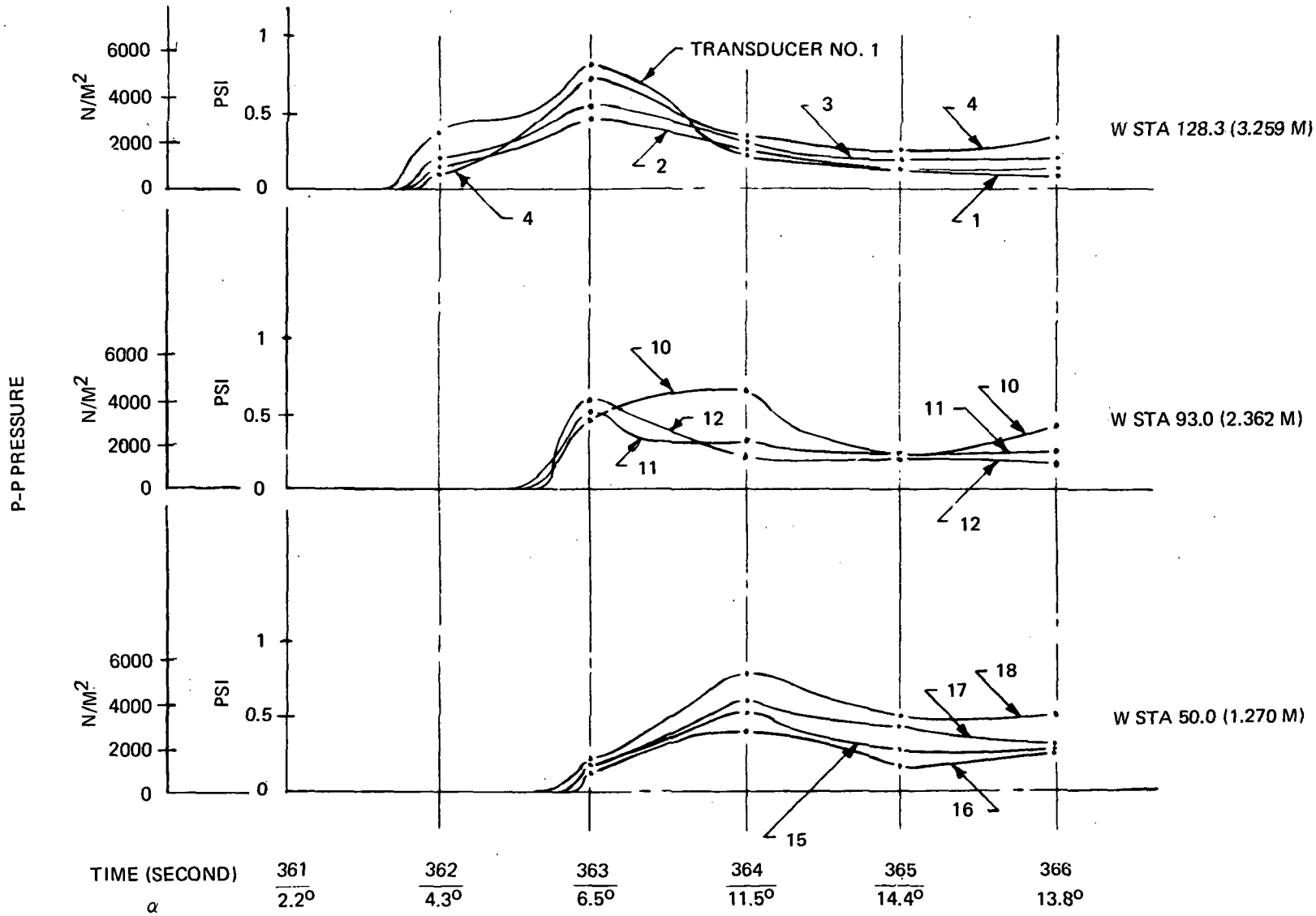

Figure 35. Peak-To-Peak Pressure Histories at Various Wing Stations, Run 7, Flight 825, $M_o = 0.75$, $h = 7,772$ m, $\delta_n = 0°$, $\delta_f = 0°$

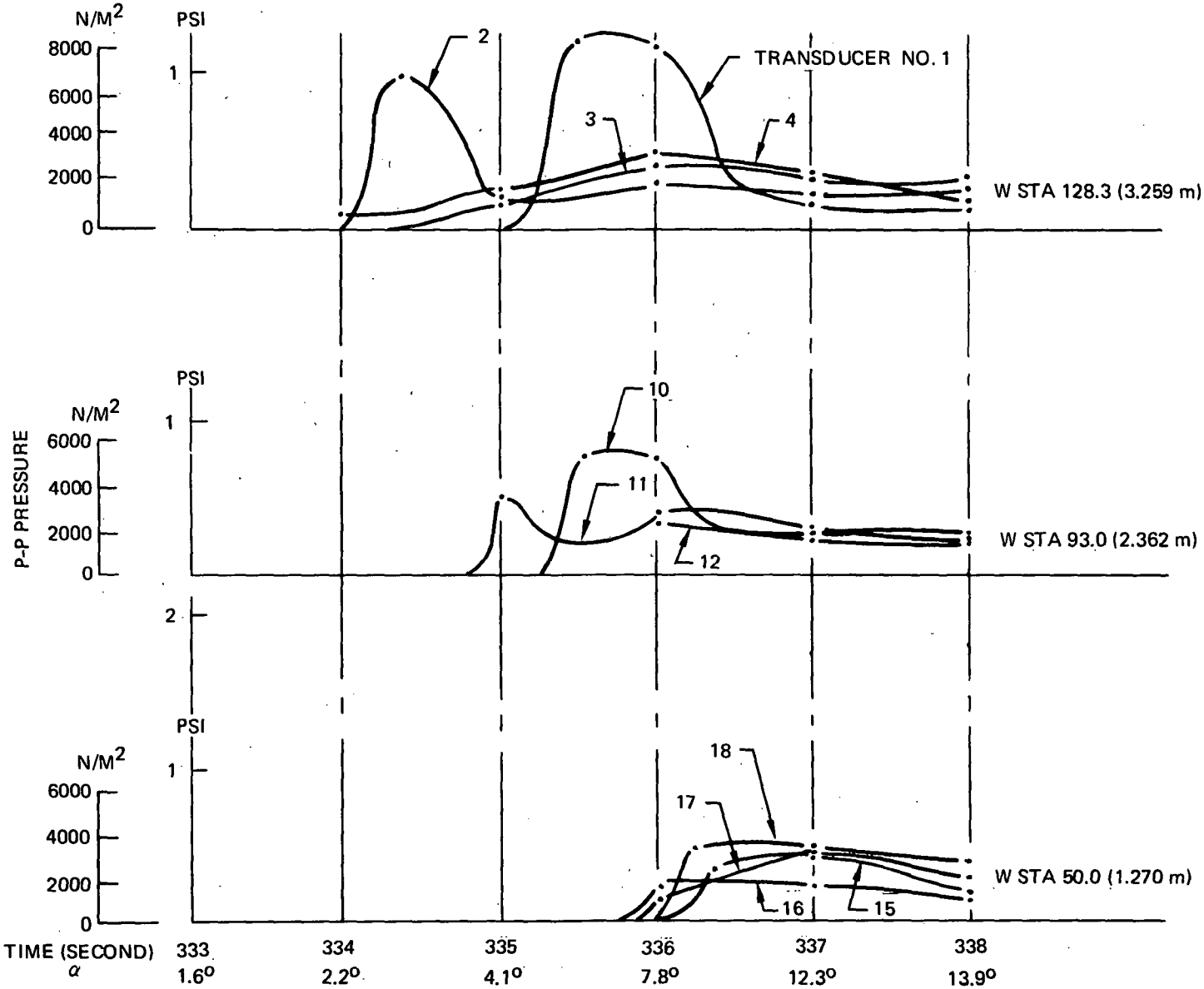

Figure 36. Peak-To-Peak Pressure Histories at Various Wing Stations, Run 5, Flight 825, $M_o = 0.925$, h = 10,668 m, $\delta_n = 0°$, $\delta_f = 0°$

Referring to Figure 34(a) corresponding to a maneuver conducted at $M_o = 0.75$, the buffet onset appeared to be caused by leading-edge-induced separation. The regions of separation developed at the outboard wing first and spread inboard. From the initial separation at the wingtip to the complete separation over the entire wing, a time lag of approximately 2.2 seconds was detected. During this period the aircraft α increased from approximately 3.7° to 11.5°. Since the separation was leading-edge-induced, there was not much chord-wise variation in the dynamic pressures with time at a fixed span-wise station. Once separation occurred at the leading edge, the entire region downstream was affected.

The pressure turbulence along a given chord appeared to peak shortly after the onset point with a subsequent decrease for higher angle of attack (see Figure 35). This was to be expected for leading-edge-induced separation; i.e., at the critical α or slightly greater, the separated shear layer was relatively close to the surface. Therefore, the resulting turbulence was impressed on the wing surface. With increasing α, the shear layer moved away from the surface. The resulting turbulence was attenuated somewhat before it was felt at the surface.

The separation boundary movement and peak-to-peak pressure histories for $M_o = 0.925$ were given in Figures 34(c) and 36. For this case, the buffet onset appeared to be caused by shock-induced separation. The growth of the separation region was characterized by a movement in the chordwise (forward) direction especially at the early stage of the maneuver. The shock also spread from the wingtip to the inboard regions of the wing as the angle of attack increased.

Referring to Figure 36, the high values at the buffet onset point at W.S. 128.3 and 93.0 could be attributed to the shock oscillating over the particular transducer. The inboard pressure (W.S. 50.0) did not show any strong shock ocillations as at the other two wing stations. The separation in this region appeared to develop simultaneously similar to the $M_o = 0.75$ data. In this case, the inboard separation resulted from the inboard spread of the outboard separation region. It is interesting to note that once the flow on the top surface of the wing was completely separated, the level of the peak-to-peak turbulence was similar to the leading edge induced data at $M_o = 0.75$. This was to be expected for as the shock approached the leading edge, the resulting downstream separation could be expected to resemble leading-edge-induced separation characteristics.

The development of the separation boundary for $M_o = 0.85$ (Figure 34 (b)) followed a pattern which was intermediate in nature and resembled to some extent either of the

two extreme cases ($M_o = 0.75, 0.925$). The separated flow seemed to be induced initially by a weak shock (i.e., a weaker shock as compared to the $M_o = 0.925$ case). As the angle of attack increased, the shock moved toward the leading edge swiftly. In the later phase of the maneuver, the expansion of the separation boundary in the inboard portion of the wing was very similar to those of the $M_o = 0.925$ case.

Figure 37, taken from Reference 26, indicates the separation boundaries of the F-5A Wing based on tuft data. The data were collected at h = 10,668 m (35,000 ft) corresponding to three Mach numbers ($M_o = 0.81, 0.86, 0.91$). During the flight, the leading edge and trailing edge flaps were retracted. A major difference in the test aircraft configuration on which the data of Figure 37 were based was that the aircraft had a clean wing, while wingtip missiles were attached in the present program. Referring to Figure 37, the case corresponding to $M_o = 0.81$ indicated that the separation was leading-edge-induced, as was the case for Run 7, Flight 825 ($M_o = 0.75$, h = 7,772m) discussed previously. For the remaining two cases of Figure 37 ($M_o = 0.86, 0.91$), the separation seemed to be induced by local shock.

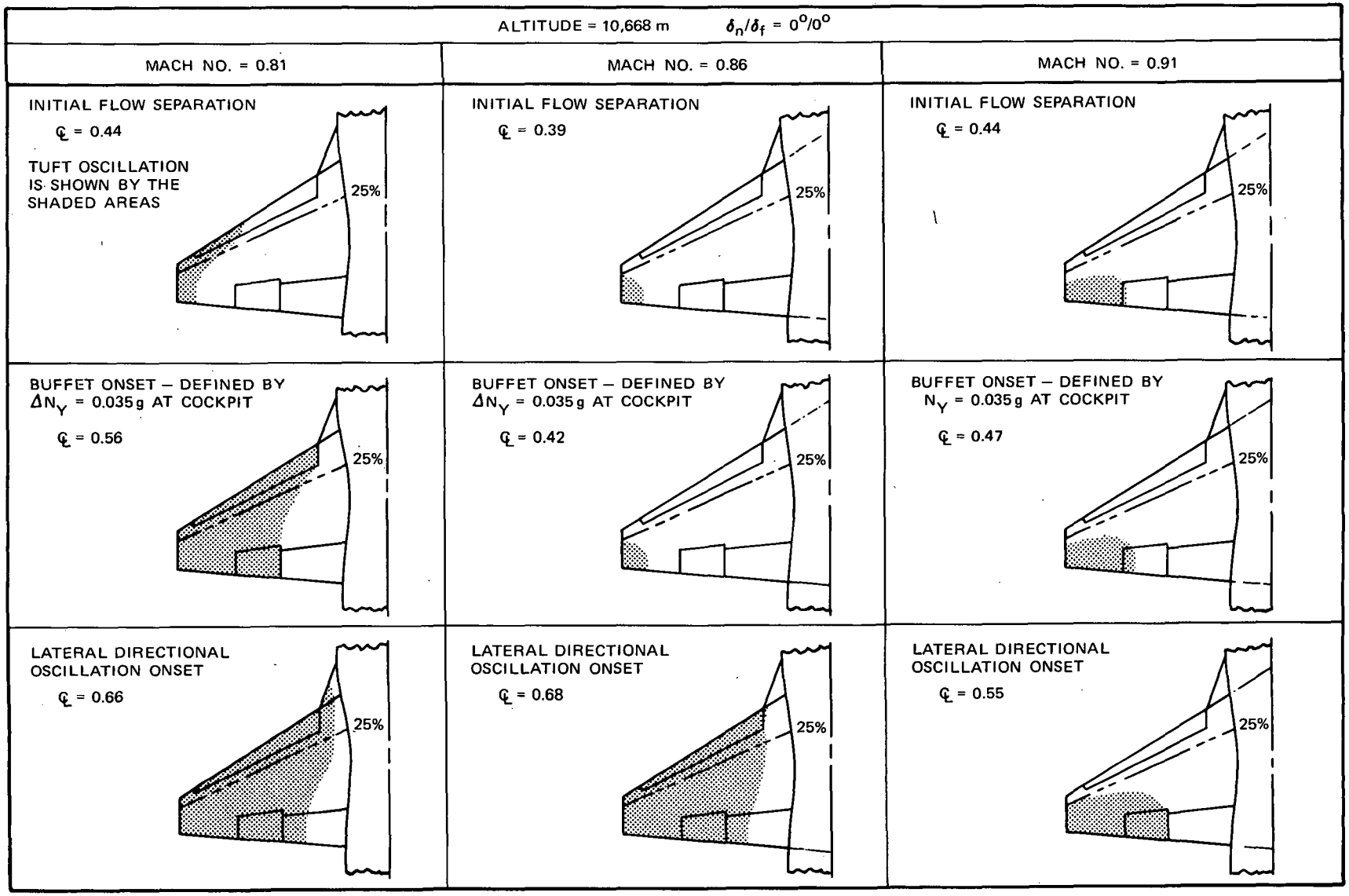

Figure 37. Wing Tuft Results, h = 10,668 m, δ_n = 0°, δ_f = 0° (From Reference 26)

Section 4

SPECTRAL AND STATISTICAL PROCESSINGS OF BUFFET DATA

In the previous section, the real-time buffet pressure and response data were presented. The dynamic pressure data covered a wide frequency range. Excluding distinct physical behaviors such as the shock pressure oscillations, etc., the data within a given time span may be considered random. Assuming that the random data were stationary within a limited time span, standard spectral processing techniques may be applied. In this manner, certain general conclusions may be drawn based on the processed pressure and response data. Furthermore, the spectral processing made analytical correlation feasible in case the basic aircraft response function was assumed linear.

The spectral processing consisted of the determination of the power spectral densities of the pressure and response data, as well as the cross-spectral densities of any two sets of data. For the latter case, the spatial correlation of the data sets came into play. In general, a high degree of spatial correlation may be observed if the two sets of data are caused by a single source, or if a given physical phenomenon is moving in space at a distinct speed (convection speed). In addition to spectral processing, other statistical processing techniques were also applied to the buffet data acquired in the flight test program.

4.1 Processing Techniques

The spectral and statistical processings of the digitized buffet data applied in the present program followed the common procedures used in most flight test and other experimental programs. For completeness in presentation, and to prevent ambiguity in definitions of certain functions, a brief outline of the processing techniques is described below, to be followed by systematic presentation of the processed results.

Consider a stationary ergodic random process x(t). Let x(t) be so truncated that it becomes zero outside the interval (o, T). The truncated function is denoted by $x_T(t)$. The Fourier transform of $x_T(t)$ exists provided that the absolute value of $x_T(t)$ is integrable and $x_T(t)$ is bounded:

$$x_T(t) = \int_{-\infty}^{\infty} F_X(f)\, e^{i2\pi ft}\, df \tag{4-1}$$

where

$$F_X(f) = \frac{1}{T}\int_o^T x_T(t)\, e^{-i2\pi ft} dt \tag{4-2}$$

If $F_X^*(f)$ denotes the complex conjugate, then $F_X^*(-f) = F_X(f)$, since $x_T(t)$ is real in the present case.

The auto-correlation function is defined as:

$$R_X(\tau) = \lim_{T\to\infty} \frac{1}{T}\int_o^T x(t)\, x(t+\tau)\, dt \tag{4-3}$$

and

$$R_X(-\tau) = R_X(\tau),\ R_X(o) \geq \left| R_X(\tau) \right| \text{ for all } \tau \tag{4-4}$$

For stationary data, the power spectral density function and the auto-correlation function are related by a Fourier transform as follows:

$$\begin{aligned} \phi_X(f) &= 2\int_{-\infty}^{\infty} R_X(\tau)\, e^{-i2\pi f\tau}\, d\tau \\ &= 4\int_o^{\infty} R_X(\tau) \cos 2\pi f\tau\, d\tau \end{aligned} \tag{4-5}$$

The mean square value of x(t) is given by:

$$\begin{aligned} \overline{x^2} &= \lim_{T\to\infty} \frac{1}{T}\int_o^T \dot{x}^2(t)\, dt \\ &= \int_o^{\infty} \phi_X(f)\, df = R_X(0) \end{aligned} \tag{4-6}$$

Applying Parseval's theorem, the power spectral density function may be expressed as follows (see Reference 47):

$$\phi_X(f) = 2T \left| F_X(f) \right|^2 \tag{4-7}$$

Similarly, for two sets of stationary ergodic random data x(t) and y(t), the cross-correlation function is defined as:

$$R_{xy}(\tau) = \lim_{T\to\infty} \frac{1}{T}\int_o^T x(t)\, y(t+\tau)\, dt \tag{4-8}$$

and

$$R_{xy}(-\tau) = R_{yx}(\tau) \tag{4-9}$$

The cross-spectral-density function and the cross correlation function are related by the Fourier transform:

$$\phi_{xy}(f) = 2\int_{-\infty}^{\infty} R_{xy}(\tau)\, e^{-i2\pi f\tau}\, d\tau \tag{4-10}$$

Two useful formulations relating auto-and cross-power spectra are:

$$\phi_{yx}(f) = \phi_{xy}^{*}(f) = \phi_{xy}(-f) \tag{4-11}$$

$$\left|\phi_{xy}(f)\right|^2 \leq \phi_x(f)\,\phi_y(f) \tag{4-12}$$

The coherence function is a real-valued quantity given by:

$$\gamma_{xy}^2(f) = \frac{\left|\phi_{xy}(f)\right|^2}{\phi_x(f)\,\phi_y(f)} \leq 1 \tag{4-13}$$

When $\gamma_{xy}^2(f) = 0$ at a particular frequency, x (t) and y (t) are said to be uncorrelated at that frequency. If x (t) and y (t) are statistically independent, then $\gamma_{xy}^2(f) = 0$ for all frequencies. When $\gamma_{xy}^2(f) = 1$ for all f, then x (t) and y (t) are said to be fully coherent or perfectly correlated. A quantity equivalent to coherence function in the time domain is the correlation function coefficient (normalized cross-covariance function) which is defined by:

$$\rho_{xy}(\tau) = \frac{R_{xy}(\tau) - \mu_x \mu_y}{\sqrt{\left[R_x(0) - \mu_x\right]\left[R_y(0) - \mu_y\right]}} \tag{4-14}$$

$$-1 \leq \rho_{xy}(\tau) \leq 1 \quad \text{for all } \tau\text{'s} \tag{4-15}$$

where μ_x and μ_y are the mean values of x (t) and y (t) respectively. The function $\rho_{xy}(\tau)$ measures the degree of linear dependence between x (t) and y (t) for a displacement of τ in y (t) relative to x (t).

The cross-correlation measurement between two sets of random data may yield the time delay information when the data are properly correlated. For this case, the time delay may be determined by noting the time displacement associated with an observed peak in the cross-correlogram.

The probability density function for random data x (t) describes the probability that the data will assume a value within some defined range $x < x(t) \leq x + \Delta x$ at any time instant:

$$p(x) = \lim_{\Delta x \to o} \lim_{T \to \infty} \frac{1}{T} \frac{T_x}{\Delta x} \tag{4-16}$$

where T_x is the total amount of time that x(t) falls inside the range $(x, x+\Delta x)$ during an observation time T. The cumulative probability distribution function which describes the probability that the instantaneous value x(t) is less than or equal to some value x is defined by

$$P(x) = \text{Prob}\,[x(t) \leq x] = \int_{-\infty}^{x} p(\xi)\, d\xi \tag{4-17}$$

and it is bounded by zero and unity.

4.2 Digitized Power Spectra

The digitizing process converted the continuous flight test data into discrete numerical data. The sampling rate for high-frequency digitization procedure used in the subject program was 5,000 samples per second, corresponding to a cut-off frequency of 2,500 Hz. The highest frequency in the presented data was limited to 1,000 Hz, which was considered sufficient to handle the buffet pressure and response data of a full scale aircraft. In order to achieve detail spectral coverage in the low-frequency range where all major structural modes of the aircraft were located, a separate low-frequency processing procedure was used.

The sampling rate for low-frequency digitization procedure was 1,000 samples per second. The frame rate was 0.001 second and the cutoff frequency was 500 Hz. Sampling rate other than the ones quoted above were also used depending on specific application. In order to avoid the aliasing problem, the high-frequency components were filtered out prior to sampling.

There are two methods to generate the power spectral data:

1. Fourier transform method — The digital time history functions are first converted to Fourier transforms utilizing Equations (4-1) and (4-2) as follows:

$$x_n = x(n\Delta t) = A_o + \sum_{m=1}^{N/2} A_m \cos\left(\frac{2\pi mn}{N}\right) + \sum_{m=1}^{(N/2)-1} B_m \sin\left(\frac{2\pi mn}{N}\right)$$

$$n = 1, 2, \ldots, N \tag{4-18}$$

$$A_o = \frac{1}{N}\sum_{n=1}^{N} x_n$$

$$A_m = \frac{2}{N}\sum_{n=1}^{N} x_n \cos\left(\frac{2\pi mn}{N}\right) \qquad m = 1, 2, \ldots, \frac{N}{2} - 1$$

$$A_{N/2} = \frac{1}{N}\sum_{n=1}^{N} x_n \cos(\pi n) \tag{4-19}$$

$$B_m = \frac{2}{N}\sum_{n=1}^{N} x_n \sin\left(\frac{2\pi mn}{N}\right) \qquad m = 1, 2, \ldots, \frac{N}{2} - 1$$

where N is the sample size, and Δt is the time increment (equal to a multiple of the frame rate) which has been selected to produce a sufficiently high-frequency cutoff, $f_c = 1/(2\Delta t)$. The associated basic time span T is $N\,\Delta t$. The frequency increment is $1/T$.

Application of equation (4-7) yields the power spectral data. For high frequency data, more time segments have to be used. The final results are obtained by averaging over all the segments.

2. Correlation method — The digital data are first converted to auto correlation functions utilizing Equation (4-3) as follows:

$$R_\ell = R(\ell \Delta t)$$

$$= \frac{1}{N-\ell}\sum_{n=1}^{N-\ell} x_n\, x_{n+\ell} \qquad \ell = 0, 1, 2, \ldots, L \tag{4-20}$$

where L is the maximum correlation lag. Let B_e be the desired equivalent resolution bandwidth for PSD calculation, then

$$L = \frac{1}{B_e\,\Delta t} \quad . \tag{4-21}$$

The sample size N is chosen such that (Reference 47)

$$N = \frac{L}{\epsilon^2} \quad , \text{ or } \epsilon^2 = \frac{1}{B_e T} = \frac{L}{N} \tag{4-22}$$

where ϵ is the normalized standard error for spectral calculations, and the associated minimum time span T is $T = N \Delta t$. Equation (4-22) establishes the normalized standard error of power spectra as a function of the resolution band width B_e and the sample data time span T. This equation places certain restrictions on the spectral processing of the transonic maneuver data where the sampling time is limited. This point will be discussed further in a later subsection.

In digital processing of the power spectral data, Reference 47 suggests that the raw estimate $\tilde{\Phi}(f)$ of a true power spectral density function $\Phi_x(f)$ be calculated only at L + 1 discrete frequencies:

$$f = \frac{k f_c}{L} = \frac{k}{2 L \Delta t} \qquad k = 0, 1, 2, \ldots, L \tag{4-23}$$

At these discrete frequency points,

$$\tilde{\Phi}_k = \tilde{\Phi}\left(\frac{k f_c}{L}\right) = 2 \Delta t \left[R_o + 2 \sum_{\ell=1}^{L-1} R_\ell \cos\left(\frac{\pi \ell k}{L}\right) + (-1)^k R_L \right] \tag{4-24}$$

A final estimate of the power spectral density Φ_k is obtained using the following smoothing process. Smoothing is necessary since the raw estimate given by Equation (4-24) is an inefficient estimate of the true spectral density (Reference 47).

$$\begin{aligned} \Phi_o &= 0.5\, \tilde{\Phi}_o + 0.5\, \tilde{\Phi}_1 \\ \Phi_k &= 0.23\, \tilde{\Phi}_{k-1} + 0.54\, \tilde{\Phi}_k + 0.23\, \tilde{\Phi}_{k+1} \qquad k = 1,2,\ldots,L-1 \\ \Phi_L &= 0.5\, \tilde{\Phi}_{L-1} + 0.5\, \tilde{\Phi}_L \end{aligned} \tag{4-25}$$

In digital computation, at the discrete frequencies $f = k/(2L\Delta t)$, $k = 0, 1, 2 \ldots\ldots, L$, the coherence function is estimated by:

$$\gamma_{xy}^2(k) = \frac{\left| \Phi_{xy}(k) \right|^2}{\Phi_x(k)\, \Phi_y(k)} \tag{4-26}$$

4.3 Typical Pressure and Response Power Spectra

In this subsection typical power spectra obtained from the real-time buffet data are presented. The variation in spectral make-up trends corresponding to various phases of the maneuver is discussed. (A systematic presentation of the bulk of the spectral data is given in subsection 4.4.) Also included in this subsection are the low-frequency spectral data which are important in aircraft response studies. The low-frequency response is significant because all the major structural modes are located in this frequency range.

The pressure data were processed and converted into power spectra for a wind-up turn at $M_o = 0.75$ and h = 7,772 m, Run 7, Flight No. 825. Figure 38 shows the pressure power spectra obtained at the top surface of Wing Station 128.31, 85% semi-span and 90% chord position for a separated flow condition, Pressure Station No. 4, Figure 3. The power spectrum in the frequency range above 100 Hz seems to follow the -5/3 slope indicated by the inserted broken line. While not claiming any physical similiarity between the separated flow behavior described here and the case of the homogeneous turbulent flow, it is worthy of noting that the -5/3 slope is predicted by the theory of universal equilibrium in homogeneous turbulent flow. (See Reference 38, "The Structure of Turbulent Shear Flow," by A.A. Townsend, page 45.) The time span during which the spectral data of Figure 38 were acquired was t = 363.4 - 364.22. During this time, the flow on the complete upper wing surface became separated, as was shown in Figure 34(a). A typical power spectrum plot for an inboard pressure station located on the trailing edge flap, Pressure Station No. 18, Figure 3, acquired at the same time interval is shown in Figure 39. Figure 39 shows that the PSD level was quite high at this time; it represents an overall peak in spectral power for Station No. 18 during the complete maneuver. The high spectral power at Station No. 18 was attributed to the high turbulence when the local flow became separated where the shear layer was relatively close to the surface.

In order to examine the variations of the wing surface pressure power spectrum with angle of attack, the mean PSD function for various angle of attack ranges encountered in the wind-up turn maneuver was calculated. (The term "mean PSD" was used because a finite time increment corresponding to the angle of attack range variation was used to define the PSD function; hence, the requirement of stationarity was not exactly satisfied.) Furthermore, very narrowband spectral peaks were dropped to reveal the overall pattern.

Typical results of the type described above for Pressure Station No. 4 are shown in Figure 40. In Figure 40 the PSD function for $M_o = 0.75$ is presented for five angle of attack ranges. For $\alpha = (2.2° - 3.8°)$, the flow was essentially unseparated on the top of the wing. Except for very low frequencies, a PSD in the 47.54 $(N/M^2)^2/Hz$ (10^{-6} psi^2/Hz) range was observed. The pressure PSD showed a substantial increase as the angle of attack was increased to the range $(4.3° - 6.0°)$. For the remaining period of the maneuver, the PSD below 100 Hz did not vary greatly. Above 100 Hz, some amplitude changes were observed. The drop in PSD with an increasing α in this frequency range is believed due to the thickening of the separated flow region above the station where the pressure was measured, as mentioned previously in the report.

Two similar PSD trend plots for Pressure Station Nos. 4 and 1 are given in Figures 41 and 42 corresponding to $M_o = 0.925$, h = 10,668 m. Figure 41 shows the relatively small change in spectral power level at Station No. 4 throughout the transonic maneuver across the frequency band. Compared to Figure 40, it shows clearly the Mach number effect at the early stage of the maneuver. For $M_o = 0.75$, the flow at W.S. 128.31 did not become separated until the angle of attack reached at least 4° or more. Very low spectral level was thus recorded in Figure 40 corresponding to $\alpha = (2.2° - 3.8°)$. For $M_o = 0.925$, the flow became separated at the same section at a smaller angle of attack. This trend was clearly reflected in Figure 41 in the relatively high spectral level at $\alpha = (2.2° - 3.3°)$. Another point of interest was the similarity in spectral patterns for frequencies above 100 Hz corresponding with the two Mach numbers.

When compared to Figure 41, the spectral plot for Pressure Station No. 1 (Figure 42) shows the essential difference in dynamic pressure behavior at various chordwise positions of a wing section at $M_o = 0.925$. At low angle of attack, Station No. 1 registered very-low-level spectral power because the local flow was unseparated and was unaffected by the shock which appeared downstream. However, part of the low level spectra may be attributed to the instrumentation noise.

The PSD of Pressure Station No. 1 (Figure 42) was highest at $\alpha = (4.2° - 6.2°)$ when the local shock caused an oscillating pressure pattern. As the maneuver progressed, the pressure PSD level dropped somewhat.

In Figures 40-42, the PSD's corresponding to the recovery phase of the maneuvers after the peak angle of attack has been reached are not included. In general, the PSD levels corresponding to the recovery phase were comparatively high, which were attributed to the fluctuating pressures generated by the wing during the rapid recovery as well as the local fluctuating pressures generated by the deflected control surfaces. Sample data corresponding to this phase are given in the following subsection.

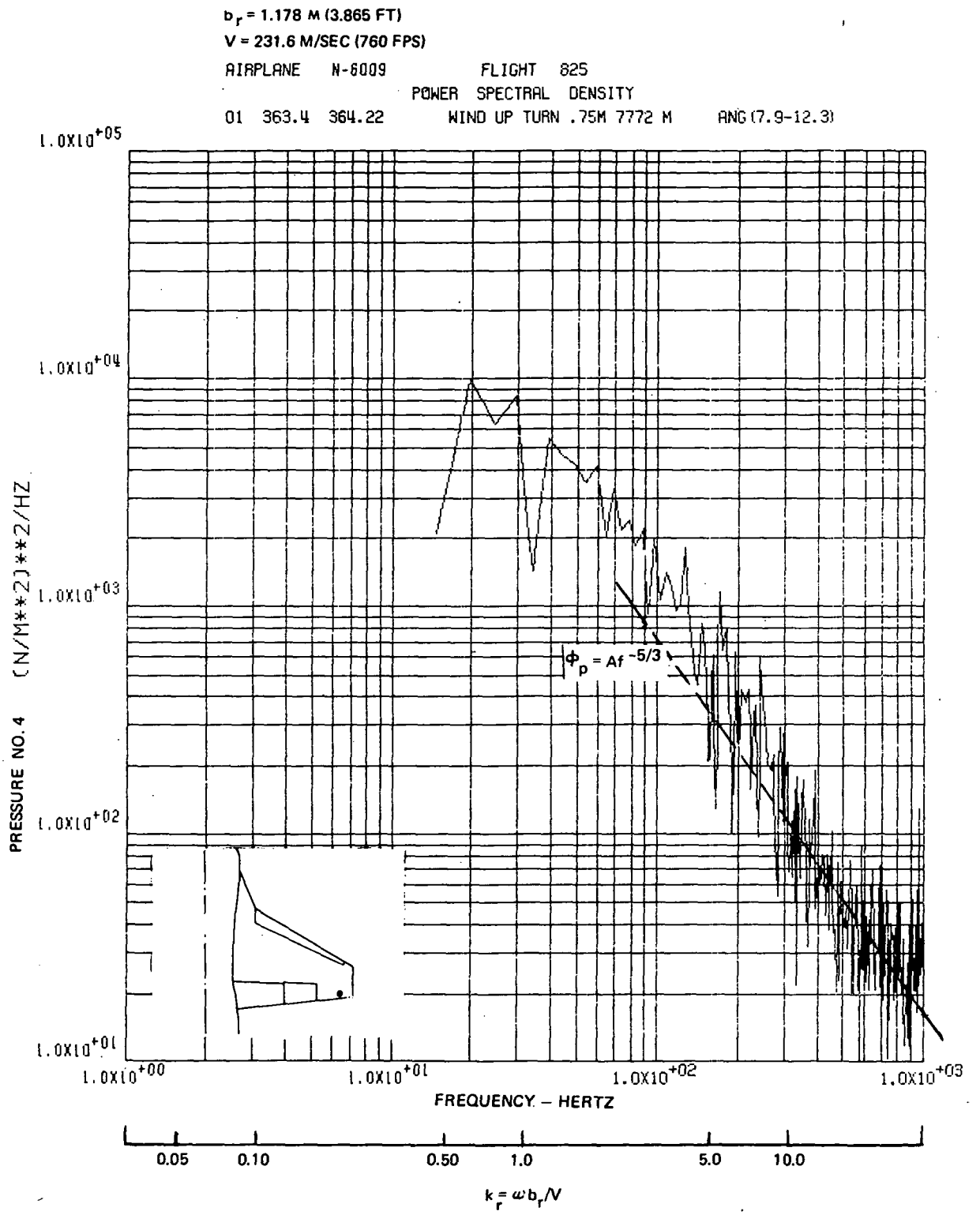

Figure 38. Power Spectrum of Buffet Pressure at Wing Station 128.31, 90% Chord Position, for $M_o = 0.75$, $h = 7,772$ m, $\delta_n = 0°$, $\delta_f = 0°$

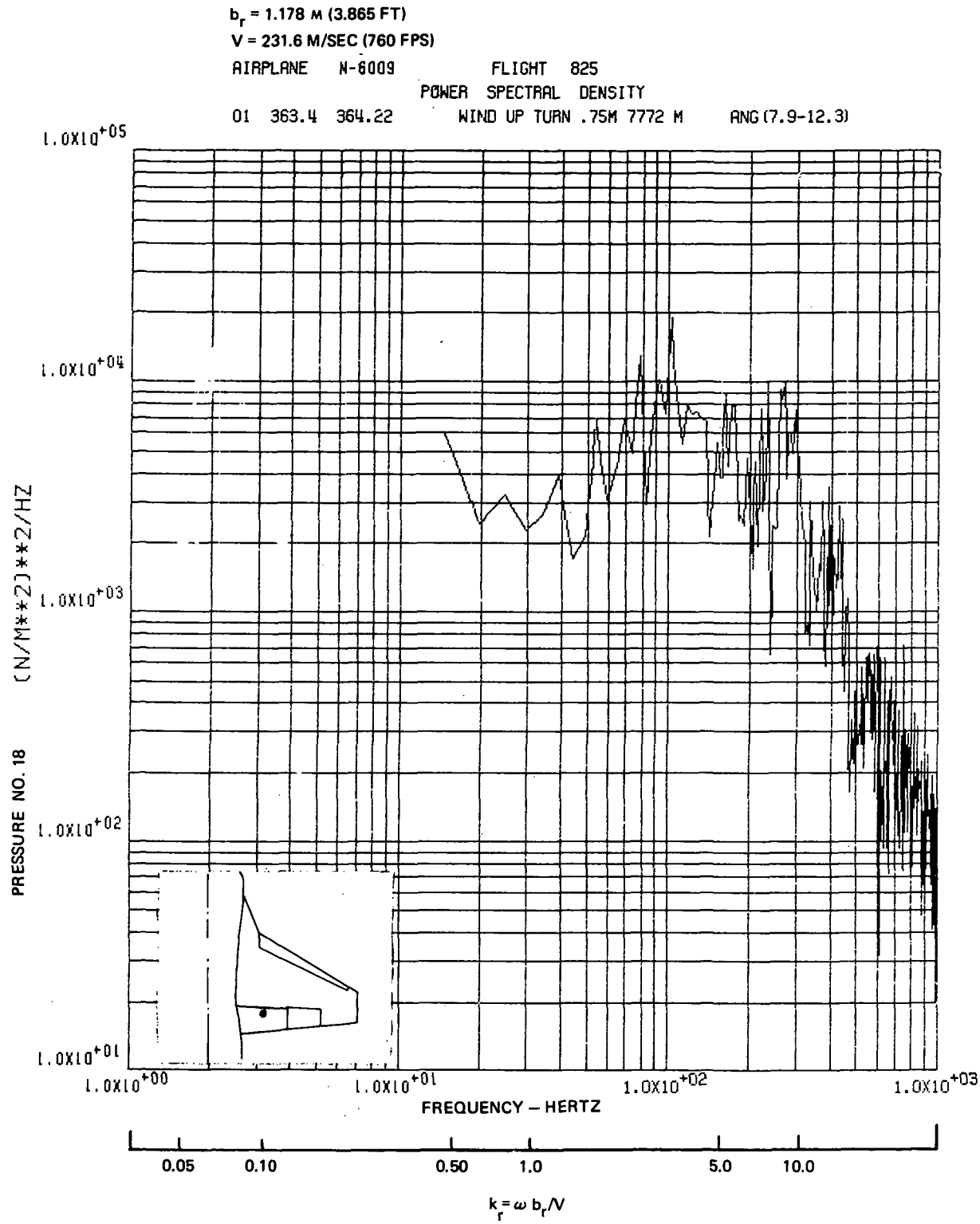

Figure 39. Power Spectrum of Buffet Pressure at Wing Station 50.00, 80% Chord Position, for $M_o = 0.75$, h = 7,772 m, $\delta_n = 0°$, $\delta_f = 0°$

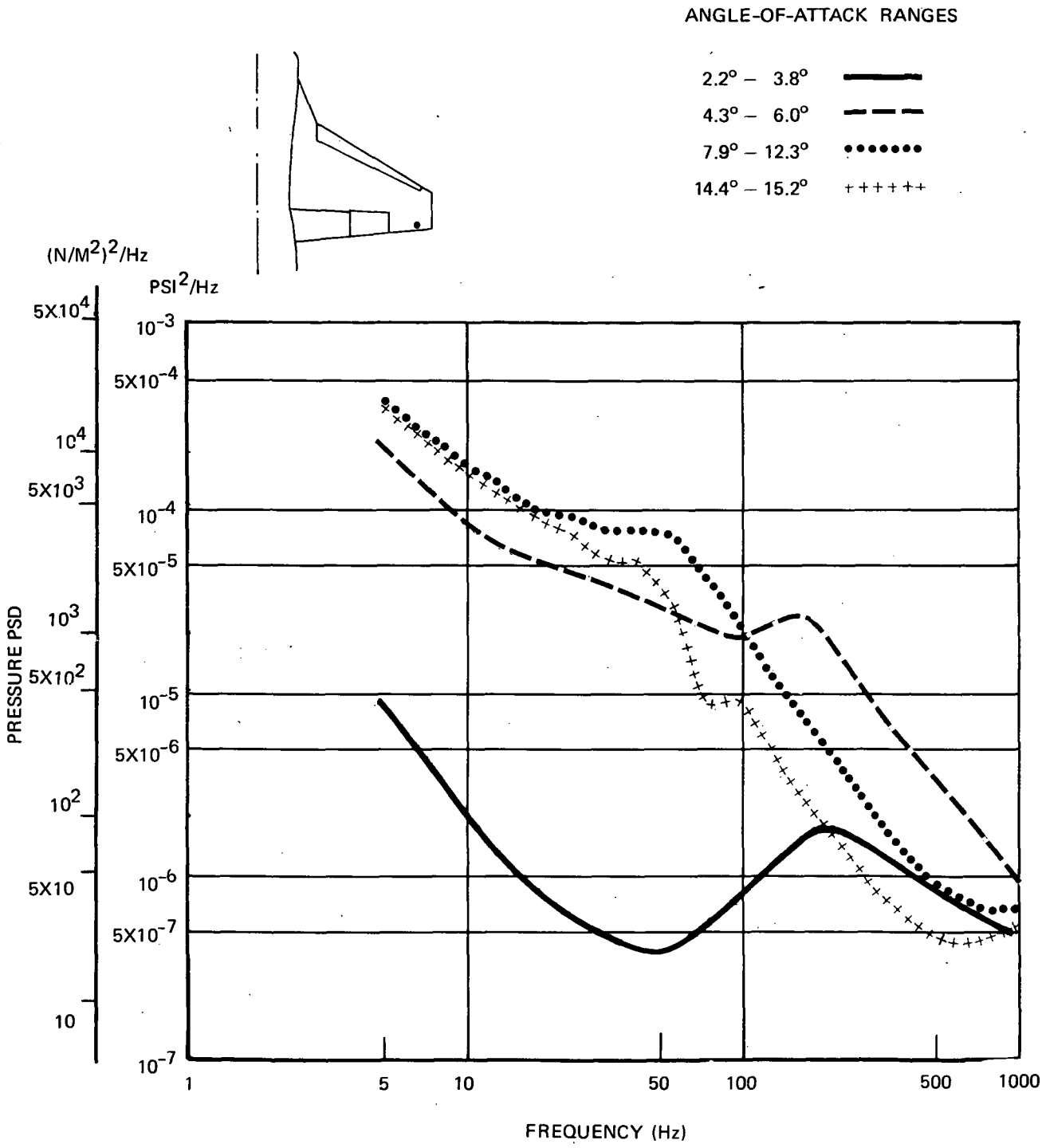

Figure 40. Trends of Buffet Pressure Spectra at Station No. 4 Corresponding to Various Angles of Attack During a Wind-Up Turn, $M_o = 0.75$, h = 7,772 m, $\delta_n = 0°$, $\delta_f = 0°$

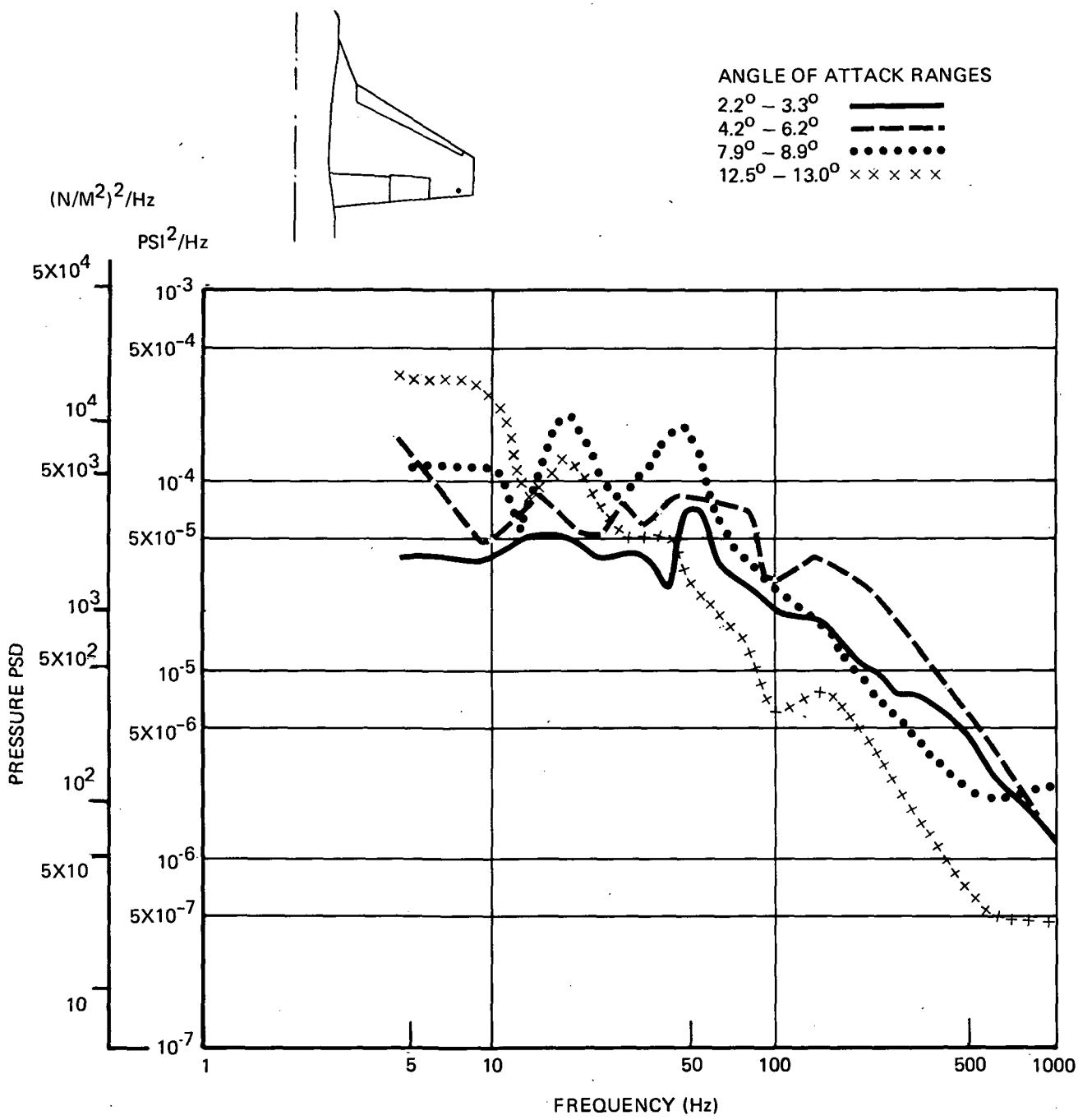

Figure 41. Trends of Buffet Pressure Spectra at Station No. 4 Corresponding to Various Angles of Attack During a Wind-Up Turn, $M_o = 0.925$, h = 10,668 m, $\delta_n = 0°$, $\delta_f = 0°$

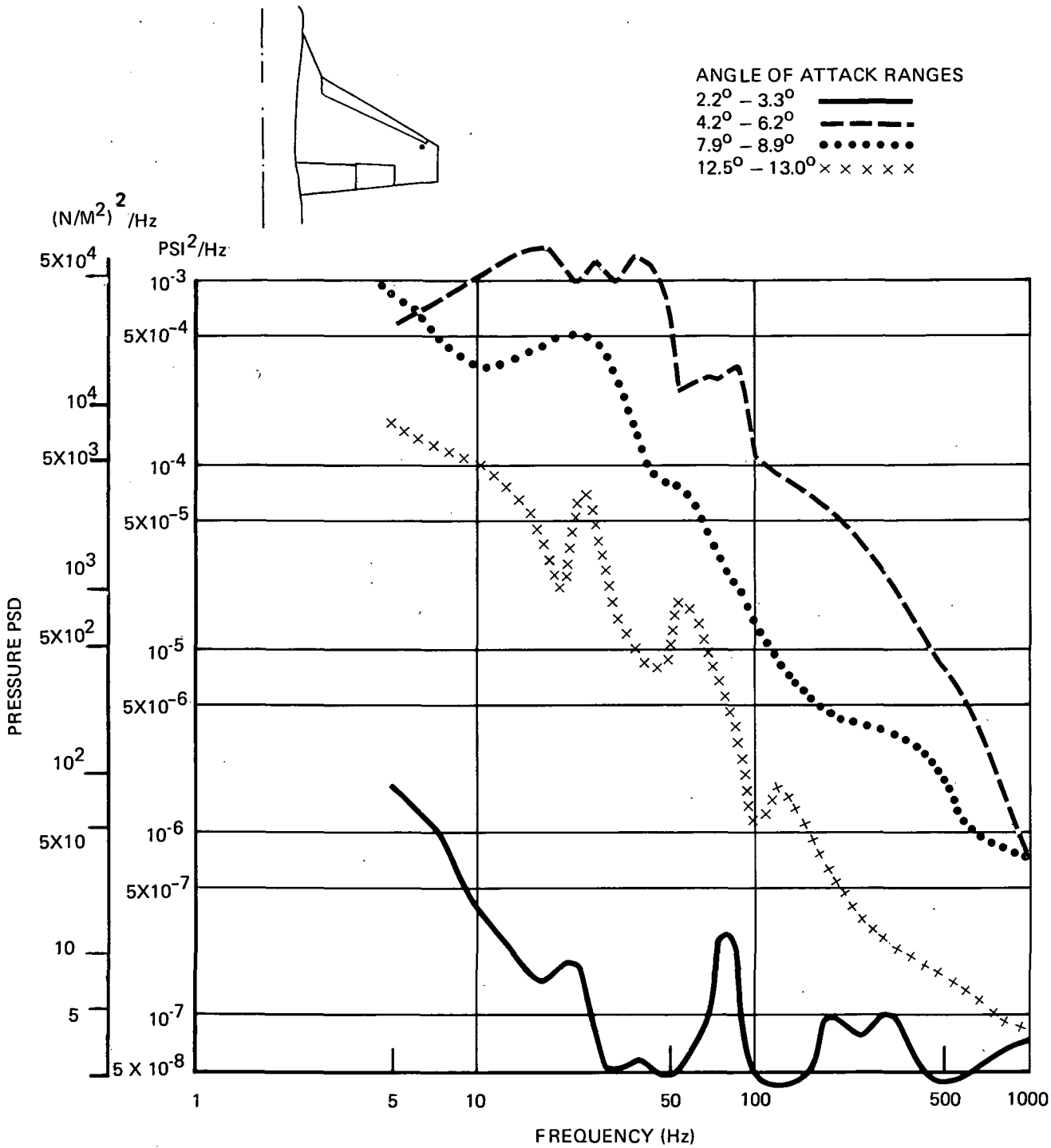

Figure 42. Trends of Buffet Pressure Spectra at Station No. 1 Corresponding to Various Angeles of Attack During a Wind-Up Turn, $M_o = 0.925$, h = 10,668 m, $\delta_n = 0°$, $\delta_f = 0°$

4.4 Power Spectra Corresponding to Various Phases of the Transonic Maneuver

In this subsection, auto power spectra of pressure and responses are presented in a systematic manner corresponding to various phases of the transonic maneuver. As mentioned previously, the transonic maneuver was dynamic in nature. The local buffet pressure and the response data were nonstationary in a strict sense. Within a short time interval (1 or 2 seconds) when no drastic change in local physical behavior took place, the data may be considered random and near-stationary so that the spectral processing technique may be applied.

For data acquired in Run 5, Flight 825, ($M_o = 0.925$, $h = 10,668$ m, $\delta_n/\delta_f = 0°/0°$), five time segments were chosen for spectral processing. Each time segment represented 1.025 seconds. Roughly, the five time segments may be classified as follows (also see Figure 34(c)).

Designation	Starting Time	α Initial	Description
A	334.0	2.2°	Initiated wind-up turn. Shock appeared at localized area.
B	335.03	4.1°	Buffet onset.
C	336.06	7.8°	Separation region expanded.
D	337.09	12.3°	Separated flow covered the complete wing surface.
E	338.12	13.9°	Recovery initiated.

The five PSD plots for each function corresponding to the time segments (A) through (E) are presented in one figure. For Run 5, seven pressure data sets were selected. These are Pressure Station Numbers 1, 3, 4, 6, 12, 18, and 23, whose PSD's are shown in Figures 43-49 respectively. Following the pressure PSD plots are four sets of response PSD plots. These are normal acceleration PSD at C. G. (Figure 50), normal acceleration PSD at forward and aft stations of right-hand wingtip (Figures 51, 52), and right-hand aileron hinge moment PSD (Figure 53).

Of the PSD plots described above, it may be mentioned that starting at t = 336.06, some low-frequency vibrations appeared in the aircraft. These vibrations were noted in the acceleration PSD plots as minor peaks. All the acceleration PSD plots (Figures 50-52) showed very high peaks between 400-500 Hz. It is possible that

these peaks were caused by the aircraft electrical noise because of the insufficient shielding of the lead wires and other unidentified disturbances. (The accelerometer harness was installed inside the aircraft perviously to acquire low- frequency response data.)

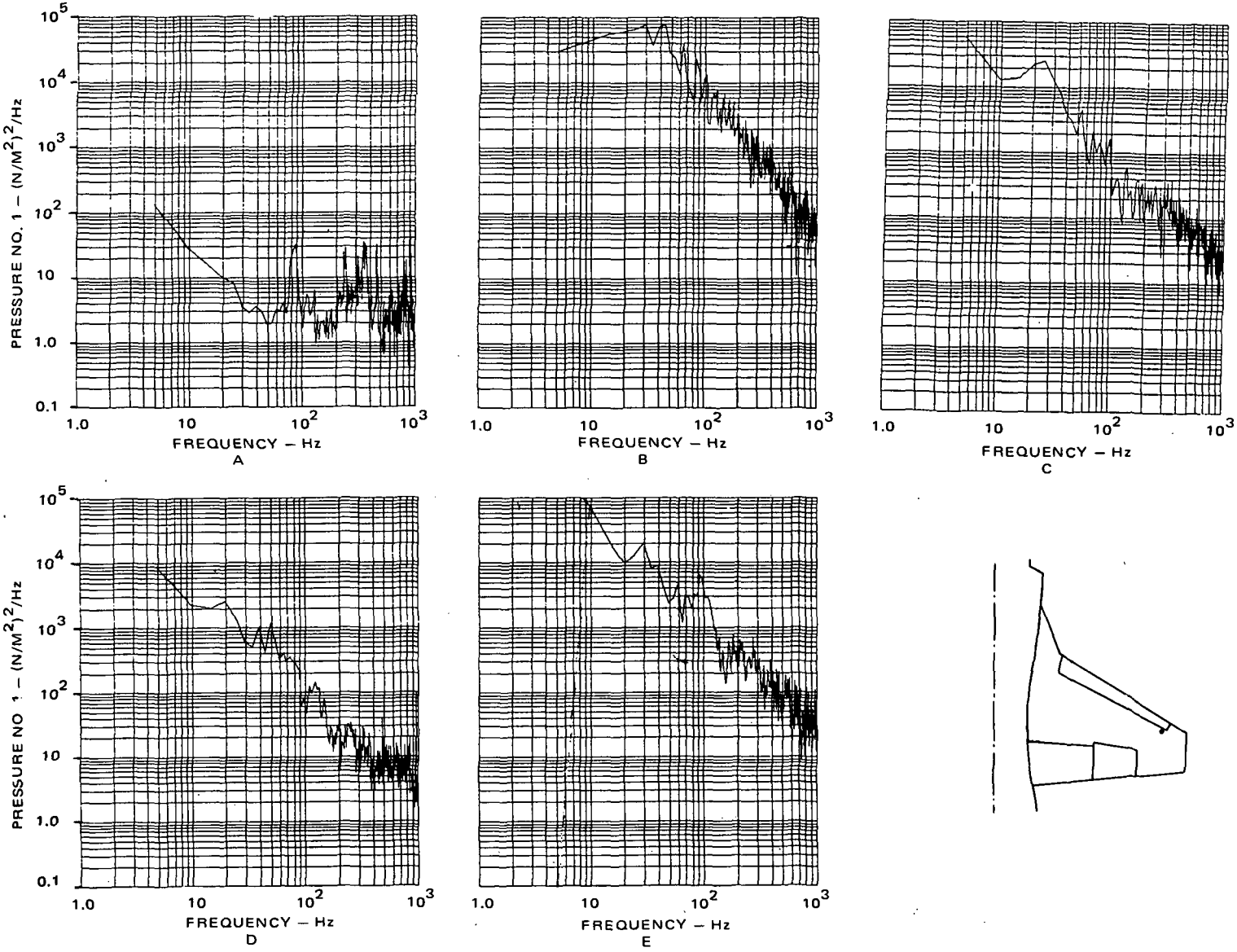

Figure 43. PSD's of Pressure No. 1 Based on Various Segments of Real Time Data, $M_o = 0.925$, h = 10,668m, $\delta_n/\delta_f = 0°/0°$

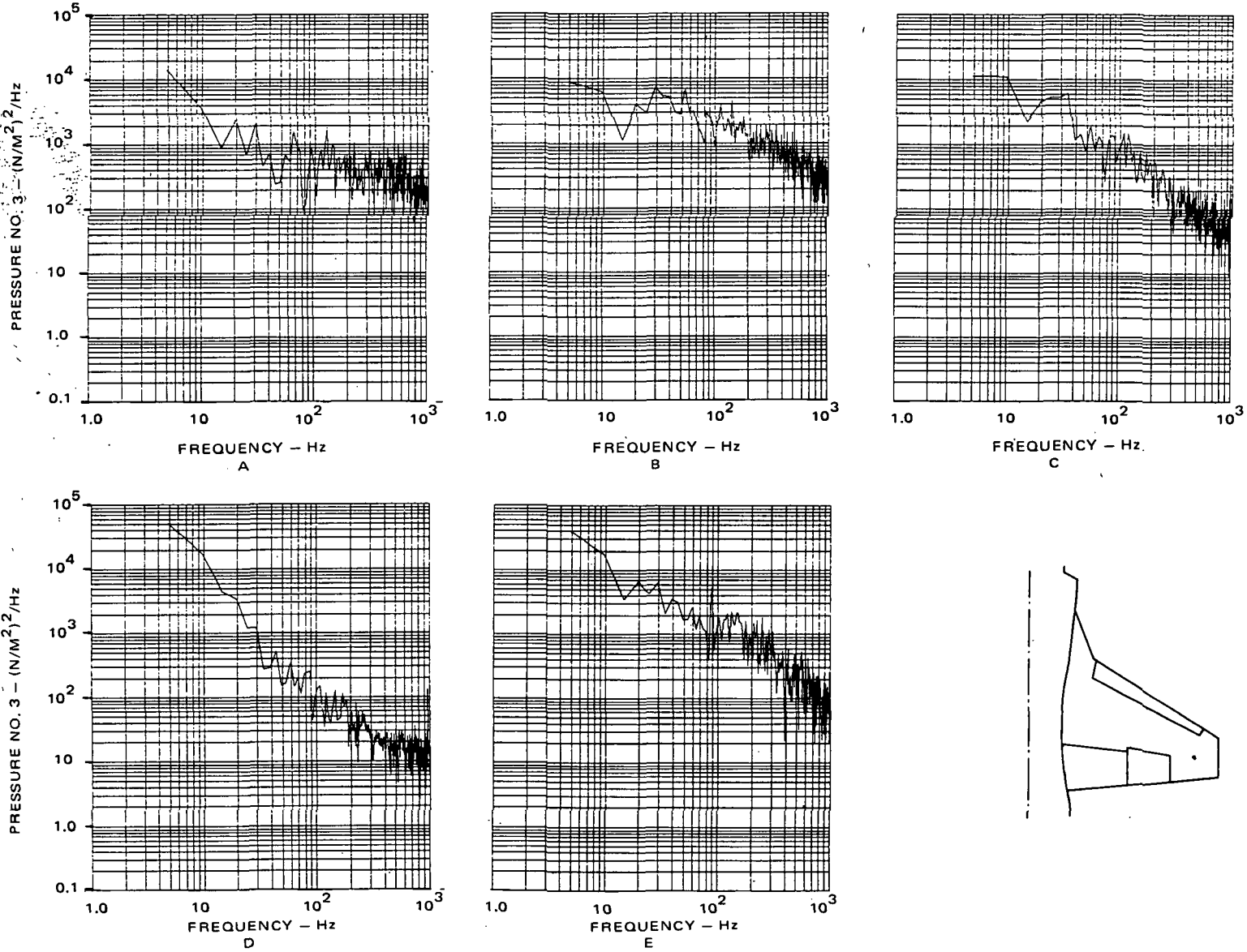

Figure 44. PSD's of Pressure No. 3 Based on Various Segments of Real Time Data, $M_o = 0.925$, $h = 10,668$m, $\delta_n/\delta_f = 0°/0°$

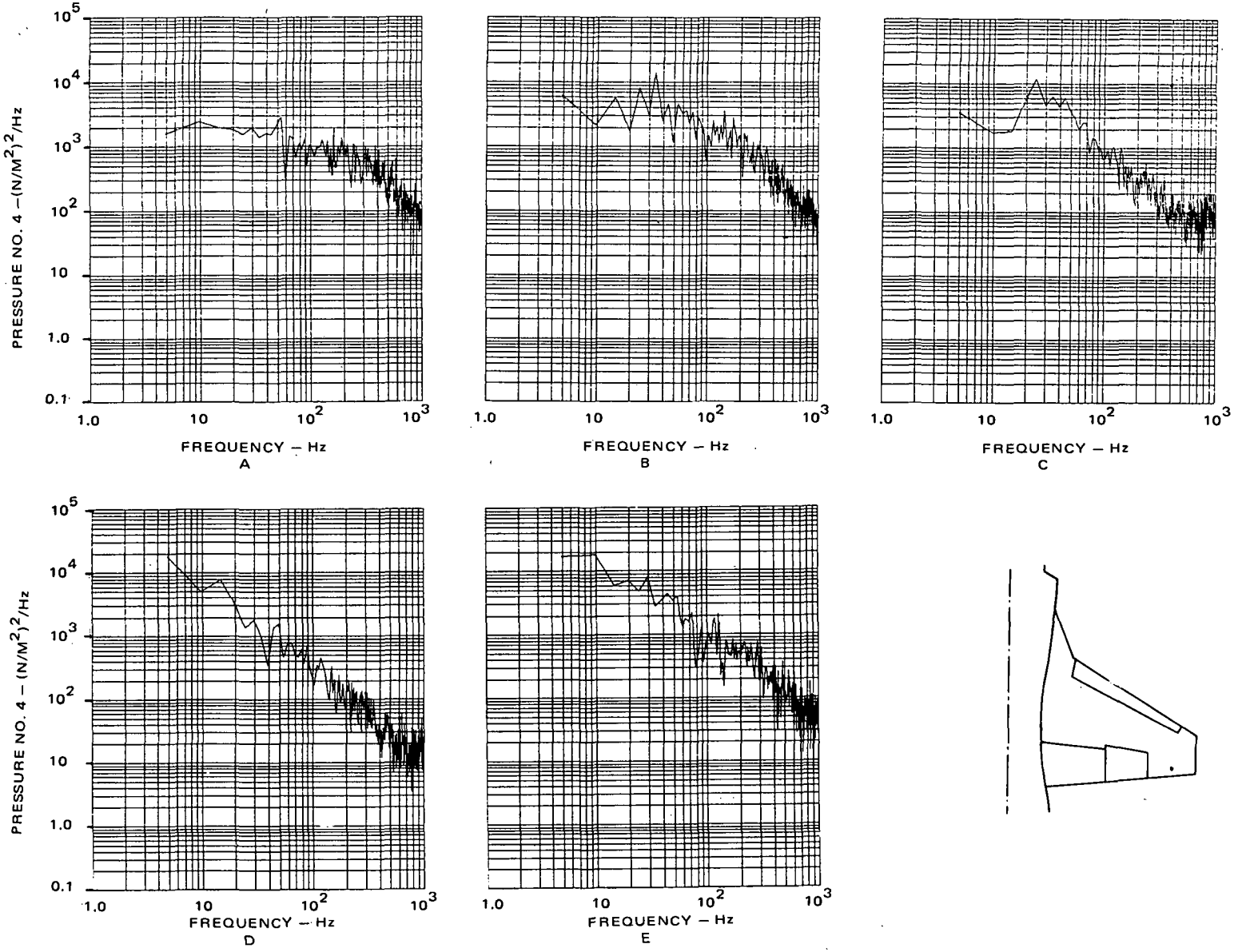

Figure 45. PSD's of Pressure No. 4 Based on Various Segments of Real Time Data, $M_o = 0.925$, $h = 10,668$m, $\delta_n/\delta_f = 0°/0°$

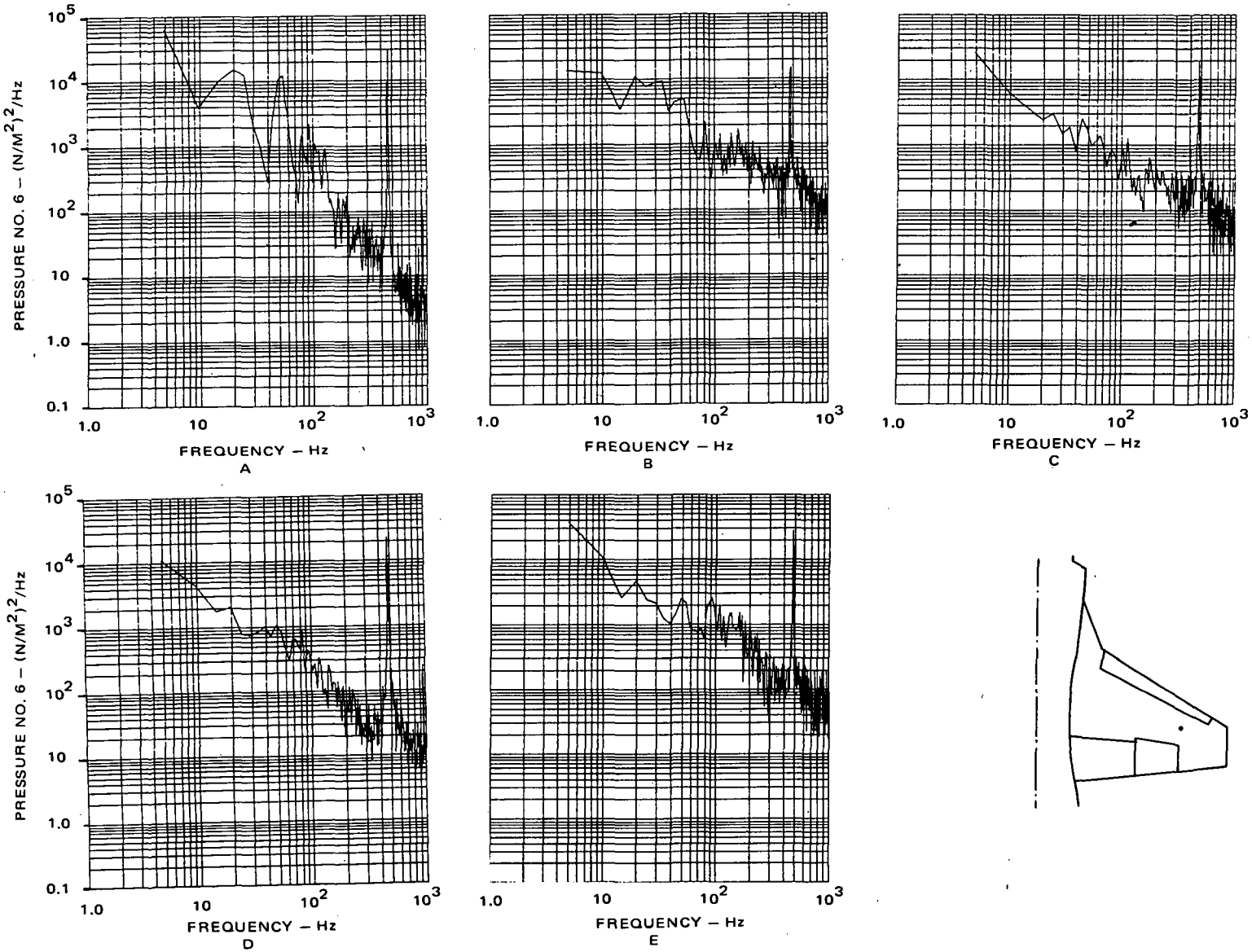

Figure 46. PSD's of Pressure No. 6 Based on Various Segments of Real Time Data, $M_o = 0.925$, $h = 10,668$m, $\delta_n/\delta_f = 0°/0°$

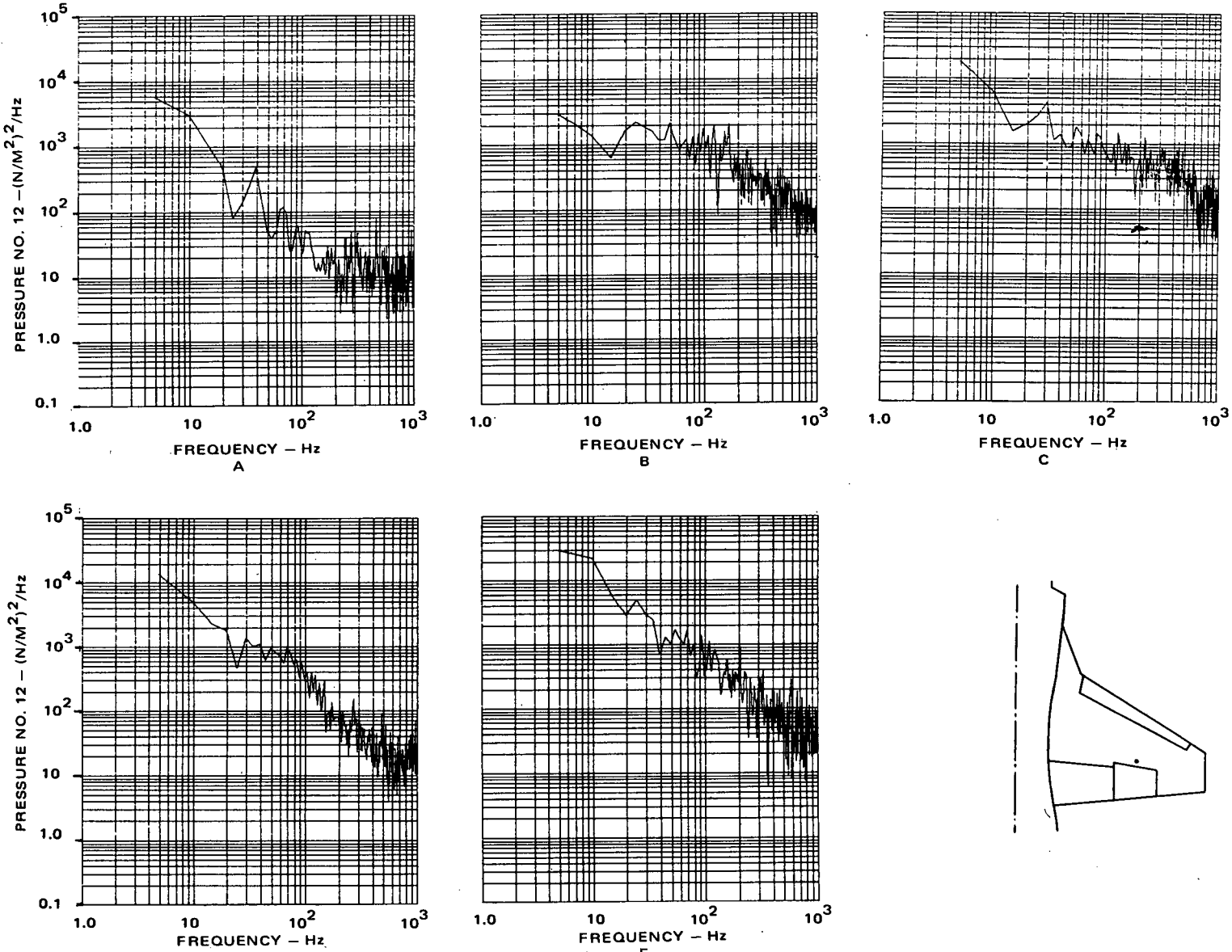

Figure 47. PSD's of Pressure No. 12 Based on Various Segments of Real Time Data, $M_o = 0.925$, h = 10,668m, $\delta_n/\delta_f = 0°/0°$

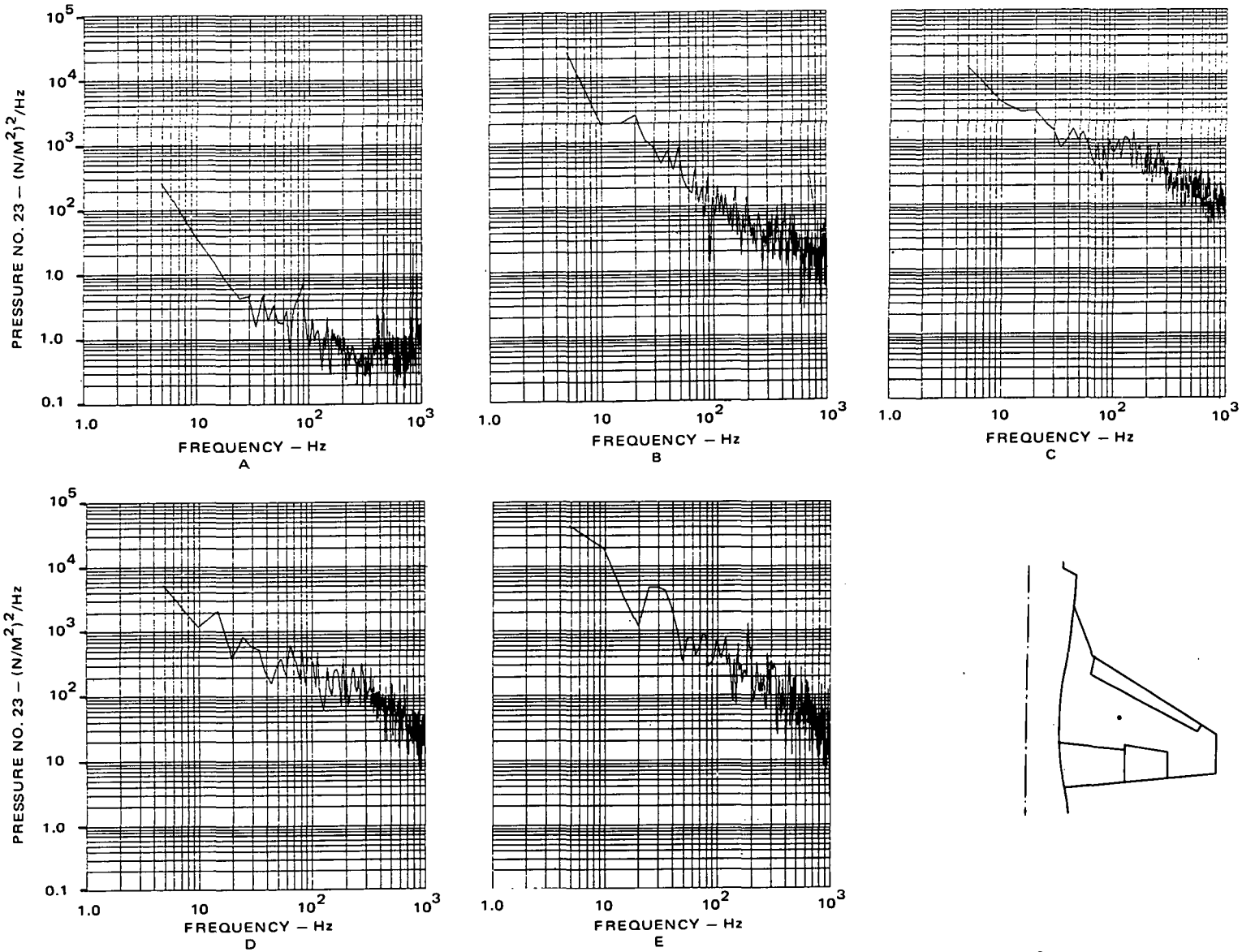

Figure 48. PSD's of Pressure No. 23 Based on Various Segments of Real Time Data, $M_o = 0.925$, h = 10,668m, $\delta_n/\delta_f = 0°/0°$

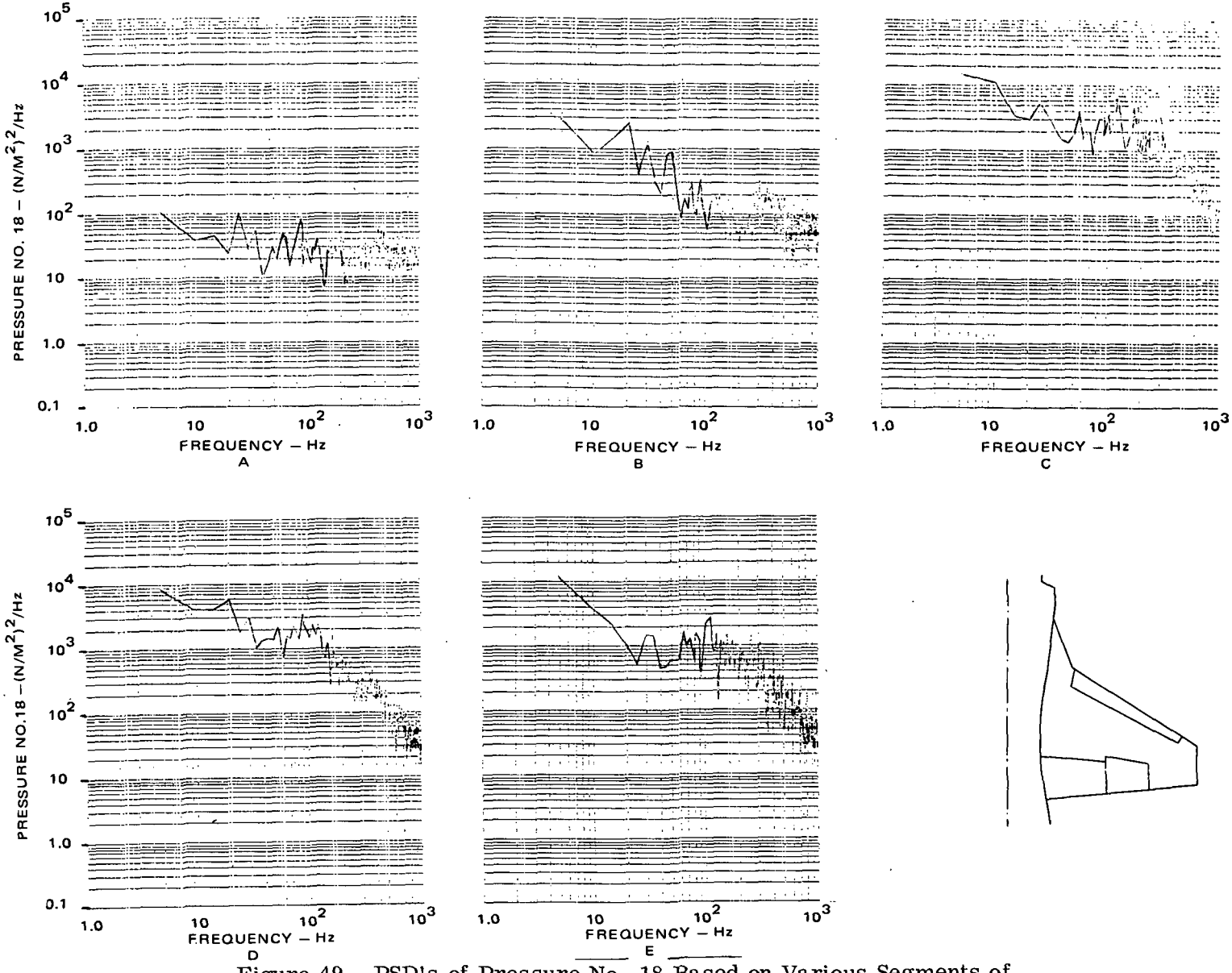

Figure 49. PSD's of Pressure No. 18 Based on Various Segments of Real Time Data, $M_o = 0.925$, h = 10,668m, $\delta_n/\delta_f = 0°/0°$

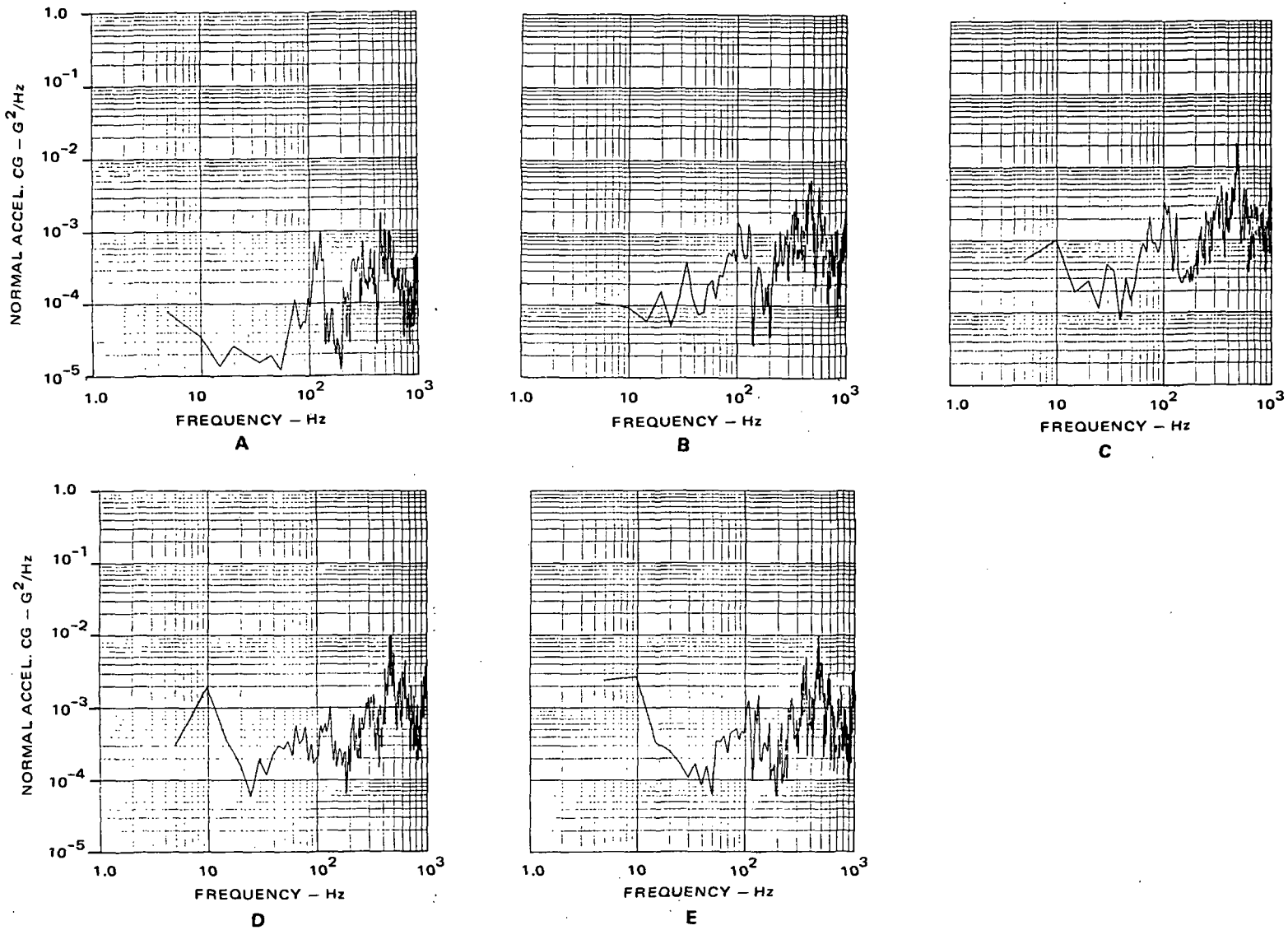

Figure 50. PSD's of C.G. Normal Acceleration Based on Various Segments of Real Time Data, $M_o = 0.925$, h = 10,668 m, $\delta_n/\delta_f = 0°/0°$

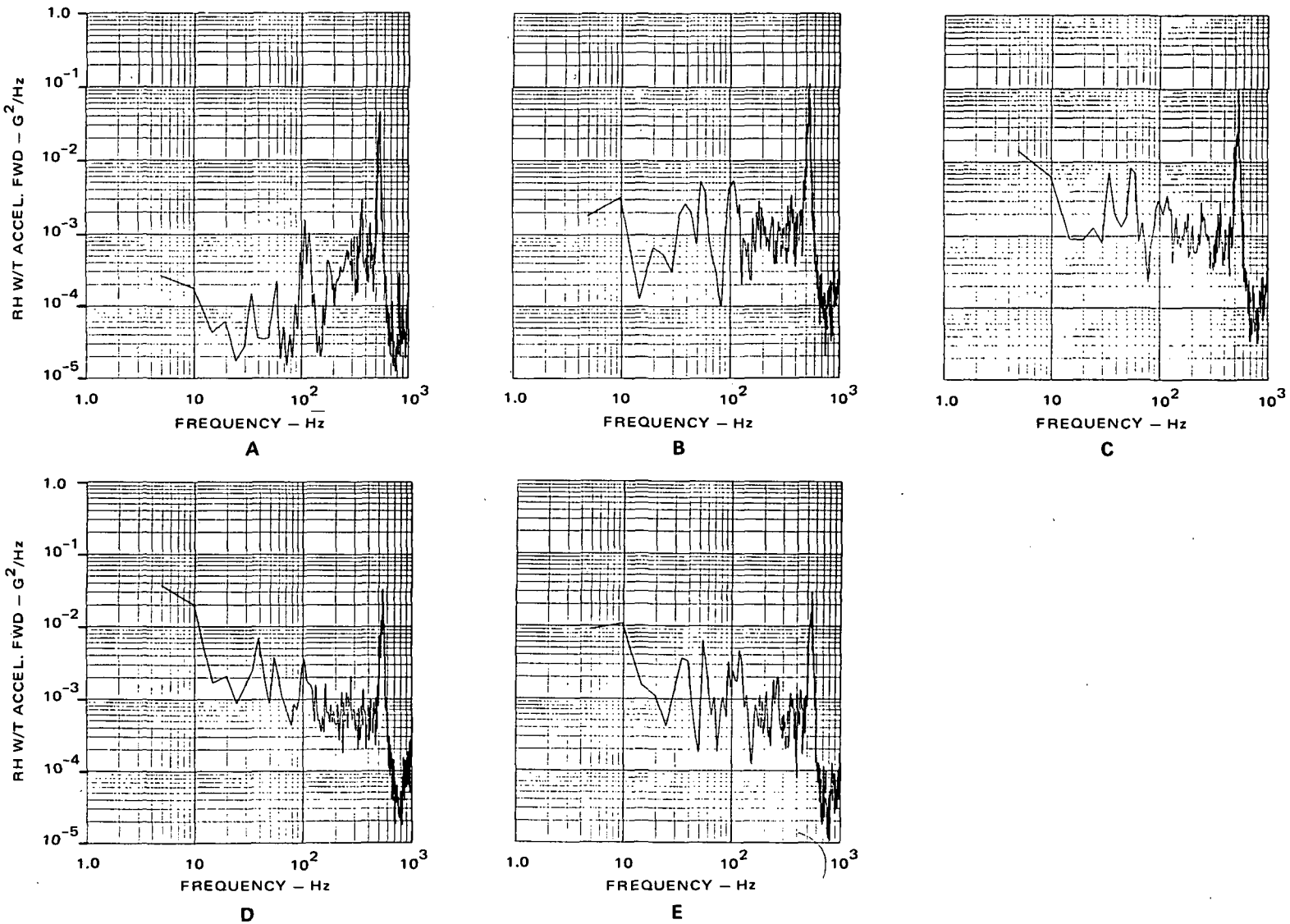

Figure 51. PSD's of Righthand Wing Tip Acceleration Forward Based on Various Segments of Real Time Data, $M_o = 0.925$, h = 10,668 m, $\delta_n/\delta_f = 0°/0°$

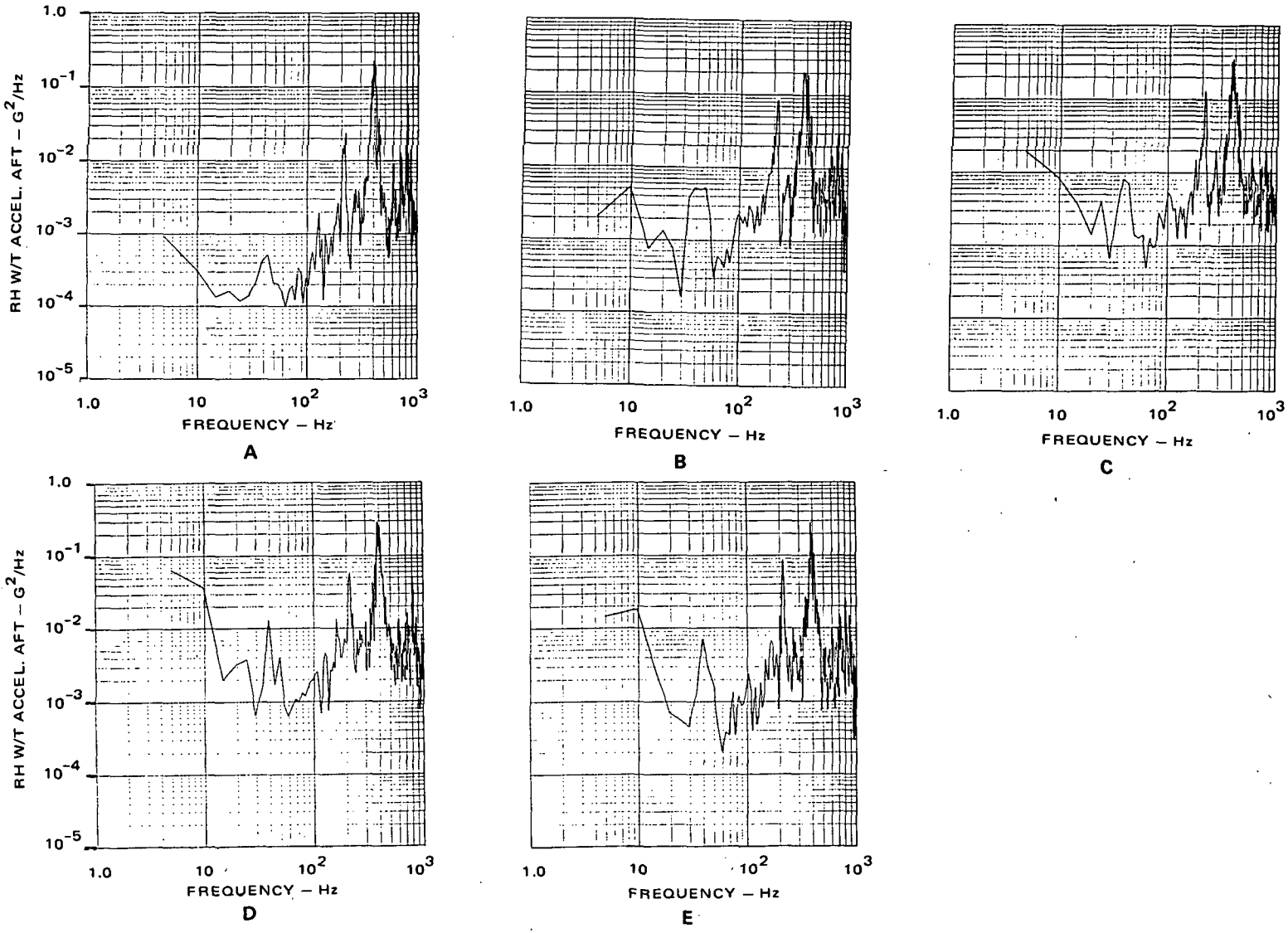

Figure 52. PSD's of Righthand Wing Tip Acceleration Aft Based on Various Segments of Real Time Data, $M_o = 0.925$, h = 10,668 m, $\delta_n/\delta_f = 0°/0°$

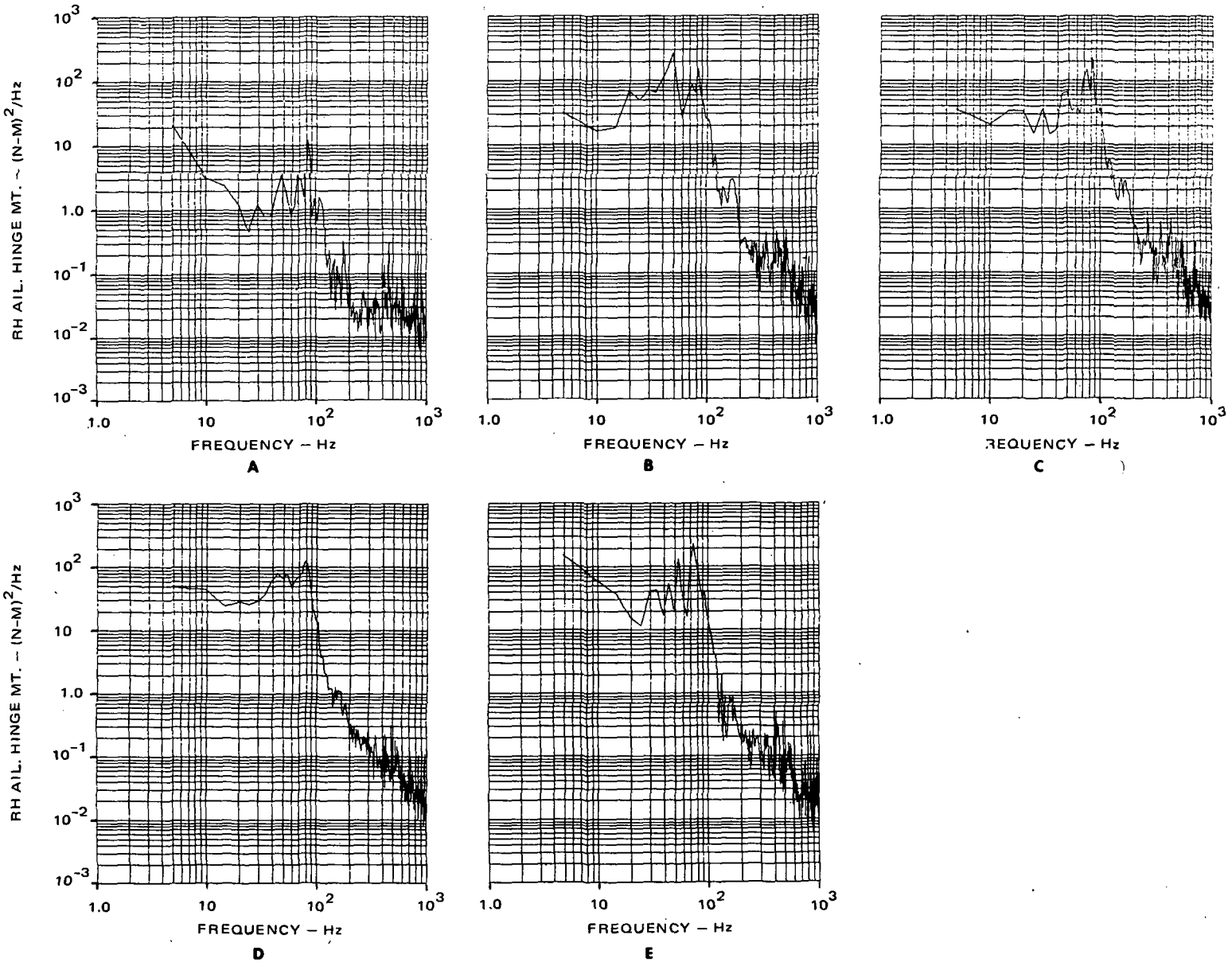

Figure 53. PSD's of Right Hand Aileron Hinge Moment Based on Various Segments of Real Time Data, $M_o = 0.925$, $h = 10,668$m, $\delta_n/\delta_f = 0°/0°$

Corresponding to the eleven sets of PSD plots for Run 5, Flight 825 ($M_o = 0.925$) presented in Figures 43-53, five sets of PSD plots were generated based on Run 7 of the same flight ($M_o = 0.75$). The time segments for the latter run were chosen in such a manner that the angle of attack at the beginning of each time segment was comparable to those of Run 5, with the exception of the fifth time segment where the initial angle of attack was substantially lower for Run 7. The five sets of PSD data are shown in Figures 54-58. Figures 54, 55, and 56 are for Pressure Stations No. 1, 3, and 23. Figures 57, 58 show the PSD's for the normal cg acceleration and the right-hand wingtip acceleration (forward station) respectively.

A comparison of Figures 43 and 54 showed that for Pressure Station No. 1 (20% chord and 85% semi-span) the pressure PSD was substantially higher for $M_o = 0.75$ at the initial stage of the maneuver. This was due to the leading-edge-induced separation corresponding to $M_o = 0.75$ discussed previously in reference to Figure 42. For an inboard station such as Pressure Station No. 23, a comparison of Figures 48 and 56 shows close similarity in the two sets of the PSD plots except in the low-frequency region.

A typical set of fluctuating pressure PSD plots for Run 6 of Flight 825 at $M_o = 0.85$ is shown in Figure 59. The PSD's are for Pressure Station No. 1. These plots may be evaluated against similar data for $M_o = 0.925$, 0.75 presented above (Figures 43, 54). In the case of Run 6, six (6) time segments were chosen covering the maneuver. The successive segments were designated A through F. Referring to Figure 59, the spectral trend plots reflected the relatively low fluctuating pressure prior to local flow separation (Segment A), the increase in power when the shock induced separation passed the locality (Segment C). The PSD level dropped with further α increase when the separation boundary moved inboard (Segment E). The behavior was similar to the case of $M_o = 0.925$ (see Figure 42). Subsequently, the PSD level increased at the end of the maneuver (Segment F).

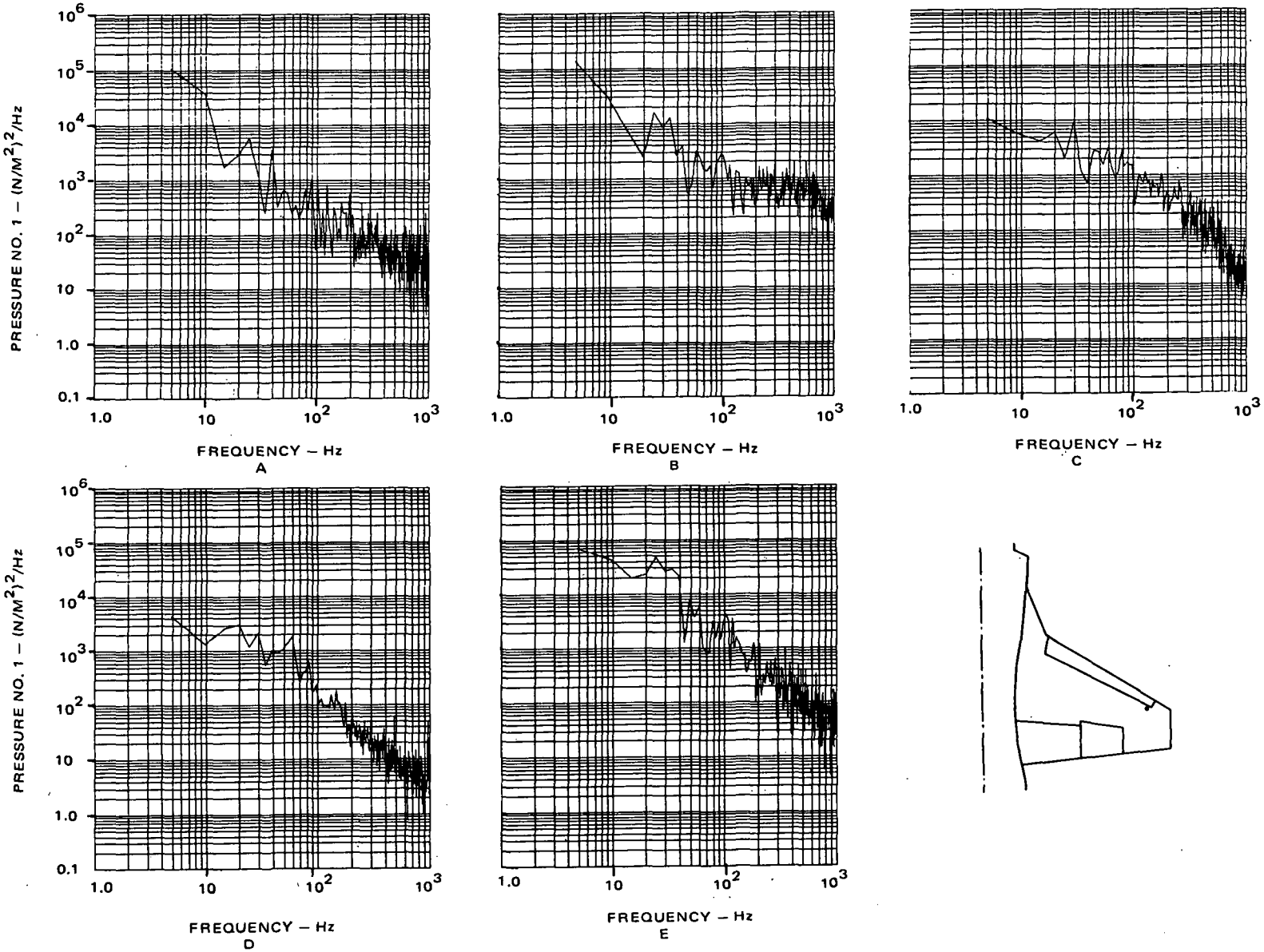

Figure 54. PDS's of Pressure No. 1, Based on Various Time Segments of the Real Time Data, $M_o = 0.75$, $h = 7,772$m, $\delta_n/\delta_f = 0°/0°$

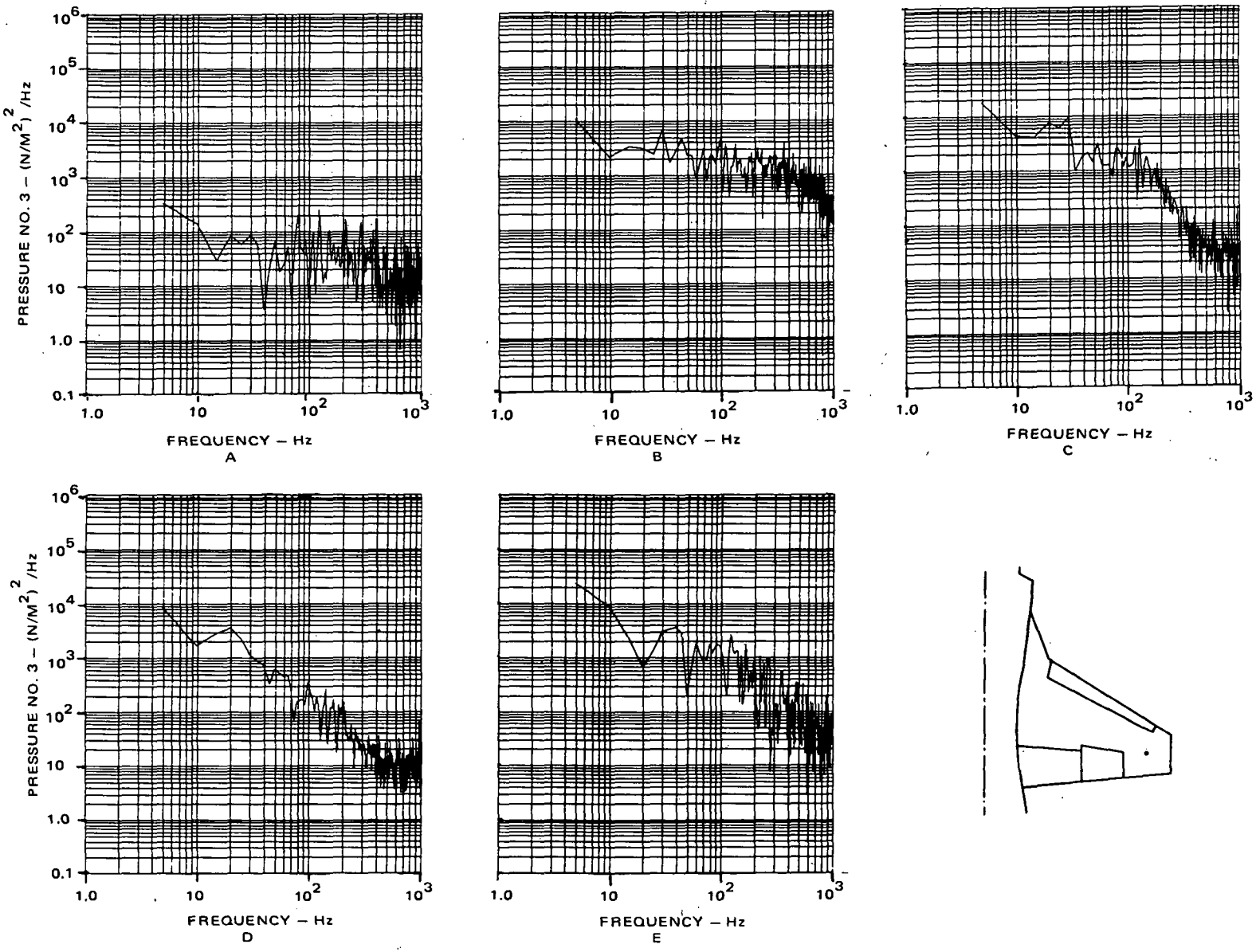

Figure 55. PSD's of Pressure No. 3, Based on Various Time Segments of the Real Time Data, $M_o = 0.75$, $h = 7,772$m, $\delta_n/\delta_f = 0°/0°$

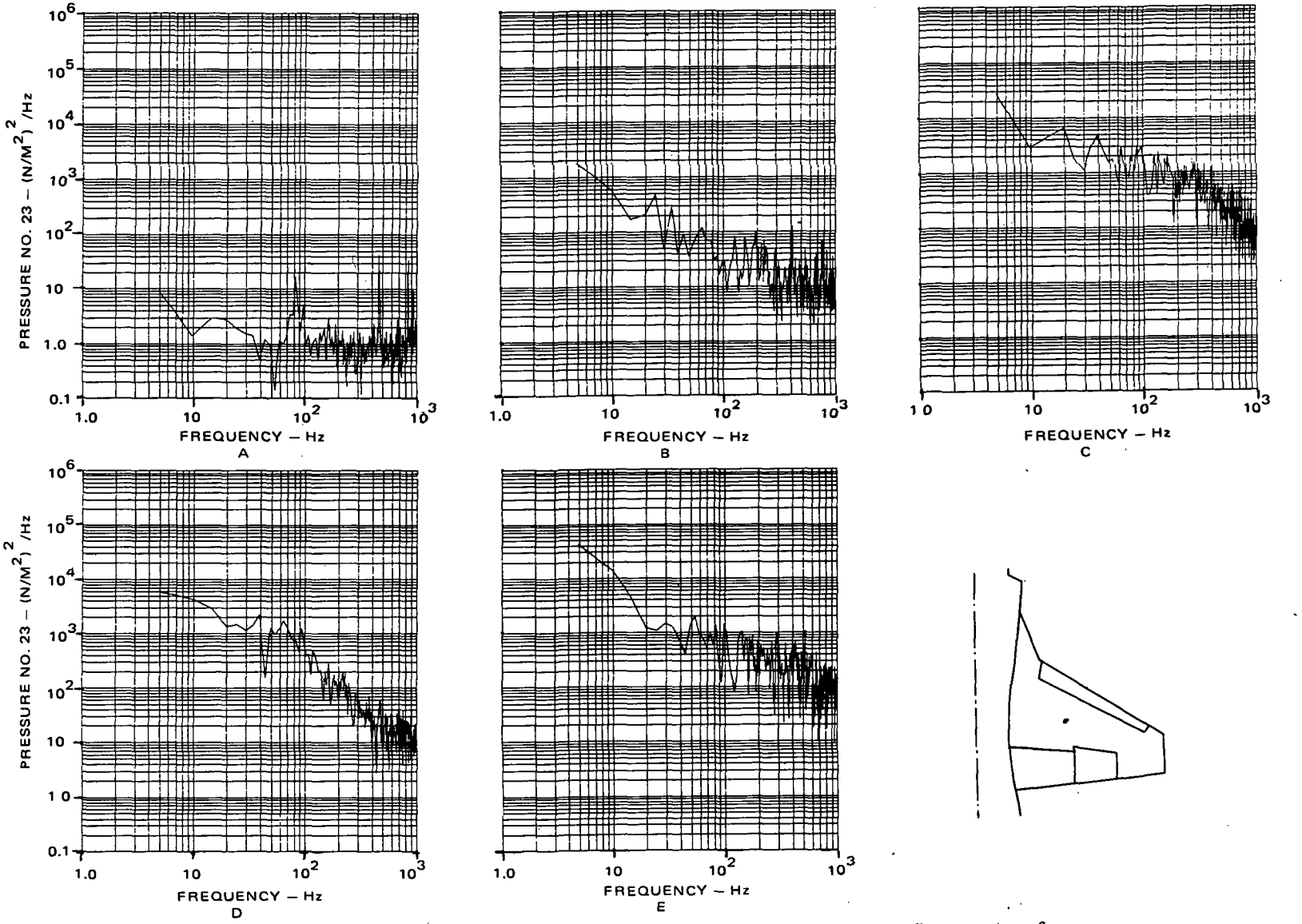

Figure 56. PSD's of Pressure No. 23, Based on Various Time Segments of the Real Time Data, $M_o = 0.75$, $h = 7,772$m, $\delta_n/\delta_f = 0°/0°$

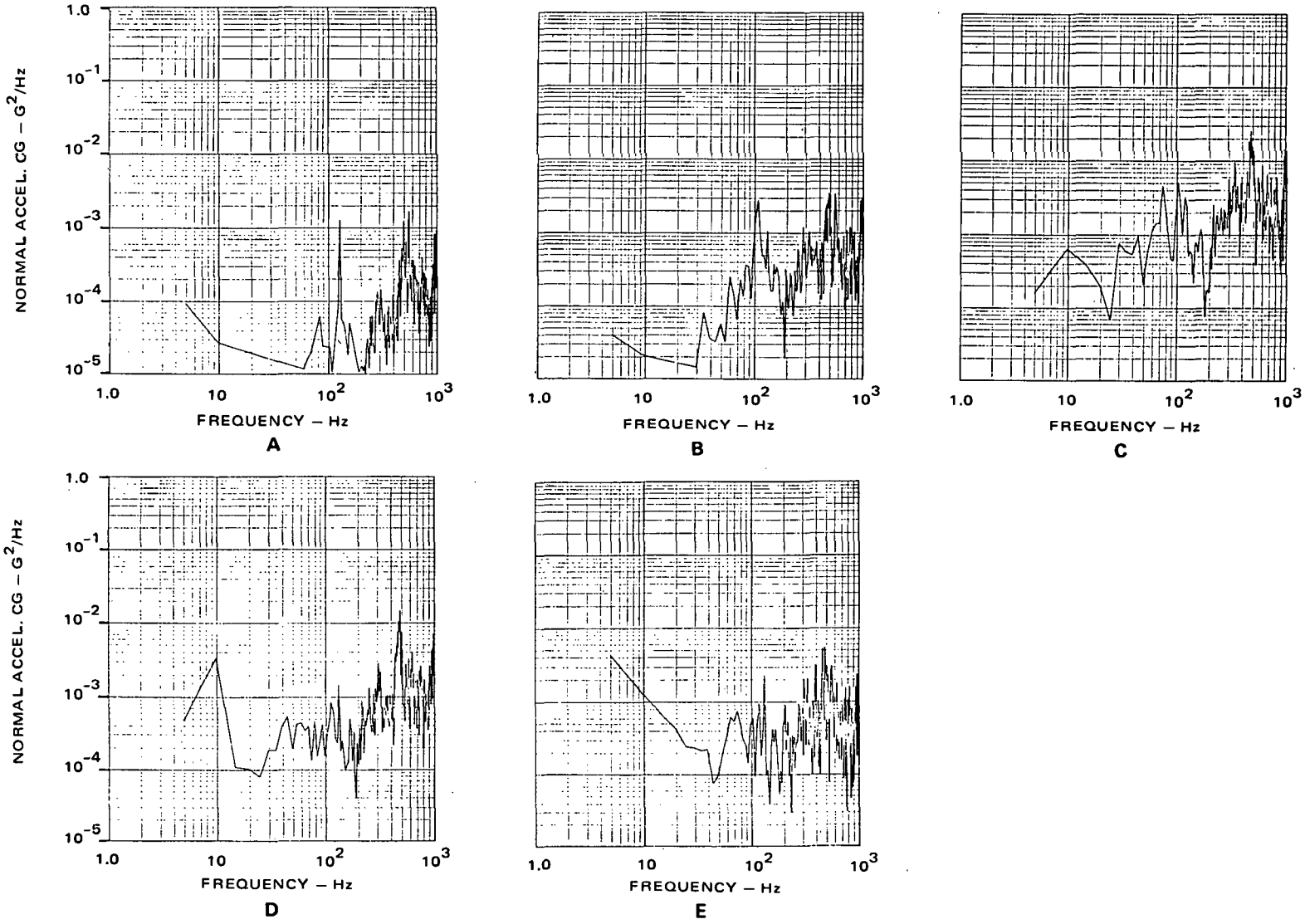

Figure 57. PSD's of Normal C.G. Acceleration Based on Various Time Segments of Real Time Data, $M_o = 0.75$, h = 7,772 m, $\delta_n/\delta_f = 0°/0°$

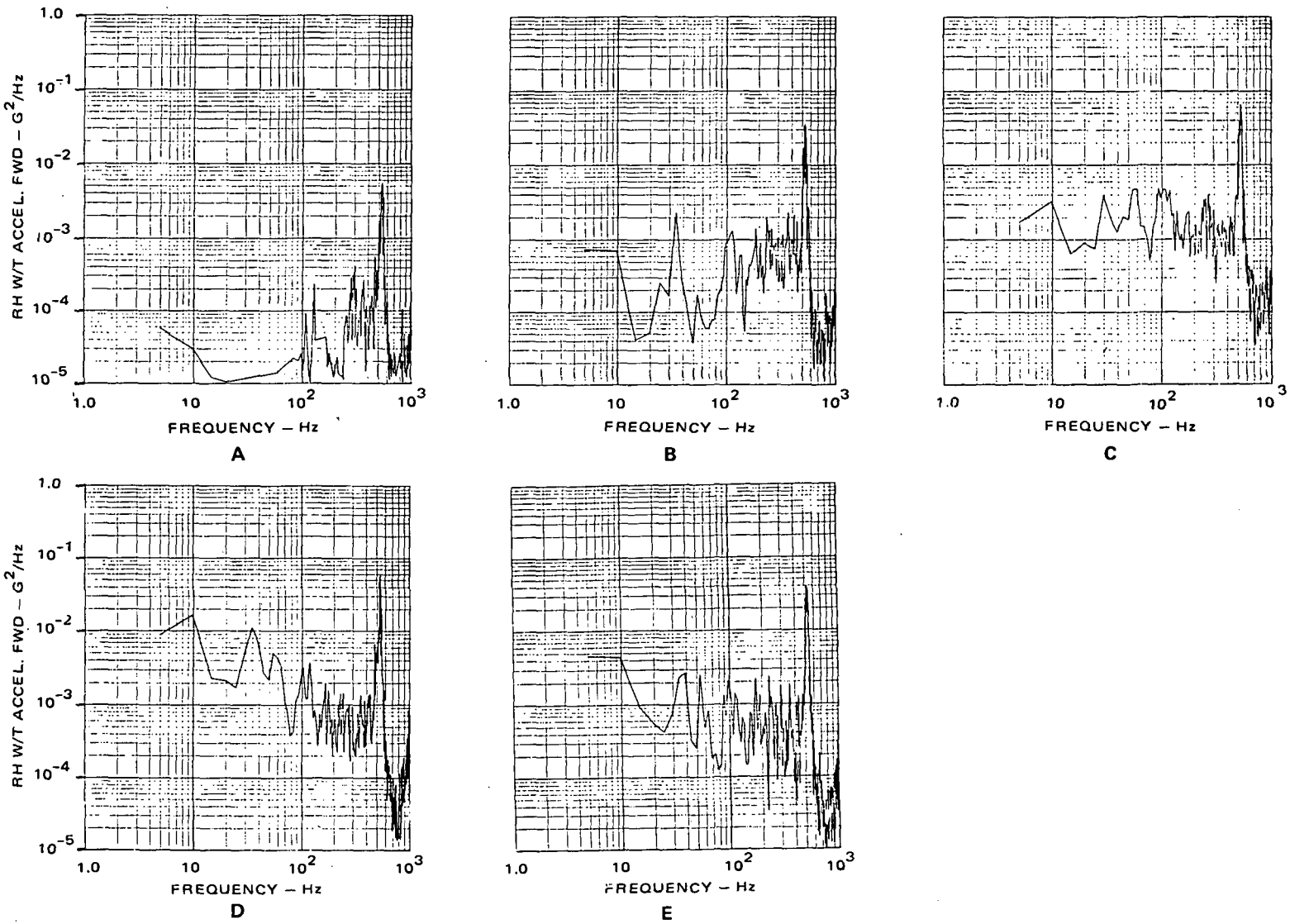

Figure 58. PSD's of Righthand Wing Tip Acceleration (Forward) Based on Various Time Segments of Real Time Data, $M_o = 0.75$, h = 7,772 m, $\delta_n/\delta_f = 0°/0°$

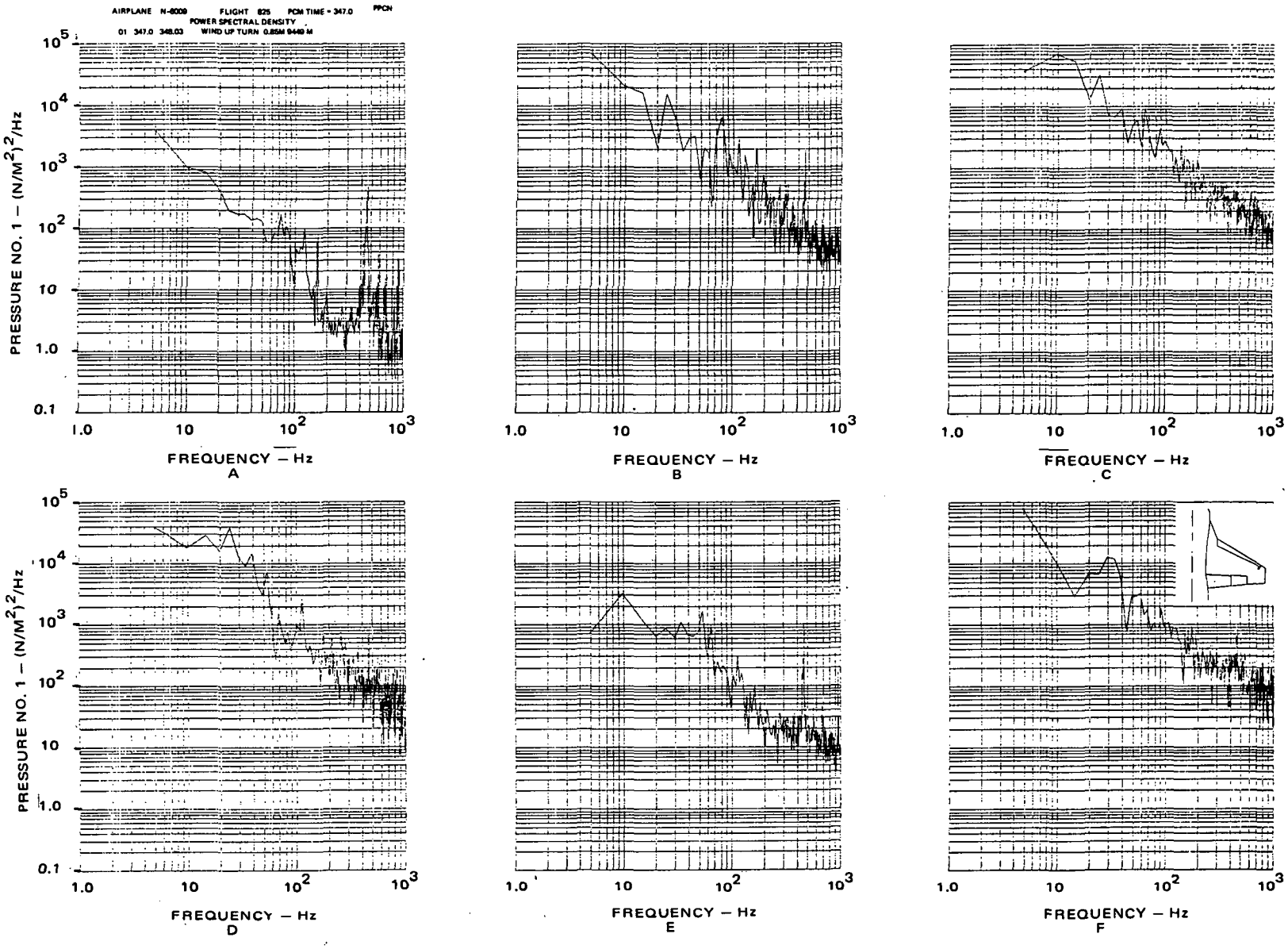

Figure 59. PSD's of Pressure No. 1 Based on Various Segments of Real Time Data, $M_o = 0.85$, $h = 9{,}449$ m, $\delta_n/\delta_f = 0°/0°$

4.5 Correlation and Coherence Study of Buffet Data

Following the approach in Subsections 4.1 and 4.2, the cross-correlation functions for two sets of digital data x_n and y_n at lag numbers $\ell = 0, 1, 2 \ldots, L$ may be defined as $R_{xy}(\ell \Delta t)$ based on Equation (4-8). Furthermore, the cross-correlation coefficient ρ_{xy} and the raw estimate of the cross spectral density $\tilde{\Phi}_{xy}$ may be defined based on Equations (4-14) and (4-10) respectively. A smoothed estimate for the cross-spectral density Φ_{xy} is obtainable using the same smoothing process of Equation (4-25). The coherence function is determined by Equation (4-26).

Two types of cross-correlation and coherence functions are presented in this subsection: the first type is the correlations between wing root structural loads and the dynamic pressures; the second is the correlations between the pressure transducer pairs. All the data are taken from Flight 871, Run 2, low-frequency digital tape. The time span covers the period from 079.5 to 081.6 second. The time increment is 0.002 second and the frequency increment is 0.488 Hz. The maximum time lag is 1.024 seconds.

Three sets of data are presented covering the correlations between the wing root structural loads and the computed pressure loads. The computed pressure loads are:

Total Bending Moment

$$\Sigma PY = \int p\,y\,dA$$

y = bending moment arm from W.S. 32

Total Torsional Moment

$$\Sigma PX = \int p\,x\,dA$$

x = torsional moment arm referred to elastic axis at W.S. 32

Summation of the Measured Pressures

$$\Sigma P = \int p\,dA$$

Corresponding to the computed pressure loads, correlation data were computed as indicated below.

1. The lower part of Figure 60 shows the correlation (as defined in Equation 4-8) between the bending moment at W.S. 32.0 and the total bending moment contributed by the measured buffet pressures. The maximum cross-correlation coefficient $|\rho| = 0.573$ occurs at time lag $\tau = -0.022$ second. (See Equation 4-14 for definition of ρ.)

2. Figure 61 shows the correlation between the torsional moment at W.S. 32.0 and the total torsional moment contributed by the measured buffet pressures. The maximum cross-correlation coefficient $|\rho| = 0.4$ occurs at $\tau = -0.016$ second.

3. Figure 62 shows the correlation between the shear force at W.S. 32.0 and the summation of the measured buffet pressures. The maximum cross-correlation coefficient $|\rho| = 0.666$ occurs at $\tau = -0.014$ second.

For the above three cases, the maximum correlation coefficients appeared at a small negative τ. This indicates that corresponding to the major modal responses, the buffet pressure loads always lead the structural loads by a small phase angle. In other words, the impedance of the aircraft (including structural and aerodynamic damping) is such that a small positive damping exists corresponding to the major response modes.

The coherence function plots show large-amplitude changes from frequency to frequency. A contributing factor to the large amplitude fluctuations is the fact that the combination of a relatively small equivalent resolution frequency and the limited sample time span caused a large normalized mean square error of the spectral data. It is worthy of note that the coherence function between the pressure pairs showed less fluctuation when the same procedure was applied to the same batch of low frequency data. This point will be discussed in the following paragraphs.

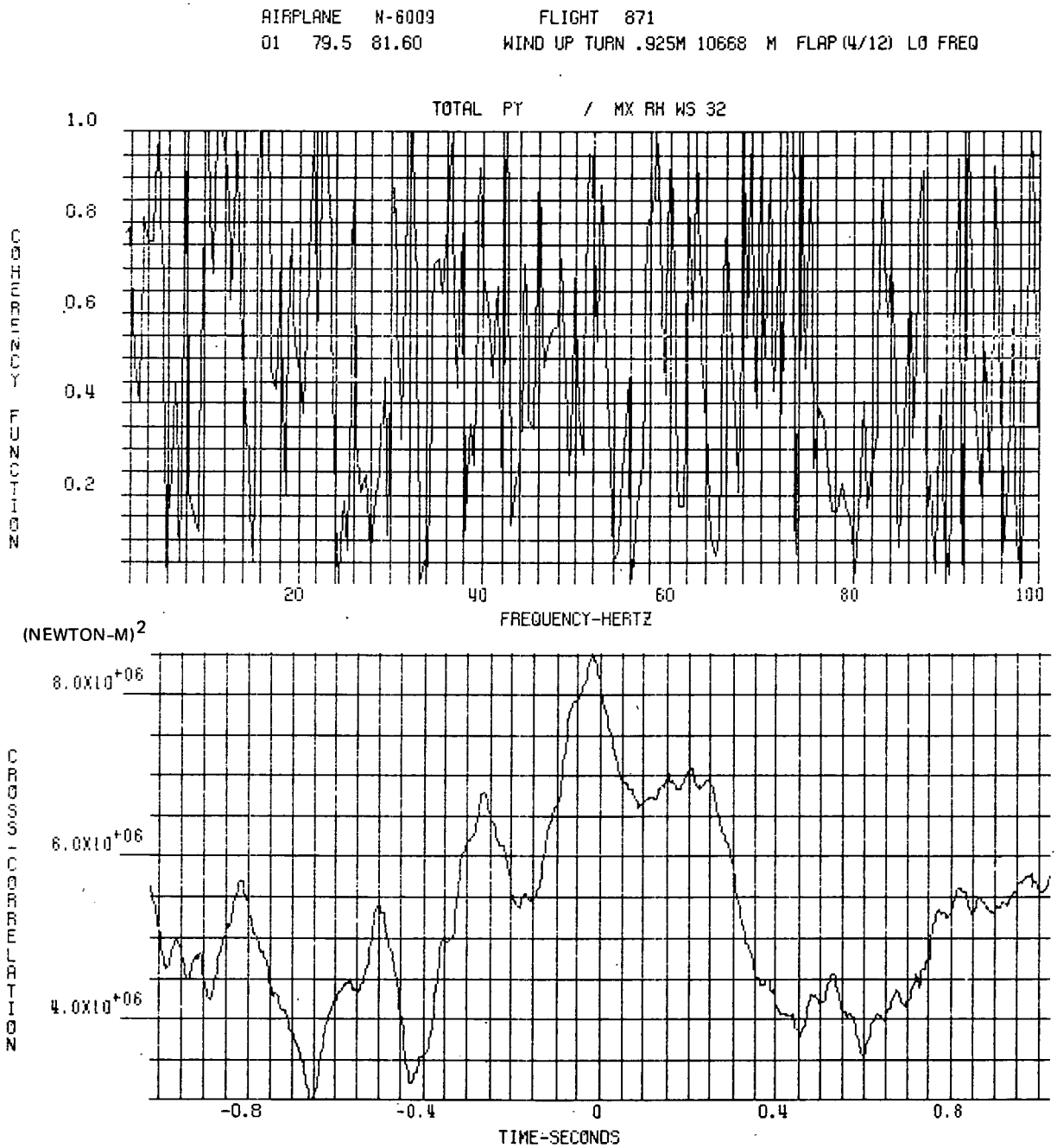

Figure 60. Correlation Between the Wing Root Bending Moment and the Corresponding Moment of Pressures, $M_o = 0.925$, h = 10,668 m, $\delta_n = 4°$, $\delta_f = 12°$.

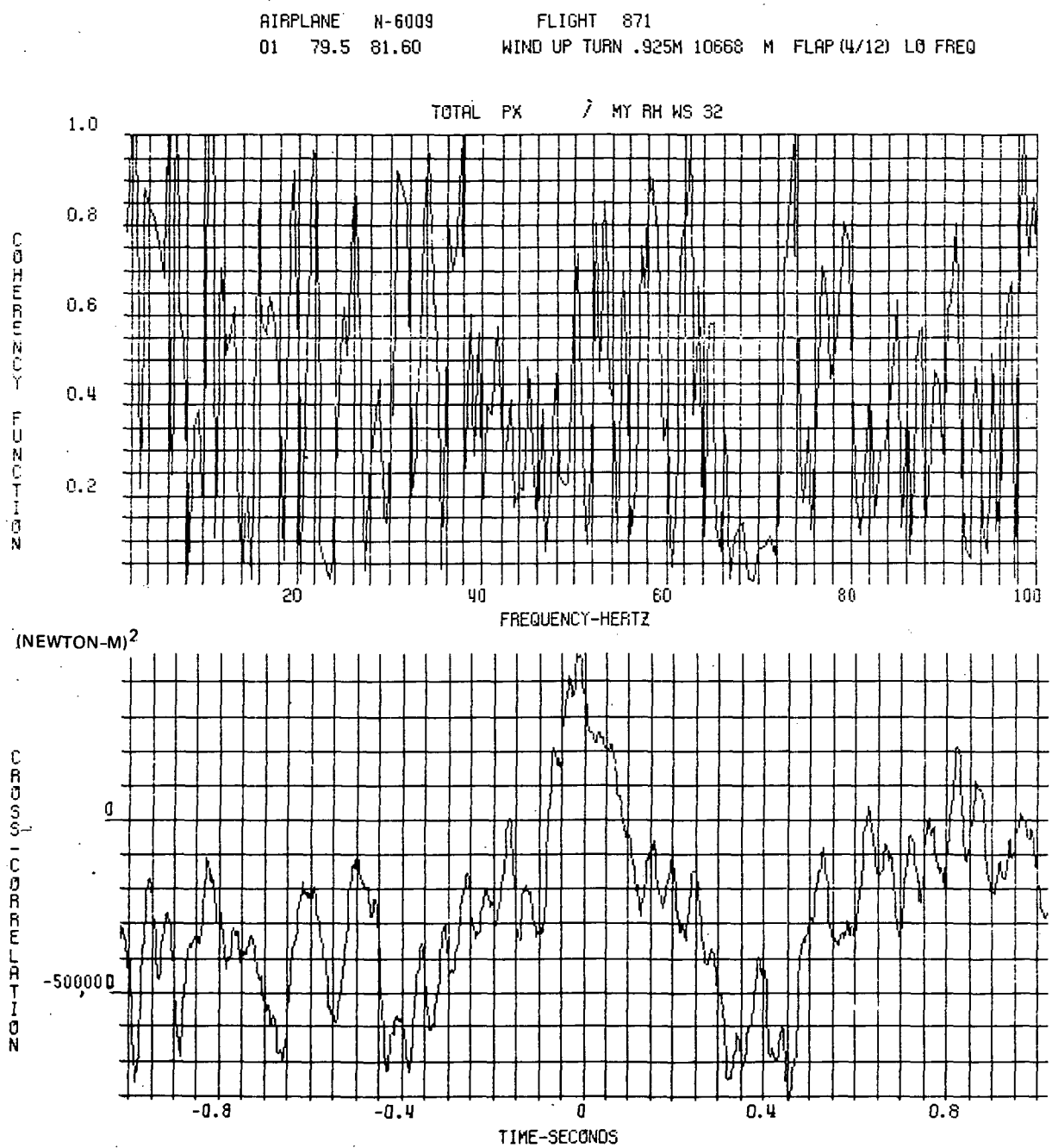

Figure 61. Correlation Between the Wing Root Torsion and The Corresponding Moment of Pressures, $M_o = 0.925$, h = 10,668 m, $\delta_n = 4°$, $\delta_f = 12°$.

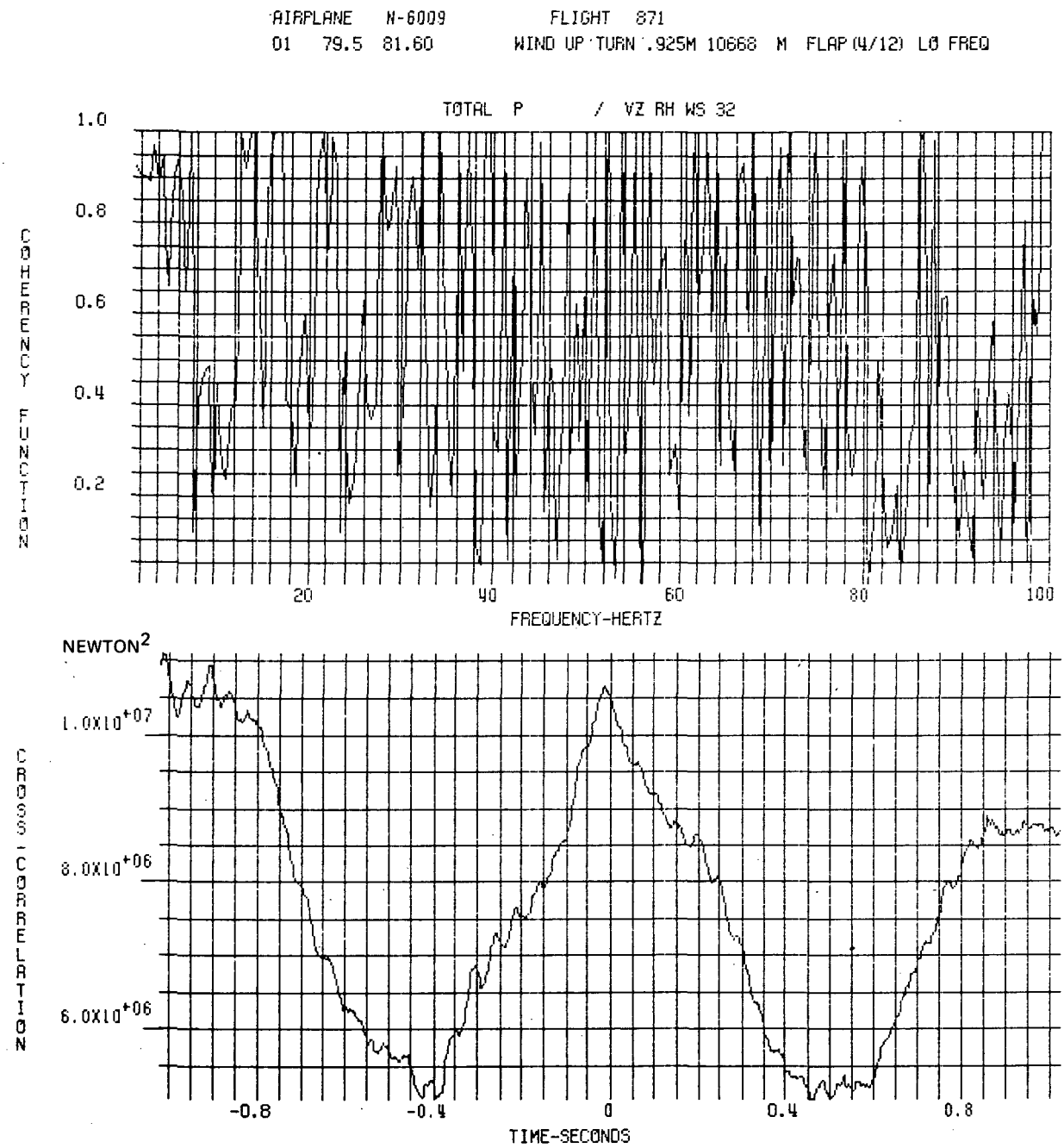

Figure 62. Correlation Between the Wing Root Shear Force and the Summation of Pressures, $M_o = 0.925$, $h = 10,668$ m, $\delta_n = 4°$, $\delta_f = 12°$.

In the following, the correlation of the pressure data for two transducer locations is studied. Specifically, the cross correlation, the coherence function, as well as the phase angle of the cross spectra of the pressure data yield information about the pressure spatial correlation. For instance, if a condition of pure convection independent of frequency exists, then the phase angle of the cross spectral density function is proportional to frequency.

In general, if two stations are fairly close to one another and the disturbances at the two locations are caused by the same source, it is expected that their auto-correlation functions and auto power spectra are of the same general shape at one station as the other. A plausible model of the correlation function for any two Stations 1, 2 was proposed in Reference 30 (Equation 5-8, p. 43) as:

$$R_{12}(r,\tau) = \sigma_1 \sigma_2 e^{-\delta|r|} \rho_o(\tau-\tau') \tag{4-27}$$

where σ_1, σ_2 denote the rms values (with zero mean), r is the distance between the two points, δ is the spatial decay coefficient, τ is time,and τ' relates to the time of convection of the pressure from one point to the other. ρ_o denotes the normalized auto-correlation function. Based on the above assumption of identical or near-identical auto-correlation functions (different only in amplitude), the phase angle θ of the cross spectral density Φ_{12} and the cross-correlation coefficient as defined by Equation (4-14) may be expressed in the following:

$$\theta = -2\pi f \tau' \tag{4-28}$$

$$\rho_{12}(r,\tau') = e^{-\delta|r|} \simeq \gamma_{12}(r, f) \tag{4-29}$$

In Equation (4-29), γ_{12} is the square root of the coherence function defined by Equation (4-13). Apparently, γ_{12} is assumed to be independent of frequency f. Based on (4-29), the spatial decay constant δ may be determined.

Equation (4-28) shows that for a constant τ' corresponding to a specific convection speed of the disturbance, the phase angle is a linear function of frequency passing through the origin of the θ - f plot. For this case, the convection speed $V_c = r/\tau'$. In the following, correlation data based on pressure transducer pairs (1, 2), (2, 3), (2, 4), and (1, 6) as presented in Figure 63 to 66 are discussed. In these four figures, each

has four plots. The two plots on the left side give the modulus and phase angle of cross PSD $\emptyset_{xy}(f)$ as shown in Equation (4-10). The two plots on the right side give the coherence function $\gamma^2_{xy}(f)$ and the correlation function $R_{xy}(\tau)$ respectively. The cross PSD modulus has been normalized and the normalization factor is given on top of the plot.

Referring to Figure 63, the distance between transducer pair (1, 2) is approximately 22.86 cm (9 in.) along the chordwise direction. The shape of the cross-correlation function is similar to the shape of the auto-correlation function of either transducer. The phase angle θ of cross spectrum density function is approximately proportional to the frequency with $\tau' = 0.002$ second. The τ' data is consistent with the time delay based on the major peak in the cross-correlation plot. The above observations indicate that for transducer pair (1, 2), a convection velocity exists and the V_c value is approximately 114.3 m/sec or 375 fps, with $\rho_{max} = 0.814$. A similar conclusion may be drawn for transducer pairs (2, 3) and (2, 4) located at the same semi-span station. Figure 64 shows $\tau' = 0.004$ second for transducer pair (2, 3) with $\rho_{max} = 0.710$. The corresponding convection velocity is 57.2 m/sec (188 fps). Figure 65 shows $\tau' = 0.01$ second, with r = 57.15 cm (22.5 in.) for transducer pair (2, 4). The corresponding convection velocity is 57.2 m/sec (188 fps), which is identical to that of transducer pair (2, 3). The ρ_{max} value is 0.567 for transducer pair (2, 4).

Between two pressure locations, the mean of the square root of the coherence function $\gamma_{xy}(r)$ may be determined by an averaging process covering a certain frequency range. In case there is a dominating convection effect, then according to Equation (4-29), the mean of γ_{xy} (r, f) may be determined by the normalized cross-covariance function as defined in Equation (4-14). Based on this method, and using pressure data obtained in Run 2 of Flight 871, the contours of equal γ_{xy} are plotted in Figure 67 for Station Number 2. The contours are plotted only in the area where the convection effect is observed so that the approximate formulation of Equation (4-29) is applicable. The curves are left broken at locations where the convection effect is not observed. Figure 67 indicates that a distinct convection effect existed in the area near the wingtip. This effect is most prominent along the chordwise direction.

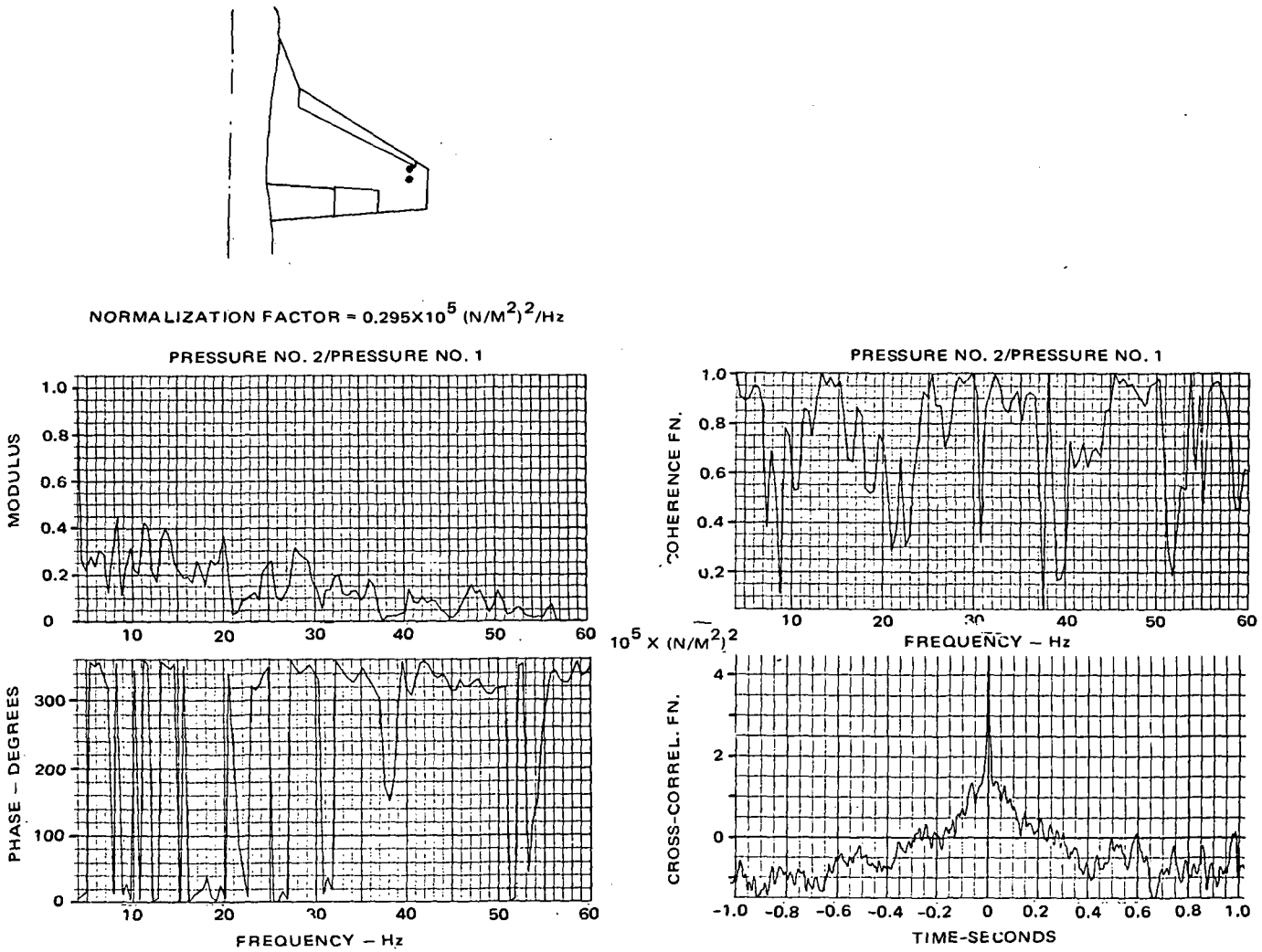

Figure 63. Correlation Between the Pressure Transducer Pair (1, 2), $M_o = 0.925$, h = 10,668 m, $\delta_n = 4°$, $\delta_f = 12°$

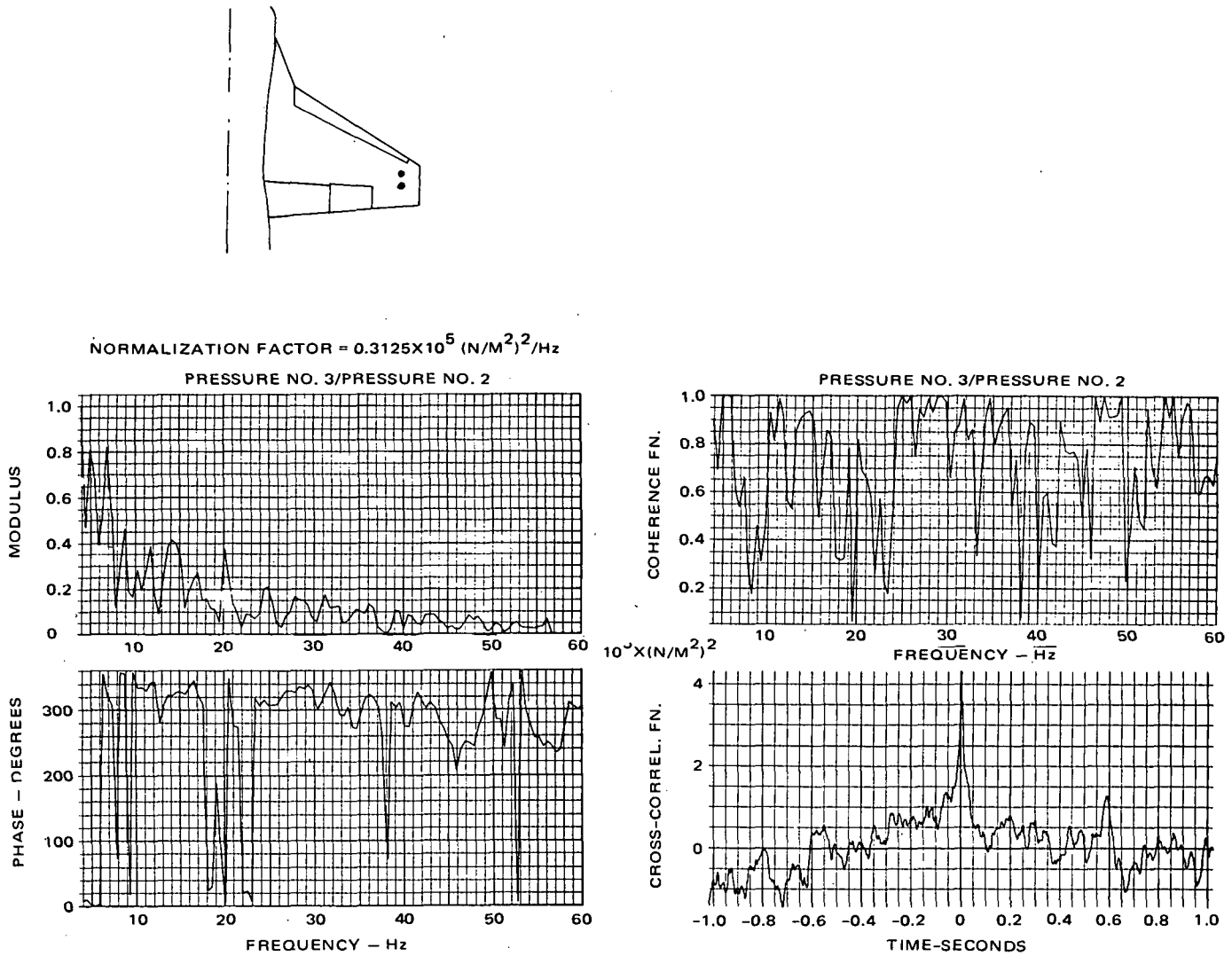

Figure 64. Correlation Between the Pressure Transducer Pair (2-3), $M_o = 0.925$, h = 10,668 m, $\delta_n = 4°$, $\delta_f = 12°$

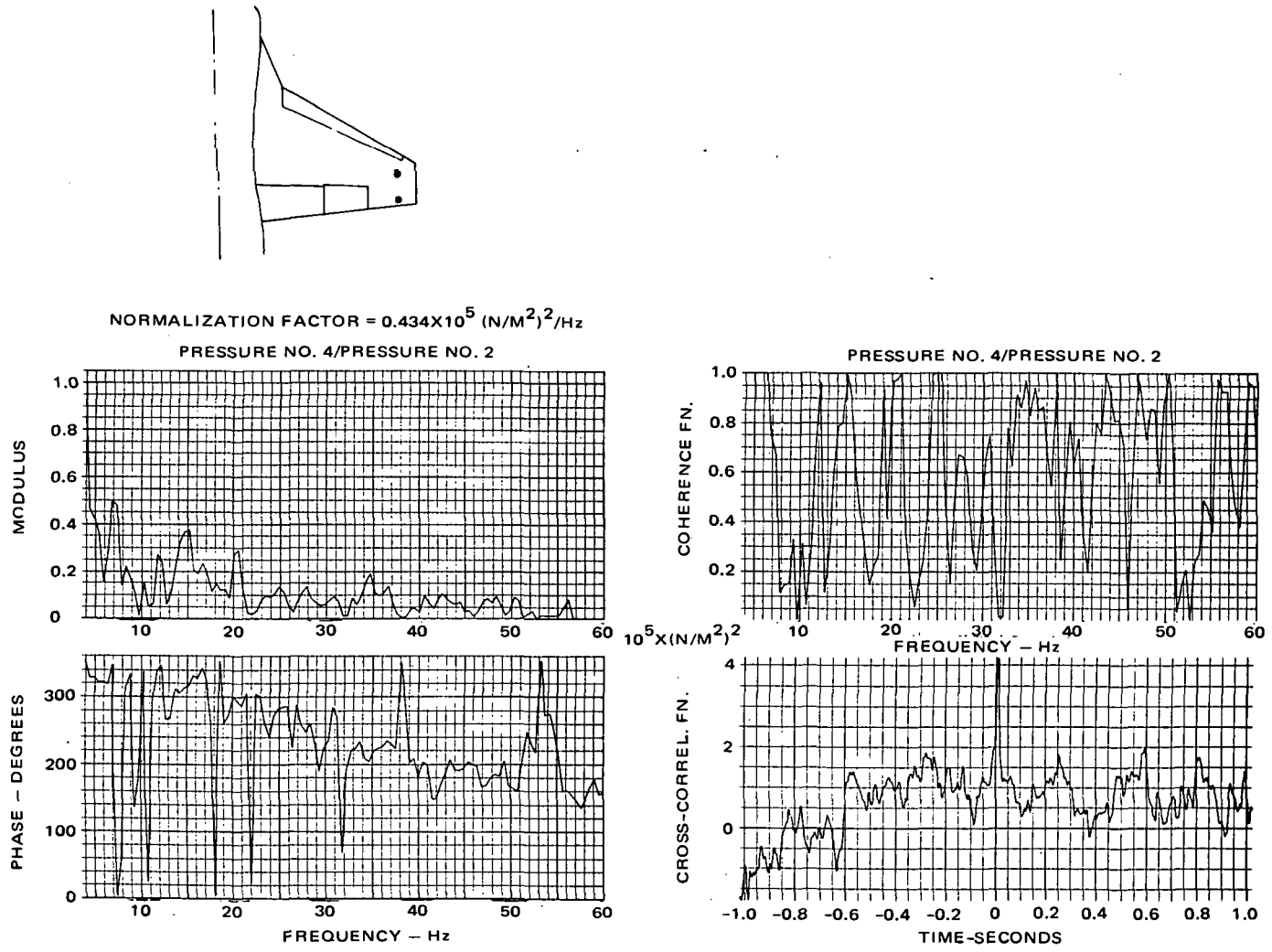

Figure 65. Correlation Between the Pressure Transducer Pair (2-4), $M_o = 0.925$, h = 10,668 m, $\delta_n = 4°$, $\delta_f = 12°$

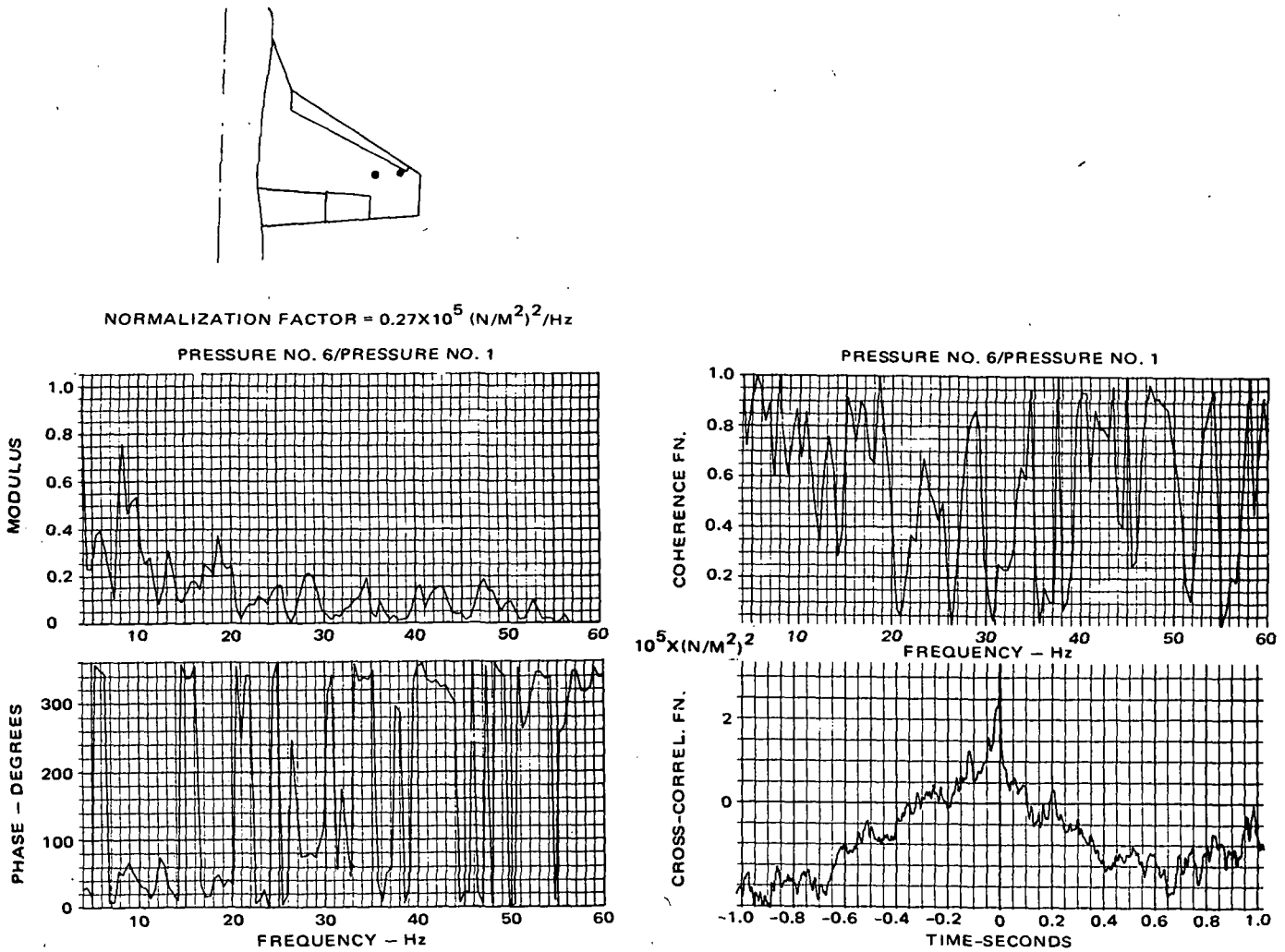

Figure 66. Correlation Between the Pressure Transducer Pair (1-6), $M_o = 0.925$, h = 10,668 m, $\delta_n = 4°$, $\delta_f = 12°$

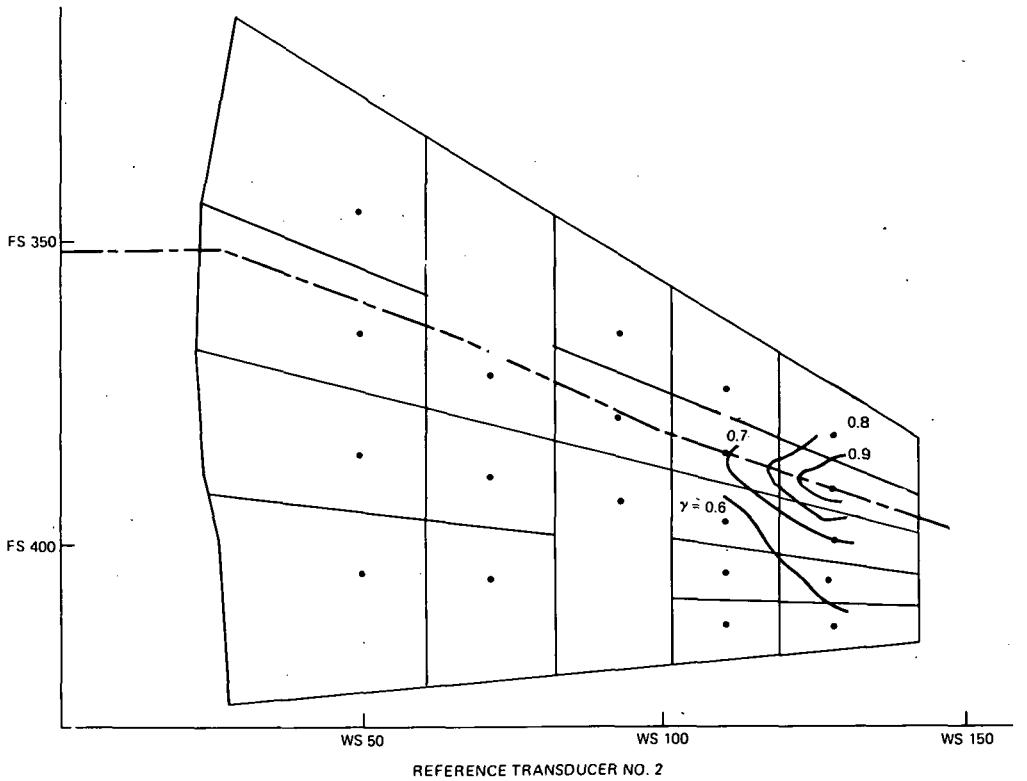

Figure 67. Contour of Mean Square Root Values of Coherence Function γ_{xy} for Buffet Pressures Obtained in Run 2, Flight 871, $M_o = 0.925$, h = 10,668 m, $\delta_n = 4°$, $\delta_f = 12°$

4.6 Statistical Distribution

The definitions of the probability density function p(x) and cumulative probability distribution function P(x) are given by Equations (4-16) and (4-17) respectively. An estimate of p(x) is obtained in digital form by dividing the range for x into an appropriate number of class intervals and by tabulating the number of observations and the percentage of data in each interval. An estimate P(x) is obtained as the sum of the number of observations and the percentage of data from the class intervals.

Typical statistical nondimensionalized probability density and distribution functions of pressure transducers 1, 6, and 23 are presented in Figures 68 to 70. The ordinate of a nondimensionalized probability density function plot represents the ratio of the event counts falling in a pressure level internal to the total number of event counts. The data are based on Flight 825, Run 7 low-frequency digital tape. The time span covers the period from 364.5 to 366.0 second when separation was fully developed over the upper wing surface. The time increment is 0.001 second. In general, the pressure data do not follow a normal distribution as would be the case for a purely random natural phenomenon. The data do not have a zero mean within the chosen time interval even though the complete batches of data representing the maneuver have zero mean.

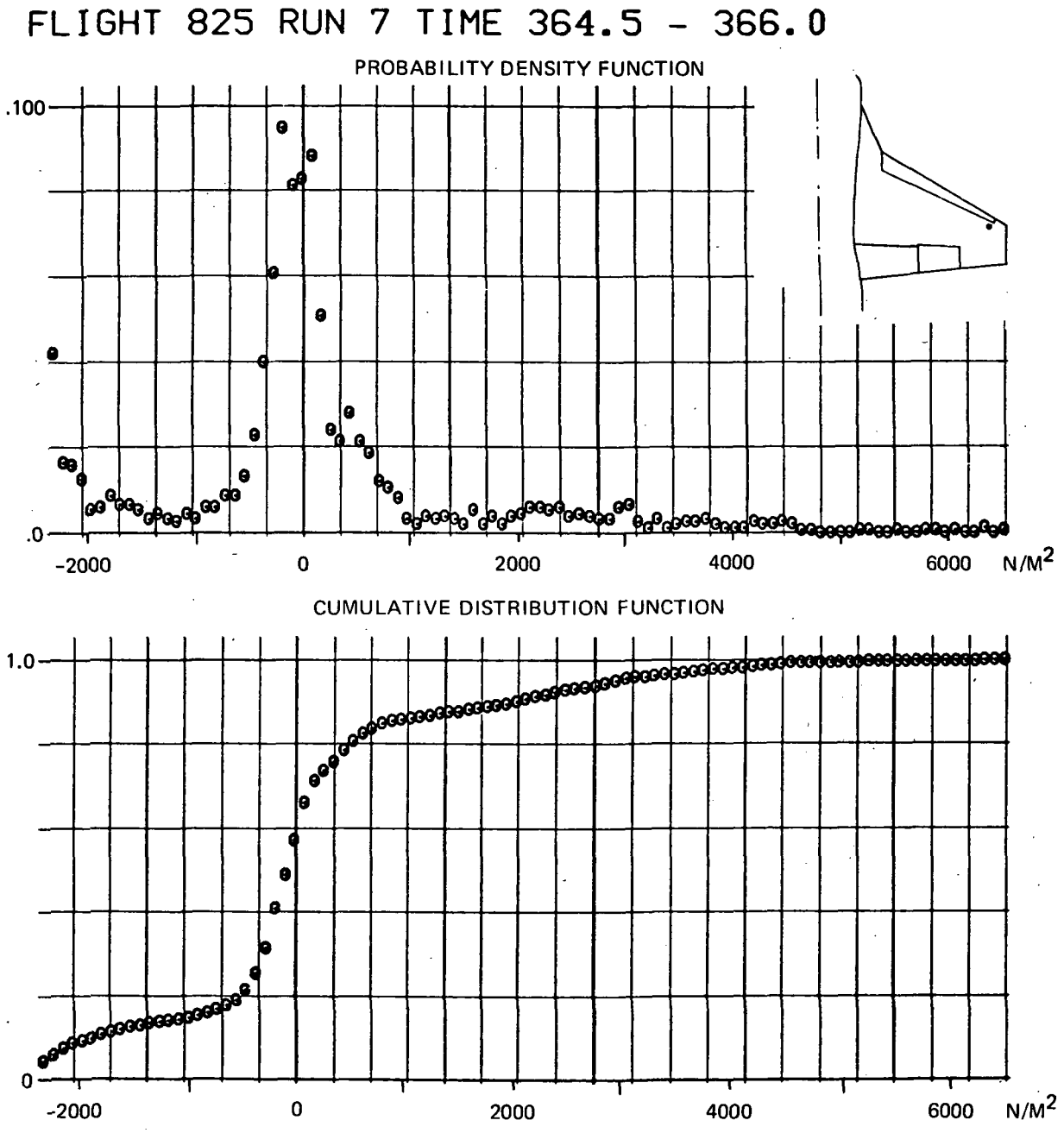

Figure 68. Typical Probability Density and Distribution Functions of Pressure No. 1, $M_o = 0.75$, h = 7,772 m, $\delta_n = 0°$, $\delta_f = 0°$

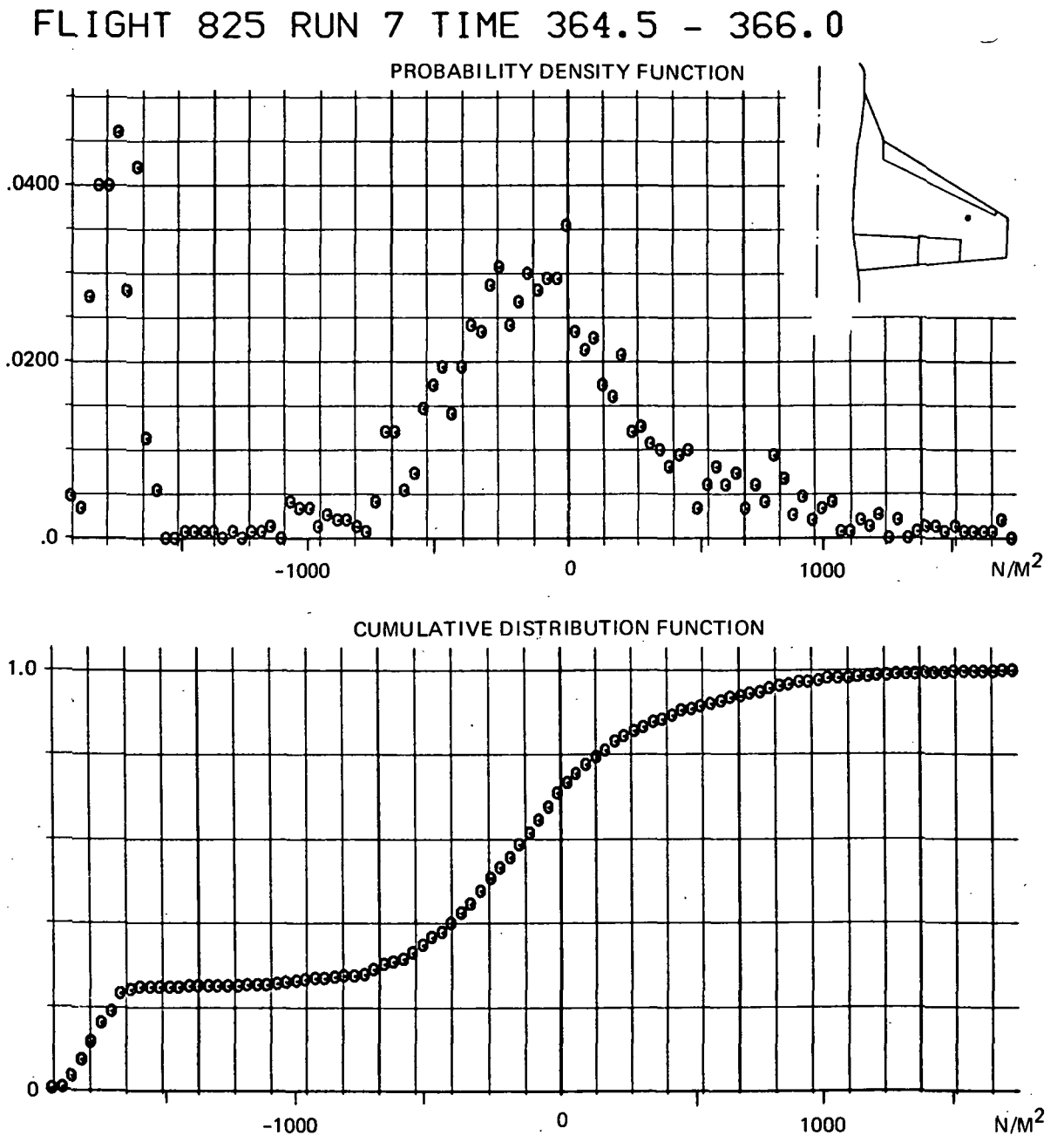

Figure 69. Typical Probability Density and Distribution Functions of Pressure No. 6, $M_o = 0.75$, h = 7,772 m, $\delta_n = 0°$, $\delta_f = 0°$

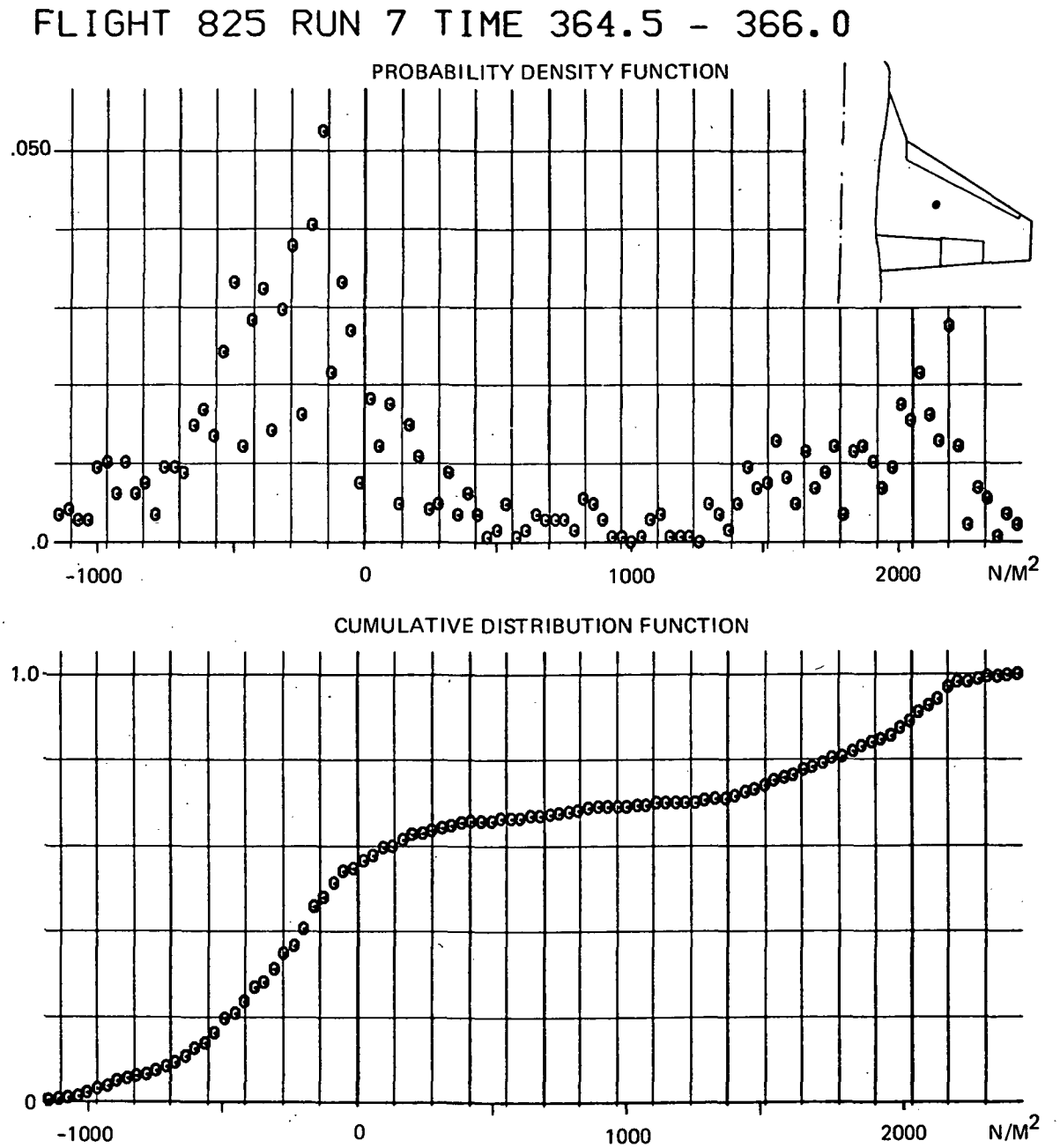

Figure 70. Typical Probability Density and Distribution Functions of Pressure No. 23, $M_o = 0.75$, h = 7,772 m, $\delta_n = 0°$, $\delta_f = 0°$

SECTION 5

ANALYTICAL PROGRAM

The dynamic buffet pressure applied on the aircraft is quite complicated. Its origin may be traced to the turbulence in the separated and, possibly, unseparated flow regions, as well as to the fluctuating pressure characteristic of the unstable shock and the movement of the separation boundaries. In case the buffet pressure may be assumed to be stationary or near-stationary within a certain time period, and the auto- and cross-power spectra of the pressure exist,* then an analytical procedure may be applied to compute the aircraft response due to buffet. The analytical response data may then be compared with the flight test response data to examine the validity of the analytical procedure.

The analytical procedure is applied in two different approaches. In the first approach, the data covering a substantial time span of the transonic maneuver are used which are assumed to be stationary. In order to correlate the average response behavior in the late phase of the maneuver including wing rock, the data covering the initial phase, i.e., prior to buffet onset are excluded. This averaging approach is considered to be more suitable to low Mach number case ($M_o = 0.75$) where the large amplitude local shock oscillations do not exist. In the second approach, the time span covering the transonic maneuver is divided into a number of consecutive time segments. Within each time segment, the fluctuating pressure data are assumed to be stationary. The aircraft response is then computed based on the same linear response transfer function and the segmentwise stationary buffet loads.

The second approach mentioned above takes into consideration the ever changing buffet loads at various phases of the maneuver. It has the disadvantage that the time

*An alternate condition is that the Fourier transforms of the pressure data at all collocation stations exist and the spatial correlations between any two stations are specified. Two extreme cases corresponding to the latter condition are described in this section and in Appendix I of the Report.

span of each segment becomes so small that the normalized standard error ϵ of the power spectra is large based on a given equivalent resolution bandwidth B_e (see Equation 4-22). For the aircraft under consideration, the more significant natural modes are located in a narrow frequency range. In order to resolve the closely packed modes, a small frequency increment Δf is necessary. Since $B_e = 2\Delta f$ in the applied processing technique (see p. 290, Reference 47), some compromise has to be reached in order to obtain a reasonable resolution and an acceptable level of spectral data error. In the following subsection, alternate methods of organizing the buffet pressure data and the results of varying bandwidth are described. The subsection is followed by a general description of the aircraft response transfer function, subsequent to which the response data obtained by the two analytical approaches are presented.

5.1 Force Input Based on Measured Buffet Pressure

In order to compute the aircraft responses, force input based on the measured buffet pressure data is organized in matrix form using either the Fourier transform functions or the auto- and cross-power spectra. To assemble the force input data, the wing planform is divided into a number of subareas, with the pressure transducers located inside, as shown in Figure 71. The power spectral densities of pressure are assumed to be uniform over each subarea. Perfect spatial correlation is assumed between any two points lying within a subarea. In the following, the term "pressure" refers to the pressure over a subarea.

Two methods, the Fourier Transform Method and the Correlation Method, are available to generate the pressure input data for the frequency response calculation program. Theoretically, the Correlation Method will yield the exact response solution to the problem since it accounts for the actual spatial correlation of pressures. But the pressure input involves a 20 x 20 (total number of transducers on the top surface) Hermitian matrix whose elements are the auto- or cross-power spectral densities of the corresponding pressure transducer pairs, for each given forcing frequency. As a result, tremendous amounts of data have to be generated and sorted. The Fourier Transform Method generates only 20 Fourier transforms of pressures for each forcing frequency. The auto power spectrum is formed by the complex conjugate product of the Fourier transform function. Based on the Fourier

transform functions of the subarea pressures, the corresponding power spectral matrix for the pressure input may be generated for two extreme cases. These are:

1. Two subareas are perfectly correlated. For this case, the elements of the spectral matrix representing the pressure input are formed by the complex conjugate product of the Fourier transform functions of the two sets of the pressure data.

2. Two subareas are uncorrelated spatially. For this case, the spectral matrix is a diagonal matrix whose diagonal elements are the auto power spectra of the subarea pressures.

In reality, the spectral matrix of the buffet pressures should be somewhere between the two extreme cases. Because of the large amount of computation needed to deal with the spatial correlation of any two subareas individually (see Section 4), the analytical computation is limited to the extreme cases with which the experimental results are compared.

In order to determine the normalized standard error and its effect on spectral data, PSD's are generated in two ways for Pressure Transducers 1, 4, 6, and 18 data corresponding to Run 7, Flight 825 ($M_o = 0.75$, $\delta_n/\delta_f = 0°/0°$).

Firstly the PSD data are generated using a low frequency digital tape covering a time span T of 4.096 seconds (362.00 - 366.096). The low frequency tape has a frame rate of 1000 per second, i.e., the time between samples is .001 second. A new set of data is then generated from the data samples using a 0.002 time increment. (The new time increment is an integer times the time between samples in order to obtain a desired frequency resolution.) The effective resolution frequency B_e used in the process is 0.9766 Hz. The normalized standard error is then

$$\epsilon = (B_e T)^{-1/2} = 0.500$$

which is very high. The PSD's for the same data recorded on a higher frequency digital tape are also generated. The high frequency tape has a frame rate of 5000 per second. The cut-off frequency of this tape is 2500 Hz. With T = 4.915 seconds, $B_e = 9.766$ Hz, the normalized standard error is:

$$\epsilon = (B_e T)^{-1/2} = 0.144$$

The PSD data for pressure stations 1, 4, 6, 18 obtained from the high and low frequency tapes are plotted one over the other in Figures 72-75. (Only the low frequency portions of the high frequency PSD are plotted.) Referring to the figures, except for lack of certain details in the high frequency PSD in the low-frequency region, the high-frequency and low-frequency PSD's for any one set of pressure data are considered consistent. This observation gives credence to the use of the low frequency (high resolution) PSD's in the response study in case a certain amount of the normalized standard error can be tolerated.

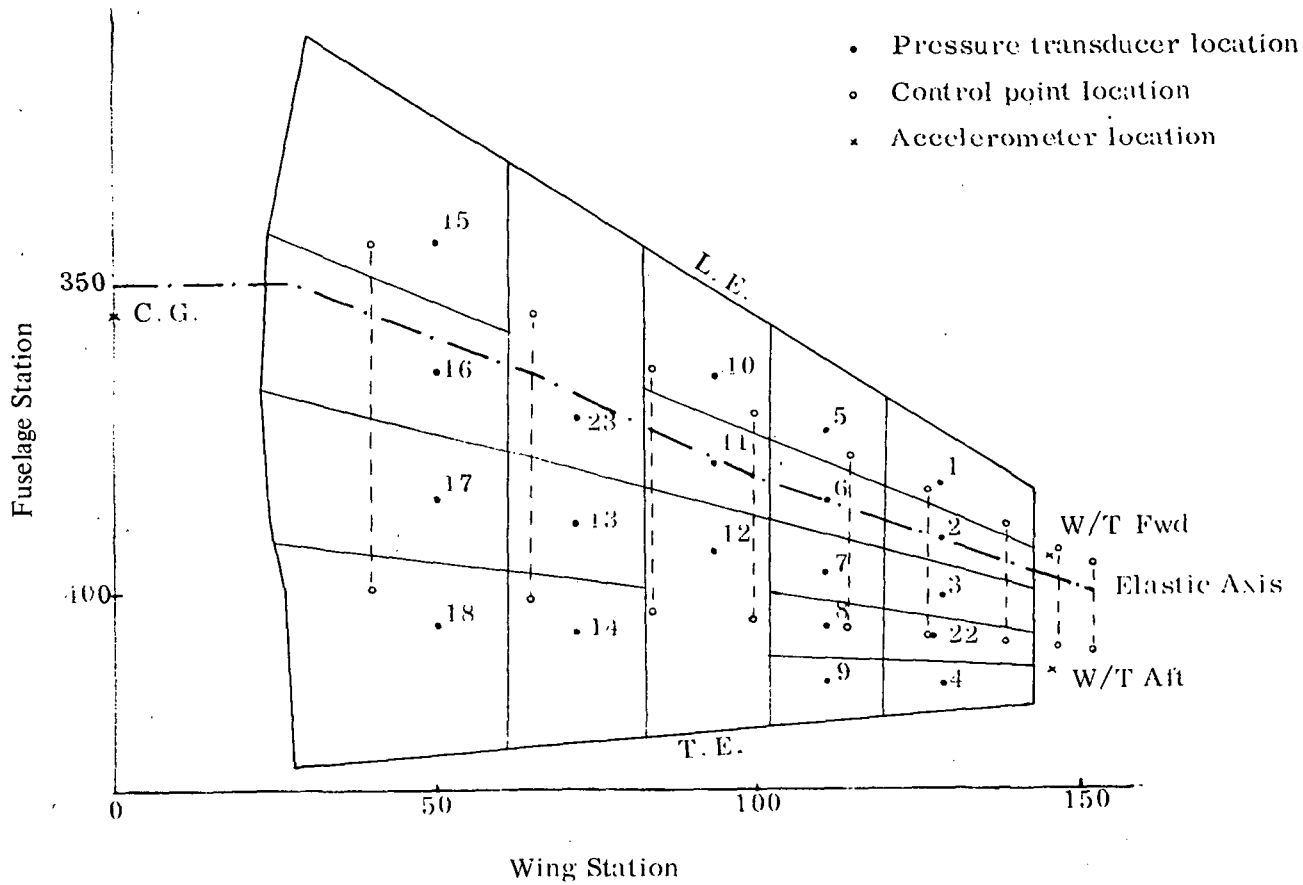

Figure 71. Locations of Pressure Transducers, Accelerometers, and Control Points

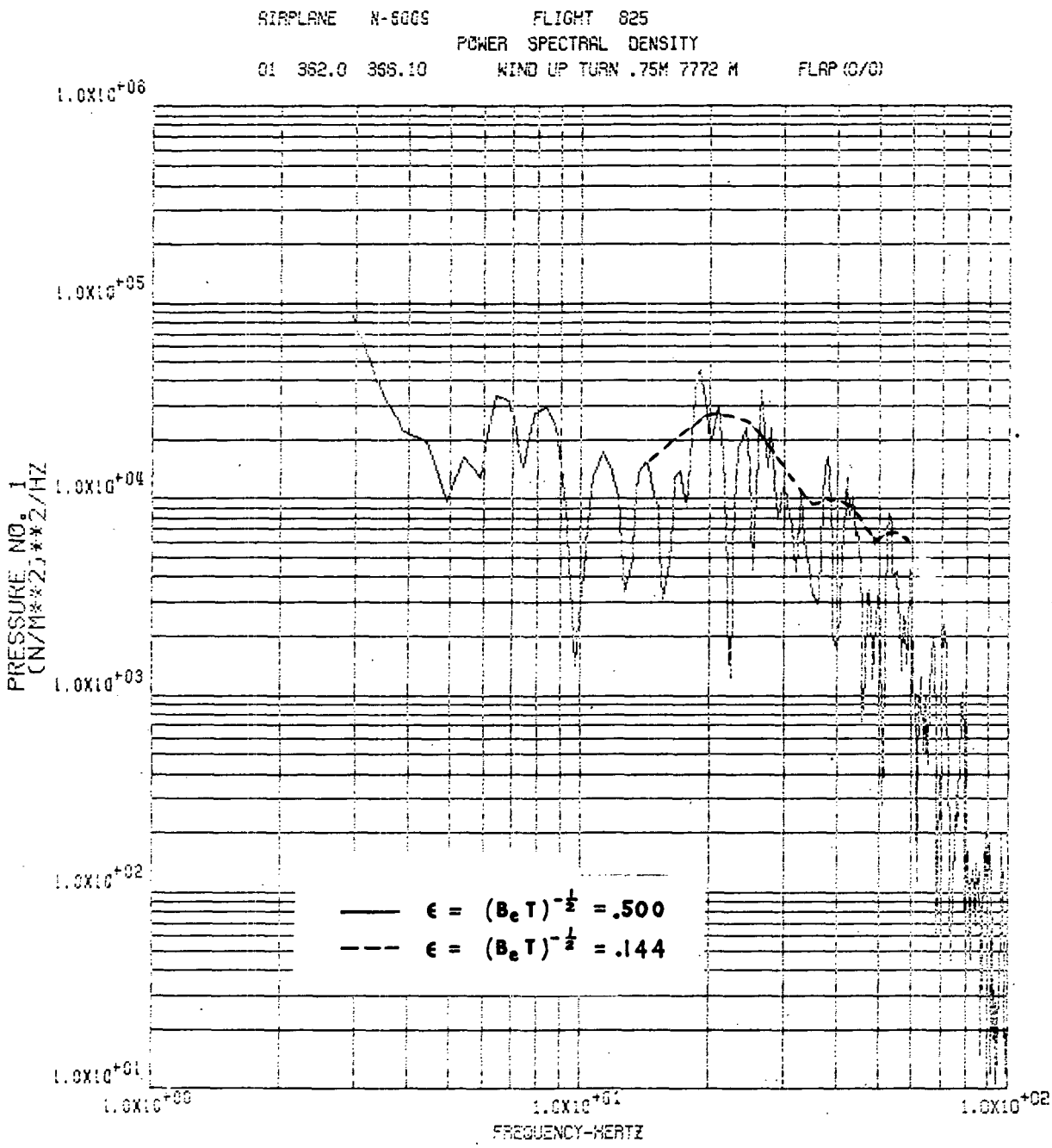

Figure 72. Low Frequency PSD Plot of Pressure No. 1, $M_o = 0.75$, $h = 7,772$m, $\delta_n = 0°$, $\delta_f = 0°$

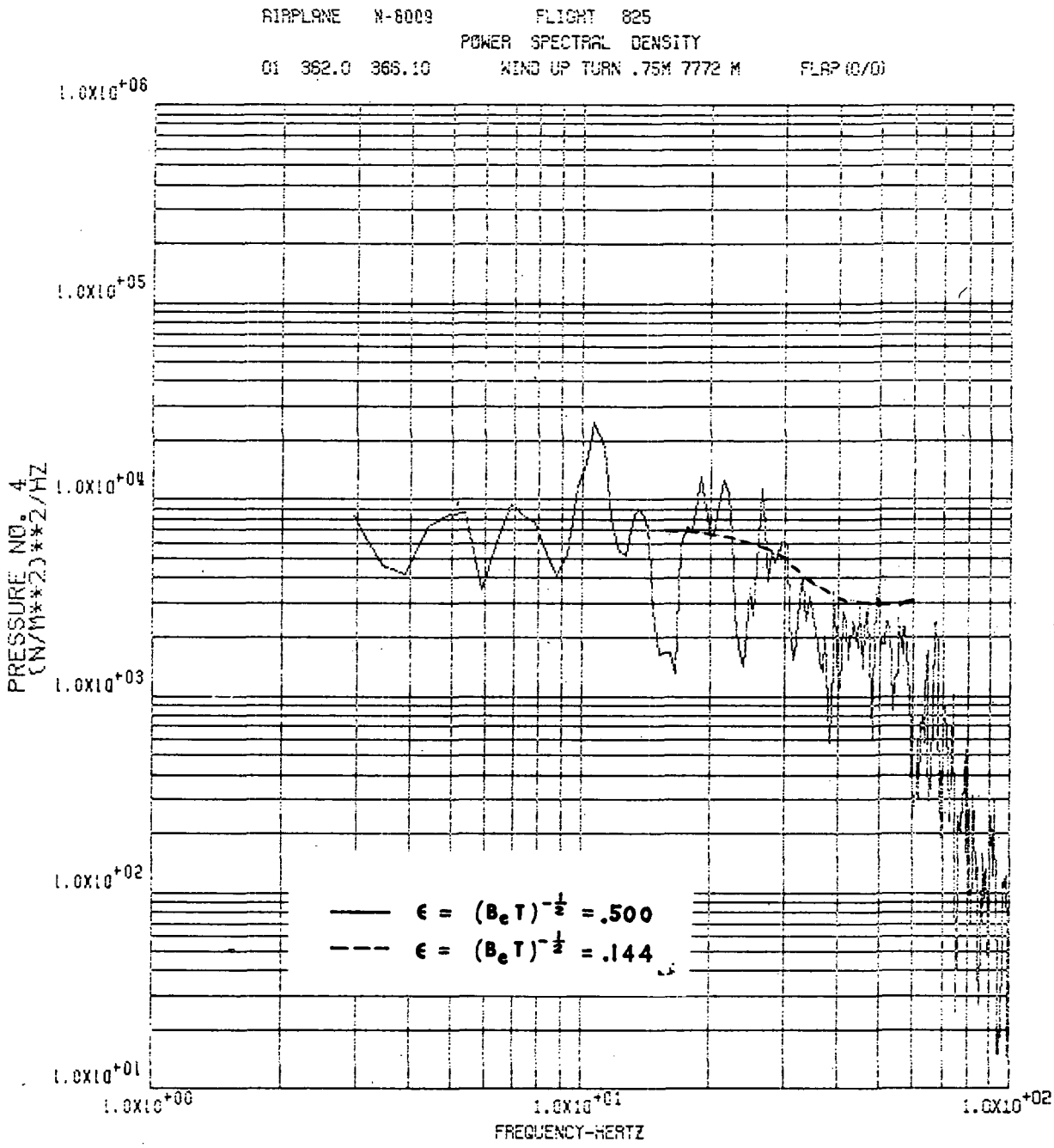

Figure 73. Low Frequency PSD Plot of Pressure No. 4, $M_o = 0.75$, h = 7,772m, $\delta_n = 0°$, $\delta_f = 0°$

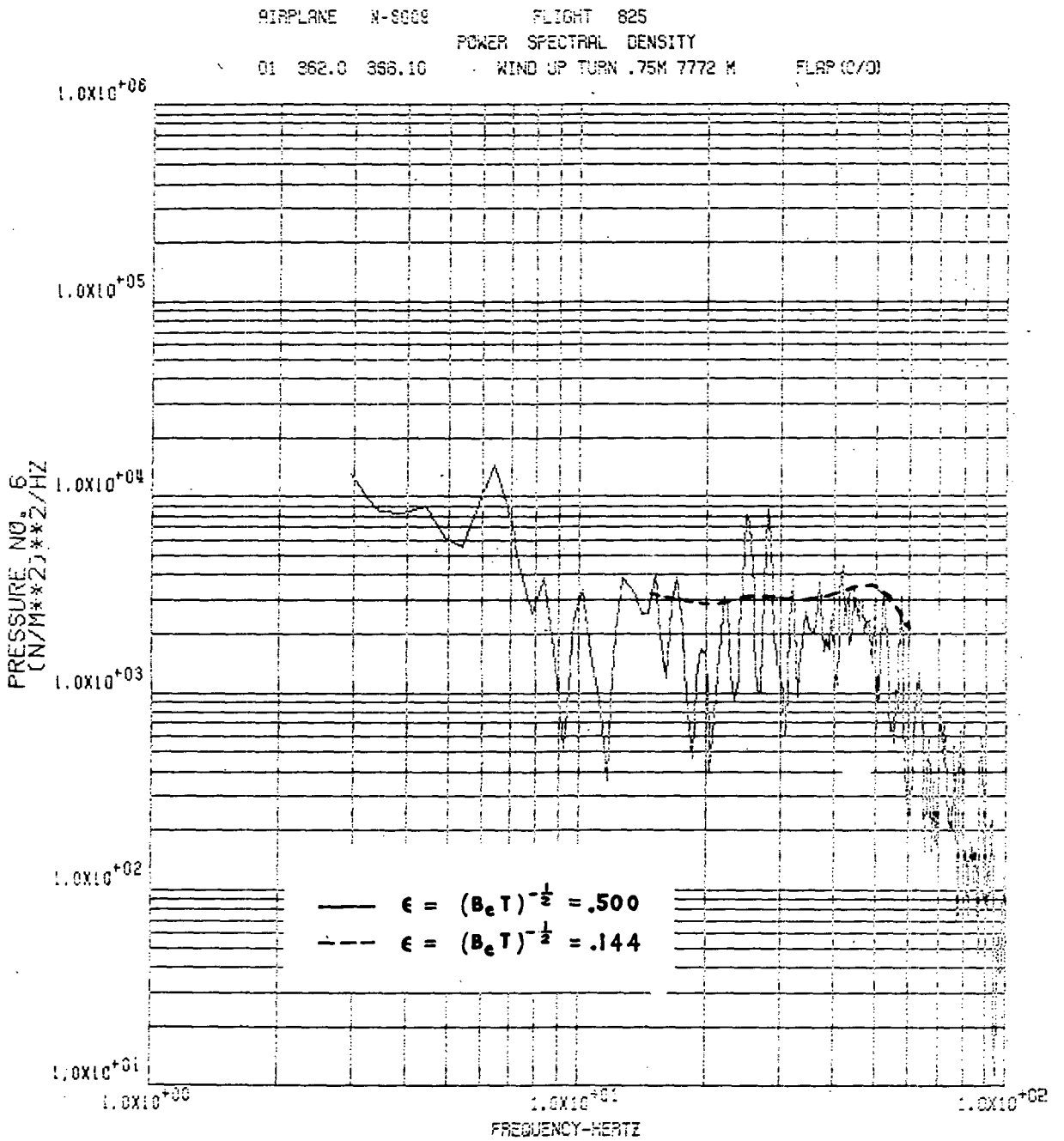

Figure 74. Low Frequency PSD Plot of Pressure No. 6, $M_o = 0.75$, $h = 7,772$m, $\delta_n = 0°$, $\delta_f = 0°$

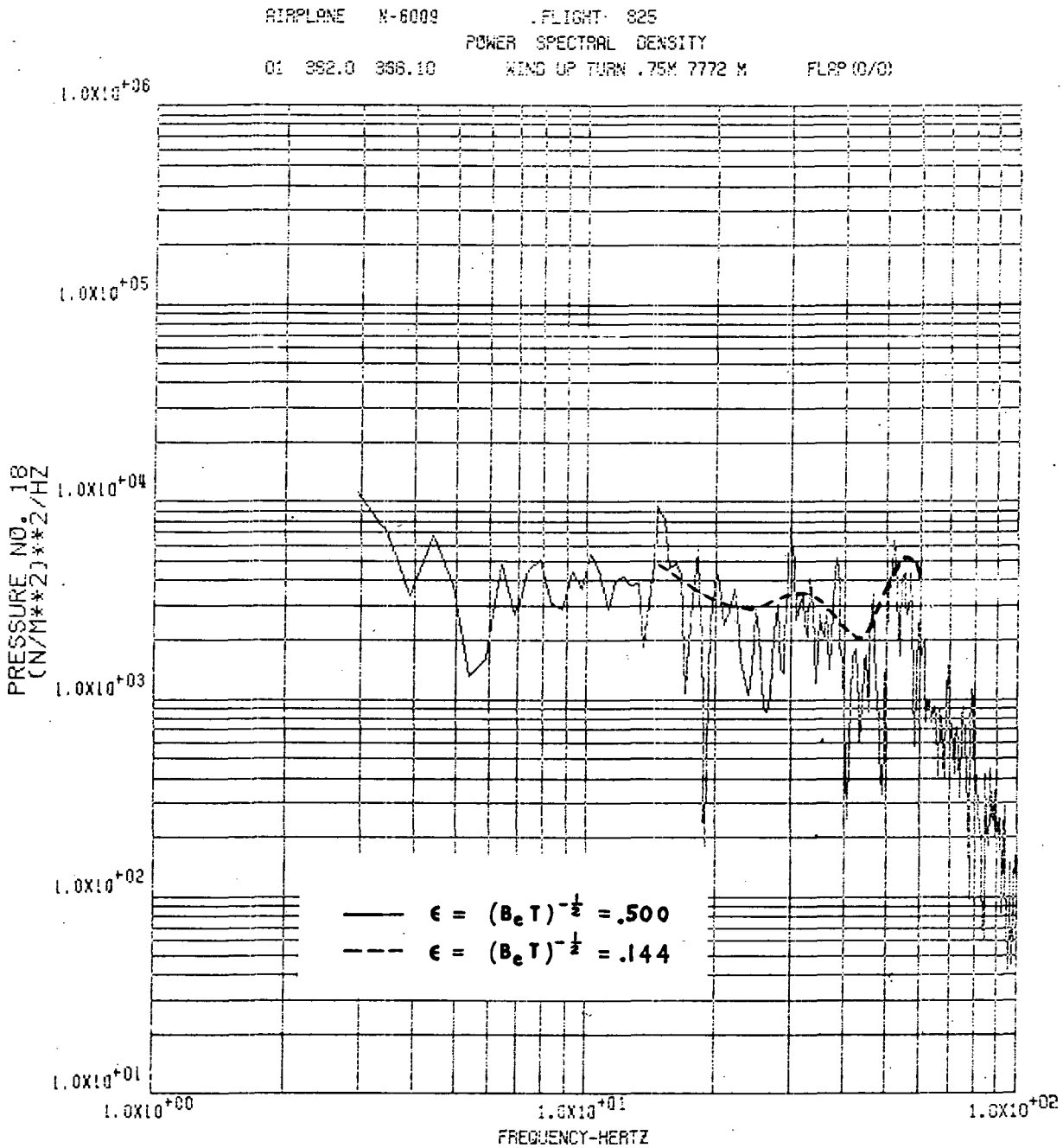

Figure 75. Low Frequency PSD Plot of Pressure No. 18, $M_o = 0.75$, h = 7,772m, $\delta_n = 0°$, $\delta_f = 0°$

5.2 Aircraft Response Function

The aircraft is assumed in a basic configuration, i.e., full fuselage tank, gear up, bare wing except that AIM-9B missiles are attached to both wingtips. In the symmetrical frequency response computation, a total of 40 control points are used which represent the normal deflections of the aircraft. The detailed control point geometry is given in Figure 76. In addition to those listed in this report, the weight, inertia, and stiffness data of the aircraft may be found in Reference 32.

A total of 12 free-free flexible modes are utilized in the analysis. The highest eigen frequency is 54.19 Hz. Two rigid body modes are considered, i.e., vertical translation and pitch rotation. The structural modal damping coefficient is assumed to be 0.05 for all the modes. The above modal data are used for response computation dealing with Run 7, Flight 825, $M_o = 0.75$ case. Simplified modal data are used for a nonstationary response computation dealing with Run 2, Flight 871, $M_o = 0.925$ case, The latter case is described in subsection 5.4 of this report.

For a number of frequencies within the band of interest the aircraft response functions are computed using a modal approach. For this purpose, the basic elastic modes of the aircraft are generated, and are used as the normal modes in the response formulation.

The equations of motion for the determination of the frequency response functions are programmed using both the cantilever and the free-free modal solutions which are synthesized (see Appendix I). The frequency response functions are determined for deflection, acceleration, control point load, shear, bending moment, torque, and stress at specified locations. In this subsection, the basic building blocks used in the aircraft response analysis are described.

Mass Stiffness Model

The aircraft is represented by a system of control points with concentrated masses. Additional intermediate masses are suspended on massless bars connecting the control points (Figure 76). The control point masses and intermediate masses are calculated such that the mass and inertia properties of the system are matched with those of the aircraft. The control point and intermediate masses are used to derive the coupled mass matrix for a dynamically equivalent system. Additional control points with no associated masses are added at locations which are required to correlate the response data with measured flight test data. The elastic axis of the wing is the

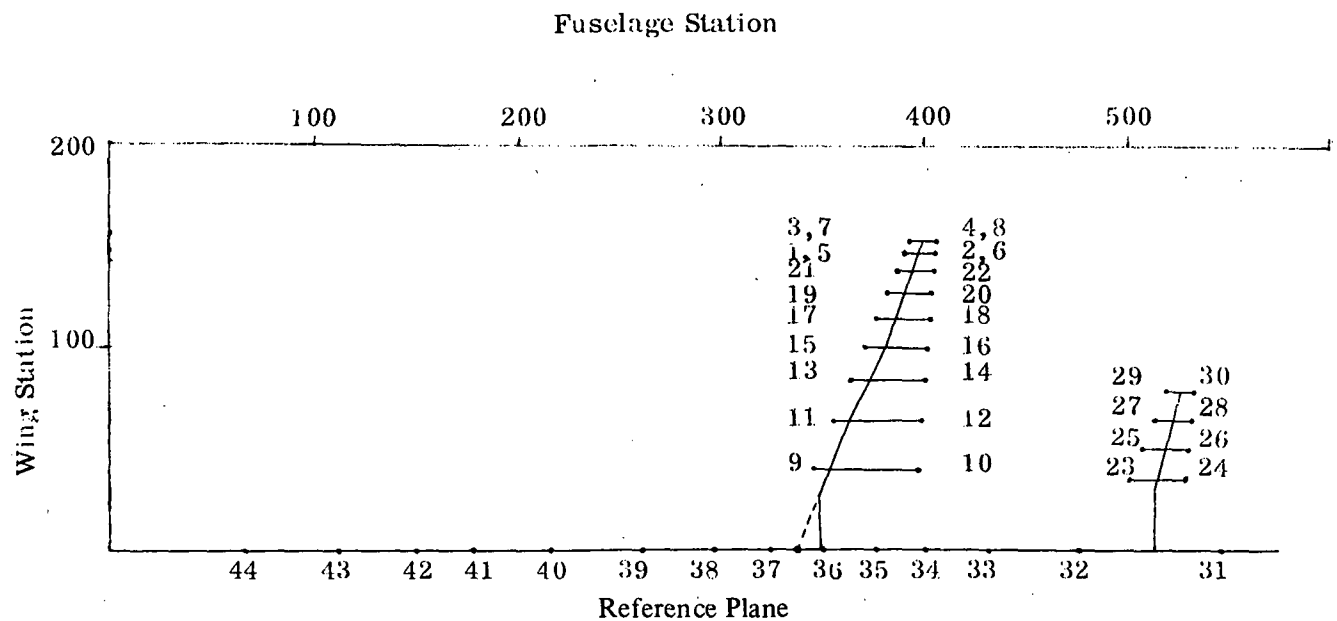

Figure 76. F-5A Wing, Fuselage, and Horizontal Tail Control Point Geometry for Symmetrical Analysis

35% local chord near the root and moves toward the 40% local chord near the tip. The control points are located at 25% and 75% local chord locations as shown in Figures 71 and 72. The flexibility matrix is calculated and merged for each of the three main sections of the model: right wing panel plus tip-store combination, forward fuselage and aft fuselage plus horizontal-tail combination.

Modal Data for the F-5A Fighter

The natural vibration mode data based on the mass-stiffness data described above are computed. (See Appendix II for computer program organization.) The frequency and mode description are tabulated in Table 5. Also listed in the table are typical ground vibration natural frequency data for the same aircraft configuration. The detailed flexible modal data are plotted in Figures 77 and 78. Only symmetrical modes are presented.

TABLE 5

THE F-5A FIGHTER NATURAL FREQUENCY MODE DATA

MODES	F(Hz)	GROUND VIBRATION TEST FREQUENCY (Hz)	DESCRIPTION OF MOTION
1	4.049	4.45	1st Wing Bending, Fuselage Bending (wingtip and fuselage nose are out of phase)
2	6.522	6.60	1st Wing Torsion
3	8.378	10.2	1st Fuselage Bending, Wing Bending (wingtip and fuselage nose are in phase)
4	16.983	17.20	1st Horizontal Stabilizer Bending
5	18.850	18.40	2nd Wing Bending, Fuselage Bending (wingtip and fuselage nose are out of phase)
6	21.989		2nd Fuselage Bending, Wing Bending (wingtip and fuselage nose are in phase)
7	31.037		3rd Fuselage (Forward Fuselage) Bending
8	36.620		2nd Wing Torsion, Forward Fuselage Bending
9	40.048		
10	45.880		
11	52.801		
12	54.192		

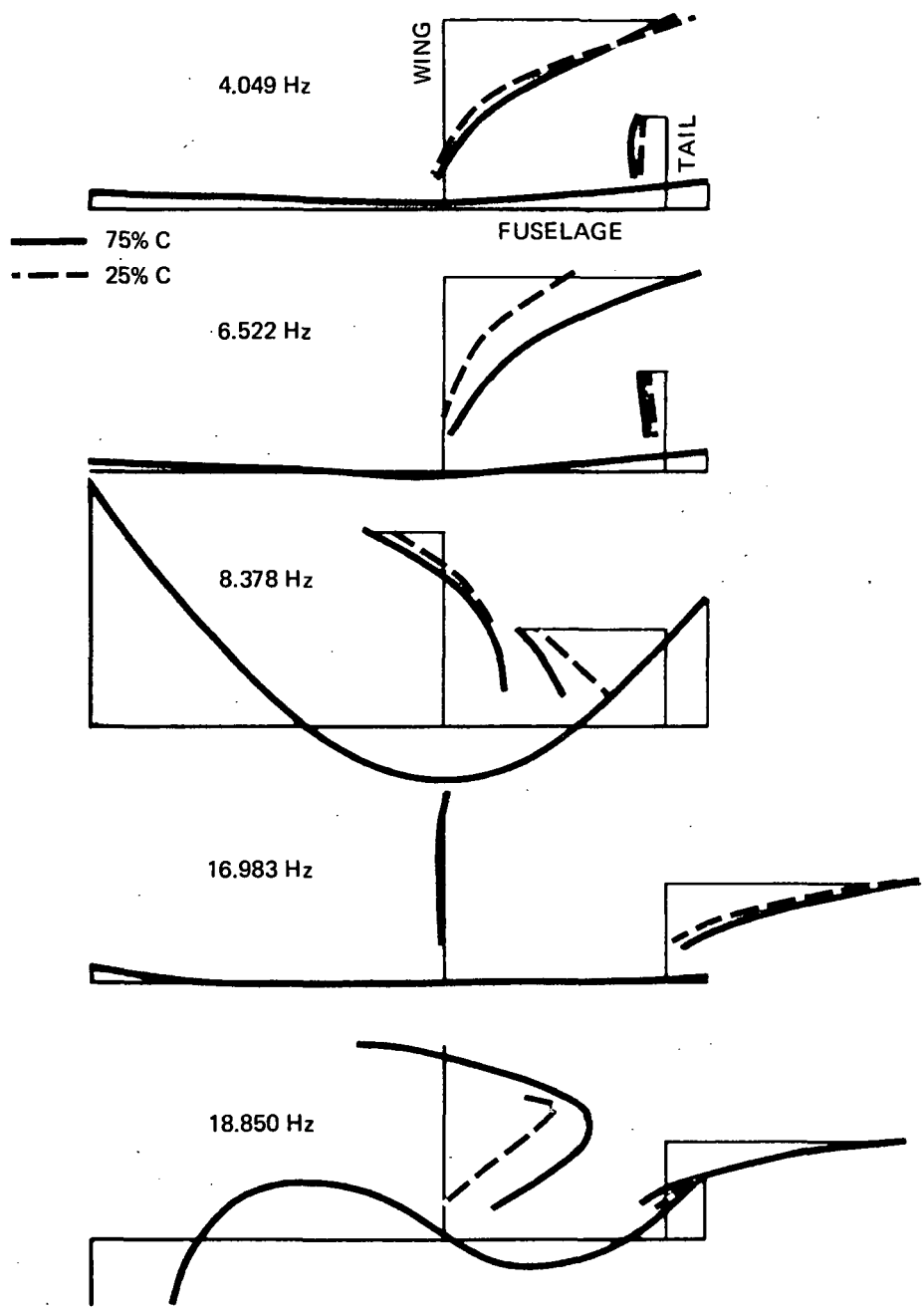

Figure 77. Free-Free Modes of F-5A, Symmetrical Case

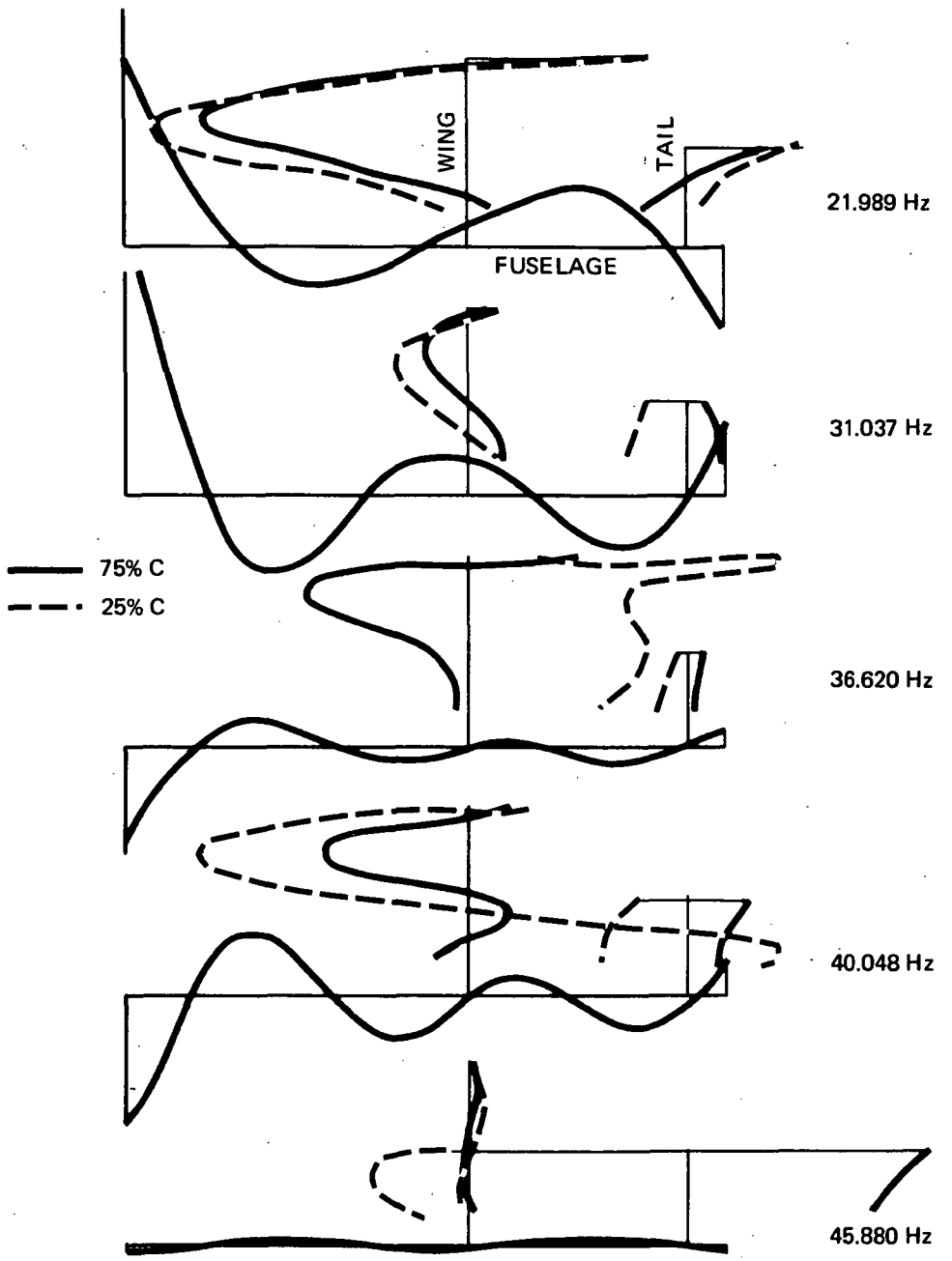

Figure 78. Higher Symmetrical Modes of F-5A

As described previously, the buffet pressure data were acquired on the right-hand wing. No comparable data were available on the left-hand wing. Furthermore, the wind-up turn did induce certain lateral motion of the aircraft. The extent of participation of the antisymmetrical structural modes in aircraft buffet response was not clear. No conclusive information was obtained from the left-hand wingtip accelerometer because of the variation in types of accelerometers used and the excessive noise picked by the left side accelerometer. It is due to lack of information, rather than theoretical considerations, that only the symmetrical modes are used for the aircraft response computations.

Aerodynamics

The oscillatory aerodynamic influence coefficients (AIC's) are computed based on unsteady aerodynamic theory assuming thin airfoil lifting surfaces and slender bodies. The AIC's relate the control point deflections whose time derivatives are the downwash velocities. Aerodynamic forces expressed in terms of AIC's for motion are given in Equation (I-8) of Appendix I. The resulting AIC's are functions of planform, Mach number, and reduced frequency.

The AIC's for wing and tail motion are based on lifting surface theory. The basis of the lifting surface theory is found in the aerodynamic integral equation that relates the pressures on the surface to the downwash at the surface. A number of solutions to these integral equations by collocation methods have been proposed. The methods are based on certain approximate treatments of the kernel of the integral equation. In the subsonic range, the kernel of Watkins, Runyan, and Woolston is used (Reference 41). The method of solution is based on the expansion of the kernel function into a fifth-order power series in reduced frequency and was originated by Runyan and Woolston (References 42, 43, and 44). It consists of adjusting the amplitudes of an assumed series of modes for the pressure corresponding to the downwash produced at the control points by a system of chordwise replacement loads.

Tail downwash due to wing lift is accounted for (see Reference 45). The wing and tail AIC matrices are assumed to be decoupled.

The AIC's for the fuselage due to motion are derived from the slender-body theory (References 43 and 46). The method employs the momentum theory of Munk and Jones (Reference 3). The disturbance flow component considered in the momentum computation is two-dimensional and is located in a plane normal to the direction of

flight. These fuselage AIC's are independent of Mach number. In the following paragraphs, the buffet pressures based on measured fluctuating pressure data are defined. The natural modal data and the unsteady aerodynamic coefficients are combined to form the aircraft transfer functions subject to the buffet pressures.

In subsection 5.1, the spatial correlation and its effect to the pressure PSD matrix have been discussed. Another factor to be considered involves the separation of the measured pressure into proper components for analytical correlation purpose. Specifically, the measured dynamic pressure distribution may be separated into two components: the pressure induced by wing motion, and a dynamic pressure due to flow separation, etc., which can be considered as the genuine buffet pressure. The modal force components corresponding to the pressure components are indicated by f_i, f_b respectively. The measured force f_m due to these pressure components can be written as:

$$\left\{f_m\right\} = \beta\left\{f_i\right\} + \left\{f_b\right\} \tag{5-1}$$

where β is a fraction factor defining the portion of induced pressure to be assigned to the subarea under consideration. For instance, if the induced pressure is assumed to be distributed evenly on the top and bottom wing surfaces, and if f_m is composed only of upper surface pressures where the significant buffet pressure appears, then $\beta = 1/2$.

The upper-surface force induced by wing motion is:

$$\beta\left\{f_i\right\} = \beta\omega^2\left[\bar{A}\right]\left\{\alpha\right\} \tag{5-2}$$

where $\{\alpha\}$ represents the modal amplitudes and $\left[\bar{A}\right]$ is the generalized AIC matrix. The matrix equation of motion is then:

$$\left[Z - \left(1-\beta\right)\omega^2\,\bar{A}\right]\left\{\alpha\right\} = \left\{f_m\right\} \tag{5-3}$$

where Z is the modal impedance matrix and ω is the circular frequency. The detail mechanization of Equation (5-3) is described in the next subsection and in Appendix I. Substituting Equations (5-2), (5-3) into Equation (5-1), the genuine buffet force due to flow separation may be obtained as follows:

$$\left\{f_b\right\} = \left\{f_m\right\} - \beta\omega^2\left[\bar{A}\right]\left[Z - (1-\beta)\,\omega^2\,\bar{A}\right]^{-1}\left\{f_m\right\} . \tag{5-4}$$

5.3 Aircraft Response Analysis Considering a Major Portion of the Maneuver as Stationary

The aircraft response functions are computed for a number of frequencies within the band of interest using the modal approach. The dynamic equations used in the response computation are matrix equations for a damped elastic system considering the buffet pressure input and the induced aerodynamic forces. Approximate solutions minimizing the errors for all degrees of freedom are obtained applying the Galerkin method.

The computer program mechanization of the spectral response calculation is given in Appendix II. The computation starts with generating the symmetrical free-free modal data of the aircraft upon receiving proper idealized structural data as input. For a given Mach number, the aerodynamic influence coefficient matrices for wing, tail, and fuselage are generated separately corresponding to a sequence of reduced frequencies. The measured real-time pressure data are converted into Fourier transforms in the frequency domain. The frequency response program generates the Fourier components as well as the power spectral data of the response quantities based on the available modal, AIC, and pressure data. Assume that the measured pressures are random and ergodic. Two extreme cases of the spatial correlation between pressures are considered in the response computation as described below.

1. Perfect spatial correlation condition: For this case the coherence functions for pressures always equal unity. The frequency response computer program computes the Fourier Components of the response quantities. The corresponding PSD values may be obtained as follows:

$$\phi_r(\omega) = \frac{T}{\pi} \left| F_r(\omega) \right|^2 \quad , \tag{5-5}$$

where T is the time span and F_r is the Fourier component of the response quantity. Equation (I-27) in Appendix I is a special case of Equation (5-5) where $F_r(\omega) = (-\omega^2/G)\, h_{1i}(\omega)$ is the Fourier transform of acceleration at control point i.

The disturbance pressures due to flow separation may be computed based on Equation (5-4).

2. Spatially uncorrelated condition. For this case the modal force PSD matrix $\left[\phi_f\right]$ is formed by a diagonal pressure PSD matrix. The coherence functions of the pressures in two subareas are always equal to zero. The PSD's of the response functions are generated directly. The matrix equation equivalent to Equation (5-3) is of the following form:

$$\left[\phi_a\right] = \left[Z - (1-\beta)\omega^2 \bar{A}\right]^{-1} \left[\phi_f\right] \left[\left[Z^* - (1-\beta)\omega^2 \bar{A}^*\right]^{-1}\right]^T \quad (5\text{-}6)$$

$$= \left[H(\omega)\right] \left[\phi_f\right] \left[H(\omega)^*\right]^T$$

In Equation (5-6), $\phi_a(\omega)$ is the matrix of the modal response PSD. Equation (I-28) in Appendix I is identical to Equation (5-6), except that a factor $(\omega^2/G)^2$ is added to convert the displacement PSD matrix into an acceleration PSD matrix.

In case (2), the measured force cannot be physically separated into two components corresponding to Equation (5-1), as for case (1) where the pressure data were perfectly correlated in a spatial sense. For the actual case where spatial correlation between pressure subareas exists to a certain degree depending on the flight condition and the relative locations of the pressure subareas, Equation (5-6) still applies. The exception is that the matrix $\left[\phi_f\right]$ for the latter case is formed by a full-pressure PSD matrix whose elements are the Fourier transforms of the auto- or cross-correlation functions.

Using the above formulation, the analytical computation of aircraft response functions was performed for the following configuration:

Flight number	825, Run 7
Mach number	0.75
Altitude	7,772 m (25,500 ft)
Flap settings	(0°/0°)
Total time span	362-367 sec
Low frequency digital tape frame rate	0.001 sec
Time increment	0.002 sec
Frequency increment	0.488 Hz
Spectral frequency range	3.5 - 46.5 Hz

The comparison between the flight test response data and the computed response data of the aircraft are based on the PSD of acceleration at key locations including the forward wingtip, the aft wingtip, and the C.G., Figures 79-81. In these figures the test data are represented by heavy solid lines. The analytical data based on the perfectly correlated pressure are shown as dotted lines, while those based on spatially uncorrelated pressures are represented by light solid lines. The differences in PSD's between the two sets of analytical data are indicated by the shaded area.

Referring to Figures 79, 80, the differences of computed PSD's based on zero correlation and perfect correlation are in most cases limited to about a factor of 10 db. In general, the computed data based on zero correlation are somewhat closer to the PSD based on flight test response data. A major deviation between test and computed response PSD's appears in the frequency range above 25 Hz. In this range, the test data indicate substantially higher bending type vibrations, while the computed data indicate high amplitude torsional vibrations. In Figure 81, the substantial C.G. responses to the primary wing bending and torsion modes (at 4.049 and 6.522 Hz) are not properly reflected in the analytical data.

The large deviations between the analytical and test response PSD's are attributed to a number of factors. These are listed below:

1. The transonic maneuver is a nonstationary process. The 5-second interval used in the present computation does not take into consideration the nonstationary dynamic effect apparent during the interval. This factor is remedied by the segmentwise stationary computation carried out in a subsequent subsection.

2. The analytical data are computed based on the assumption that the buffet pressures on both wings are symmetric about the center section of the fuselage. The nonsymmetrical components of the actual buffet pressure distribution, if any, are ignored. The peaks corresponding to antisymmetrical modes are thus missing from the analytical plots. Furthermore, the dynamic contribution by the tail surfaces can be significant and is ignored.

3. The spatial correlations of pressures are neither perfectly correlated nor noncorrelated. The degree of spatial correlation is dependent on the transducer locations. For example, the measured pressures near tip locations are highly correlated, while the pressures in the other region, especially those near the wing root, seem to be lightly correlated or uncorrelated.

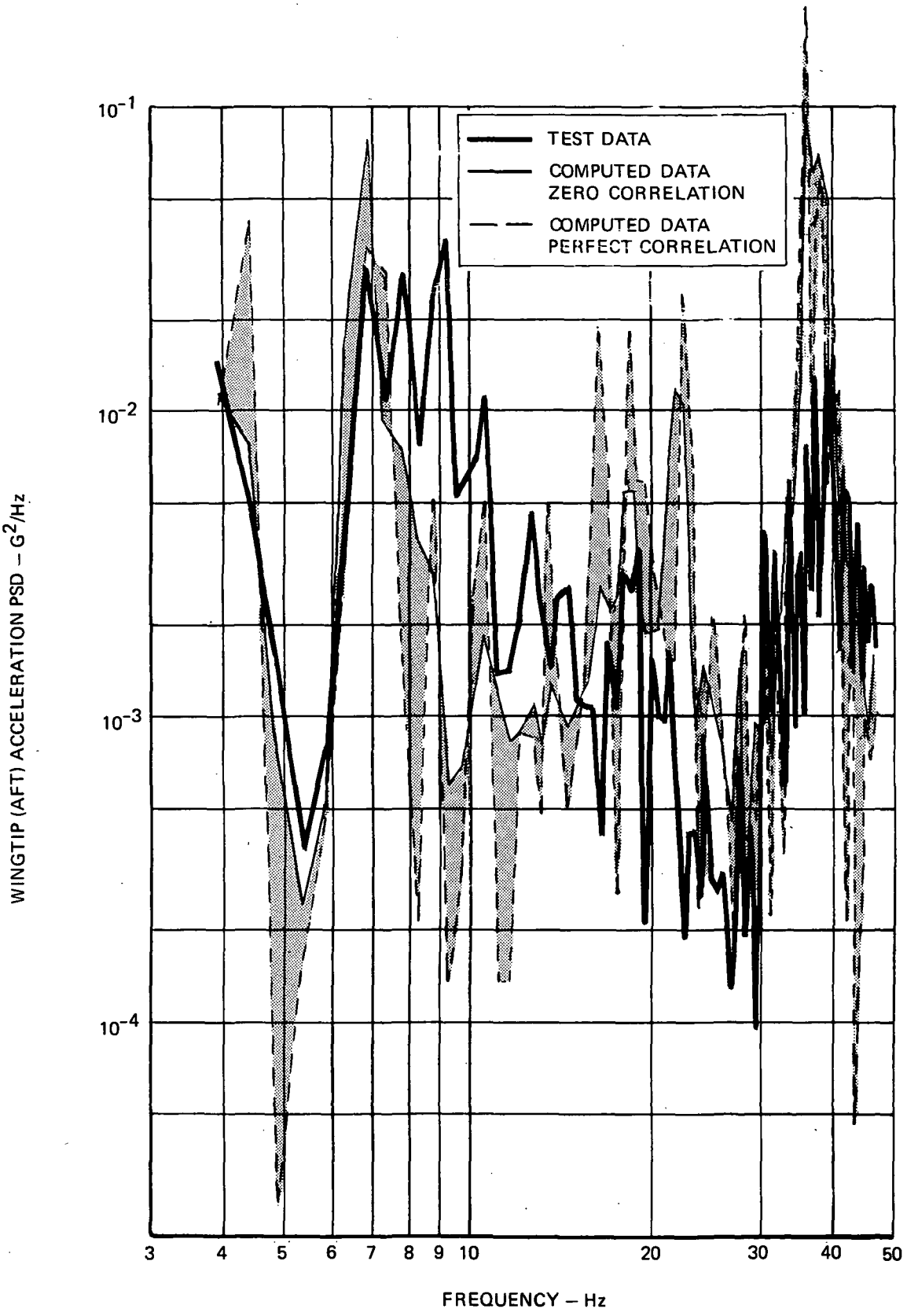

Figure 79. Experimental and Analytical Data of Right-Hand Wingtip (Aft) Acceleration Power Spectral Density, $M_o = 0.75$, h = 7,772 m, $\delta_n = 0°$, $\delta_f = 0°$, Real Time Data Based on Time Span (362-367 sec)

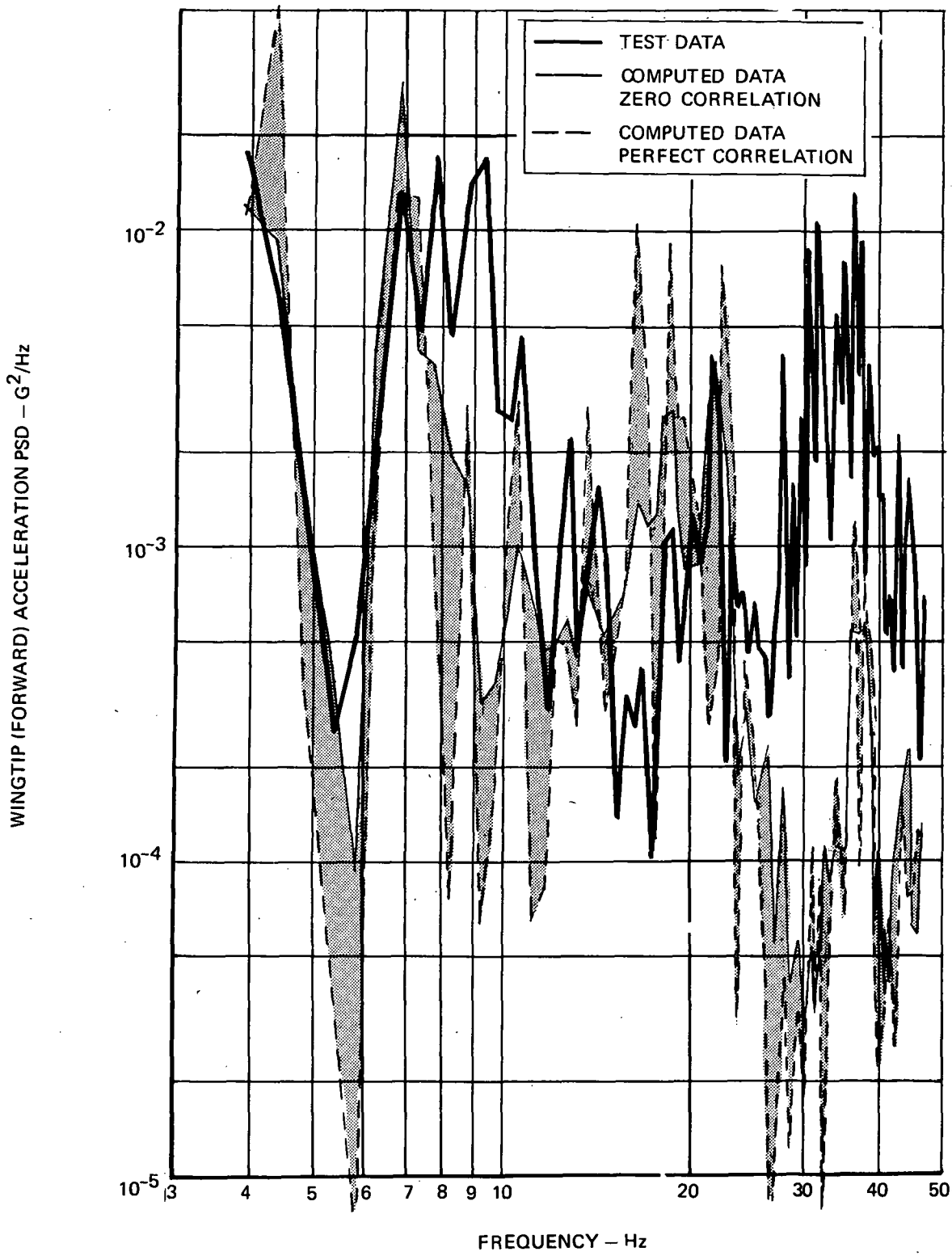

Figure 80. Experimental and Analytical Data of Right-Hand Wingtip (Forward) Acceleration Power Spectral Density, $M_o = 0.75$, h = 7,772 m, $\delta_n = 0°$, $\delta_f = 0°$, Real Time Data Based on Time Span (362-367 sec)

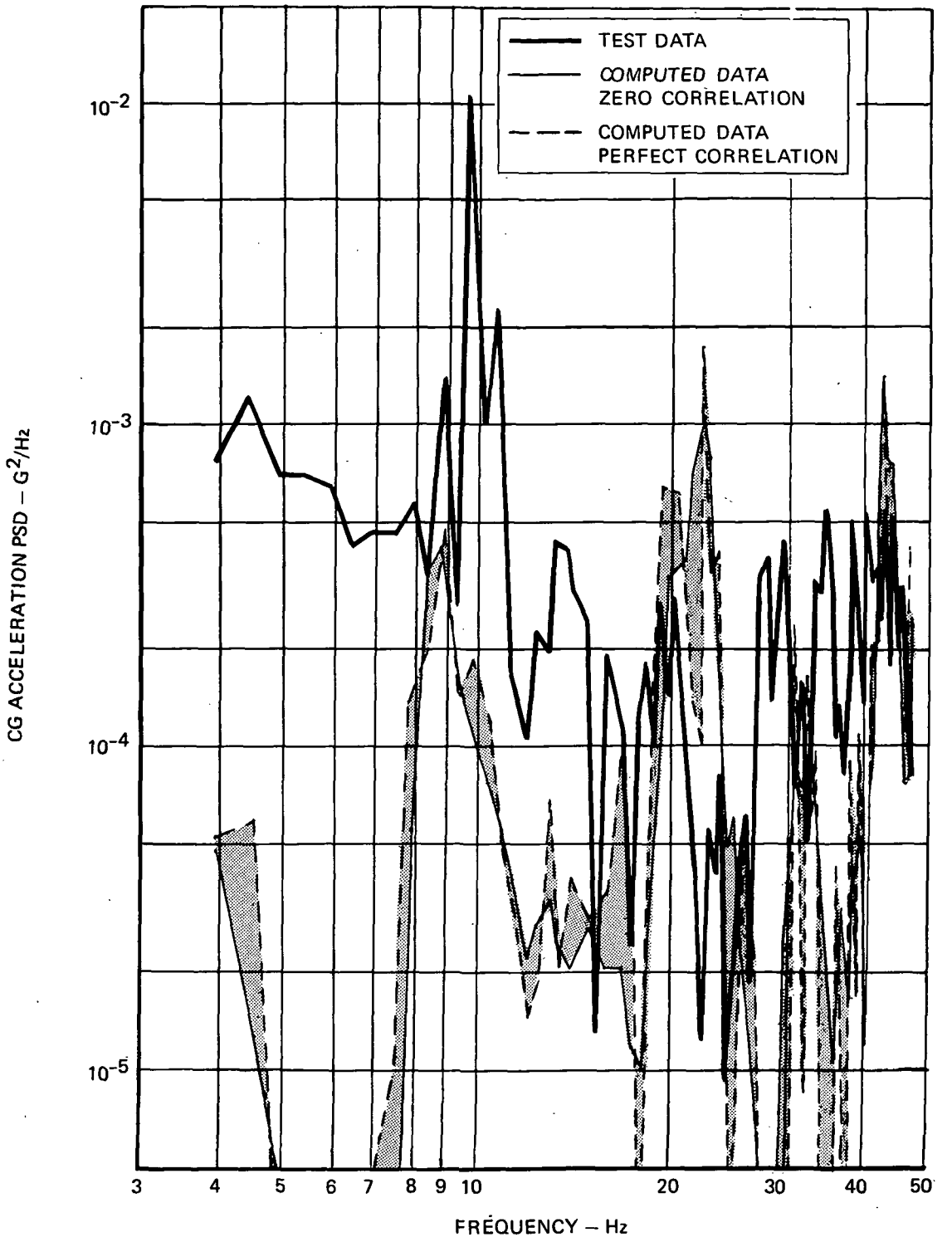

Figure 81. Experimental and Analytical Data of cg Acceleration Power Spectral Density, $M_o = 0.75$, h = 7,772 m, $\delta_n = 0°$, $\delta_f = 0°$, Real Time Data Based on Time Span (362-367 sec)

4. The computed response data, especially the frequency shift at the resonance frequencies, depend on the induced pressure contribution parameter of β which is arbitrarily assumed. The frequency shift is sensitive to the β changes because the imaginary part of the unsteady aerodynamic force is of the same order as the structural damping force which determines the response peak frequency shift. The real part of the unsteady aerodynamic force is usually substantially smaller than the spring force of the structure. Also, improvement can be made on the analytical AIC matrix.

5. In the neighborhood of a natural frequency, the computed response PSD level depends strongly on the modal damping coefficient input g_F, which is assumed to be 0.05 in the present investigation. Furthermore, in order to streamline the computation, simplified structural models are used.

6. Normalized standard errors in PSD computation are introduced in both test and analytical data.

Induced Aerodynamic Pressure in Buffet

A subject of interest in a buffet test program is the magnitude of the induced aerodynamic forces (as a function of frequency) relative to the overall dynamic pressure force during buffet. In these subsections, the computed induced aerodynamic pressure data based on the measured buffet pressure distribution and the aircraft responses are presented.

For the case of pressure distribution with perfect spatial correlation, it is possible to separate the genuine pressure p_b due to flow separation from the measured pressure p_m. Since the Fourier transforms of the total pressure p_i induced by wing motion in a uniform flow may be computed, the relative magnitude of the induced pressure at the top surface of the wing to the measured oscillatory pressure p_m may be determined by:

$$\zeta = \beta \left| p_i \right| / \left| p_m \right| = \left| 1 - p_b/p_m \right| \qquad (5\text{-}7)$$

at different transducer locations as functions of frequency. Typical pressure ratio plots at Transducer Locations 1, 4, 18, 23 are shown in Figure 82. The peak locations in the plots correspond either to a resonance frequency which induces a large deflection at that transducer location, or a very low value of the measured pressure.

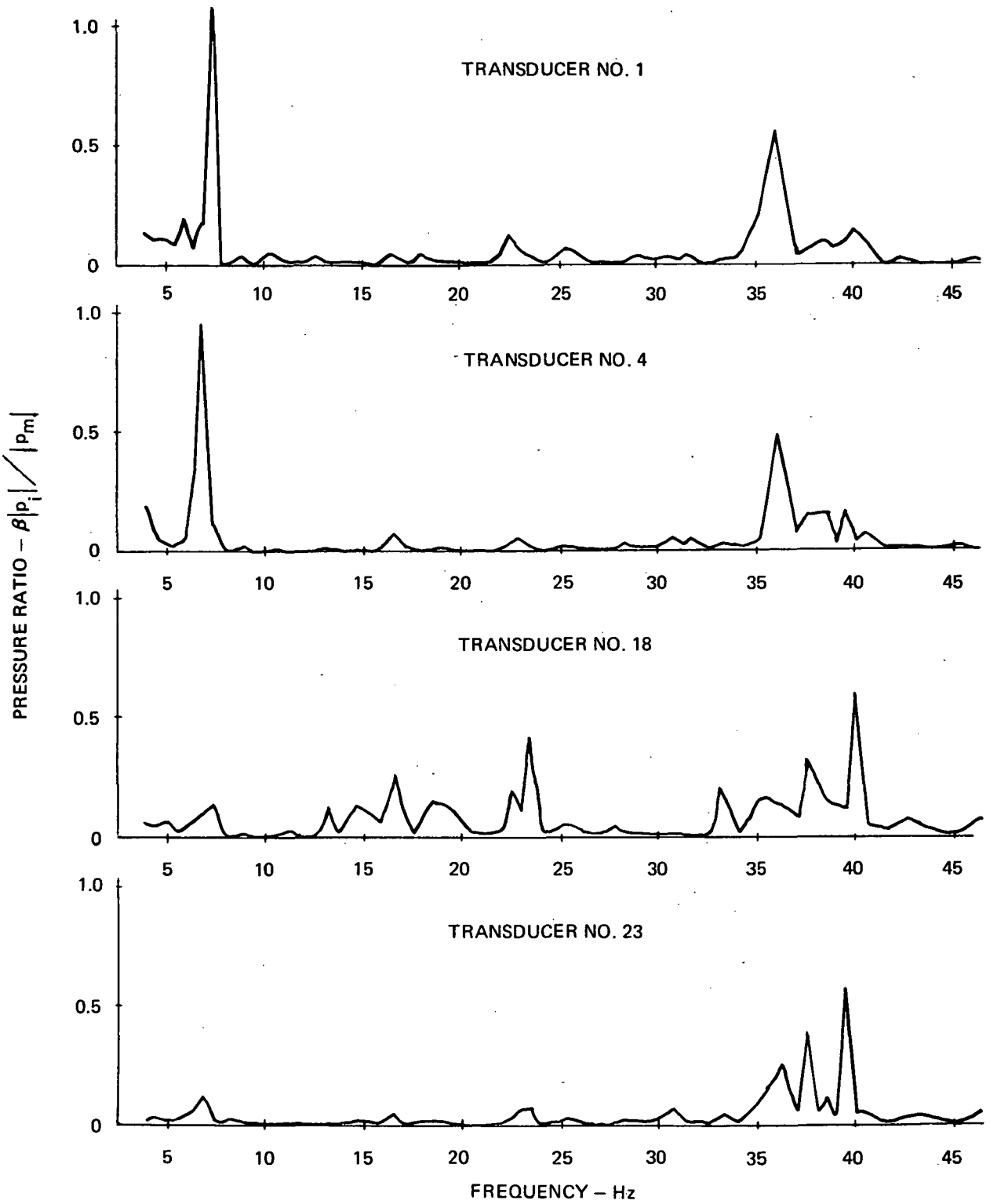

Figure 82. Relative Magnitude of Induced Aerodynamic Pressure to Measured Pressure Acting on F-5A Wing Top Surface, M = 0.75, h = 7,772 m, δ_n = 0°, δ_f =0°

In general, the ratio ζ is less than 0.3. In other words, the genuine buffet pressure p_b dominates in most frequency ranges, while the induced pressure is less significant in the response computation. The top plot of Figure 82 shows the ζ values for Transducer No. 1 where the relative amplitude of the induced aerodynamic pressure yields a very high peak:

$$f = 7.324 \text{ Hz}$$

$$\zeta = 1.086$$

$$p_m = (-7.31 + i\,5.81)\text{N/M}^2, \qquad |p_m| = 9.31 \text{ N/M}^2$$

$$\beta p_i = (-2.12 - i\,9.92)\text{N/M}^2, \qquad \beta|p_i| = 10.14 \text{ N/M}^2$$

$$p_b = (-5.18 + i\,15.73)\text{N/M}^2, \qquad |p_b| = 16.56 \text{ N/M}^2$$

The highest peak occurs near the second eigen frequency where Transducer Location 1 has a large deflection. For this case, even though ζ is greater than unity, $|p_b|$ is still 1.6 times the value of $\beta|p_i|$ while the two complex pressure vectors βp_i and p_b are out of phase.

5.4 Aircraft Response Analysis Considering the Maneuver as Segmentwise Stationary

In order to improve the analytical correlation of aircraft response results, the major portion of a transonic maneuver is divided into a number of segments. In each segment, the buffet pressure data are assumed to be stationary. The aircraft is then subjected to the consecutive application of the buffet loads and the cumulative dynamic effects are reflected in the time varying PSD of response. The detail formulation of the segmentwise stationary approach and the computation flow diagram are given in Appendix III of the report.

The approach is applied to the following set of flight test data:

Flight number	871, Run 2
Mach no.	0.925
Altitude	10,668 m (35,000 ft)
Flap settings	(4°/12°)
Low frequency digital tape frame rate	1000 per sec

Time increment	0.002 sec
Frequency increment	0.488 Hz
Spectral frequency range	1.4 – 20.0 Hz

The real-time data of this run are given in Figures 19-28. Altogether, dynamic pressure data covering the time span 073.00-082.10 second are used. The data, assumed to be perfectly correlated, are divided into four (4) equal time segments. The computation is carried out using the rigid body plunging mode and the first three symmetrical flexible modes (see Table 5 in subsection 5.2). The pitch mode is not included because of lack of tail surface dynamic loads data. Corresponding to the above flight condition, and considering plunge-pitch coupling, the natural frequency of the short period mode of the aircraft is 0.3947 Hz. The damping ratio of the short period mode is 0.245.

Figure 83 gives the time varying influence function of the aircraft corresponding to the first flexible mode (first wing bending) and during the first time segment. The absolute values of the influence function $\left| I^{a}_{1,1}(t,\omega) \right|$ are plotted in G-level per unit modal force. (See Appendix III, Equations III-12 and III-23, for definition.) Corresponding to a rectangular shaped time function $e_1(t)$, the influence function is independent of frequency at the initial time. It peaks at the natural mode frequency as time passes. The function value drops rapidly in frequency ranges other than the natural frequency at the end of the time segment. This behavior illustrates the dynamic carry-over effect of the modal response in the subsequent time segment.

Figure 84 gives the mean square values of the rigid body (plunging) mode and three flexible mode forces corresponding to the four time segments of the transonic maneuver. Only the mean square contributions within the frequency range 1.4-20.0 Hz are taken into account. The relatively high modal forces in the second time segment reflect the shock oscillations at buffet onset (see, for instance, Figures 19, 22). The modal forces diminish in values in the third time segment and reach their peaks in the last and fourth time segment when the angle of attack reaches a maximum.

Based on the preliminary data such as shown in Figure 83, 84, the nonstationary response PSD's for the C.G. and two stations of the right wing tip are computed at specific times, one each within the four time segments. These results are plotted in Figures 85-87. Also plotted are the corresponding segmentwise stationary PSD's based on the flight test response data. For the two sets of response PSD's at the right-

hand wing tip, the computed data are too high in the first segment. This is believed due to the higher damping (of the Coulomb type) at the initial phase of the maneuver not accounted for in the computation. The correlation is more satisfactory in the third and the fourth segments when wing rock takes place. For the C.G. acceleration PSD's, Figure 87, the computed first segment PSD values are low because more spectral energy has been contributed to wing vibrations at this time segment as explained above. For the later segments, with some exceptions, a somewhat better correlation between the computed and flight test PSD data is realized.

In Figure 88, the time varying mean square acceleration for the C.G. and the two stations of the right-hand wing tip based on the segmentwise stationary formulation are plotted. Again, only spectral contributions in the frequency range 1.4-20.0 Hz are accounted for. The figure reflects the very low C.G. response in the first time segment as described above. The substantial differences in mean square accelerations between the two wingtip stations reveal substantial wing torsion mode participation. In general, the correlation of analytical and test response PSD data is more satisfactory using the segmentwise stationary approach as compared to the approach where a major portion of the transonic maneuver is considered stationary.

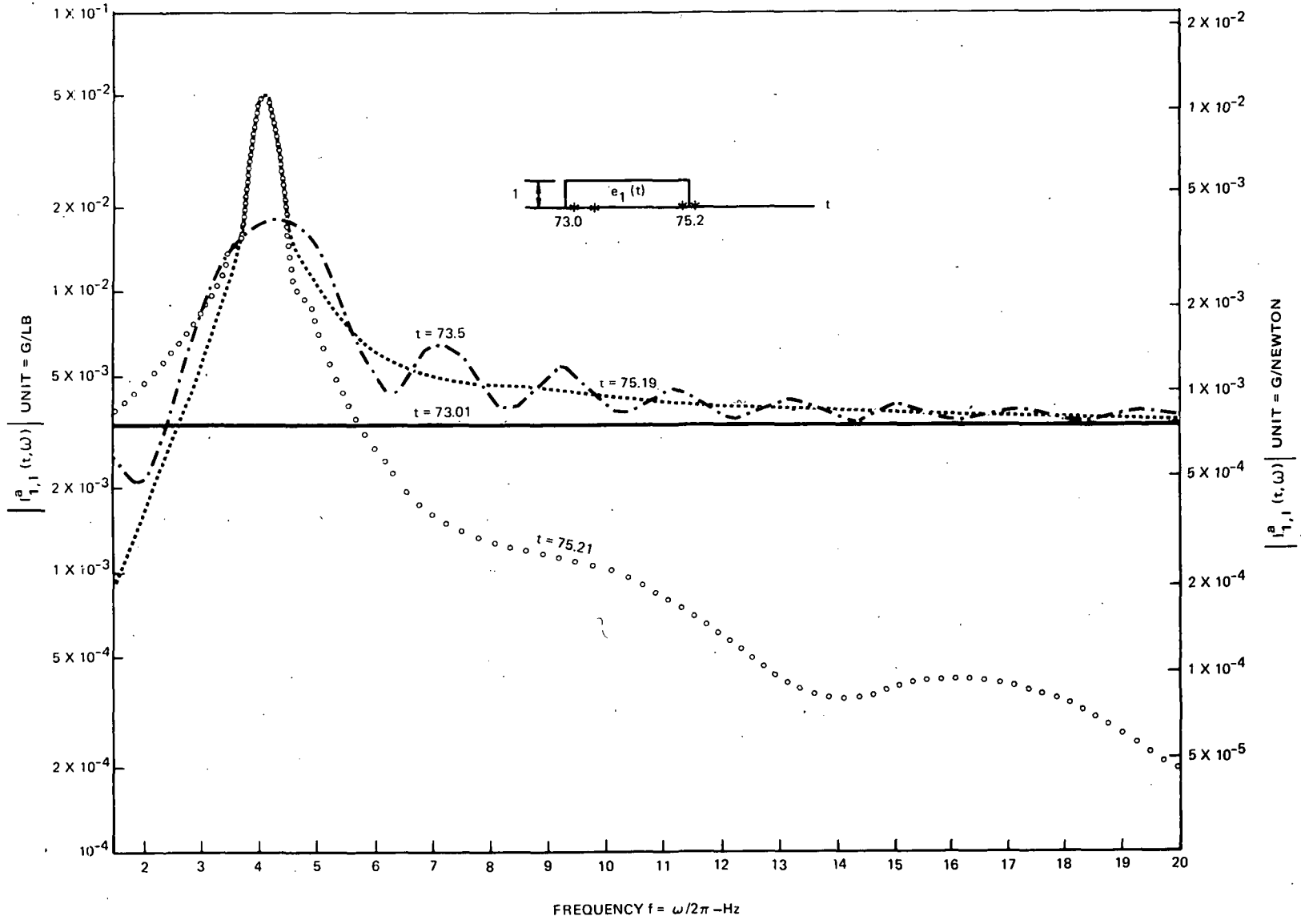

Figure 83. Nonstationary Influence Function of F-5A Corresponding to the First Wing Bending Mode

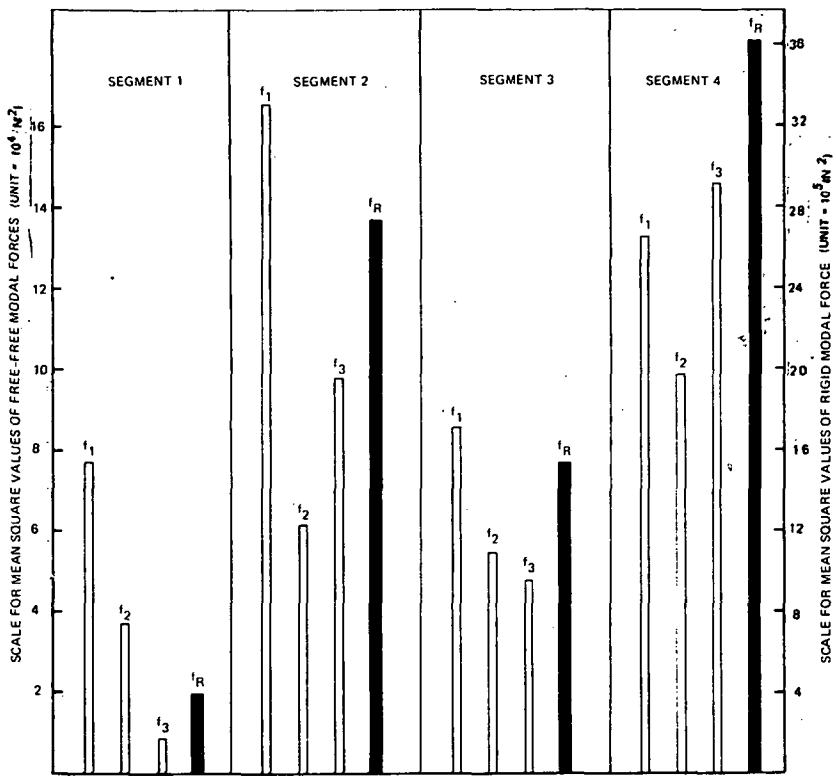

Figure 84. Mean Square Values of the Modal Forces Corresponding to the Four Time Segments of the Transonic Maneuver, Run 2, Flight 871, $M_o = 0.925$, h = 10,668 m, $\delta_n = 4°$, $\delta_f = 12°$

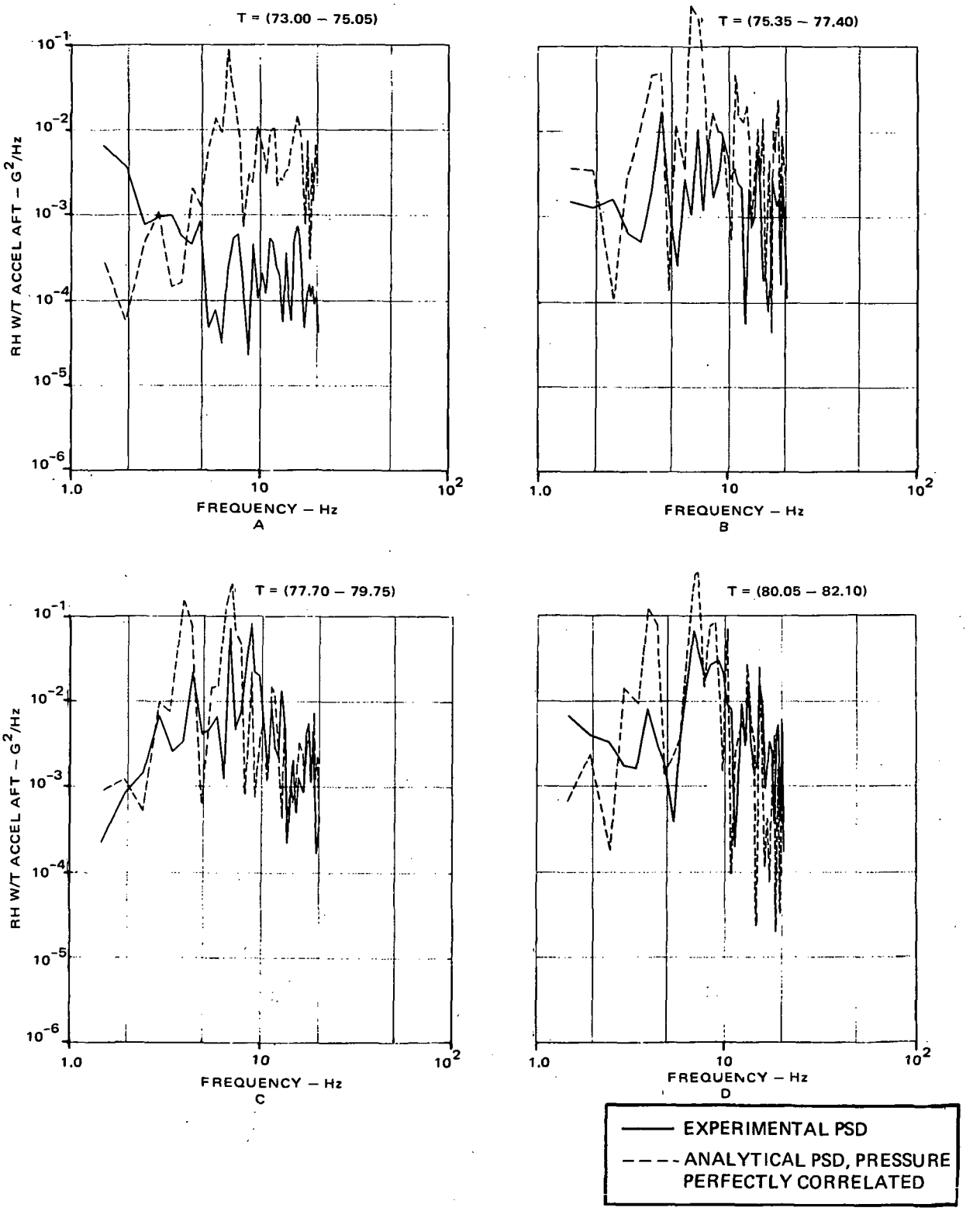

Figure 85. Time Varying PSD's of Right-Hand Wingtip (Aft) Acceleration — Experimental and Analytical Results, $M_o = 0.925$, $h = 10,668$ m, $\delta_n = 4°$, $\delta_f = 12°$

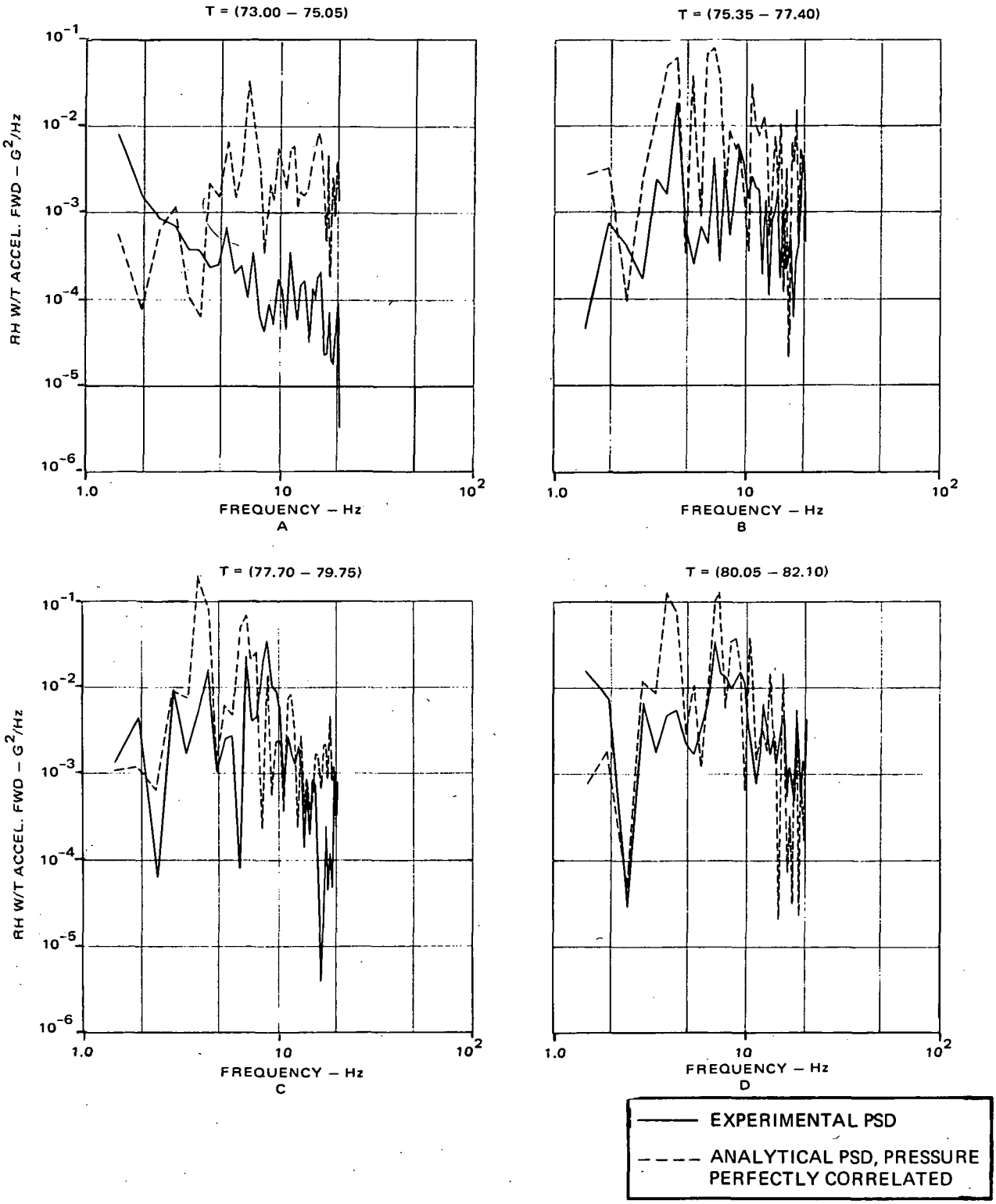

Figure 86. Time Varying PSD's of Right-Hand Wingtip (Fwd) Accelerations — Experimental and Analytical Results, $M_o = 0.925$, h = 10,668 m, $\delta_n = 4°$, $\delta_f = 12°$

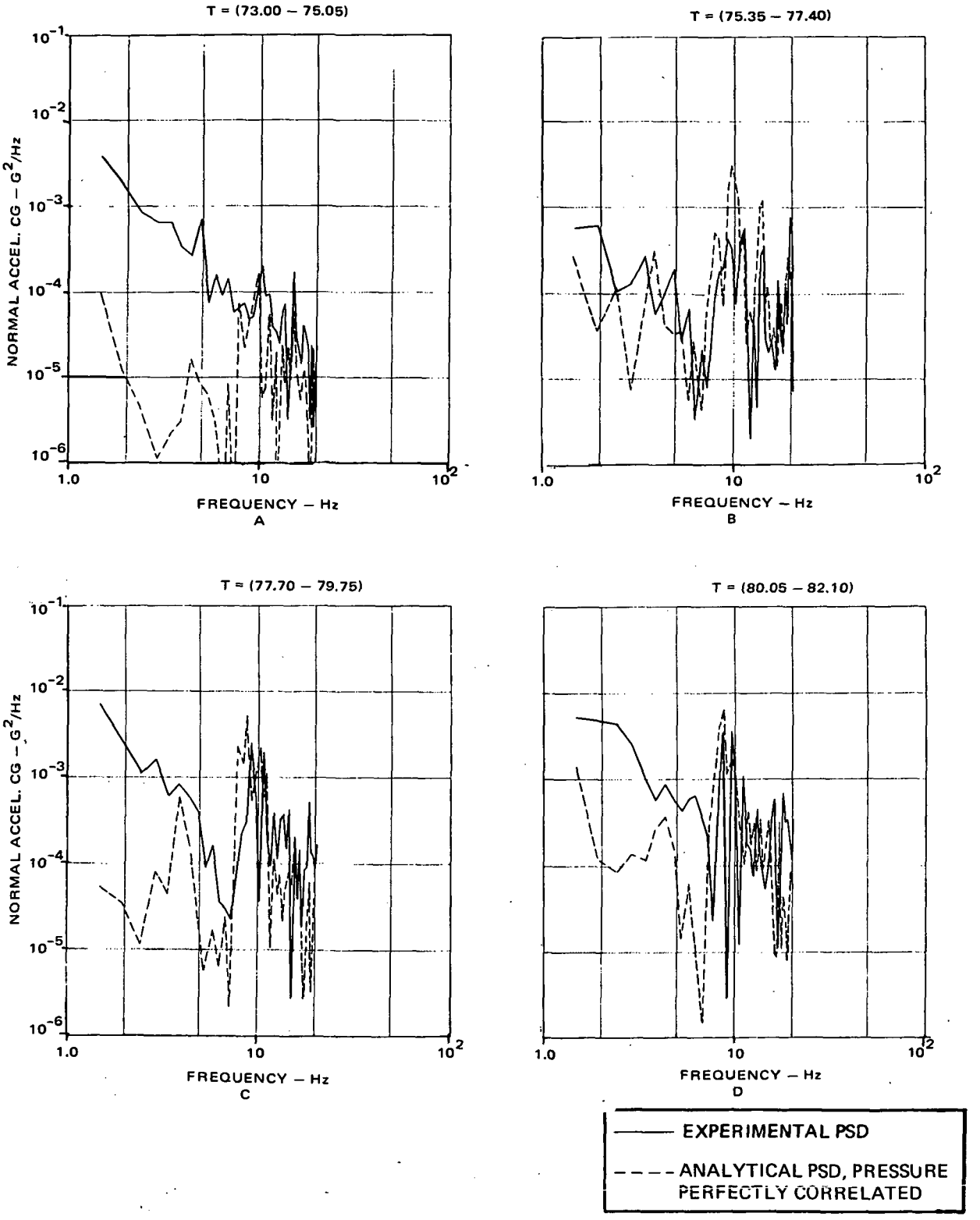

Figure 87. Time Varying PSD's of CG Normal Acceleration — Experimental and Analytical Results, $M_o = 0.925$, h = 10,668 m, $\delta_n = 4°$, $\delta_f = 12°$

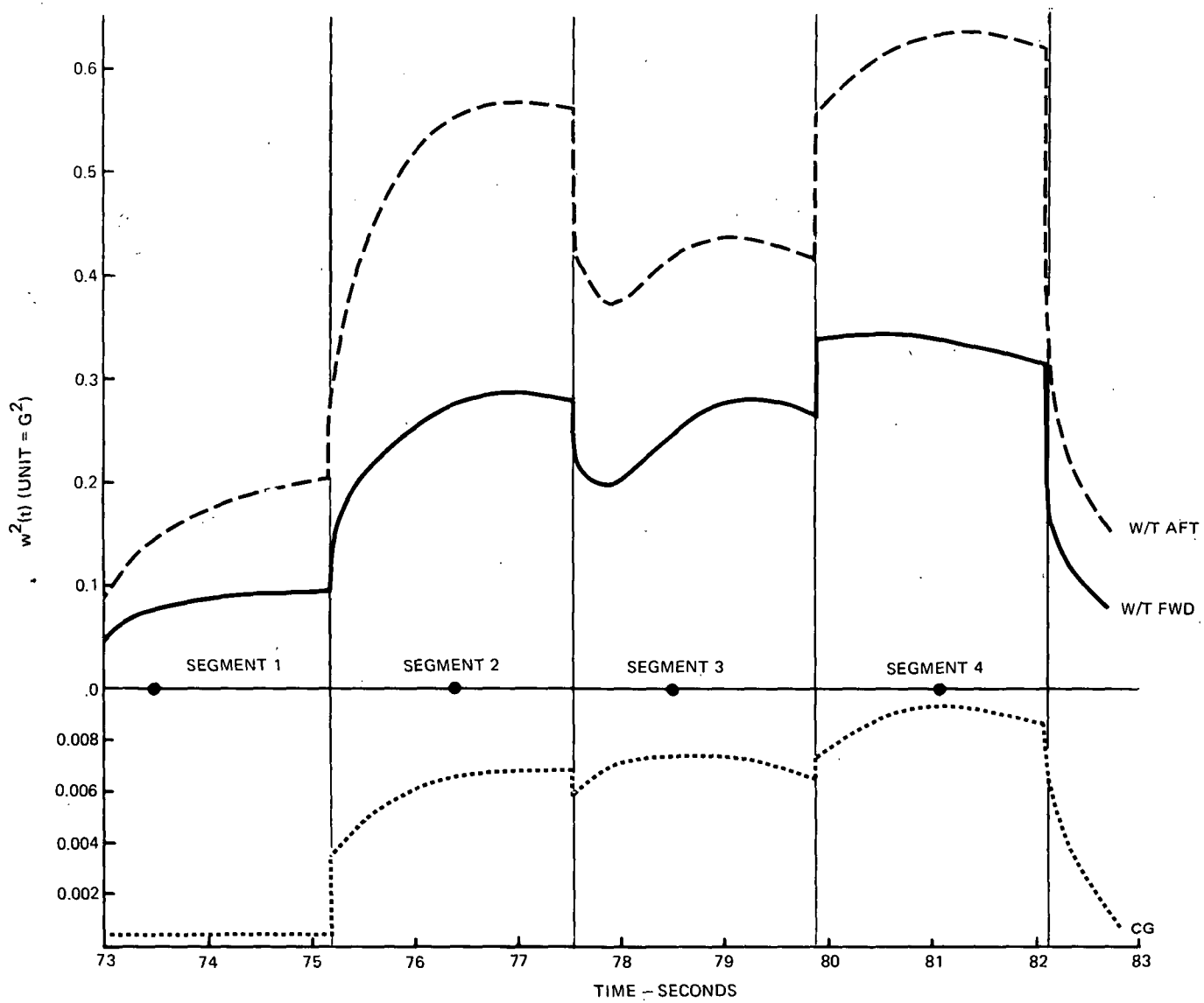

Figure 88. Time Varying Accelerations of the CG and Right-Hand Wingtip During the Transonic Maneuver, Run 2, Flight 871, $M_o = 0.925$, h = 10,668 m, $\delta_n = 4°$, $\delta_f = 12°$

(Analytical Data)

Section 6

CONCLUSIONS AND RECOMMENDATIONS

In the previous sections of this report, the findings of the buffet flight test program, the processed data, and the analytical correlation results have been presented. Typical buffet onset data of F-5A which may be found in previous literature (Reference 26) are not included in this report.

The emphasis of the present program is on the acquisition of the dynamic buffet pressure and response data. Substantial effort has been dedicated to the spectral and statistical processing. The results have been presented in the report. Certain conclusions and observations relating to the flight test and processed results have been given, together with the presented data. In this section, major conclusions and recommendations are outlined.

6.1 Conclusions

1. Precise and detailed dynamic pressure data acquisition for aircraft during transonic buffet is feasible and can be productive. No significant adverse effect of the added instrumentation and change of airfoil geometry to the natural flow pattern was observed based on the dynamic flow development on the wing and the comparison with the tuft data. Fairly consistent mapping of the separation boundaries was achieved.

2. Shock instability in a steady-state uniform flow has been observed in previous wind tunnel and theoretical treatments under specific conditions depending on Reynolds number and local Mach number. The dynamic pressure of the F-5A showed definite oscillations where the separation boundary was located. It is uncertain whether the cause of the shock oscillation was solely due to the inherent shock instability, the cause might be partially attributable to the interaction with aircraft motion and angle of attack changes. This point remains to be resolved. In general, the amplitude and pattern of the shock oscillations were such that they were expected to contribute significantly to the aircraft motion.

3. The pressure PSD distributions of a buffeting aircraft were such that the establishment of a mathematical model based on a number of flight condition parameters was feasible. Whether the mathematical model is general enough to cover various types or designs of aircraft is a matter subject to future investigation.

4. The spatial correlation of the buffet pressures at various locations of the wing was either high or moderately high in the outboard stations near the wingtip. Substantially lower spatial correlation was observed for pressures between inboard stations or between one inboard and one outboard station.

5. Given detail buffet pressure data, the aircraft responses were predicted in the low-frequency range using linear transfer function technique. The segmentwise stationary approach was the preferred approach. With additional refinements in both buffet pressure model formulation and aircraft transfer function computation, a practical method can be developed for aircraft buffet response prediction.

6.2 Recommendations

Based on the observations and conclusions presented above, a number of recommendations are listed below which may be used as guidelines in future research and development work on aircraft buffet.

1. It is most desirable to acquire steady-state pressure data for the same aircraft under identical flight conditions in order to reach a better understanding of the shock and separated flow interaction as well as other aerodynamic effects of a buffeting aircraft.

2. The flight test and processed data presented in the report may serve as an excellent set of baseline data to study the Reynolds number and scaling effects in transonic wind tunnel testing where a scale model is used. Items such as the effect of angle of attack change during data acquisition, the adequacy of using transition strips in low Reynolds number tunnel testing, and the method of correlation of scale model and full-scale data are of utmost interest and should contribute to the state of art in transonic wind tunnel test techniques.

3. The extent of participation of the rigid body modes (symmetrical and anti-symmetrical) as well as the participation of the anti-symmetrical structural modes in aircraft buffet should be investigated. Dynamic loads on the tail surface which are subject to wake flow are to be included. Analytical and experimental work should be carried out simultaneously on this subject.

4. It is considered fruitful to further develop a mathematical model of the buffet pressures for a type or family of aircraft. The spatial correlation of the buffet pressures is a subject worthy of additional work. Definite progress may be achieved in establishing and improving the analytical prediction techniques for aircraft buffet responses.

5. Design refinements and/or flight maneuver techniques should be looked into with a view to delaying the buffet onset or to reducing the amplitude of wing rock during a transonic maneuver.

APPENDIX I

METHOD OF FREQUENCY RESPONSE CALCULATION

In this appendix, a detailed derivation of the equations of motion and the response quantities (deflection, acceleration) are represented. The equations are developed by the collocation method extended to the approximate modal solution using Galerkin's method. Using the modal solution, the frequency response functions due to an external sinusoidal force or the Fourier transform of a stationary ergodic random pressure field are determined. In the analysis, the following sign conventions are used: The coordinates (x, y, z) and the forces and deflections are positive forward, starboard, and downward.

The analytical computation of the response data starts with the determination of the natural frequency modes of the aircraft as a free-free body. The reduced eigen equation for a free-free system may be expressed in the following form, as shown in Reference 50:

$$\left[k_{11} + k_{11}T\, M_{22}^{-1}\, T^T M_{11}\right] \left\{\chi_1\right\} = \omega_F^2 \left[M_{11}\right] \left\{\chi_1\right\} \qquad \omega_F^2 \neq 0 \tag{I-1}$$

where χ_1 is the eigen vector matrix of the control points, k_{11} is the stiffness matrix for the system with the reference point fixed (i.e., no rigid body motion), M_{11} is the mass matrix of the control points, T is the rigid body transformation matrix, and ω_F is the associated circular eigen frequency. The corresponding reference point mode shape χ_2 may be expressed as a function of χ_1

$$\left\{\chi_2\right\} = -\left[M_{22}^{-1}\, T^T M_{11}\right] \left\{\chi_1\right\} \tag{I-2}$$

where M_{22} is the reference point mass matrix and $\left[M_{12}\right]$ is assumed to be a null matrix.

Let X_1 and X_2 be the modal matrices whose columns are composed of the eigenvectors χ_1 and χ_2 respectively. The modal matrices satisfy the following orthogonal conditions:

$$\left[X_1^T M_{11} X_1 + X_2^T M_{22} X_2\right] = \left[M_F\right] \tag{I-3}$$

$$\left[X_1 - TX_2 \right]^T \left[k_{11} \right] \left[X_1 - TX_2 \right] = \left[k_F \right] = \left[M_F \right] \left[\omega_F^2 \right] \tag{I-4}$$

where M_F is the generalized mass matrix in diagonal form. In the frequency domain the equation of motion of a damped elastic system free in space may be written as:

$$-\omega^2 \left[M_{11} \right] \left\{ h_1 \right\} + \left(i\omega \left[C \right] + \left[k_{11} \right] \right) \left\{ h_1 - Th_2 \right\} = \left\{ f_1 (\omega) \right\} \tag{I-5}$$

$$-\omega^2 \left[T^T M_{11} \right] \left\{ h_1 \right\} - \omega^2 \left[M_{22} \right] \left\{ h_2 \right\} = \left[T \right]^T \left\{ f_1 (\omega) \right\} + \left\{ f_2 (\omega) \right\} \tag{I-6}$$

where h and f represent the Fourier transforms of the deflections and the external forces respectively. The subscript 1 in the above equations refers to the control points while the subscript 2 refers to the reference point. C is the damping matrix for the system. Equation (I-5) is the equation of motion of the control points if the reference point is held stationary. Equation (I-6) is the equation of motion of the reference point when all inertia forces and external forces are accounted for through the use of the transformation matrix T. The external forces are assumed arising from the motion and from some external sources such as the buffet pressure, etc., thus:

$$\left\{ f (\omega) \right\} = \left\{ f_i (\omega) \right\} + \left\{ f_b (\omega) \right\} \tag{I-7}$$

In case the pressure distribution is measured through pressure transducers at various locations, the relationship between the measured pressures and the buffet pressures is defined in Equation (5-1). Then Equation (I-7) may be expressed in an alternate form as follows:

$$\left\{ f(\omega) \right\} = (1 - \beta) \left\{ f_i (\omega) \right\} + \left\{ f_m (\omega) \right\} \tag{I-7a}$$

The forces due to the motion may be expressed in terms of the oscillatory AIC's:

$$\left\{ f_i (\omega) \right\} = \rho \omega^2 b_r^2 \, S \left[W \right] \left[C_h (\omega) \right] \left\{ h (\omega) \right\} \tag{I-8}$$

where ρ = air density, Kg/m^3

b_r = reference semichord, m

S = semispan length, m

$\left[W \right]$ = aerodynamic weighting matrix

$\left[C_h \right]$ = oscillatory AIC matrix

Based on the modal data obtained previously, the structure deformation may be represented as:

$$\left\{h_1\right\} = \left[X_1\right]\left\{\alpha_F\right\} + \left[T\right]\left\{\alpha_R\right\} \tag{I-9}$$

$$\left\{h_2\right\} = \left[X_2\right]\left\{\alpha_F\right\} + \left\{\alpha_R\right\} \tag{I-10}$$

where α_F and α_R are the free-free and the rigid body modal amplitude respectively.

Premultiplying Equation (I-5) by T^T and subtracting from Equation (I-6) yields the equation of motion of the rigid components:

$$-\omega^2\left[\bar{M}_{22}\right]\left\{h_2\right\} - \left[T\right]^T\left(i\omega\left[C\right] + \left[k_{11}\right]\right)\left\{h_1 - Th_2\right\} = \left\{f_{2m}(\omega)\right\} \tag{I-11}$$

Substituting Equations (I-7a) — (I-10) into Equations (I-6), (I-5), and (I-11) yields:

$$-\omega^2\left[\bar{M}_{RF}\right]\left\{\alpha_F\right\} - \omega^2\left[\bar{M}_{RR}\right]\left\{\alpha_R\right\} = \left[T\right]^T\left\{f_{1m}(\omega)\right\} + \left\{f_{2m}(\omega)\right\} \tag{I-12}$$

$$\left[-\omega^2\left[\bar{M}_{11}X_1\right] + \left(i\omega\left[C\right] + \left[k_{11}\right]\right)\left[X_1 - TX_2\right]\right]\left\{\alpha_F\right\} - \omega^2\left[\bar{M}_{11}T\right]\left\{\alpha_R\right\} = \left\{f_{1m}(\omega)\right\} + \left\{\epsilon_F\right\} \tag{I-13}$$

$$-\left(\omega^2\left[\bar{M}_{22}X_2\right] + \left[T\right]^T\left(i\omega\left[C\right] + \left[k_{11}\right]\right)\left[X_1 - TX_2\right]\right)\left\{\alpha_F\right\} - \omega^2\left[\bar{M}_{22}\right]\left\{\alpha_R\right\} = \left\{f_{2m}(\omega)\right\} + \left\{\epsilon_R\right\} \tag{I-14}$$

where

$$\left[\bar{M}_{RF}\right] = \left[T^T\bar{M}_{11}X_1 + \bar{M}_{22}X_2\right] \tag{I-15}$$

$$\left[\bar{M}_{RR}\right] = \left[T^T\bar{M}_{11}T + \bar{M}_{22}\right] \tag{I-16}$$

$$\bar{M} = M + (1-\beta)\,\rho\, b_r^2\, S\left[W\right]\left[C_h(\omega)\right] \tag{I-17}$$

$\left\{\epsilon_F\right\}$, $\left\{\epsilon_R\right\}$ = errors

Applying the Galerkin principle to the equations of motion, (I-13) and (I-14), the following equation is established:

$$\left[X_1\right]^T\left\{\epsilon_F\right\} + \left[X_2\right]^T\left\{\epsilon_R\right\} = 0 \tag{I-18}$$

Equation (I-18) leads to the generalized equation of motion:

$$\left(-\omega^2\left[\bar{M}_{FF}\right]+ i\omega\left[C_F\right]+\left[k_F\right]\right)\left\{\alpha_F\right\}-\omega^2\left[\bar{M}_{RF}\right]^T\left\{\alpha_R\right\}$$
$$=\left[X_1\right]^T\left\{f_{1m}\right\}+\left[X_2\right]^T\left\{f_{2m}\right\} \qquad \text{(I-19)}$$

where $$\left[\bar{M}_{FF}\right]=\left[X_1^T\,\bar{M}_{11}\,X_1+X_2^T\,\bar{M}_{22}\,X_2\right] \qquad \text{(I-20)}$$

In order to simplify the problem the generalized damping matrix C_F is assumed to be a diagonal matrix:

$$\left[C_F\right]=\left[X_1-TX_2\right]^T\left[C\right]\left[X_1-TX_2\right]=\frac{1}{\omega_F}\left[k_F\right]\left[g_F\right] \qquad \text{(I-21)}$$

where g_{F_i} is the structural damping coefficient in the i^{th} free-free mode and k_F is defined in Equation (I-4).

The rigid modal amplitude α_R is found by solving Equation (I-12):

$$\left\{\alpha_R\right\}=-\frac{1}{\omega^2}\left[\bar{M}_{RR}\right]^{-1}\left(\omega^2\left[\bar{M}_{RF}\right]\left\{\alpha_F\right\}+\left[T\right]^T\left\{f_{1m}\right\}+\left\{f_{2m}\right\}\right) \qquad \text{(I-22)}$$

Substituting Equation (I-22) into Equation (I-19) leads to the final response equation:

$$\left\{\alpha_F\right\}=\left[A_F\right]^{-1}\left(\left[B_1\right]\left\{f_{1m}\right\}+\left[B_2\right]\left\{f_{2m}\right\}\right) \qquad \text{(I-23)}$$

where:
$$\left[A_F\right]=-\omega^2\left(\bar{M}_{FF}-\bar{M}_{RF}^T\,\bar{M}_{RR}^{-1}\,\bar{M}_{RF}\right)+i\omega\left[C_F\right]+\left[k_F\right] \qquad \text{(I-24)}$$

$$\left[B_1\right]=\left[X_1\right]^T-\left[\bar{M}_{RF}^T\,\bar{M}_{RR}^{-1}\,T^T\right] \qquad \text{(I-25)}$$

$$\left[B_2\right]=\left[X_2\right]^T-\left[\bar{M}_{RF}^T\,\bar{M}_{RR}^{-1}\right] \qquad \text{(I-26)}$$

The Fourier transforms of the control point deflections are then obtained from Equation (I-9).

In case the pressure transducer locations are different from the control points, Equation (I-25) may be expressed in an alternate form as follows:

$$\left[B_1\right]=\left[Q_F\right]^T-\left[\bar{M}_{RF}^T\,\bar{M}_{RR}^{-1}\,Q_R^T\right]$$

where: $\left[Q_F\right]$ and $\left[Q_R\right]$ are the flexible and rigid modal matrices respectively, corresponding to the pressure transducer locations.

For an ergodic random pressure field, the PSD of the control point accelerations depends on the spatial distribution of the pressures. In the calculation, two extreme cases are considered:

1. Perfect spatially correlated pressure field:

$$\left(\phi_{\ddot{h}_1}(\omega)\right)_i = \frac{T}{\pi}\left|h_{1i}(\omega)\right|^2\left(\frac{\omega^2}{G}\right)^2 \tag{I-27}$$

where $\phi_{\ddot{h}_i}(\omega)$ is the PSD of acceleration at a control point, subscript i identifies the control point, T is the time span, G is the gravitational acceleration.

2. Spatially uncorrelated pressure field and $f_{2m} = 0$. The condition $f_{2m} = 0$ indicates that buffet pressures are applied only at the control points and not at the reference point.

$$\left[\phi_{\ddot{h}_1}(\omega)\right] = \frac{\omega^4}{G^2}\left[H(\omega)\right]\left[\phi_{f_{1m}}(\omega)\right]\left[H^*(\omega)\right]^T \tag{I-28}$$

where

$$\left(\phi_f(\omega)\right)_{ij} = \frac{T}{\pi}\left|f_{1m_j}(\omega)\right|^2 \delta_{ij} \tag{I-29}$$

and

$$\left[H(\omega)\right] = \left[X_1 - X_2\,\overline{M}_{RR}^{-1}\,\overline{M}_{RF}\right]\left[A_F^{-1}\right]\left[B_1\right] - \frac{1}{\omega^2}\left[X_2\,\overline{M}_{RR}^{-1}\,X_2^T\right] \tag{I-30}$$

Equation (I-28) is an expression for the acceleration PSD. On the right-hand side, by dropping the factor ω^4/G^2, the remaining portion gives the response (deformation) PSD of the aircraft. This latter expression is identical to the right hand of Equation (5-6).

APPENDIX II

COMPUTER PROGRAM MECHANIZATION OF FREQUENCY RESPONSE CALCULATION

The flow diagram to generate the free-free frequency response data of an aircraft is shown in Figure 102. There are nine functionally independent programs involved as described below:

1. Program F019

   It generates the flexibility matrices for wing, fuselage, and tail with reference point(s) fixed. Only beam elements with torsion and one-way bending stiffness are considered. The flexibility matrices are punched out by the program.

2. Program RF040

   It performs the free-free modal analysis for the complete aircraft upon receiving as input the flexibility, mass, and rigid body motion matrices of all components. The program generates in punched-out data form the free-free mode shapes and the natural frequencies in Hz.

3. Program AA

   It computes the corresponding values of reduced velocity $\left(k_r^{-1}\right)$ of the frequencies of interest which are consistent with those of the pressure input generated by program SPECTRAL. Additional input is the aircraft velocity, the reference semi-chord, and the prearranged indices for the frequency input.

4. Program RHM15

   It formulates the AIC matrices for the fuselage based on the slender body theory. Each computed AIC matrix which corresponds to a given reduced velocity $\left(k_r^{-1}\right)$ is stored on disc file Number 16 identified by its prearranged index number.

5. Program RF022

It formulates the AIC matrices for the wing and the tail based on the unsteady lifting surface theory. The computed AIC matrices which correspond to a given reduced velocity $\left(k_r^{-1}\right)$ and a specified Mach number are stored on Disc File Number 15 for the wing and on Disc File Number 17 for the tail, identified by the prearranged index number for that frequency $\left(\text{or } k_r^{-1}\right)$ respectively.

6. Program MØFIT

Since the pressure transducer locations are different from the control points on the wing, the computer program "MØFIT" is developed to compute the corresponding modal displacements at the pressure transducer locations for each flexible and rigid-body mode. Corresponding to each mode, the program defines the deformation curve of the elastic axis of the wing based on the least square of a polynomial up to the third order:

$$h = A_o + A_1 y + A_2 y^2 + A_3 y^3$$

The chordwise movements are assumed to be a rigid body rotation about the elastic axis.

Program MØFIT punches out the output matrices $[A][Q_F]$ and $[A][Q_R]$, where $[Q_F]$ and $[Q_R]$ are the flexible and rigid-body modal matrices corresponding to the transducer locations respectively, and $[A]$ is a diagonal matrix whose elements represent the wing subarea corresponding to the transducer locations. The products of matrices $[A][Q_F]$, $[A][Q_R]$ and the Fourier transforms of the measured pressures yield the appropriate modal forces acting on the wing.

7. Program R009H

It calculates the frequency response quantities (deflections, stress, etc.) due to external sinusoidal forces (i.e., the Fourier transforms of the external forces at that frequency) based on the Galerkin's method. The general input includes the free-free mode shapes, the corresponding natural frequencies, the rigid body modes, the modal damping coefficients, the matrices $[A]$ $[Q_F]$ and $[A]$ $[Q_R]$ from program MØFIT, and some parameters such as ρ, V, b_r, the reduced velocity, the corresponding S, etc. The frequency-dependent input includes Fourier transforms of the measured pressures at transducer locations and the AIC matrices which are read directly from

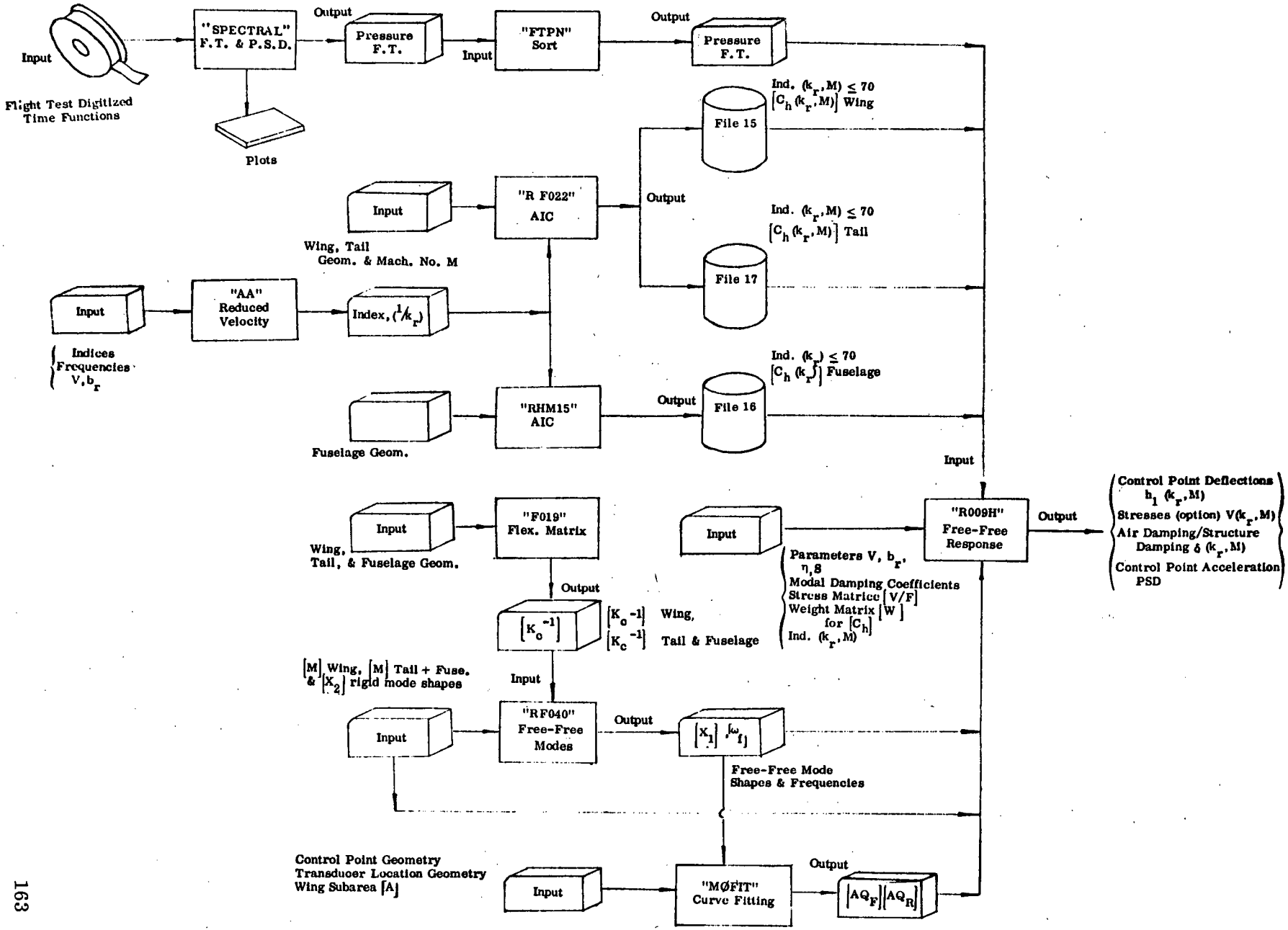

Figure 89. Flow Diagram for Generating Free-Free Response Data

the disc files. Two kinds of pressure spatial correlation are considered: perfect correlation and zero correlation.

8. Program SPECTRAL

The spectral analysis program generates the Fourier transforms and the power spectral data for all the recorded pressures and responses. The program receives the low-frequency digitized tape as input. It plots the output data listed below:

a. Fourier transforms
b. Auto- and cross-power spectral densities
c. Auto- and cross-correlation functions
d. Coherence functions

The Fourier transforms of the pressures are punched out in a consecutive order with a specified frequency increment.

9. Program FTPN

The program reads in and sorts the punched output (Fourier transforms of pressures) from program SPECTRAL. Its output is another set of punched cards in a specified format consistent with the input requirements of the frequency response computer program R009H.

APPENDIX III

MULTI-MODAL RESPONSE OF AIRCRAFT TO SEGMENTED STATIONARY RANDOM EXCITATION

The formulation is an expansion of a nonstationary response analysis developed in References 51–53. The origin of the references may be traced to still earlier work on nonstationary analysis (for instance, Reference 54). The input function is assumed to be the sum of n functions defined in consecutive time segments. Each function is the product of $e_r(t)$ and $f_{\ell r}(t)$. $e_r(t)$ is a deterministic function. In the present study, it is assumed to be unity within the time span (t_{ra}, t_{rb}) and zero elsewhere. $f_{\ell r}(t)$ is a stationary random function. The development of the multi-modal response due to the segmentwise stationary input modal forces $Q_\ell(t)$ are described below.

I. Modal Forces

$$Q_\ell(t) = \sum_{r=1}^{n} e_r(t)\, f_{\ell r}(t) \qquad \text{(III-1)}$$

ℓ = mode index

Cross correlation of modal forces Q_ℓ and Q_m

$$R_{Q_\ell Q_k}(t_1, t_2) = \sum_{r=1}^{n} \sum_{s=1}^{n} e_r(t_1)\, e_s(t_2)\, R_{f_{\ell r} f_{ks}}(t_1 - t_2) \qquad \text{(III-2)}$$

ℓ, k = mode indices

r, s = time segment indices

Cross PSD of modal forces Q_ℓ and Q_k:

$$S_{Q_\ell Q_k}(\omega_1, \omega_2) = \frac{1}{4\pi^2} \iint_{-\infty}^{\infty} R_{Q_\ell Q_k}(t_1, t_2) \exp\left[-i(\omega_1 t_1 - \omega_2 t_2)\right] dt_1\, dt_2$$

$$= \sum_{r=1}^{n} \sum_{s=1}^{n} \int_{-\infty}^{\infty} S_{f_{\ell r} f_{ks}}(\omega)\, A_r(\omega - \omega_1)\, A_s^*(\omega - \omega_2)\, d\omega \quad \text{(III-3)}$$

ω_1, ω_2 = frequency coordinates

$$A_r(\omega - \omega_1) = \frac{1}{2\pi} \int_{-\infty}^{\infty} e_r(t_1) \exp\left[i(\omega - \omega_1) t_1\right] dt_1$$

$$= \frac{\exp\left[i(\omega - \omega_1) t_{rb}\right] - \exp\left[i(\omega - \omega_1) t_{ra}\right]}{2\pi i (\omega - \omega_1)} \quad \text{(III-4)}$$

$A_r(\omega - \omega_1)$ is the Fourier transform of $e_r(t_1)$.

II. Segmented Stationary Modal Forces

Modal forces for r^{-th} segment

$$\left\{f_r(t)\right\} = [X]^T \lceil A \rfloor \left\{p_r(t)\right\} \quad \text{(III-5)}$$

where

$[X] = \left[[Q_F][Q_R]\right]$ = modal matrix corresponding to pressure transducer locations

$[Q_F]$ = free-free mode shapes

$[Q_R]$ = rigid body mode shapes

$\{p(t)\}$ = measured pressures

$\lceil A \rfloor$ = subareas associated to transducers

PSD matrix of segmented stationary modal forces f_r and f_s

$$\left[S_{f_r f_s}(\omega)\right] = [X]^T \lceil A \rfloor \left[S_{p_r p_s}(\omega)\right] \lceil A \rfloor [X] \qquad \text{(III-6)}$$

where

$$\left[S_{p_r p_s}(\omega)\right]_{ij} = \frac{\Delta T}{2\pi} F_{p_{ri}}(\omega, \Delta T_r) F^*_{p_{sj}}(\omega, \Delta T_s). \begin{cases} 1 & \text{perfect spatial correlation} \\ \delta_{ij} & \text{zero spatial correlation} \end{cases} \qquad \text{(III-7)}$$

i, j = indices of spatial locations

ΔT = time span for each segment

$F_p(\omega, \Delta T)$ = Fourier transforms of measured pressures over a finite period ΔT.

III. Modal Responses

PSD matrix of modal coordinates α

$$[S_\alpha(\omega_1, \omega_2)] = [H(\omega_1)] [S_Q(\omega_1, \omega_2)] [H^*(\omega_2)]^T$$

$$= \sum_{r=1}^{n} \sum_{s=1}^{n} \int_{-\infty}^{\infty} A_r(\omega - \omega_1) [H(\omega_1)] [X]^T \lceil A \rfloor \left[S_{p_r p_s}(\omega)\right] \lceil A \rfloor$$

$$[X] [H^*(\omega)_2]^T A^*_s(\omega - \omega_2)\, d\omega \qquad \text{(III-8)}$$

where

$[H(\omega)]$ = the modal transfer function matrix. Similar matrix is shown in Equation (5-6) in the stationary analysis.

IV. Structural Response

Structural deflection response at a specified location (i.e., accelerometer location)

$$w = \lfloor Y \rfloor \{\alpha\} \qquad \text{(III-9)}$$

where

$\lfloor Y \rfloor$ = the modal shape matrix corresponding to the specified location

Power spectral density of w and mean square value $\overline{w^2(t)}$.

$$S_w(\omega_1, \omega_2) = \sum_{r=1}^{n}\sum_{s=1}^{n} \int_{-\infty}^{\infty} A_r(\omega - \omega_1) \lfloor Y \rfloor \left[H(\omega_1)\right] [X]^T \lceil A \rfloor \left[S_{p_r p_s}(\omega)\right]$$

$$\lceil A \rfloor [X] \left[H^*(\omega_2)\right]^T \left\{Y^T\right\} A_s^*(\omega - \omega_2)\, d\omega \qquad \text{(III-10)}$$

$$\overline{w^2(t)} = \iint_{-\infty}^{\infty} S_w(\omega_1, \omega_2) \exp\left[i(\omega_1 - \omega_2)\, t\right] d\omega_1\, d\omega_2$$

$$= \sum_{r=1}^{n}\sum_{s=1}^{n} \int_{-\infty}^{\infty} \lfloor Y \rfloor \left[I_r(t, \omega)\right] [X]^T \lceil A \rfloor \left[S_{p_r p_s}(\omega)\right] \lceil A \rfloor [X]$$

$$\left[I_s^*(t, \omega)\right]^T \left\{Y^T\right\} d\omega \qquad \text{(III-11)}$$

where

$$\left(I_r(t, \omega)\right)_{ij} = \int_{-\infty}^{\infty} \left(H(\omega_1)\right)_{ij} A_r(\omega - \omega_1) \exp(i\omega_1 t)\, d\omega_1 \qquad \text{(III-12)}$$

= an influence function corresponding to time segment r.

$\left(H(\omega)\right)_{ij}$ = elements of the modal matrix $\left[H(\omega)\right]$ as shown in section V below

i, j = row and column indices

V. Aircraft Modal Transfer Functions

The dynamic equation of the aircraft in terms of the free-free and rigid body modes is:

$$\begin{bmatrix} -\omega^2[\bar{M}_{FF}] + \lceil M_F \omega_F (\omega_F + ig_F \omega) \rfloor & -\omega^2[\bar{M}_{RF}]^T \\ -\omega^2[\bar{M}_{RF}] & -\omega^2\left[\bar{M}_{RR}\right] \end{bmatrix} \begin{Bmatrix} \{\alpha_F\} \\ \{\alpha_R\} \end{Bmatrix} = \begin{Bmatrix} [Q_F]^T \lceil A \rfloor \{Fp\} \\ [Q_R]^T \lceil A \rfloor \{Fp\} \end{Bmatrix} \qquad \text{(III-13)}$$

The modal transfer function matrix is:

$$\left[H(\omega)\right] = \begin{bmatrix} -\omega^2\left[\bar{M}_{FF}\right] + \left[M_F\omega_F(\omega_F + ig_F\omega)\right] & -\omega^2\left[\bar{M}_{RF}^T\right] \\ -\omega^2\left[\bar{M}_{RF}\right] & -\omega^2\left[\bar{M}_{RR}\right] \end{bmatrix}^{-1} \qquad \text{(III-14)}$$

where

$\{\alpha_F\}$ = free-free modal amplitudes

$\{\alpha_R\}$ = rigid body modal amplitudes

$\{F_p\}$ = Fourier transforms of the measured pressures

M_F = generalized masses

ω_F = non-zero natural circular frequencies

g_F = modal damping coefficients

For $\left[M_{22}\right] \equiv 0$, $\left[\bar{M}_{22}\right] \equiv 0$ case, $\left[T^T M_{11} X_1\right] = 0$, the modal mass terms are defined below:

$$\left.\begin{aligned} \left[\bar{M}_{FF}\right] &= \left[X_1^T \bar{M}_{11} X_1\right] \\ \left[\bar{M}_{RF}\right] &= \left[T^T \bar{M}_{11} X_1\right] \\ \left[\bar{M}_{RR}\right] &= \left[T^T \bar{M}_{11} T\right] \end{aligned}\right\} \quad \text{AIC included} \qquad \text{(III-15)}$$

The detail derivation and the definitions of the terminologies used in Section V are given in Appendix I of this report related to stationary response analysis.

VI. Modified Impedance functions

Assuming that no aeroelastic coupling exists between the rigid body modes and the free-free modes, the impedance function matrix may be rewritten as follows:

$$\left[H(\omega)\right]^{-1} = \begin{bmatrix} -\omega^2\left[\overline{M}_{FF}\right] + \left[M_F\omega_F(\omega_F + ig_F\omega)\right] & 0 \\ 0 & Z_R(\omega) \end{bmatrix} \qquad \text{(III-16)}$$

In actual computation the following expressions are used:

$$\left[\overline{M}_{FF}(\omega)\right]_{\ell\ell} = (M_F)_{\ell\ell}\left(g_A(\omega)\right)_\ell \simeq (M_F)_\ell\left(g_A(\omega_\ell)\right)_\ell \qquad \text{(III-17)}$$

$$g_{A_\ell} = 1 + \epsilon_\ell + i\beta_\ell$$

It is noted that the modal aero-damping coefficient at $\omega = \omega_\ell$ approximately equals to $(\epsilon_\ell + i\beta_\ell)/(1-\beta)$. ϵ_ℓ and β_ℓ will be used later in Equation (III-19).

$Z_R(\omega)$ is a (2 x 2) matrix corresponding to the downward displacement and the pitch angle. The elements of $Z_R(\omega)$ are:

$$\left[Z_R(\omega)\right]_{11} = -\frac{1}{2}\rho V^2 S\left[\frac{\omega^2 c}{2V^2}\left(\frac{4m}{\rho Sc} - C_{z\dot{\alpha}}\right) + \frac{i\omega}{V}C_{z\alpha}\right]$$

$$\left[Z_R(\omega)\right]_{12} = -\frac{1}{2}\rho V^2 S\left(\frac{i\omega c}{2V}\right)\left(\frac{4m}{\rho Sc} + C_{zq}\right)$$

$$\left[Z_R(\omega)\right]_{21} = -\frac{1}{2}\rho V^2 Sc\left(-\frac{\omega^2 c}{2V^2}C_{m\dot{\alpha}} + \frac{i\omega}{V}C_{m\alpha}\right)$$

$$\left[Z_R(\omega)\right]_{22} = -\frac{1}{2}\rho V^2 Sc\left(\frac{\omega^2 c^2}{4V^2}\, i_B + \frac{i\omega c}{2V}C_{mq}\right) \qquad \text{(III-18)}$$

where

$$i_B = 8(\rho Sc^3)^{-1} B$$

B = aircraft moment of inertia about the y-axis.

The detail derivation of the impedance matrix $Z_R(\omega)$ and the definitions of the aerodynamic derivatives in (III-18) may be found in Chapter 6, Reference 55. In the

present case, because of lack of tail surfaces dynamic load data, only the rigid body plunging mode is used. In other words, $Z_R(\omega)$ in Equation (III-16) is replaced by $Z_R(\omega)_{11}$.

For a free-free mode with index ℓ, the modal influence function is:

$$\left(I_r(t,\omega)\right)_{\ell\ell} = \frac{1}{2\pi i m_\ell}\int_{-\infty}^{\infty} \frac{\left\{\exp\left[i(\omega-\omega_1)t_{rb}\right] - \exp\left[i(\omega-\omega_1)\,t_{ra}\right]\right\}\exp\left(i\omega_1 t\right)}{(\omega-\omega_1)\left[\omega_\ell^2 + ig_\ell\omega_1\omega_\ell - (1+\epsilon_\ell+i\beta_\ell)\omega_1^2\right]}\, d\omega_1 \tag{III-19}$$

where

$$m_\ell = (M_F)_{\ell\ell}$$

$$g_\ell = (g_F)_{\ell\ell}$$

When $g_\ell > |\beta_\ell|$, three poles exist in integral (III-19), one of which is located on the positive real axis of the ω_1-plane; the remaining two are located on the upper half of the complex plane.

For the plunging mode, the modal influence function is:

$$\left(I_r(t,\omega)\right)_{RR} = \frac{i}{\pi\rho VS}\int_{-\infty}^{\infty} \frac{\left\{\exp\left[i(\omega-\omega_1)t_{rb}\right] - \exp\left[i(\omega-\omega_1)\,t_{ra}\right]\right\}\exp\left(i\omega_1 t\right)}{(\omega-\omega_1)\,\omega_1\left[\frac{c}{2V}\left(\frac{4m}{\rho Sc} - C_{z\dot{\alpha}}\right)\omega_1 + C_{z\alpha}\,i\right]}\, d\omega_1 \tag{III-20}$$

The three poles of the integral I_r for the rigid body mode are located at the origin, the positive real axis and the positive imaginary axis of the complex ω_1-plane.

In Equations (III-19, III-20), the corresponding influence functions for modal accelerations may be obtained by adding a factor $(-\frac{\omega}{G})^2$ to the two integrands. These functions are denoted by $\left(I_r^a(t,\omega)\right)_{\ell\ell}$, $\left(I_r^a(t,\omega)\right)_{RR}$.

VII. Acceleration Response of the Aircraft

$$\overline{\ddot{w}^2(t)} = \int_{-\infty}^{\infty} \sum_{r=1}^{n} \sum_{s=1}^{n} \lfloor Y \rfloor \lceil I_r^a(t,\omega) \rfloor \left[AX\right]^T \left[S_{p_r p_s}(\omega)\right] \left[AX\right]$$

$$\lceil I_s^a{}^*(t,\omega) \rfloor \left\{Y^T\right\} d\omega \qquad \text{(III-21)}$$

where

$$\left[S_{p_r p_s}(\omega)\right] = \frac{1}{\Delta\omega} \left\{F_{p_r}(\omega)\right\} \lfloor F_{p_s}^{*\,T}(\omega) \rfloor$$

$$\left[S_{p_s p_r}(\omega)\right] = \left[S_{p_r p_s}^*(\omega)\right]^T$$

$$\left[S_{p_r p_s}(-\omega)\right] = \left[S_{p_r p_s}^*(\omega)\right]^T$$

$$\left[S_{p_s p_r}(-\omega)\right] = \left[S_{p_r p_s}(\omega)\right]^T$$

$$\left\lceil I_r^a(t,\omega) \right\rfloor = \begin{bmatrix} I_{r_F}^a(t,\omega) & 0 \\ 0 & I_{r_R}^a(t,\omega) \end{bmatrix} \qquad \text{(III-22)}$$

$\Delta\omega$ = frequency increment = $2\pi/\Delta T$

For fth free-free mode, the influence function is obtained by carrying out the integration:

$$I_{r_f}^a(t,\omega) = \frac{1}{2Gm_f(1+\epsilon_f+i\beta_f)\left[(ib_f-\omega)^2-a_f^2\right]a_f} \cdot \begin{cases} 0 & t < t_{ra} \\ \left[2a_f\omega^2 \exp(i\omega t) - P_f(t_{ra},t,\omega)\right] & t_{ra}<t<t_{rb} \\ \left[P_f(t_{rb},t,\omega)-P_f(t_{ra},t,\omega)\right] & t_{rb}<t \end{cases}$$

(III-23)

where

$$a_f = \frac{\omega_f}{1 + \epsilon_f + i\beta_f}\left(1 + \epsilon_f + i\beta_f - g_f^2/4\right)^{1/2}$$

$$b_f = \frac{\omega_f}{1 + \epsilon_f + i\beta_f}\frac{g_f}{2}$$

$$P_f(t_o, t, \omega) = \exp(i\omega t_o)\ \{-(-a_f + ib_f - \omega)(a_f + ib_f)^2 \exp\left[i(a_f + ib_f)(t - t_o)\right]$$

$$+ (a_f + ib_f - \omega)(-a_f + ib_f)^2 \exp\left[i(-a_f + ib_f)(t - t_o)\right]\} \qquad \text{(III-24)}$$

and G = gravitational acceleration.

For the plunging mode, integration of the modified expression (III-20) yields:

$$I^a_{r_R}(t, \omega) = \frac{1}{(m + \rho Sc)(\omega - i\gamma)G} \cdot$$

$$\begin{cases} 0 & t < t_{ra} \\ \{\omega \exp(i\omega t) - \gamma i \exp(i\omega t_{ra}) \exp\left[-\gamma(t - t_{ra})\right]\} & t_{ra} < t < t_{rb} \\ i\gamma\{\exp(i\omega t_{rb}) \exp\left[-\gamma(t - t_{rb})\right] - \exp(i\omega t_{ra}) \exp\left[-\gamma(t - t_{ra})\right]\} & t_{rb} < t \end{cases}$$

(III-25)

$$\gamma = \frac{-C_{z\alpha}}{\frac{c}{2V}\left(\frac{4m}{\rho Sc} - C_{z\dot{\alpha}}\right)} \qquad \text{(III-26)}$$

The infinite frequency integral in expression $\overline{\ddot{w}^2(t)}$ may be truncated as follows:

$$\overline{\ddot{w}^2(t_k)} \cong \Delta\omega \sum_{i=i_1}^{i_2} \sum_{r=1}^{n} \sum_{s=1}^{n} [Y] \left(\left[I_r^a (t_k, \omega_i) \right] [AX]^T \left[S_{p_r p_s} (\omega_i) \right] [AX] \left[I_s^{a*} (t_k, \omega_i) \right] + \left[I_r^a (t_k, -\omega_i) \right] [AX]^T \left[S^*_{p_r p_s} (\omega_i) \right] [AX] \left[I_s^{a*} (t_k, -\omega_i) \right] \right) \{Y^T\} \quad \text{(III-27)}$$

where

$\omega_{i_1} = i_1 \Delta\omega$ = lower limit of integration

$\omega_{i_2} = i_2 \Delta\omega$ = upper limit of integration

The first summation sign on the right hand of equation (III-27) covers the frequency range $(\omega_{i_1}, \omega_{i_2})$ with increment $\Delta\omega$. In the computation based on dynamic buffet pressure of Run 2, Flight 871, the following data are used:

$\omega_f/2\pi$ = 4.049, 6.522, 8.378 Hz

$\omega_{i_1}/2\pi$ = 1.465 Hz

$\omega_{i_2}/2\pi$ = 20.0 Hz

} 38 frequency values

$\Delta\omega/2\pi$ = 0.488 Hz

$t_{1a} = 0$, $t_{1b} = t_{2a} = 2.20$ sec, $t_{2b} = t_{3a} = 4.55$ sec, $t_{3b} = t_{4a} = 6.90$ sec,

$t_{4b} = 9.10$ sec

A computer program flow chart showing the computation procedure is given in Figure 90. The numerical results based on the above mentioned flight data are presented in Subsection 5.4 where the time varying PSD's of C.G. and wingtip accelerations are given in Figures 85-87.

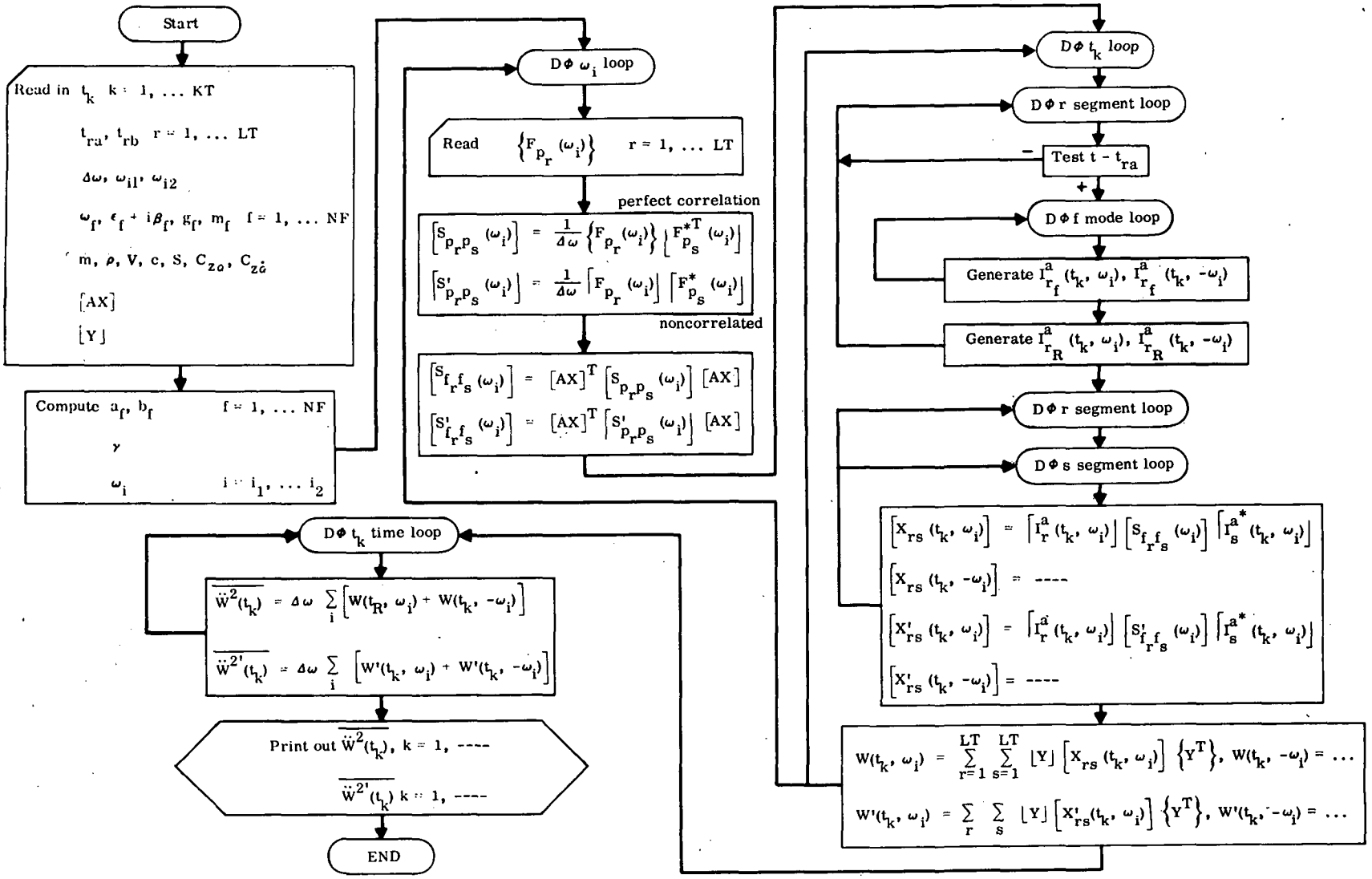

FIGURE 90. COMPUTER PROGRAM FLOW CHART

REFERENCES

1. Rauscher, N., "Model Experiments on Flutter at the Massachusetts Institute of Technology," J. Aeronautical Sciences, Vol. 3, No. 2., March 1936.

2. Studer, H.L., "Experimental Research on Flutter," Mitt. Institute Aerodyn. Zurich, No. 4/5, 1936.

3. Bisplinghoff, R.L., Ashley, H., and Halfman, R.L., Aeroelasticity, Addison-Wesley Publication Co. Inc., Reading, Mass., 1955, p. 626.

4. Huston, Wilbur B., Rainey, A. Gerald, and Baker, T.F., "A Study of the Correlation Between Flight and Wind-Tunnel Buffeting Loads," NACA RM L55E16b, 1955.

5. Huston, Wilbur B., and Skopinski, T.H., "Probability and Frequency Characteristics of Some Flight Buffet Loads," NACA TN 3733, 1956.

6. Huston, Wilbur B., and Skopinski, T.H., "Measurement and Analysis of Wing and Tail Buffeting Loads on a Fighter-Type Airplane," NACA TN 3080, 1954.

7. Skopinski, T.H., and Huston, Wilbur B., "A Semiempirical Procedure for Estimating Wing Buffet Loads in the Transonic Region," NACA RM L56E01, 1956.

8. Humphreys, M.D., "Pressure Pulsations on Rigid Airfoils," NACA RM L51112, December 1951.

9. Coe, C.F., and Mellenthin, J.A., "Buffeting Forces on Two-dimensional Airfoils as Affected by Thickness and Thickness Distribution," NACA RM A53K24, February 1954.

10. Sutton, F.B., and Lautenberger Jr., W., "A Buffet Investigation at High Subsonic Speeds of Wing-Fuselage-Tail Combinations having Swept-Back Wings with NACA 64A Thickness Distributions, Fences, Leading Edge Extension, and Body Contouring," NACA RMA 54F06a, August 1957.

11. Chapman, D.R., Kuehn, D.M., and Larson, H.K., "Investigation of Separated Flows in Supersonic and Subsonic Streams with Emphasis on the Effect of Transition," NACA TR-1356, 1958.

12. Pearcy, H.H., "A Method for the Prediction for the Onset of Buffeting and Other Separation Effects from Wind Tunnel Tests on Rigid Models," ARC Report No. 20631, AGARD Report 223, 1958.

13. Lachmann, G.V., Ed., Boundary Layer and Flow Control, First Edition, Volume 2, Pergamon Press, New York, 1961, pp. 1166-1344; Chapter by Pearcey, H.H., "Shock-Induced Separation and Its Prevention by Design and Boundary Layer Control."

14. Eckhaus, W., "A Theory of Transonic Aileron Buzz, Neglecting Viscous Effects," J. Aerospace Sciences, 29, 6, June 1962.

15. Landahl, M. T., Unsteady Transonic Flow, Chapter 10, p. 110, Pergamon Press, New York, 1961.

16. Mabey, D. G., "Comparison of Seven Wing Buffet Boundaries Measured in Wind Tunnel and in Flight," C. P. No. 840, ARC, 1966.

17. Mitchell, C. G. B., "Calculation of the Low-Speed Buffeting of a Slender Wing Aircraft," RAE Symposium on Structural Dynamics, Paper D-4.

18. Blackwell, J. A., Jr., "Effect of Reynolds Number and Boundary-Layer Transition Location on Shock-Induced Separation," NASA TN D-5003, December 1968.

19. Loving, D. L., "Wind Tunnel-Flight Correlation of Shock-Induced Separated Flow," NASA TN D-3580, 1966.

20. Stanewsky, E., and Hicks, G., "Scaling Effects on Shock-Boundary Layer Interaction in Transonic Flow," AFFDL TR-68-11, March 1968.

21. Jones, J. L., "Problems of Flow Simulation in Wind Tunnels," AIAA Paper No. 69-660, June 1968.

22. Ray, E. J., and Taylor, R. T., "Buffet and Static Aerodynamics Characteristics of a Systematic Series of Wings Determined From a Subsonic Wind-Tunnel Study," NASA TN D-5805, June 1970.

23. Cahill, J. F., and Cooper, B. L., "Flight Test Investigation of Transonic Shock-Boundary Layer Phenomena," AFFDL TR-68-84, July 1968.

24. Fischel, J., and Friend, E. L., "Preliminary Assessment of Effects of Wing Flaps on High Subsonic Flight Buffet Characteristics of Three Airplanes," NASA TM X-2011, May 1970.

25. Mayes, J. F., et al., "Transonic Buffet Characteristics of a 60° Swept Wing with Design Variations," J. Aircraft, 7, 6, p. 524, Dec. 1970.

26. Titiriga, A., Jr., "F-5A Transonic Buffet Flight Test," Report No. AFFDL-TR-69-110, Air Force Flight Dynamics Laboratory, Oct. 1969.

27. Damstrom, E. K., and Mayes, J. F., "Transonic Flight and Wind Tunnel Buffet Onset Investigation of the F-8D Aircraft," J. 8, 4, April 1971.

28. Hollingsworth, E. G., and Cohen, M., "Determination of F-4 Aircraft Transonic Flight Buffet Characteristics," J. Aircraft, Volume 8, Number 10, pp. 757-763, October 1971.

29. Cohen, M., "Buffet Characteristics of the Model F-4 Airplane in the Transonic Flight Regime," AFFDL-TR-70-56, April 1970.

30. Mullans, R. E., and Lemley, C. E., "Buffet Dynamic Loads During Transonic Maneuvers," AFFDL-TR-72-46, July 1972.

31. Jacobs, F. D., "F-5A/B Dynamic Response, Gust Loads, Flight Test Results," Rept NOR-63-39, Northrop Corporation, August 1966.

32. Hwang, C., Kamberg, B. D., Pi, W. S., and Cross, A. K., "Design Calculations on Proven Trainer and Fighter Aircraft for the Verification of a Gust Design Procedure," AFFDL-TR-66-82, July 1966.

33. Kistler, A. L., "Fluctuating Wall Pressure Under a Separated Supersonic Flow," J. Acoustical Soc. Am. 36, 3, p. 543, March 1964.

34. Bendat, J. S., Enochson, L. D., and Piersol, A. G., "Test for Randomness, Stationarity, Normality, and Comparison of Spectra," AFFDL TR-65-74, August 1965.

35. Speaker, W. F., and Ailman, C. M., "Spectra and Space-Time Correlations of the Fluctuating Pressure at a Wall Beneath a Supersonic Turbulent Boundary Layer Perturbed by Steps and Shock Waves," NASA CR-486, 1966.

36. Coe, C. F., and Rechtien, R. D., "Scaling and Spatial Correlation of Surface Pressure Fluctuations in Separated Flow at Supersonic Mach Numbers," Proceedings AIAA 10th Structures, Structural Dynamics, and Materials Conference, April 1969.

37. Batchelor, G. K., The Theory of Homogeneous Turbulence, The Cambridge University Press, 1953.

38. Townsend, A. A., The Structure of Turbulent Shear Flow, The Cambridge University Press, 1956.

39. Hinze, J. O., Turbulence, New York: McGraw-Hill Book Co., 1959.

40. Fung, Y. C., An Introduction to the Theory of Aeroelasticity, New York: John Wiley and Sons, 1956.

41. Watkins, C. E., Runyan, H. L., and Woolston, D. S., "On the Kernel Function of the Integral Equations Relating the Lift and Downwash Distributions of Oscillating Finite Wings in Subsonic Flow," NASA Report 1234, 1955.

42. Runyan, H. L., and Woolston, D. S., "Method of Calculating the Aerodynamic Loading on Oscillating Finite Wing in Subsonic and Sonic Flow," NASA Report 1322, 1957.

43. Rodden, W. P., and Revell, J. D., "The Status of Unsteady Aerodynamic Influence Coefficients," SMF Fund Paper No. FF-55, January 1962.

44. Rodden, W. P., Forkas, E. F., and Oyama, R. K., "Subsonic and Sonic Aerodynamic Influence Coefficients from Unsteady Lifting Surface Theory: Analytical Development and Procedure for IBM 7090 Computer," Report NOR 61-056, Northrop Corporation, April 1961.

45. Bennett, F. V., and Pratt, K. G., "Calculated Responses of a Large Sweptwing Airplane to Continuous Turbulence with Flight-Test Comparison," NASA Technical Report R-69, 1960.

46. Nielson, J. N., Missile Aerodynamics, McGraw-Hill Book Company, Inc., New York, N. Y., 1960.

47. Bendat, J. S., and Piersol, A. G., Measurement and Analysis of Random Data, John Wiley & Sons, Inc., 1966.

48. Fung, Y. C., An Introduction to the Theory of Aeroelasticity, John Wiley & Sons, Inc., New York, 1955.

49. Friend, E. L., and Sefic, W. J., "Flight Measurements of Buffet Characteristics of the F-104 Airplane for Selected Wing Flap Deflections," NASA TN D-6943, August 1972.

50. Newman, M., and Ojalvo, I. U., "Nonzero Free-Free Frequencies of Structures Idealized by Matrix Methods," AIAA Journal, 7, 12, p. 2343, September 1969.

51. Caughey, T. K., and Stumpf, H. J., "Transient Response of a Dynamic System Under Random Excitation," Transactions of the ASME; Ser. E: Journal of Applied Mechanics, Vol. 28, No. 4, Dec. 1961, pp. 563-566.

52. Barnoski, R. L., and Maurer, J. R., "Mean-Square Response of Simple Mechanical Systems to Nonstationary Random Excitation," Transactions of the ASME; Ser. E: Journal of Applied Mechanics, Vol. 36, No. 2, June 1969, pp. 221-227.

53. Holman, R. E., and Hart, G. C., "Structural Response to Segmented Nonstationary Random Excitation," AIAA Journal, 10, 11, November 1972, pp. 1473-1478.

54. Silverman, R. A., "Locally Stationary Random Processes," Trans. IRE, Inf. Theory, IT-3, September 1957.

55. Etkin, B., Dynamics of Flight, John Wiley & Sons, Inc., New York, 1959.

NATIONAL AERONAUTICS AND SPACE ADMINISTRATION
WASHINGTON, D.C. 20546

OFFICIAL BUSINESS
PENALTY FOR PRIVATE USE $300

SPECIAL FOURTH-CLASS RATE
BOOK

POSTAGE AND FEES PAID
NATIONAL AERONAUTICS AND
SPACE ADMINISTRATION
451

U.S.MAIL

POSTMASTER: If Undeliverable (Section 158 Postal Manual) Do Not Return

"The aeronautical and space activities of the United States shall be conducted so as to contribute . . . to the expansion of human knowledge of phenomena in the atmosphere and space. The Administration shall provide for the widest practicable and appropriate dissemination of information concerning its activities and the results thereof."

—NATIONAL AERONAUTICS AND SPACE ACT OF 1958

NASA SCIENTIFIC AND TECHNICAL PUBLICATIONS

TECHNICAL REPORTS: Scientific and technical information considered important, complete, and a lasting contribution to existing knowledge.

TECHNICAL NOTES: Information less broad in scope but nevertheless of importance as a contribution to existing knowledge.

TECHNICAL MEMORANDUMS: Information receiving limited distribution because of preliminary data, security classification, or other reasons. Also includes conference proceedings with either limited or unlimited distribution.

CONTRACTOR REPORTS: Scientific and technical information generated under a NASA contract or grant and considered an important contribution to existing knowledge.

TECHNICAL TRANSLATIONS: Information published in a foreign language considered to merit NASA distribution in English.

SPECIAL PUBLICATIONS: Information derived from or of value to NASA activities. Publications include final reports of major projects, monographs, data compilations, handbooks, sourcebooks, and special bibliographies.

TECHNOLOGY UTILIZATION PUBLICATIONS: Information on technology used by NASA that may be of particular interest in commercial and other non-aerospace applications. Publications include Tech Briefs, Technology Utilization Reports and Technology Surveys.

Details on the availability of these publications may be obtained from:

SCIENTIFIC AND TECHNICAL INFORMATION OFFICE

NATIONAL AERONAUTICS AND SPACE ADMINISTRATION

Washington, D.C. 20546